

HIGH ACCURACY WIRELESS RANGING FOR PHASE ALIGNMENT IN DISTRIBUTED
MICROWAVE BEAMFORMING ARRAYS

By

Sean Michael Ellison

A DISSERTATION

Submitted to
Michigan State University
in partial fulfillment of the requirements
for the degree of

Electrical Engineering – Doctor of Philosophy

2020

ABSTRACT

HIGH ACCURACY WIRELESS RANGING FOR PHASE ALIGNMENT IN DISTRIBUTED MICROWAVE BEAMFORMING ARRAYS

By

Sean Michael Ellison

In recent years, there has been an increasing interest in distributed antenna arrays due to their potential to provide improvements in performance, scalability, robustness, and cost over classic phased antenna arrays. Distributed arrays synthesize a large aperture using small, low-cost, and low-power devices, supporting improvements that would otherwise be too costly or bulky to achieve in a single system. Such arrays also have the flexibility to be scaled by adding or removing elements from the array, depending on the application at hand. Within distributed antenna arrays, there are generally two classes that are considered: incoherent distributed arrays, where little or no coordination is performed between nodes in the array, yielding a collection of individual wireless systems; and coherent distributed arrays, where element coordination is performed at the level of the radio frequency phase. While incoherent arrays are easier to implement, their improvements, such as gain and signal-to-noise ratio, generally scale only as the square-root of the number of elements, yielding diminishing returns. Coherent arrays achieve sensitivity improvements directly proportional to the number of elements in the array, yielding significant improvements as the array scales. However, distributed coherence requires significantly more coordination between nodes. The electrical states that need to be aligned to enable coherent beamforming include: each device's internal clock frequencies; relative timing of information symbols; and alignment of the beamforming phase. In general, there are two methods to achieve alignment: closed-loop and open-loop. Closed loop is only feasible to applications that have reliable feedback from the receive location, such as communications systems. Open-loop requires the nodes to coordinate without feedback, but opens the application space to instances where there is no feedback from the destination such as radar and remote sensing.

In this work, I focus on the alignment of the phase of the beamforming signals in open-loop coherent distributed antenna arrays. I present a distributed antenna array supporting open-loop distributed beamforming at 1.5 GHz. Based on a scalable, high-accuracy internode ranging technique, I demonstrate open-loop beamforming experiments using three transmitting nodes. To support distributed beamforming without feedback from the destination, the relative positions of the nodes in the distributed array must be known with accuracies below $\frac{\lambda}{15}$ of the beamforming carrier frequency to ensure that the array maintains at least 90% coherent beamforming gain at the receive location. For operations at microwave frequencies, this leads to range estimation accuracies of centimeters or less. I present scalable, high-accuracy waveforms and new approaches to refine range measurements to significantly improve the estimation accuracy. Using one of the designed waveforms with a three-node array, I demonstrate high-accuracy ranging simultaneously between multiple nodes, from which phase corrections on two secondary nodes are implemented to maintain beamforming with the primary node, thereby supporting open-loop distributed beamforming. Upon movement of the nodes, the range estimation is used to dynamically update the phase correction, maintaining beamforming as the nodes move. I show the first open-loop distributed beamforming at 1.5 GHz with two-node and three-node arrays, demonstrating the ability to implement and maintain phase-based beamforming without feedback from the destination.

TABLE OF CONTENTS

LIST OF TABLES	vii
LIST OF FIGURES	viii
CHAPTER 1 INTRODUCTION	1
CHAPTER 2 RANGING WAVEFORM CLASSIFICATION METRICS AND CLASSIC RANGING WAVEFORMS	16
2.1 Derivation of Waveform Estimation Characteristics	16
2.1.1 Ambiguity Function	16
2.1.2 Cramer_Rao Lower Bound (CRLB)	17
2.1.3 Relative Positional and Oscillator Phase Accuracy Requirements to Coherently Beamform	20
2.1.4 Signal-to-Noise Ratio (SNR)	23
2.2 Radar Ranging Waveforms	24
2.2.1 Linear Frequency Modulated Waveform (LFMW)	24
2.2.2 Stepped-Frequency Waveform (SFW)	27
2.2.3 Pulsed Two-Tone Waveform (PTTW)	34
CHAPTER 3 WAVEFORMS DESIGNED FOR HIGH-ACCURACY RANGING FOR DISTRIBUTED BEAMFORMING ARRAYS	40
3.1 Time Domain Duplex: Joint Range-Doppler Estimation Using Prolate Spheroidal Wave Functions (PSWF)	40
3.1.1 Theory of Prolate Spheroidal Wave Functions	41
3.1.2 Numerical Approximation of the PSWFs	42
3.1.3 Range and Doppler Estimation Bounds	44
3.1.4 Remote Sensing Waveform Design Based on PSWF of the Zeroth Order	45
3.1.4.1 Simulation	55
3.1.4.2 Measurements	56
3.2 Time Domain Duplex: Joint Phase Alignment and Frequency Transfer for Wideband Systems	59
3.2.1 Waveform Design	59
3.2.1.1 Ambiguity Function	60
3.2.1.2 Range Estimation Lower Bounds	74
3.2.1.3 Frequency Estimation Lower Bound	76
3.2.2 Experimental Setup and Signal Processing	77
3.2.2.1 Waveform Processing	78
3.2.2.2 Experimental Results	79
3.3 Frequency Division: Phase Alignment for Networked Systems	84
3.3.1 Orthogonal Frequency Division Multiplexing (OFDM)	84
3.3.2 IEEE 802.11 Standards and Legacy Preamble Format	85

3.3.3	Theoretical ranging Accuracy of the Legacy Preamble and the Stepped-Frequency Waveform	88
3.3.4	Experimental Validation	92
3.4	Pulse Encoding: Two-Tone Stepped Frequency Waveform (TTSFW)	96
3.4.1	Frequency Domain Multiplexing (FDM) Approach	97
3.4.2	Waveform Design	98
3.4.3	Measurements	106
3.4.3.1	Waveform Properties	106
3.4.3.2	Wireless Ranging Measurements	109
3.5	Comparison to Traditional Wideband Ranging Methods	115
 CHAPTER 4 DEMONSTRATION OF WIRELESS PHASE ALIGNMENT IN DISTRIBUTED BEAMFORMING		117
4.1	Range Estimation Waveform	117
4.2	Ranging Requirements for Open-Loop Distributed Beamforming	118
4.3	Range Estimation Refinement for Node Motion	120
4.4	Distributed Antenna Array and Open-Loop Distributed Beamforming Experiments	122
4.5	Two-Node Experiment	124
4.6	Three-Node Experiment	127
 CHAPTER 5 APPLICATION OF PHASE ALIGNED COHERENT DISTRIBUTED ARRAYS		129
5.1	Antenna Array Dynamics and Impacts on Wireless Communication	130
5.1.1	Estimation of Bit-Error-Rate of Communications Signals	132
5.1.2	Simulation	134
5.2	Dynamic Distributed Antenna Array Design and implementation	135
5.2.1	Ranging Waveform	136
5.2.2	Estimation Ability	137
5.3	Experimental Validation of Secure Communication	138
 CHAPTER 6 CONCLUSION		144
 APPENDICES		146
APPENDIX A	MATLAB FORMULATION OF BASEBAND PSWF	147
APPENDIX B	MATLAB FORMULATION OF DUAL PULSE PSWF	151
APPENDIX C	MATLAB PSWF SIMULATION	157
APPENDIX D	MATLAB PSWF MEASUREMENT PROCESSING	164
APPENDIX E	MATLAB NETWORK SYSTEM SIMULATION	172
APPENDIX F	MATLAB NETWORK SYSTEM MEASUREMENT PROCESSING	175
APPENDIX G	MATLAB TTSFW SIMULATION	180
APPENDIX H	MATLAB DISTRIBUTED BEAMFORMING MEASUREMENT PROCESSING	184
APPENDIX I	MATLAB SECURE TRANSMISSION SIMULATION FOR THE LINEAR CASE	186

APPENDIX J	MATLAB SECURE TRANSMISSION MEASUREMENT PROCESS- ING FOR THE LINEAR CASE	191
APPENDIX K	MATLAB SECURE TRANSMISSION SIMULATION FOR THE SINUSOIDAL CASE	194
APPENDIX L	MATLAB SECURE TRANSMISSION MEASUREMENT PROCESS- ING FOR THE SINUSOIDAL CASE	198
BIBLIOGRAPHY	201

LIST OF TABLES

Table 3.1: Processing Gain	79
Table 3.2: Comparison of discussed waveform attributes	106
Table 3.3: Comparison of Waveform Performance	116

LIST OF FIGURES

Figure 1.1: Relative gains that can be obtained through incoherent and coherent beamforming methods.	2
Figure 1.2: Transmission from independent wireless systems, signal 1 and signal 2, adding destructively due to phase mismatch. This example is a worst case scenario of where signals cancel each other out. For in-phase operations, the individual signal amplitudes sum, boosting the overall signal.	3
Figure 1.3: Transmission from independent wireless systems, signal 1 and signal 2, with two separate reference frequencies. Here the combination of the two signals creates an baseband modulation equivalent to the frequency difference. For operations at the same underlying frequency, a constant amplitude signal would be apparent.	3
Figure 1.4: Transmission from independent wireless systems, signal 1 and signal 2, with time misalignment. The phase mismatches due to phase encoded data create an amplitude modulation to the signal and, at worst case, can result in destructive interference essentially nulling out the signal. For a time aligned signal, all information pulses should add constructively, essentially summing the individual signals. This is much like the phase alignment aspect but on a pulse by pulse basis.	4
Figure 1.5: Transmission from independent wireless systems, signal 1 and signal 2, providing perfect ideal coherence by applying phase alignment, frequency synchronization, and time alignment.	5
Figure 1.6: Receiver-coordinated distributed transmit beamforming allows a network of transmitters to achieve longer communication ranges or higher data rates [1]. . .	6
Figure 1.7: Phase synchronization using receiver feedback based on the received SNR [2]. .	6
Figure 1.8: M -source distributed beamforming system model using round-rip synchronization [3].	7
Figure 1.9: System model with an N -node transmit cluster and a single target node. Node 0 corresponding to the target and node 1 corresponding to the primary node are assumed to have a direct link to the transmit nodes [4].	8
Figure 1.10: Communication model for a sensor network with minimal feedback from the target [5].	9

Figure 1.11: Coherent operation of radar sensor network through GPS synchronization [6].	11
Figure 1.12: Model for a sensor network with feedbackless coordination where θ_1 , θ_2 , and θ_3 are the corresponding phase shifts provided from internode distances [7].	11
Figure 1.13: Range estimation based phase alignment of a hierarchical primary-secondary topology.	13
Figure 2.1: Degradation of coherent gain with relative oscillator phase errors between node internal oscillators [8].	21
Figure 2.2: Degradation of coherent gain with relative internode positional errors [8].	22
Figure 2.3: (a) LFMW waveform in the time domain. (b) LFMW in the frequency domain.	24
Figure 2.4: (a) Ambiguity function of the LFMW waveform. (b) Intensity plot of the ambiguity function. (c) LFMW matched filter (zero Doppler cut). (d) LFMW Doppler response (zero time cut).	26
Figure 2.5: (a) Representation of the SFW with 50% duty cycle time domain. (b) SFW time-frequency plot.	28
Figure 2.6: (a) Ambiguity function of the SFW. (b) Intensity plot of the ambiguity function. (c) Matched filter of the SFW (zero Doppler cut). (d) Doppler response of SFW (zero time cut).	32
Figure 2.7: (a) The baseband PTTW in the time domain. (b) PTTW in the frequency domain.	35
Figure 2.8: (a) Ambiguity function of the PTTW. (b) Intensity plot of the ambiguity function. (c) Matched filter of the PTTW (zero Doppler cut). (d) Doppler response of the PTTW (zero time cut).	37
Figure 3.1: CRLB for Doppler (2.11) and range (2.12) of the baseband PSWFs for the cases of $c = \pi$ (a), $c = 4\pi$ (b), $c = 7\pi$ (c), and $c = 10\pi$ (d) on the right and left respectively.	46
Figure 3.2: Time domain representation of the temporally bifurcated waveform formed from concatenating two $n = 0$ PSWFs. This example was taken at $c = 3\pi$	48
Figure 3.3: Time and frequency bifurcated waveform with 100% (left) and 10% (right) time modulation and 100% (a), 50% (b), and 10% (c) modulation in frequency.	49

Figure 3.4: (a) Comparison of the optimal CRLB to the CRLB of the spatial uncertainty of the dual pulse waveform with varying spectral bandwidth where the percentage refers to $\frac{2W}{\Delta f}$. (b) Comparison of the optimal CRLB to the CRLB of the frequency uncertainty of the dual pulse waveform with varying temporal instantaneous bandwidth where the percentage refers to $\frac{2T'}{T}$ 50

Figure 3.5: (a) Time representation of the waveform with 10% modulation. (b) Spectral representation with 10% modulation. (c) Ambiguity function of the dual pulse PSWF. (d) Intensity plot of the ambiguity function showing ambiguous nature in both time and frequency. (e) Matched filter of the dual pulse PSWF (zero Doppler cut). (f) Doppler response of the dual pulse PSWF (zero time cut). 52

Figure 3.6: Pseudo-random white noise for disambiguation for 10% occupation of both time and frequency, relative to the measurement waveform (left), and 25% occupancy in time and frequency (right). (a) Pseudo-random white noise in the time domain. (b) Time-frequency plot of the pseudo-random white noise. (c) Matched filter response for the measurement waveform (blue) and disambiguation (red). (d) Doppler response of the measurement waveform (blue) and disambiguation (red). (e) Combined ambiguity function of measurement waveform and disambiguation demonstrating suppression of side-lobes in both time and Doppler. 53

Figure 3.7: LFMW for disambiguation for 10% occupation of both time and frequency, relative to the measurement waveform (left), and 25% occupancy in time and frequency (right). (a) LFMW in the time domain. (b) Time-frequency plot of the LFMW. (c) Matched filter response for the measurement waveform (blue) and disambiguation (red). (d) Doppler response of the measurement waveform (blue) and disambiguation (red). (e) Combined ambiguity function of measurement waveform and disambiguation demonstrating suppression of sidelobes in both time and Doppler. 54

Figure 3.8: (a) Block diagram of the wireless experimental setup. (b) Image of experimental setup in the semi-enclosed arch range. 57

Figure 3.9: (a) Time-frequency plot of a measured waveform with $T = 10 \mu s$ and $W = 6$ MHz. (b) Comparison of measured results, simulation, and CRLB for the dual pulse PSWF as a spatial estimator. (c) Comparison of measured results, simulation, and CRLB for the dual pulse PSWF as a frequency estimator. 58

Figure 3.10: Ranging is based on widely-spaced two-tone signal with 100 MHz of bandwidth, with the lower tone modulated by a 10 MHz frequency reference. (a) Spectrum of the joint ranging and frequency transfer signal using single-sideband modulation. (b) Spectrum of the joint ranging and frequency transfer signal using double-sideband modulation. (c) Spectrum of the joint ranging and frequency transfer signal using amplitude modulation. 61

Figure 3.11: (a) Ambiguity function of the PTTW with single sideband modulation. (b) Intensity plot of the ambiguity function. (c) Matched filter of single sideband modulation (zero Doppler cut). (d) Doppler response of the single sideband modulation (zero time cut). 64

Figure 3.12: (a) Ambiguity function of the PTTW with double sideband modulation. (b) Intensity plot of the ambiguity function. (c) Matched filter of double sideband modulation (zero Doppler cut). (d) Doppler response of the double sideband modulation (zero time cut). 69

Figure 3.13: (a) Ambiguity function of the PTTW with amplitude modulation. (b) Intensity plot of the ambiguity function. (c) Matched filter of amplitude modulation (zero Doppler cut). (d) Doppler response of the amplitude modulation (zero time cut). 74

Figure 3.14: (a) Image of the joint ranging and frequency transfer system experimental setup in an indoor wireless test range. The distance between the transceiver and the corner reflector was 4.57 m.(b) Block diagram of measurement system used in the experiments. The transmitter, represented by the Arbitrary Waveform Generator (AWG) generates the multi-tone signal, and the oscilloscope samples the received signals. 78

Figure 3.15: Measured delay estimation accuracy versus SNR with the frequency reference included using (a) single-sideband, (b) double-sideband, and (c) amplitude modulation. The separation of the ranging tones is given in the legend, with the CRB for the 200 MHz tone separation from (3.46), (3.48), and (3.50) for (a), (b), and (c) respectively plotted as the solid line. 81

Figure 3.16: Comparison of all three modulation formats showing consistent performance regardless of the modulation format. 82

Figure 3.17: Variance on the estimate of the 10 MHz frequency reference versus SNR using (a) single-sideband modulation, (b) double-sideband modulation, and (c) amplitude modulation. The separation of the ranging tones is given in the legend. The red dashed line indicates the 18° requirement to ensure $P(G_c \geq 0.9) \approx 1$ for large arrays. The CRB given by (3.52) is shown in the solid line. 83

Figure 3.18: Channel splitting using an FDM method where the $\text{sinc}(\cdot)$ representation comes from the Fourier of a rectangular time domain envelope. The spacing of each channel is equivalent to $1/T$ to ensure that the peak is at a null of all of the other $\text{sinc}(\cdot)$ functions.	85
Figure 3.19: Visualization of Legacy preamble.	86
Figure 3.20: (a) Ambiguity function of the Legacy preamble. (b) Intensity plot of the ambiguity function. (c) Matched filter of the Legacy preamble (zero Doppler cut). (d) Doppler response of the Legacy preamble (zero time cut).	89
Figure 3.21: Time-frequency plot of the Legacy preamble training field and SFW with a 50% duty cycle.	90
Figure 3.22: (a) Simulated IEEE 802.11n waveform with 20 MHz bandwidth with payload (blue) and L-STF preamble (red). (b) SFW with $T_r = 8 \mu\text{s}$ with a 50% duty cycle and containing the 12 data sub-carriers present in the L-STF. (c) Spectrum of both the 802.11n L-STF and the SFW. (d) Normalized zero time delay matched filter output for both L-STF and SFW demonstrating the similarities in the temporal waveform shapes.	93
Figure 3.23: (a) Measured IEEE 802.11ac waveform with 160 MHz bandwidth. (b) Measured spectrum of the waveform. (c) Measured matched filter output.	95
Figure 3.24: (a) Block diagram of the ranging experiment (AWG = arbitrary waveform generator, LNA = low-noise amplifier). The corner reflector was placed a distance of 1.5 m from the ranging system. Delay estimation processing was implemented offline in MATLAB. (b) Image of experimental setup up in the semi-enclosed arch range. (c) Measurement variances along with simulated data for 1000 Monte Carlo iterations over various SNR values. The simulated performance of the SFW and Legacy preamble waveforms yielded nearly identical delay estimation, verifying the theoretical similarities of the lower bounds described earlier. The measured performance of the Legacy preamble waveform was close to the simulated performance and comparable to the lower bound (CRLB). The Legacy preamble waveform achieved a lowest ranging error of 1.9mm with a preprocessing SNR of 19 dB combined with 31 dB of processing gain for a total SNR of 50 dB.	96
Figure 3.25: Channel splitting using an FDM method for a two-tone system where half of the bandwidth is allocated to the first tone, $-\frac{\Delta f}{2}$, of the N channels and the second half is allocated to the upper tone, $\frac{\Delta f}{2}$	98
Figure 3.26: (a) Two-tone stepped-frequency waveform in the time domain. (a) TTFSFW in the time-frequency domain	99

Figure 3.27: (a) Ambiguity function of the TTSFW. (b) Intensity plot of the ambiguity function. (c) Matched filter of the TTSFW (zero Doppler cut). (d) Doppler response of TTSFW (zero time cut).	103
Figure 3.28: (a) The bounds and simulation of TTSFW vs. number of pulse with 4 MHz of bandwidth total bandwidth and 30 dB preprocessing SNR. (b) The bounds and simulation of TTSFW vs. SNR with the pulse number fixed to $N = 4$	106
Figure 3.29: (a) Measured two pulse TTSFW in time domain. (b) Two pulse TTSFW in the frequency domain.	107
Figure 3.30: Measured matched filter output of the PTTW and TTSFW waveforms produced on the X310 using two pulses	107
Figure 3.31: Comparison of variance of PTTW and TTSFW with equal Δf to the CRLB of the TTSFW.	108
Figure 3.32: (a) Measured four pulse TTSFW in time domain. (b) Four pulse TTSFW in the frequency domain.	109
Figure 3.33: Measured matched filter output of the PTTW and TTSFW waveforms produced on the X310 using four pulses.	110
Figure 3.34: (a) Schematic of single SDR in the arch range. (b) Image of experimental setup. (c) Range Measurement results. (d) Variance of measurement.	111
Figure 3.35: (a) Schematic of two SDRs in the arch range. (b) Image of experimental setup. (c) Range Measurement results. (d) Variance of measurement.	113
Figure 3.36: (a) Schematic of three SDRs in the arch range. (b) Image of experimental setup. (c) Range Measurement results. (d) Variance of measurement.	114
Figure 4.1: Measured waveform supporting ranging between two nodes: (a) time domain; (b) frequency domain.	118
Figure 4.2: Measured waveform supporting ranging between five nodes: (a) time domain; (b) frequency domain.	119
Figure 4.3: Block diagram of the Kalman filter used for range estimation refinement with moving nodes.	121
Figure 4.4: Block diagrams of the nodes.	123
Figure 4.5: RF chain internal to each of the X310 SDRs.	124

Figure 4.6:	(a) Block diagram of the distributed two-node experiment. (b) Image of the experimental setup in the semi-enclosed arch range. (c) Measured results of coherent gain with and without performing range-based phase correction.	126
Figure 4.7:	(a) Block diagram of the distributed three-node experiment. (b) Image of the experimental setup in the semi-enclosed arch range. (c) Measured results of coherent gain with and without performing range-based phase correction.	128
Figure 5.1:	Flight paths are taken over a 1 m extent at a 1.5 GHz beamforming frequency assuming a dipole transmitter and broadside beamforming direction. (a) Linear flight path (left) and resulting array radiation pattern over time (right). (b) Sinusoidal flight path (left) and resulting array radiation pattern over time (right).	131
Figure 5.2:	Comparison of BER performance of a static case of two dipoles at 1 m separation, and the estimated performance of the two designated flight paths at 1.5 GHz and 12 dB of SNR.	134
Figure 5.3:	(a) Block diagram of the simulation. (b) Simulated BER over -90° to 90° domain compared to calculated estimation for the linear case. The snapshots of data show the 100 points of demodulated data (blue) and the location of the constellation points (red) at angles -20° and 0°	135
Figure 5.4:	Method of performing alignment of electrical states of time, through high amplitude preamble, and phase, range estimation between primary and secondary elements.	136
Figure 5.5:	(a) Ranging waveform in the time domain. (b) Ranging waveform in the frequency domain.	137
Figure 5.6:	Block diagram of the experimental setup	139
Figure 5.7:	(a) Image of the experimental setup in the semi-enclosed arch range. (b) Image of the antenna setup for ranging and beamforming on each element. (c) Farthest separation of the elements mounted on the linear actuator. (d) Closest separation of the elements mounted on the linear actuator.	140
Figure 5.8:	(a) Comparison of simulated and actual flight path for the linear case. (b) Comparison of simulated and actual flight path for the sinusoidal case.	141
Figure 5.9:	(a) Comparison of simulated, measured, and calculated estimation of the BER for the linear case. (b) Comparison of simulated, measured, and calculated estimation of the BER for the sinusoidal case.	143

CHAPTER 1

INTRODUCTION

Advancements in the capabilities of wireless systems strongly depend on the achievable gain, power, and resolution of the system, and the ability to scale these metrics. With traditional single-platform systems, improving such aspects for radar, remote sensing, and communications requires modifications of the devices in the system, the system efficiency, or the antenna aperture size, all of which can represent significant cost drivers. To overcome the challenge of continually upgrading single-system capabilities, there is growing interest in distributed antenna array systems, where collections of small, low power, and relatively inexpensive wireless systems are coordinated to mimic the performance of a single, large system, thereby increasing the capabilities of the overall array system through array gain and/or larger array aperture area to achieve performance otherwise unattainable with a single platform [8–10]. To address this challenge, recent research has focused on the development of distributed wireless technologies implemented in Multiple Input Multiple Output (MIMO) [11–14] or distributed beamforming [5, 15–17] applications. Such distributed wireless systems enable direct performance scalability by adding or removing inexpensive nodes from the array [18, 19]. Applications of such disaggregated arrays include small satellites or hybrid satellite-terrestrial cooperative systems [20], cubesat swarm operations for remote sensing, drone constellations for soil moisture measurements, and distributed communications for greater throughput and higher-reliability connections [21], among others.

Distributed arrays that operate in an incoherent sense have the benefit of requiring minimal coordination to align the electrical states of the elements [22–25]. In essence, each element acts as its own entity with minimal cooperation within the system as a whole. Coherent distributed arrays are a specific subset of distributed arrays in which platforms are coordinated at the level of radio frequency (RF) phase to enable phased-array beamforming [5, 8, 26–28]. Here the elements act as a single system rather than independent entities seen in the incoherent method. While requiring additional overhead to perform coherence operations, the array gain scales proportionally

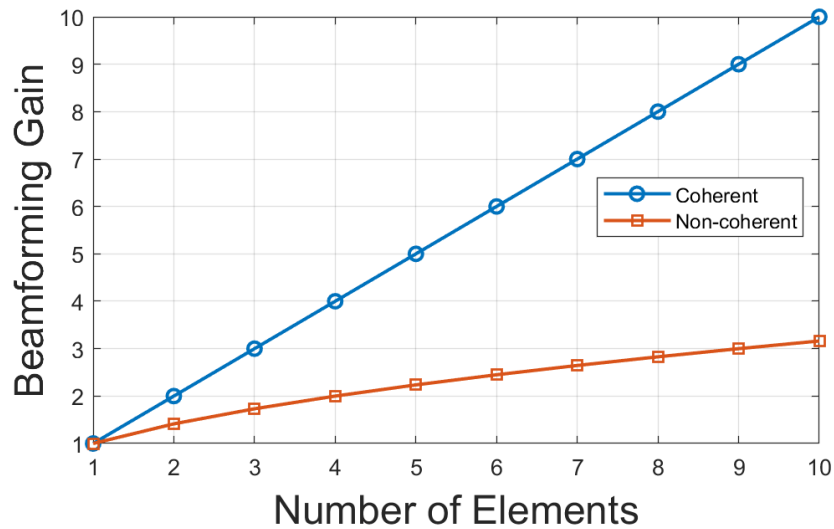


Figure 1.1: Relative gains that can be obtained through incoherent and coherent beamforming methods.

to the number of elements within the array, much like classic single platform systems, whereas the gain of the incoherent methodology scales proportionally to the square-root of the number of elements (see Fig. 1.1). This is due to the phase of coherent signals adding constructively while incoherent signals add with a random phase at the risk of destructive interference. Therefore, coherent operations allow for significantly improved signal strength enabling long range connections to be made and higher obtainable signal-to-noise ratios (SNR) thereby improving signal reliability. To support distributed coherent operations:

- The wireless systems on each platform must be phase-aligned at the level of the RF beamforming frequency phase to ensure that signals add constructively [29, 30]. A system in which the independent signals are not phase aligned can cause significant degradation in the coherent gain (see Fig. 1.2).

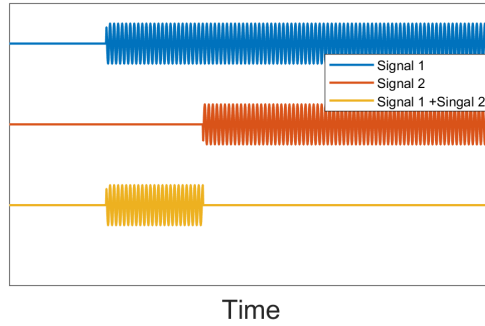


Figure 1.2: Transmission from independent wireless systems, signal 1 and signal 2, adding destructively due to phase mismatch. This example is a worst case scenario of where signals cancel each other out. For in-phase operations, the individual signal amplitudes sum, boosting the overall signal.

- Frequency synchronization must be implemented to insure all elements are operating at the same reference frequency [31–34]. A shift in the reference frequency between elements results in a frequency shift of the derived signals. This is important since the internal oscillators on separate devices in the distributed array will drift over time if left unsynchronized. This drift results in significant errors in information demodulation for communication systems and estimation errors for remote sensing and radar applications (see Fig. 1.3).

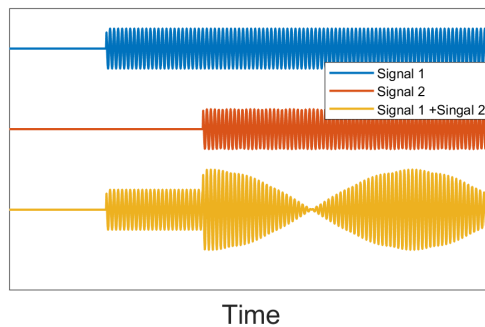


Figure 1.3: Transmission from independent wireless systems, signal 1 and signal 2, with two separate reference frequencies. Here the combination of the two signals creates an baseband modulation equivalent to the frequency difference. For operations at the same underlying frequency, a constant amplitude signal would be apparent.

- Time alignment between nodes must be implemented so that symbol information has sufficient overlap at the target destination [35–41]. This aspect of coordination is required for applications transmitting pulsed information such as symbols in communications waveforms. Mismatched time can result in phase interference between pulses making demodulation of information increasingly difficult (see Fig. 1.4).

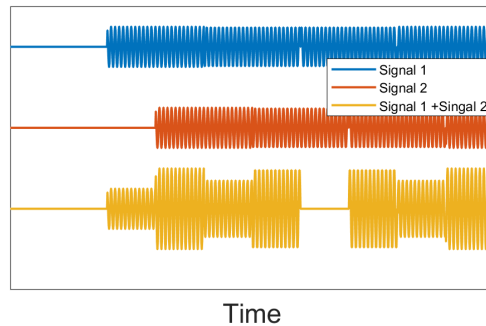


Figure 1.4: Transmission from independent wireless systems, signal 1 and signal 2, with time misalignment. The phase mismatches due to phase encoded data create an amplitude modulation to the signal and, at worst case, can result in destructive interference essentially nulling out the signal. For a time aligned signal, all information pulses should add constructively, essentially summing the individual signals. This is much like the phase alignment aspect but on a pulse by pulse basis.

Only after these aspects of coordination are addressed can coherent beamforming be accomplished. Note that time alignment is only applicable to pulsed information systems and can be neglected for continuous wave transmission signals. An image of ideal coherent beamforming completing all three tasks of alignment can be seen in Fig. 1.5.

Of these three coordination aspects, phase alignment is the more challenging task due to the high-precision required to align the carrier phases. Previous works have explored a closed-loop methodology where the task of phase alignment is performed using feedback from the target location. In this formulation, information is relayed back to the array, indicating what phase corrections need to be made to enable coherence [1–4, 42–48]. Among these closed-loop approaches are:

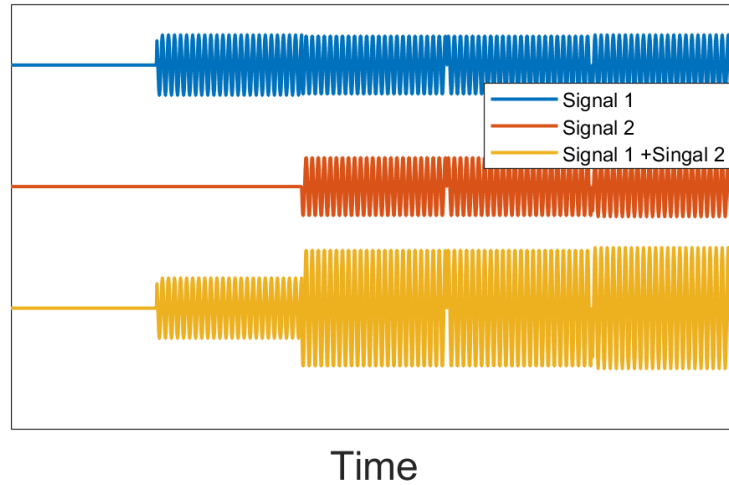


Figure 1.5: Transmission from independent wireless systems, signal 1 and signal 2, providing perfect ideal coherence by applying phase alignment, frequency synchronization, and time alignment.

1. Receiver-coordinated explicit-feedback in which carrier phase and frequency synchronization is performed with unmodulated beacon signals on each node (see Fig. 1.6). A full duplexed method of exploring separate frequency bands for beacons and beamforming carrier [43] proved to be effective for time-invariant and time-varying single-path channel environments but degrades significantly in the presence of multipath. A similar method was investigated using a half duplex system where a single frequency is used for beacons and the beamforming carrier [1]. Here a time-slotted round-trip carrier synchronization protocol is implemented which has the benefit of channel reciprocity in a multipath environment and proved to be effective in time-invariant and time-variant channels as well as multipath environments.

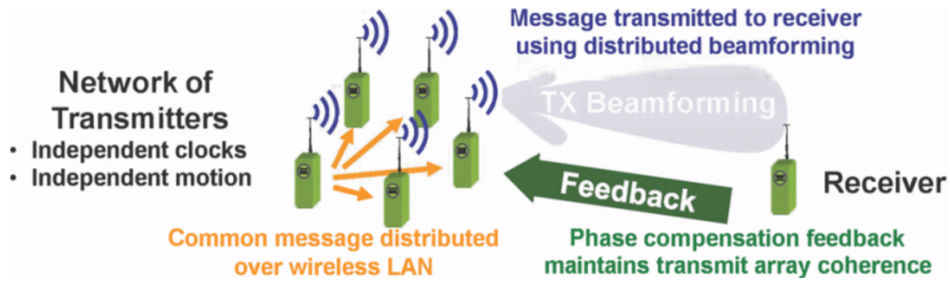


Figure 1.6: Receiver-coordinated distributed transmit beamforming allows a network of transmitters to achieve longer communication ranges or higher data rates [1].

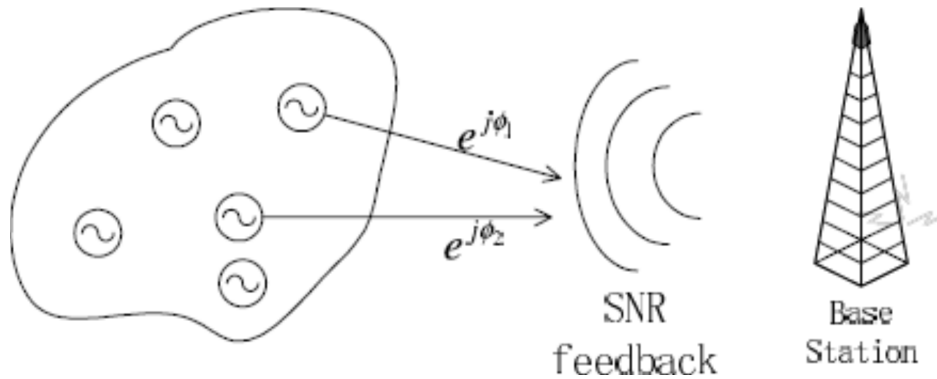


Figure 1.7: Phase synchronization using receiver feedback based on the received SNR [2].

2. A phase alignment method where the phase of each node is randomly updated and the receiver responds with a single bit indicating the impact to the received SNR (see Fig. 1.7) [2, 44]. If the phase perturbation has a negative impact, the phase is reverted to the state prior to the adjustment; if the SNR is improved or unaffected then the new phase correction is kept. This algorithm for phase alignment is scalable and converges over time. It proves to be effective for static systems with linear channels. Improvements on this method using 3-bit feedback in each timeslot [45] conveys the direction of the motion of the receiver relative to the transmitter in addition to the received signal strength extending this methodology to time-variant systems.
3. A method of round-trip synchronization (see Fig. 1.8) [3, 46] where a time slotted approach for system beacons and beamforming carrier signal utilize the same frequency. In the first time slot of this approach the base station transmits a carrier beacon to all of the elements in

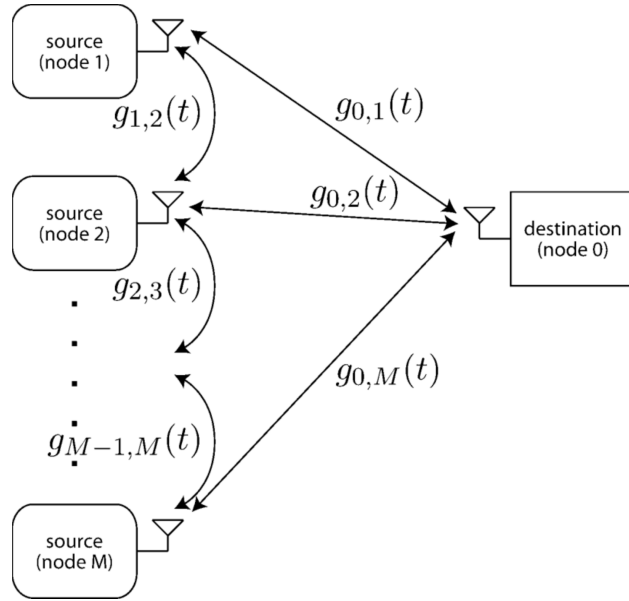


Figure 1.8: M -source distributed beamforming system model using round-rip synchronization [3].

the array where each element independently calculates the appropriate carrier phase offset as well as a reference frequency shift from this beacon signal. The subsequent time slots consist of elements within the array transmitting their relative beacons in which the rest of elements calculate local frequency and phase offsets creating a fully connected array. The final time slot is beamforming back to the base station. This method presents a solution applicable to time-invariant, time-variant, and multipath environments as well as arrays consisting of mobile nodes, but suffers from serious scalability constraints due to the increasing amount of overhead with array size. Some of the overhead constraints could potentially be alleviated using beacons on multiple frequency bands [43] but estimations will suffer due to the inapplicability of channel reciprocity.

4. A time slotted approach for a retrodirective array that corrects for time-varying phase and frequency offset. A broadcast from the primary node is sent to all the secondary nodes in the array with a message that contains the best estimate of the complex channel state based on previous estimations [4, 47, 48]. The secondary nodes then respond individually with updated predictions of future channel estimations provided from an extended Kalman filter

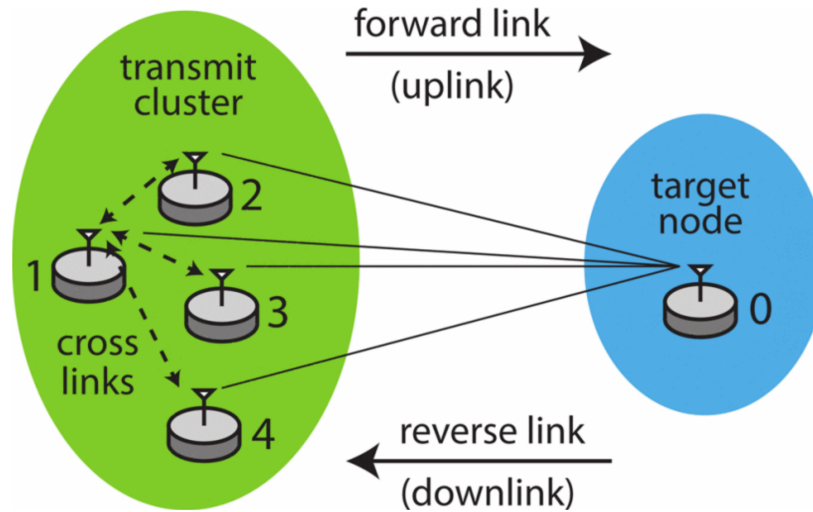


Figure 1.9: System model with an N -node transmit cluster and a single target node. Node 0 corresponding to the target and node 1 corresponding to the primary node are assumed to have a direct link to the transmit nodes [4].

(EKF) [4, 48]. This method uses minimal communication with a base station where the majority of the coordination is done by the array elements themselves. However, this approach to a retrodirective array presents limited scalability due to the increased update wait time needed from the primary node to receive a response from each individual secondary node and required upwards of 1 s to correct errors due to EKF estimation presenting limitations of extended beamforming operations.

5. A method of using an element hierarchical primary-secondary structure to perform synchronization requiring minimal feedback from the target destination (see Fig. 1.10) [5, 49]. This method uses a timeslotted approach in which signal transmissions are interleaved with beacon broadcasts, consisting of the beamforming carrier, sent from the primary element to all the subsequent secondary elements where the beamforming center frequency is shared by the beacon to ensure channel reciprocity. The secondary nodes, after individual communication with the primary node, can then perform a channel estimation based on a preamble response that precedes the beacon message and the reciprocal can be applied to the baseband signal to ensure a coherent output. This method presents issues with scalability, especially for mobile

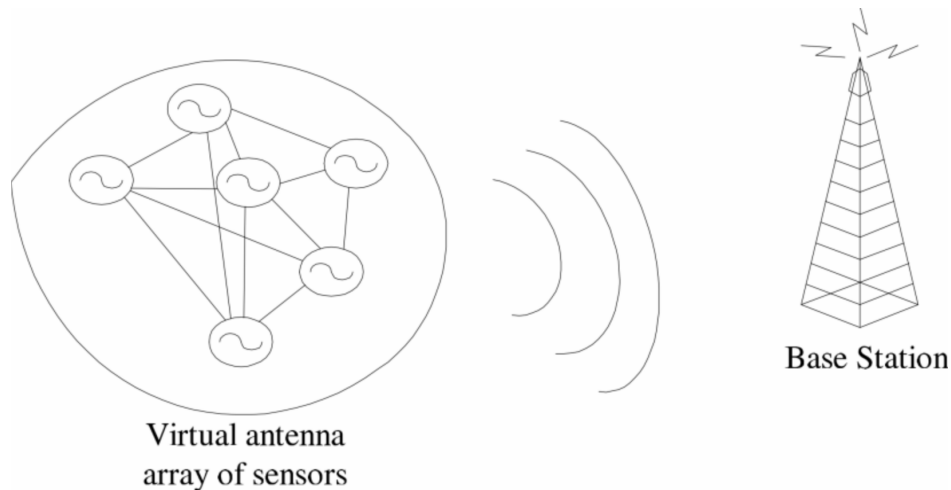


Figure 1.10: Communication model for a sensor network with minimal feedback from the target [5].

systems, due to the increasing amount of overhead with array size due to the time duplexed nature of this process. This results in a high probability of element channels changing before the transmission is sent stemming from either the physical motion of the platforms or reference clock drift over a period of time leading the channel estimation to no longer become accurate.

Although these feedback methods are effective, they are restricted to applications where reliable feedback can be provided by the receiver. Numerous situations arise where such feedback is not available, particularly in cases where individual nodes in the array do not have sufficient sensitivity to close a link to a base station on their own. Furthermore, closed-loop architectures are inherently unable to support wireless applications beyond communications, such as remote sensing, imaging, and radar where coherent feedback is generally not present.

The work presented here focuses on an open-loop array where no feedback from the destination is assumed [5–8, 49–51]. Due to this lack of feedback, the elements of the array must self align their electrical states [8, 52]. Methodologies utilizing closed-loop and retrodirective architectures do not inherently provide node localization due to the cooperative nature of these systems. For arbitrary beamforming it is necessary to obtain locations of nodes as the interference of the

beamforming phase will depend on spatial position. Although open-loop arrays are a considerably more daunting task to develop than closed-loop approaches, there are huge versatility benefits due to the ability to arbitrarily steer beams. Using open-loop concepts can extend the application space to scattering problems as well as communications but, due to the challenging nature of this problem, this method is less investigated. The current methodologies of enabling open-loop coherent distributed arrays (CDAs) include:

1. Leveraging the global positioning systems (GPS) for estimations in position and frequency reference (see Fig. 1.11) [6, 50, 51]. This method obtains position to typical trilateration operations with accuracies on the order of 10 cm and a frequency reference from the pulse-per-second (PPS) signal that has timing accuracies of approximately 10 ns. However, the information accuracy provided by GPS is far too coarse to enable coherent beamforming in the microwave region and also only provides a solution when reliable GPS signals can be obtained.
2. An alternate method of using a primary-secondary methodology where the primary node transmits a beacon signal consisting of the carrier and timing reference. The secondary nodes, with knowledge of internode distance to the primary node, can then account for the delays between said nodes with the appropriate timing and phase shift [7, 8]. The primary node can then send another trigger signal to initiate secondary nodes to begin transmission with the appropriate baseband modulation to enable coherent beamforming. While [7] presents an in-depth analysis of this operation, the method at which the internode distances are obtained is not presented and is validated through simulation alone. In [8] proof of concept of this method is experimentally validated using a single primary and secondary node but the issue of scalability based on this technique is not expressed.

From these works it can be seen that the two most fundamental aspects to enable coherent open-loop CDAs are the alignment of the phase of the beamforming signal and a stable frequency reference to which all of the elements can align to. Of these two, phase alignment presents the more

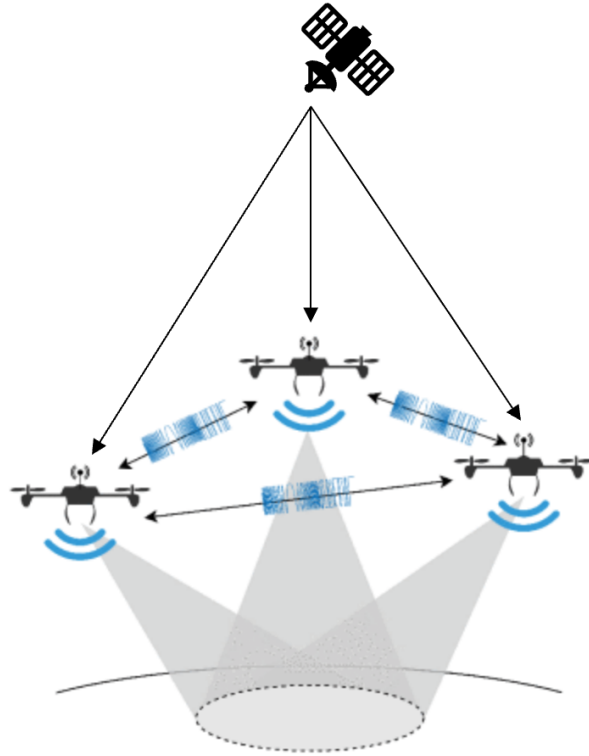


Figure 1.11: Coherent operation of radar sensor network through GPS synchronization [6].

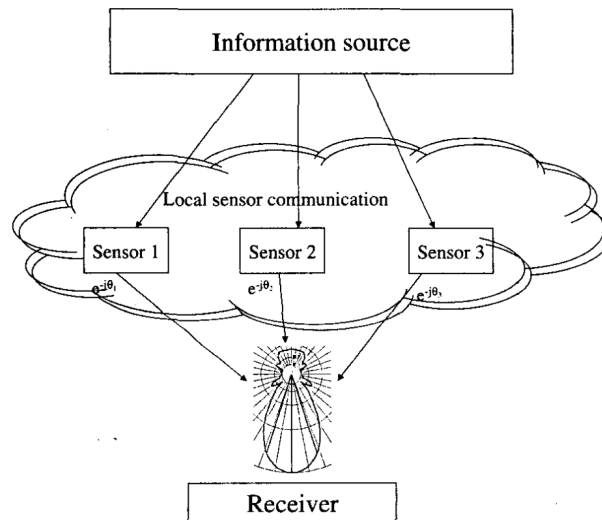


Figure 1.12: Model for a sensor network with feedbackless coordination where θ_1 , θ_2 , and θ_3 are the corresponding phase shifts provided from internode distances [7].

challenging problem due to the accuracies needed to enable beamforming in the millimeter wave and microwave regions. To achieve phase alignment and implement a phase-based beamsteering operation, the relative positions of the individual nodes must be known to within a fraction of the wavelength of the beamforming frequency. Previous works have shown that these internode ranging measurements must have accuracies of less than $\lambda/15$ to have no more than 0.5 dB reduction in coherent gain with a probability of 90% [8]. This calls for accuracies on a sub-centimeter level for millimeter wave and microwave operations. Furthermore, this accuracy must be obtained before nodes move out of coherence due to array dynamics. This has been achieved in the past using optical systems providing estimates of element locations [53, 54]. However, such systems are not easily scalable and require accurate tracking and pointing for each node connection.

This dissertation focuses on a method to perform phase alignment that is more conducive to scalability, system implementation, and cost than optical tracking by using microwave radar responses to estimate internode localization. For airborne CDAs, a microwave system also presents a solution to environmental challenges, such as cloud cover or fog, that optical systems cannot overcome due to the significant attenuation at optical frequencies. Classic microwave techniques of obtaining range estimations, through time of flight of a return signal, are often optimized through transmit waveform design. The most common radar ranging waveforms used in practice include linear frequency modulated waveforms (LFMW) [55–58] and stepped frequency waveforms (SFW) [59–62]. Waveform characteristics and estimation abilities for the LFMW and SFW are discussed in-depth in Sections 2.2.1 and 2.2.2 respectively. These waveforms are commonly used due to their ability to unambiguously estimate range, but are not designed for optimal range estimation. Previous works have shown that spectrally-sparse waveforms can achieve near-optimal ranging accuracy but come at the cost of estimation ambiguity [8]. Therefore, waveform designs optimized for range estimation, based on spectrally-sparse signals, that address the scalability needs for open-loop CDAs are derived and discussed in Chapter 3 where methods to address the challenge of measurement ambiguity are discussed as well.

The overall system structure used in this work follows the hierarchical primary-secondary

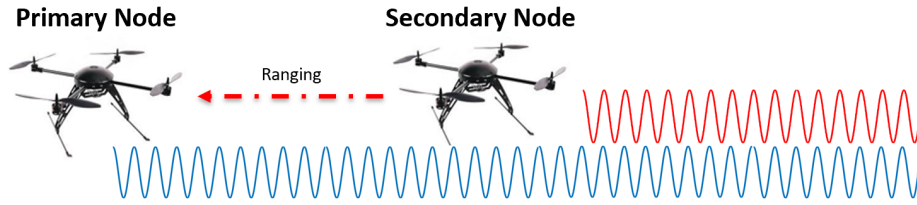


Figure 1.13: Range estimation based phase alignment of a hierarchical primary-secondary topology.

scheme seen in [5, 7, 49] due to the potential for scalability. Beamforming from the primary node sets a reference point in space to which the subsequent secondary node(s) can estimate their relative distance. With this knowledge, the secondary nodes can adjust the phase of their respective beamforming signals to account for the proportional phase shift from primary to secondary node (see Fig. 1.13) where the beamforming frequency and angle to the target destination are assumed to be known a priori. This requires all of the secondary nodes to perform their estimation signal processing independently and therefore work on a pairwise basis with the single primary node improving the robustness and scalability. This method is more conducive to the addition or subtraction of secondary nodes due to desired design constraints or node failure. To avoid the bottleneck to scalability using this approach seen in previous works, different frequency bands are utilized for the range estimation and beamforming where beamforming is typically the lower of the two due to limitations on measurement accuracies that can be achieved by practical systems. By using different frequency bands, timeslotting can be avoided, resulting in a full duplex system. A full duplexed system allows for constant range measurements to be taken, and therefore continual updates to the phase of the beamforming signal, enabling greater scalability and faster array dynamics of mobile platform by reducing the rate at which nodes move out of coherent range before the next update is given. This becomes particularly important for platforms that undergo quick relative motion, due to designated flight paths, obstacle avoidance, system vibration, or turbulence. Mobile arrays that are able to quickly change element positions will aid in applications such as synthetic aperture radar (SAR) imaging [63–66] and interferometric imaging [67, 68] where a variety of electrical baselines are needed to accommodate image resolution.

To demonstrate the feasibility and scalability of this concept, wireless experimental validation of a phase coherent distributed array with more than two nodes is shown in Chapter 4 using an estimation waveform derived in Chapter 3. Nodes undergo relative motion thereby demonstrating the ability of the system to quickly implement phase corrections for mobile systems, enabling applications such as airborne and spaceborne radar, remote sensing, and imaging. Using this method, beamforming in the L-band region is shown to be obtainable with no more than 12.5 MHz of bandwidth allocated to the range estimation waveform, making applications such as L-band SAR for vegetation and forestry measurements obtainable using off-the-shelf equipment. To expand upon these applications, a method for using array motion to increase wireless security is derived and experimentally validated in Chapter 5. This is made possible by the change of array electrical baselines resulting from array dynamics, thus changing the locations in space of constructive interference while maintaining coherence at the desired target destination. This method can be used in remote sensing applications as well, but is demonstrated through a communication signal because the performance of signal coherence over various angles can easily be observed from the bit-error-ratio (BER).

The principal contributions of this work include the following:

- New derivations and experimental evaluations of novel ranging waveforms that can easily be scaled to accommodate a large collection of nodes. The scalability methods that are investigated include time domain duplexing, frequency division multiplexing, and pulse encoding. The waveforms that are discussed include: a waveform obtaining near-optimal range and velocity estimation using an optimally approximate time- and band-limited baseband envelope; a waveform to perform joint ranging and frequency transfer based on a spectrally sparse signal model; a method of using a communications preamble that is common to many IEEE standards to perform ranging and communication within the same frequency band without interfering with the information throughput; and a highly scalable pulse encoded spectrally sparse waveform with inherent disambiguation potential.

- Experimental demonstration of phase alignment supporting up to 120 nodes with two and three transmitting nodes in a dynamic open-loop distributed beamforming array with greater than 90% coherent gain. This is performed using the primary-secondary hierarchical topology where phase compensation comes from a range estimations provided by the waveforms derived in this work. This method is directly scalable to larger arrays.
- An experimental evaluation of a novel approach to secure wireless operations using a two-element dynamic open-loop CDA with designated flight paths utilizing the beamforming approach described in this work. Methods in the literature, such as parasitic arrays [69–71], periodically switched arrays [72–74], and directional modulation [75–78], classically trade transmission power for the added benefit of security. This method of using CDAs can provide optimal power transfer as well as operational security. A wireless beamforming experiment is proven to have approximately 80% maximum power transfer, which can be improved upon by allocating more bandwidth to the estimation process or alternate flight paths, while providing high levels of confusion at off angle directions.

CHAPTER 2

RANGING WAVEFORM CLASSIFICATION METRICS AND CLASSIC RANGING WAVEFORMS

In this chapter I discuss common metrics for evaluating the performance of radar signals, namely the ambiguity function which shows a received signal response to time delay and a Doppler frequency shift and the Cramer-Rao lower bound which defines the ideal variance that can be obtained by a signal for an unknown variable. These metrics are evaluated for common waveforms used in practice, and are then used to compare the performance of different waveforms in the following chapter for the purpose of enabling phase alignment of distributed beamforming.

2.1 Derivation of Waveform Estimation Characteristics

2.1.1 Ambiguity Function

The response to a waveform in both time and frequency is given by the ambiguity function [79, 80]. The ambiguity function represented by the cross-correlation of the transmitted signal with a Doppler shifted version. The ambiguity function is given by

$$AF(t, f_D) = \int_{-\infty}^{\infty} s^*(\tau - t)s(\tau)e^{j2\pi f_D \tau} d\tau \quad (2.1)$$

where $s(t)$ is the time domain representation of the waveform and f_D is the Doppler shift. The matched filter, equivalent to the autocorrelation or zero Doppler cut of the ambiguity function, is used to measure the response in time. The matched filter is an optimal linear filter that maximizes the SNR of the measurement by correlating the transmitted and received signals providing an additional processing gain equivalent to the time-bandwidth product, TBW_r , where T is the signal time duration and BW_r is the receiver bandwidth representing a maximum measurement processing gain. The zero time cut, $t = 0$, shows the waveforms response to Doppler. The ideal variance of the main peaks of both the matched filter and Doppler cuts of the ambiguity function are equivalent to the ideal Cramer-Rao Lower Bound (CRLB).

2.1.2 Cramer_Rao Lower Bound (CRLB)

Often in remote sensing applications it is desirable to estimate both time or frequency of a measurement as these metrics provide information about the behavior of a target. A time delay measurement gives range information where a frequency shift provides radial velocity through Doppler. The theoretical accuracy of these measurements as an estimator depends on the signal variance which is inversely proportional to the Fisher Information [81]. The Fisher Information is a measure of the amount of information that can be extracted from a signal. This performance limitation is given by the CRLB. The CRLB, which is defined by the noise terms, gives a theoretical limitation on the amount of information that can be extracted from a signal but does not provide a method in which to design a waveform to achieve this theoretical bound. The general form of a radar signal can be expressed as

$$S_r(x) = \alpha s(x; \mathbf{u}) + w(x) \quad (2.2)$$

where $w(x)$ is assumed to be additive Gaussian white noise (AWGN), α is the complex coefficient containing amplitude and phase information, and \mathbf{u} is the parameter to be estimated which for this work is either velocity, given through Doppler, or position, given through the proportional time delay. For an unknown parameter \mathbf{u} and a deterministic α , the CRLB can be derived as [82]

$$\sigma^2(\hat{u} - u) \geq \frac{N_0}{2|\alpha|^2} \left(\int \left| \frac{\partial s(x; \mathbf{u})}{\partial u} \right|^2 dx - \frac{1}{E_s} \left| \int \frac{\partial s(x; \mathbf{u})^*}{\partial u} s(x; \mathbf{u}) dx \right|^2 \right)^{-1} \quad (2.3)$$

where E_s is the signal energy and $\frac{N_0}{2}$ is the noise power spectral density. For an estimation of a return signal time delay, which gives information about the radial distance, can be expressed in its general form from (2.2) as

$$s_r(t) = \alpha g(t - \tau) + w(t) \quad (2.4)$$

where τ is the delay and $g(t)$ is the transmitted signal. The variance can then be solved from (2.3) with the model (2.4) where $s(x; \mathbf{u}) = g(t - \tau)$. The first integral in (2.3) can be solved using Parseval's theorem while the second integral can be solved using Plancherel's theorem, also known as Rayleigh's theory, which states the squared modulus of a function is equal to the integral of the

squared modulus of it's spectrum. This corresponds the Parseval's theorem for conservation of energy of a Fourier series. The first integral of (2.3) can be solved for by

$$\begin{aligned}
\int \left| \frac{\partial s(x; \mathbf{u})}{\partial u} \right|^2 dx &= \int \left| \frac{\partial}{\partial \tau} g(t - \tau) \right|^2 dt \\
&= \int \left| \frac{\partial}{\partial \tau} G(f) e^{-j2\pi f \tau} \right|^2 df \\
&= \int (2\pi f)^2 |G(f)|^2 df \\
&= \zeta_f^2
\end{aligned} \tag{2.5}$$

where ζ_f^2 is the mean-squared bandwidth which is equivalent to the second moment of the frequency spectrum. A similar formation can be made for the second integral in (2.3)

$$\begin{aligned}
\left| \int \left(\frac{\partial s(x; \mathbf{u})}{\partial u} \right)^* s(x; \mathbf{u}) dx \right|^2 &= \left| \int \left(\frac{\partial}{\partial \tau} g(t - \tau) \right)^* g(t - \tau) dt \right|^2 \\
&= \left(\int 2\pi f |G(f)|^2 df \right)^2 \\
&= \mu_f^2
\end{aligned} \tag{2.6}$$

where μ_f^2 is the mean frequency equivalent to the first moment of the frequency spectrum. This results in an uncertainty of a radar time delay estimator of

$$\sigma_\tau^2 \geq \frac{N_0}{2|\alpha|^2 \left(\zeta_f^2 - \frac{1}{E_s} \mu_f^2 \right)} \tag{2.7}$$

An estimation of a return signal radial velocity can be expressed in its general with inbound velocity $v \ll c$ where c is the speed of light from (2.2) as

$$s_r(t) = \alpha g(t) e^{j2\pi f_D t} + w(t) \tag{2.8}$$

where $f_D = 2\frac{f_c v}{c}$ and f_c is the radio frequency (RF) center frequency. The variance can then be solved from (2.3) with the model (2.8) where $s(x; \mathbf{u}) = g(t) e^{j2\pi f_D t}$. The first integral of (2.3) can

be solved for by

$$\begin{aligned}
\int \left| \frac{\partial s(x; \mathbf{u})}{\partial u} \right|^2 dx &= \int \left| \frac{\partial}{\partial f_D} G(f - f_D) \right|^2 df \\
&= \int \left| \frac{\partial}{\partial f_D} g(t) e^{j2\pi f_D t} \right|^2 dt \\
&= \int (2\pi t)^2 |g(t)|^2 dt \\
&= \zeta_t^2
\end{aligned} \tag{2.9}$$

where ζ_t^2 is the mean-squared time duration equivalent to the second moment of the time spectrum.

The second integral of (2.3) can be solved by

$$\begin{aligned}
\left| \int \left(\frac{\partial s(x; \mathbf{u})}{\partial u} \right)^* s(x; \mathbf{u}) dx \right|^2 &= \left| \int \left(\frac{\partial}{\partial f_D} G(f - f_D) \right)^* G(f - f_D) df \right|^2 \\
&= \left(\int 2\pi t |g(t)|^2 dt \right)^2 \\
&= \mu_t^2
\end{aligned} \tag{2.10}$$

where μ_t^2 is the mean time duration corollary to the first moment of the time domain. The uncertainty of a radar waveform as a frequency estimator is then

$$\sigma_{f_D}^2 \geq \frac{N_0}{2|\alpha|^2 \left(\zeta_t^2 - \frac{1}{E_s} \mu_t^2 \right)} \tag{2.11}$$

Therefore, the measurement ability of a radar waveform depends on the first and second moments of the Fourier of the domain of interest. From the temporal and spectral uncertainties the estimation of radial distance and velocity can be derived. The spatial estimation is given from the uncertainty of the time delay (2.7) as

$$\sigma_x^2 \geq \frac{c^2}{4} \sigma_\tau^2 \tag{2.12}$$

where σ_x^2 is the variance over space and the factor of four comes from the two way propagation seen by typical radar measurements. The estimation of velocity can be expressed from the spectral uncertainty (2.11) as

$$\sigma_v^2 \geq \frac{c^2}{4f_c^2} \sigma_{f_D}^2 \tag{2.13}$$

where σ_v^2 is the variance in radial velocity.

2.1.3 Relative Positional and Oscillator Phase Accuracy Requirements to Coherently Beam-form

In a coherent distributed transmit operation, the set of nodes in the array transmits a waveform with the appropriate relative phasing and timing such that the transmitted waveforms arrive at the target in-phase and time aligned, ensuring that the waveforms add constructively at the destination. While there are many drivers of coordination error in open-loop distributed arrays, here I focus on two of the most prominent, which are errors in the measurement of the distances between each node pair and locking the oscillators to the same frequency. Both ensure that the phase errors are sufficiently low to enable high-gain distributed beamforming. For a distributed array of N arbitrarily-placed transmitting nodes emitting continuous-wave signals to a given direction, the signal incident at a point in the far-field of each individual node can be given by [8]

$$s_r(t) = \sum_{n=1}^N h_n \alpha_n(t) e^{j(2\pi ft + \phi_n + \phi_{s,n})} \quad (2.14)$$

where N is the number of elements in the array, h_n is the channel response between the target and node n , α_n is the amplitude, and ϕ_n is the phase error, given by

$$\phi_n = \frac{2\pi}{\lambda} (d_n + \delta d_n) \cos(\theta_n) + \delta \phi_c \quad (2.15)$$

where δd_n is the error in the antenna separation measurement, θ_n is the beamsteering angle relative to the platform orientation, and $\delta \phi_c$ is the relative phase error of the oscillator.

With perfect alignment and position measurements, the ideal received signal is

$$s_i(t) = C \sum_{n=1}^N e^{j\left(2\pi ft + \frac{2\pi}{\lambda} d_n \cos \theta_n\right)}. \quad (2.16)$$

To evaluate the effect of the antenna separation and oscillator phase error terms, the received signal power of (2.14) relative to (2.16), given by

$$G_c = \frac{|s_r s_r^*|}{|s_i s_i^*|}, \quad (2.17)$$

is evaluated. The standard deviations of the error terms (phase error σ_ϕ and internode range error σ_d) are varied, and the probability that the signal power exceeds a given threshold $P(G_c \geq X)$,

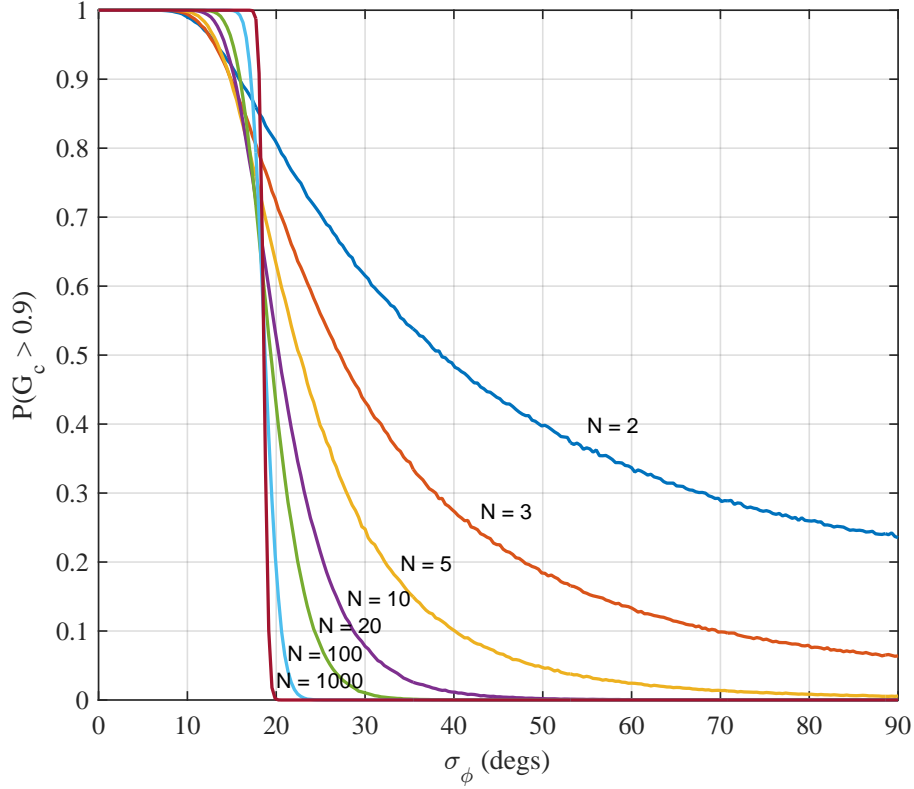


Figure 2.1: Degradation of coherent gain with relative oscillator phase errors between node internal oscillators [8].

where $0 \leq X \leq 1$ is the fraction of the ideal coherent signal power gain, is determined through Monte Carlo simulation. In this work I evaluate the probability that the received signal exceed 0.9 of the ideal gain ($X = 0.9$), corresponding to a coherent gain degradation of 0.5 dB.

In Fig. 2.1 the probability of the received signal power exceeding 0.9 is shown for errors in the oscillator phase σ_ϕ , corollary to the square-root of the CRLB of frequency in (2.11), for coherent distributed arrays consisting of $N = 2, 3, 5, 10, 20, 100$, and 1000 nodes. As the number of nodes in the system increases, the transition area where $P(G_c \geq 0.9) = 1$ becomes sharper, converging to a point below which $P(G_c \geq 0.9)$ is approximately 1, and above which is zero. The area where $P(G_c \geq 0.9) = 1$ also increases as the number of platforms increases due to the decreasing variance of the received signal power as the number of elements in the network increases. As $N \rightarrow \infty$, this cutoff error below which $P(G_c \geq 0.9) \approx 1$ approaches 18° . The oscillator phase error represents an aggregate error which may be due to a number of factors, but

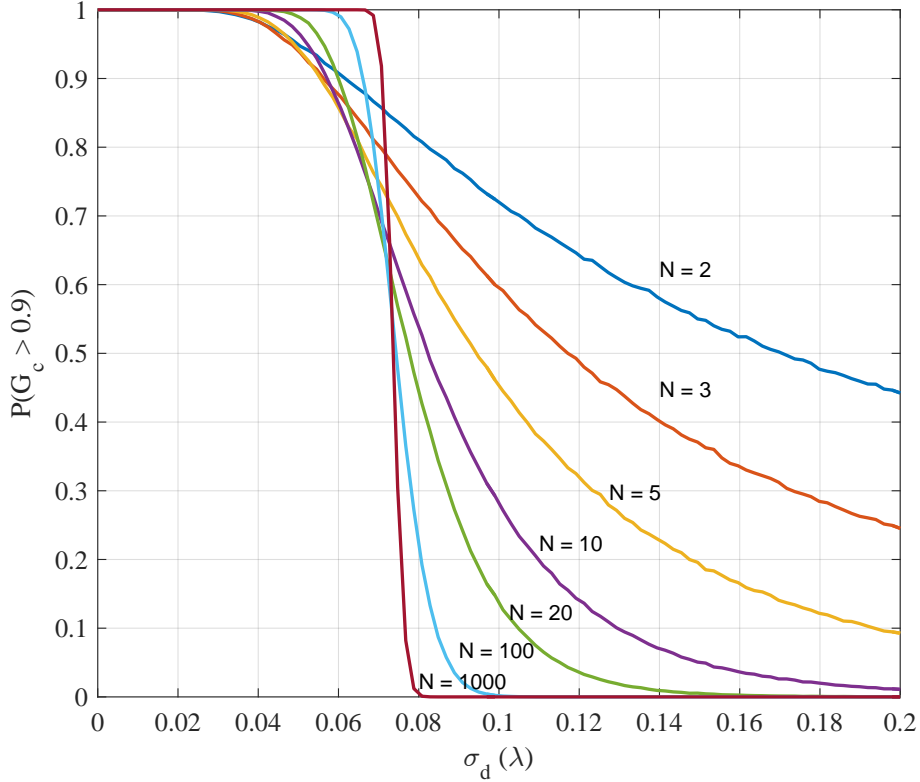


Figure 2.2: Degradation of coherent gain with relative internode positional errors [8].

the most prominent is phase migration due to frequency drift between the platform oscillators. If the oscillators are locked continuously, phase migration is minimal since the phase error output of a phase-locked loop (PLL) is theoretically zero; in this case the PLL noise may contribute as a factor in the error. In such cases the relative frequency drift contributes as the largest error driver.

In Fig. 2.2 the probability of the received signal power exceeding 0.9 is shown for errors in the inter-node range measurement σ_d , corollary to the square-root of the positional CRLB from (2.12). A similar trend with increasing array size is seen. As $N \rightarrow \infty$, this cutoff error below which $P(G_c \geq 0.9) \approx 1$ approaches $\frac{\lambda}{15}$. Note that this does not match the relative phase error of 18° , which would correlate to a phase error of $\frac{\lambda}{20}$, because the pointing angle θ_n is also a random variable, and at some angles the relative range error does not produce significant phase errors in (2.15). For example, if $\theta_n = 0^\circ$, the relative range error can be arbitrary, without increasing the total phase error while at other angles, such as end-fire $\theta_n = 90^\circ$, a more stringent approximation of $\frac{\lambda}{20}$ is required due to direct impact that position has on the total phase error.

2.1.4 Signal-to-Noise Ratio (SNR)

Determining the parametric performance of the system required an estimate of the received SNR, which is estimated in this work using an eigenvalue decomposition approach [83]. The benefit of this approach is that it can directly estimate the signal power and the noise power without needing to distinguish the individual frequencies within a signal. SNR is equivalent to $\frac{2|\alpha|^2 E_s}{N_0}$ is the CRLB equations in (2.7) and (2.11). The received signal can be represented by the sampled matrix

$$\mathbf{X} = \begin{bmatrix} \chi_{1,1} & \chi_{1,2} & \cdots & \chi_{1,L} \\ \chi_{2,1} & \chi_{2,2} & \cdots & \chi_{2,L} \\ \vdots & \vdots & \ddots & \vdots \\ \chi_{N,1} & \chi_{N,2} & \cdots & \chi_{N,L} \end{bmatrix} \quad (2.18)$$

where N is the total number of samples per capture and L is then total number of signal observations. From this the covariance matrix can be computed as

$$\mathbf{R}_x = \frac{1}{N} \mathbf{X} \mathbf{X}^H \quad (2.19)$$

where \mathbf{X}^H is the Hermitian of the matrix \mathbf{X} .

Once the covariance matrix is calculated, the eigenvalues λ_l are calculated using singular-value decomposition, and the resulting eigenvalues are rank ordered from largest to smallest. Because the various tones in the modulated signal are generated by the same system, they are correlated, yielding a single eigenvalue λ_1 which is the largest eigenvalue for non-negative SNR. The remaining $\lambda_2 - \lambda_L$ eigenvalues represent the noise, and therefore the average noise power level can be estimated by

$$\gamma^2 = \frac{1}{L-1} \sum_{l=2}^L \lambda_l \quad (2.20)$$

The signal power level then is calculated using

$$P_s = \frac{\lambda_1 - \gamma^2}{L} \quad (2.21)$$

from which the SNR can be obtained using (2.20) and (2.21) by

$$\text{SNR}_{dB} = 10 \log_{10} \left(\frac{P_s}{\gamma^2} \right) \quad (2.22)$$

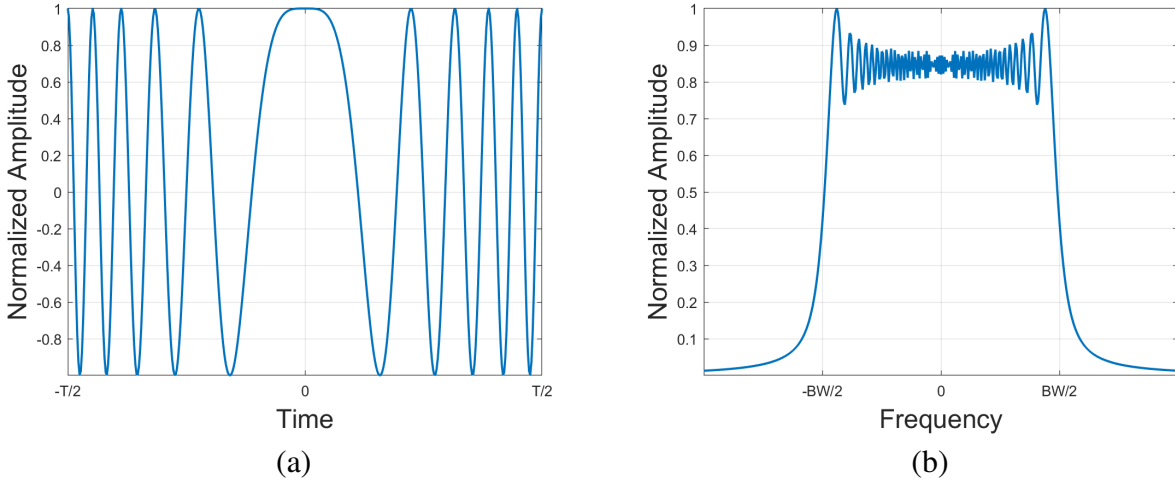


Figure 2.3: (a) LFMW waveform in the time domain. (b) LFMW in the frequency domain.

2.2 Radar Ranging Waveforms

2.2.1 Linear Frequency Modulated Waveform (LFMW)

One of the most widely used ranging waveforms is the LFMWW [55–58] due to its ability to achieve high range resolutions while providing an unambiguous estimation of the time delay. This waveform is used as a comparison to quantify the quality of the designed waveforms in the following sections and chapters. A the general form of a LFMWW utilizes a single frequency that sweeps linearly over a given time and bandwidth, given by

$$s(t) = \frac{1}{\sqrt{T}} \text{rect}\left(\frac{t}{T}\right) e^{j\pi kt^2} \quad (2.23)$$

where T is the time duration and k is modulation rate given by $k = \frac{BW}{T}$, where BW is the sweep bandwidth. An image of the time and frequency domain representations of an LFMW can be seen in Fig. 2.3.

The range and Doppler response of the LFMW can be characterized through the ambiguity function. Inputting the time domain representation of the LFMW (2.23) in the ambiguity function (2.1)

$$AF(t, f_D) = \frac{1}{T} \int_{-\infty}^{\infty} \text{rect}\left(\frac{\tau - t}{T}\right) e^{-j\pi k(\tau - t)^2} \text{rect}\left(\frac{\tau}{T}\right) e^{j\pi k\tau^2} e^{j2\pi f_D\tau} d\tau \quad (2.24)$$

Truncation of the integral can be performed due to $\text{rect}(\cdot)$ being a time limited function with the bounds $[-\frac{T}{2}, \frac{T}{2}]$. After combining exponential terms

$$\begin{aligned} AF(t, f_D) &= \frac{1}{T} \int_{-\frac{T}{2}}^{t+\frac{T}{2}} e^{-j\pi k(t^2-2\tau t)} e^{j2\pi f_D \tau} d\tau \\ &= \frac{e^{-j\pi kt^2}}{j2T\pi (kt + f_D)} \left[e^{j2\pi (kt+f_D)\left(t+\frac{T}{2}\right)} - e^{-j\pi (kt+f_D)T} \right] \end{aligned} \quad (2.25)$$

Extracting a factor of $e^{j\pi(kt+f_D)t}$ from the function so that function in the brackets contains a complex exponential subtracted by its conjugate

$$AF(t, f_D) = \frac{e^{-j\pi kt^2} e^{j\pi(kt+f_D)t}}{j2T\pi (kt + f_D)} \left[e^{j\pi(kt+f_D)(t+T)} - e^{-j\pi(kt+f_D)(t+T)} \right] \quad (2.26)$$

A sine function can now be formed from the complex exponentials where $\sin(\theta) = \frac{1}{j2} (e^{j\theta} - e^{-j\theta})$

$$AF(t, f_D) = \frac{e^{-j\pi kt^2} e^{j\pi(kt+f_D)t}}{T\pi (kt + f_D)} \sin \left(\pi (kt + f_D) (t + T) \right) \quad (2.27)$$

A sinc(\cdot) function can now be formed from the sin(\cdot) function by multiplying by $\frac{t+T}{t+T}$

$$AF(t, f_D) = e^{-j\pi kt^2} e^{j\pi(kt+f_D)t} \left(\frac{t}{T} + 1 \right) \text{sinc} \left(\pi (kt + f_D) (t + T) \right) \quad (2.28)$$

This derivation shown above represents the case of $t < 0$ case but is symmetric for the case of $t > 0$. The general case of the derivation can be represented by

$$AF(t, f_D) = e^{-j\pi kt^2} e^{j\pi(kt+f_D)t} \left(1 - \frac{|t|}{T} \right) \text{sinc} \left(\pi (kt + f_D) (T - |t|) \right) \quad (2.29)$$

The magnitude of the ambiguity function can now be taken and like terms can be combined resulting in [80]

$$|AF(t, f_D)| = \left| \left(1 - \frac{|t|}{T} \right) \text{sinc} \left(\pi (kt + f_D) (T - |t|) \right) \right| \quad (2.30)$$

where $\left| e^{-j\pi kt^2} e^{j\pi(kt+f_D)t} \right| = 1$. An image of the ambiguity function of the LFMW can be seen in Fig. 2.4.

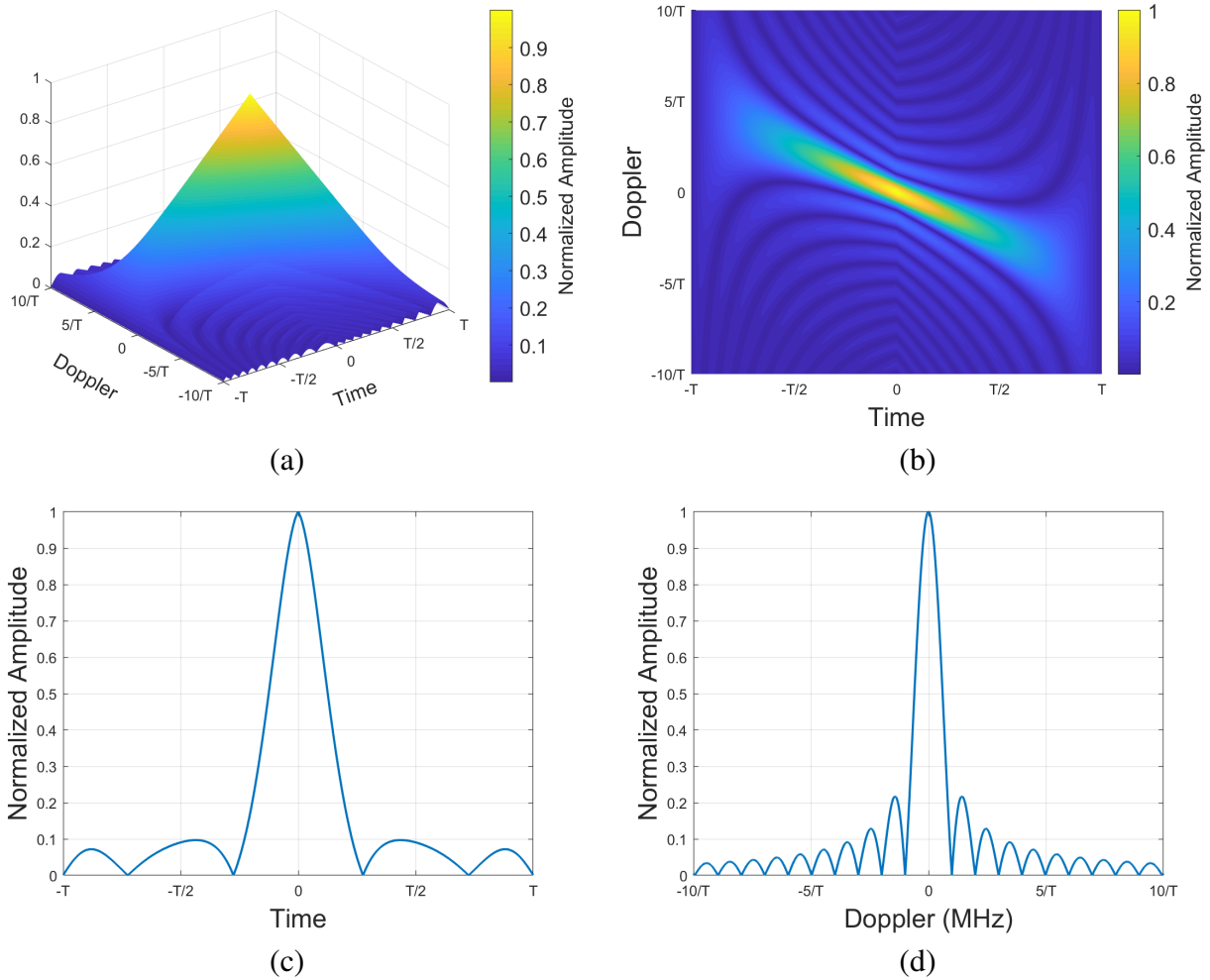


Figure 2.4: (a) Ambiguity function of the LFMW waveform. (b) Intensity plot of the ambiguity function. (c) LFMW matched filter (zero Doppler cut). (d) LFMW Doppler response (zero time cut).

The measurement ability of an LFMW as a positional estimator, by (2.12), or a velocity estimator through Doppler, (2.13), is characterized by the first and second moment of the frequency and time spectrums respectively. This waveform inherently has a zero first moment in both domains, $\mu_f = \mu_t = 0$, so therefore the estimation ability relies solely on the second moment. The second moment of the frequency spectrum can be calculated by approximating the LFMW bandwidth as a rectangular function. The normalized second moment of the frequency spectrum,

where the normalization factor is the signal energy, is given by

$$\begin{aligned}\zeta_f^2 &= \frac{\int (2\pi f)^2 |S(f)|^2 df}{\int |S(f)|^2 df} \\ &= \frac{\int (2\pi f)^2 \left| \text{rect}\left(\frac{f}{BW}\right) \right|^2 df}{\int \left| \text{rect}\left(\frac{f}{BW}\right) \right|^2 df}\end{aligned}\quad (2.31)$$

Applying the limits of integration as $[-\frac{BW}{2}, \frac{BW}{2}]$ bounded by the $\text{rect}(\cdot)$ function

$$\begin{aligned}\zeta_f^2 &= \frac{\int_{-BW/2}^{BW/2} (2\pi f)^2 df}{\int_{-BW/2}^{BW/2} df} \\ &= \frac{\frac{4\pi^2}{3} \left[\left(\frac{BW}{2}\right)^3 - \left(-\frac{BW}{2}\right)^3 \right]}{\frac{BW}{2} + \frac{BW}{2}} \\ &= \frac{\frac{4\pi^2}{3} \left[\frac{BW^3}{4} \right]}{BW} \\ &= \frac{\pi^2 BW^2}{3}\end{aligned}\quad (2.32)$$

This result can be seen in [80]. This gives a positional uncertainty of

$$\sigma_x^2 \geq \frac{3c^2}{4(\pi^2 BW^2) \text{SNR}} \quad (2.33)$$

A similar argument can be made for the second moment of the time domain due to rectangular envelope used to modulate this waveform providing an uncertainty in velocity of

$$\sigma_v^2 \geq \frac{3c^2}{4f_c^2 (\pi^2 T^2) \text{SNR}} \quad (2.34)$$

2.2.2 Stepped-Frequency Waveform (SFW)

The stepped-frequency waveform (SFW) was designed as a pulse compression method that achieves effective wideband measurements through several consecutive pulses with narrow instantaneous bandwidths [59–62]. This waveform can be thought of a discrete LFMW and is also capable of

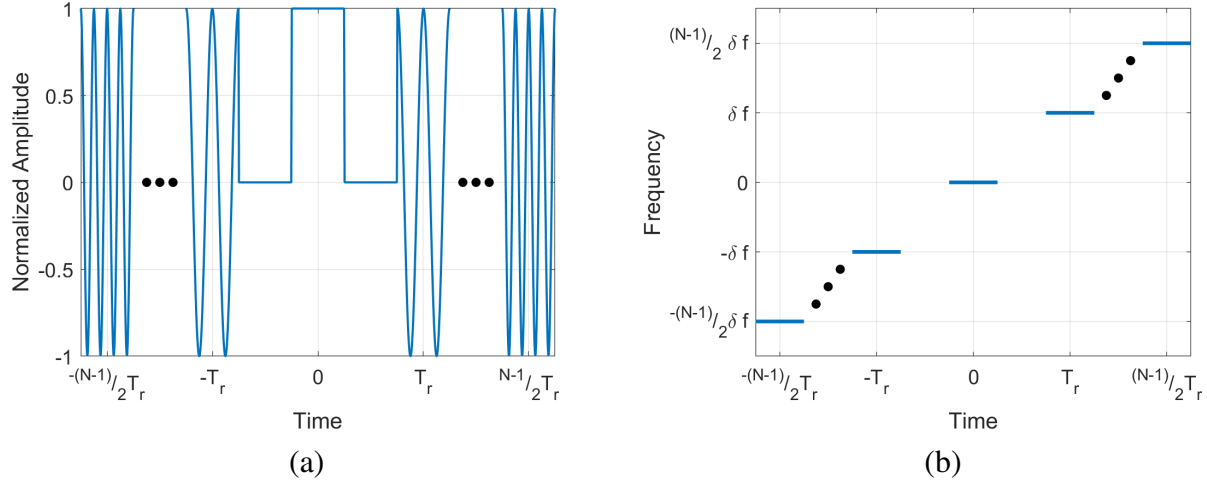


Figure 2.5: (a) Representation of the SFW with 50% duty cycle time domain. (b) SFW time-frequency plot.

achieving high range resolution. This is performed by having each consecutive narrowband pulse increase its frequency by δf and can be modeled as

$$s(t) = \frac{1}{\sqrt{N}} \sum_{n=-\frac{N-1}{2}}^{\frac{N-1}{2}} \text{rect}\left(\frac{t - nT_r}{T}\right) e^{j2\pi n \delta f t} \quad (2.35)$$

where δf is the discrete frequency step between each pulse, N is the number of pulses, T is the pulse duration, and nT_r is the center time of each pulse. An image of the waveform model, with a 50% temporal duty cycle, in both the time domain and the time-frequency domain can be seen in Fig. 2.5.

There are two main advantages to using a SFW: the range resolution is increased while maintaining narrow instantaneous bandwidth [84], and, while not completely unambiguous like the LFMW, the next highest sidelobe of the matched filter is shifted by $t = \frac{1}{\delta f}$. The ambiguity function can be solved for by inputting the time domain representation of the SFW from (2.35) in the ambiguity function equation (2.1)

$$AF(t, f_D) = \frac{1}{N} \int_{-\infty}^{\infty} \sum_{n=-\frac{N-1}{2}}^{\frac{N-1}{2}} \text{rect}\left(\frac{\tau - t - nT_r}{T}\right) e^{-j2\pi n \delta f (\tau - t)} \times \text{rect}\left(\frac{\tau - nT_r}{T}\right) e^{j2\pi n \delta f \tau} e^{j2\pi f_D \tau} d\tau \quad (2.36)$$

The summation and integral are linear processes therefore the integration can be brought inside the summation

$$AF(t, f_D) = \frac{1}{N} \sum_{n=-\frac{N-1}{2}}^{\frac{N-1}{2}} e^{j2\pi n\delta ft} \int_{-\infty}^{\infty} \text{rect}\left(\frac{\tau - t - nT_r}{T}\right) \text{rect}\left(\frac{\tau - nT_r}{T}\right) e^{j2\pi f_D \tau} d\tau \quad (2.37)$$

A substitution can be made such that $\hat{\tau} = \tau - nT_r$

$$AF(t, f_D) = \frac{1}{N} \sum_{n=-\frac{N-1}{2}}^{\frac{N-1}{2}} e^{j2\pi n\delta ft} \int_{-\infty}^{\infty} \text{rect}\left(\frac{\hat{\tau} - t}{T}\right) \text{rect}\left(\frac{\hat{\tau}}{T}\right) e^{j2\pi f_D(\hat{\tau} + nT_r)} d\hat{\tau} \quad (2.38)$$

Due to the time limited nature of the $\text{rect}(\cdot)$ function, the integral is bounded by $[-\frac{T}{2}, \frac{T}{2}]$

$$\begin{aligned} AF(t, f_D) &= \frac{1}{N} \sum_{n=-\frac{N-1}{2}}^{\frac{N-1}{2}} e^{j2\pi n(\delta ft + f_D T_r)} \int_{-\frac{T}{2}}^{t + \frac{T}{2}} e^{j2\pi f_D \hat{\tau}} d\hat{\tau} \\ &= \frac{1}{N} \sum_{n=-\frac{N-1}{2}}^{\frac{N-1}{2}} e^{j2\pi n(\delta ft + f_D T_r)} \left[\frac{1}{j2\pi f_D} \left(e^{j2\pi f_D \left(t + \frac{T}{2}\right)} - e^{-j2\pi f_D \frac{T}{2}} \right) \right] \end{aligned} \quad (2.39)$$

Extracting a factor of $e^{j\pi f_D t}$ so the function in the parenthesis contains a complex exponential subtracted by its conjugate

$$AF(t, f_D) = \frac{1}{N} \sum_{n=-\frac{N-1}{2}}^{\frac{N-1}{2}} e^{j2\pi n(\delta ft + f_D T_r)} \left[\frac{e^{j\pi f_D t}}{j2\pi f_D} \left(e^{j\pi f_D(t+T)} - e^{-j\pi f_D(t+T)} \right) \right] \quad (2.40)$$

A sine function can now be formed from the complex exponentials where $\sin(\theta) = \frac{1}{j2} \left(e^{j\theta} - e^{-j\theta} \right)$

$$AF(t, f_D) = \frac{1}{N} \sum_{n=-\frac{N-1}{2}}^{\frac{N-1}{2}} e^{j2\pi n(\delta ft + f_D T_r)} \left[\frac{e^{j\pi f_D t}}{\pi f_D} \sin\left(\pi f_D(t+T)\right) \right] \quad (2.41)$$

By multiplying by a factor of $\frac{t+T}{t+T}$, a $\text{sinc}(\cdot)$ function can now be formed

$$AF(t, f_D) = \frac{1}{N} \sum_{n=-\frac{N-1}{2}}^{\frac{N-1}{2}} e^{j2\pi n(\delta ft + f_D T_r)} \left[e^{j\pi f_D t} (t+T) \text{sinc}\left(\pi f_D(t+T)\right) \right] \quad (2.42)$$

This derivation shown above represents the case of $t < 0$ case but is symmetric for the case of $t > 0$. The general case of the derivation can be represented by

$$AF(t, f_D) = \frac{1}{N} \left[e^{j\pi f_D t} (T - |t|) \text{sinc} \left(\pi f_D (T - |t|) \right) \right] \sum_{n=-\frac{N-1}{2}}^{\frac{N-1}{2}} e^{j2\pi n(\delta f t + f_D T r)} \quad (2.43)$$

The sum in (3.59) can be evaluated by first expanding the summation

$$\begin{aligned} S_{sum} &= \sum_{n=-\frac{N-1}{2}}^{\frac{N-1}{2}} e^{j2\pi n(\delta f t + f_D T r)} \\ &= e^{-j2\pi \frac{N-1}{2}(\delta f t + f_D T r)} \dots + 1 \dots + e^{j2\pi \frac{N-1}{2}(\delta f t + f_D T r)} \end{aligned} \quad (2.44)$$

A secondary summation can be formed by multiplying (2.44) with $e^{j2\pi(\delta f t + f_D T r)}$

$$S_{sum} e^{j2\pi(\delta f t + f_D T r)} = e^{-j2\pi \frac{N-3}{2}(\delta f t + f_D T r)} \dots + 1 \dots + e^{j2\pi \frac{N+1}{2}(\delta f t + f_D T r)} \quad (2.45)$$

Subtracting the terms in (2.44) from (2.45)

$$S_{sum} e^{j2\pi(\delta f t + f_D T r)} - S_{sum} = e^{j\pi(N+1)(\delta f t + f_D T r)} - e^{-j\pi(N-1)(\delta f t + f_D T r)} \quad (2.46)$$

S_{sum} can now be solved for

$$S_{sum} = \frac{e^{j\pi(N+1)(\delta f t + f_D T r)} - e^{-j\pi(N-1)(\delta f t + f_D T r)}}{e^{j2\pi(\delta f t + f_D T r)} - 1} \quad (2.47)$$

A factor of $e^{j\pi(\delta f t + f_D T r)}$ can be extracted from both the numerator and denominator.

$$S_{sum} = \frac{e^{j\pi(\delta f t + f_D T r)} e^{j\pi N(\delta f t + f_D T r)} - e^{-j\pi N(\delta f t + f_D T r)}}{e^{j\pi(\delta f t + f_D T r)} e^{j\pi(\delta f t + f_D T r)} - e^{-j\pi(\delta f t + f_D T r)}} \quad (2.48)$$

Sine terms can be formed on the numerator and denominator where $\sin(\theta) = \frac{1}{j2} (e^{j\theta} - e^{-j\theta})$

$$S_{sum} = \frac{\sin \left(\pi N (\delta f t + f_D T r) \right)}{\sin \left(\pi (\delta f t + f_D T r) \right)} \quad (2.49)$$

Plugging (3.60) back into (3.59)

$$AF(t, f_D) = \frac{1}{N} e^{j\pi f_D t} (T - |t|) \text{sinc} \left(\pi f_D (T - |t|) \right) \frac{\sin \left(\pi N (\delta f t + f_D T r) \right)}{\sin \left(\pi (\delta f t + f_D T r) \right)} \quad (2.50)$$

The magnitude can now be taken where $|e^{j\pi f_D t}| = 1$ resulting in [85]

$$|AF(t, f_D)| = \left| \frac{1}{N} (T - |t|) \operatorname{sinc} \left(\pi f_D (T - |t|) \right) \frac{\sin \left(\pi N (\delta f t + f_D T_r) \right)}{\sin \left(\pi (\delta f t + f_D T_r) \right)} \right| \quad (2.51)$$

A plot of the SFW ambiguity function can be seen in Fig. 2.6. When looking at the $f_d = 0$ cut, this function is maximized at every $t = \frac{n}{\delta f}$ and therefore the next highest sidelobe is at $t = \frac{1}{\delta f}$. Considering the nulls of the zero Doppler cut, which occurs at $t = \pm \frac{1}{N\delta f}$, it can now easily be seen that the lobe beamwidth is inversely proportional to the number of pulses N . The disambiguation properties of this waveform can clearly be seen to be inversely proportional to the frequency step δf . Therefore large frequency steps result in unambiguous measurements but this requires a large amount of bandwidth.

The estimation ability of this waveform is again derived from the temporal and spectral uncertainty in (2.7) and (2.11). The first moment of this waveform, like the LFMW, is fundamentally zero, $\mu_t = \mu_f = 0$, and therefore can be neglected in both calculations resulting in the dictation of the CRLB calculation stemming from the second moment of the Fourier of the domain of interest. For the calculation of ζ_f^2 an approximation is made such that each pulse consists of a delta function in the frequency domain at each of the underlying pulse modulation frequencies such that

$$\begin{aligned} \zeta_f^2 &= \frac{\int (2\pi f)^2 |S(f)|^2 df}{\int |S(f)|^2 df} \\ &= \frac{\sum_{n=-\frac{N-1}{2}}^{\frac{N-1}{2}} \int (2\pi f)^2 |\delta(f - n\delta f)|^2 df}{\sum_{n=-\frac{N-1}{2}}^{\frac{N-1}{2}} \int |\delta(f - n\delta f)|^2 df} \end{aligned} \quad (2.52)$$

Due the fundamental property of delta functions being zero outside of the specified shifted value,

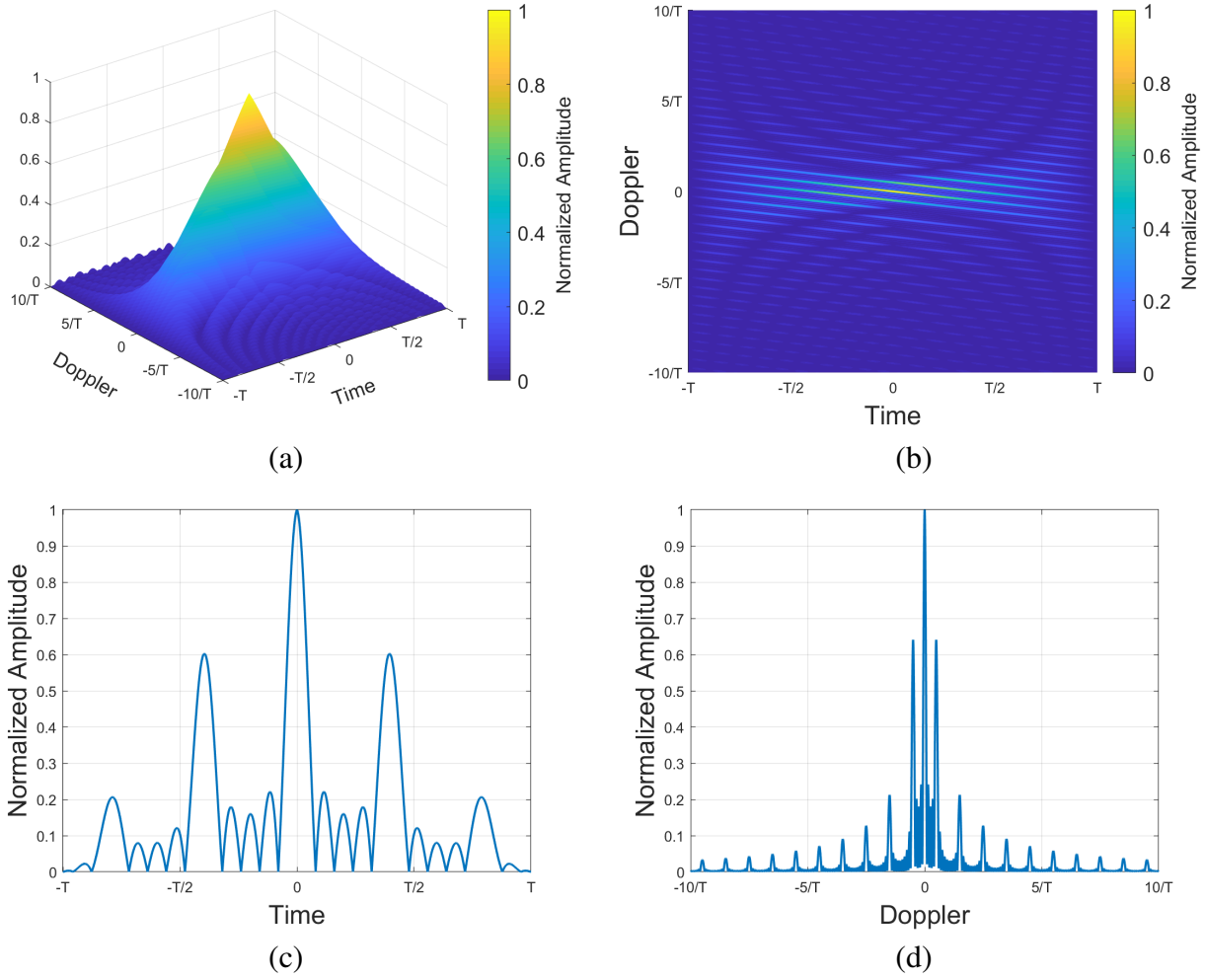


Figure 2.6: (a) Ambiguity function of the SFW. (b) Intensity plot of the ambiguity function. (c) Matched filter of the SFW (zero Doppler cut). (d) Doppler response of SFW (zero time cut).

the inner product resulting from the squared terms, can be neglected reducing this calculation to

$$\begin{aligned}
 \zeta_f^2 &= \frac{4\pi^2 \left[\sum_{n=-\frac{N-1}{2}}^{\frac{N-1}{2}} (n\delta f)^2 \right]}{N} \\
 &= \frac{4\pi^2 \delta f^2 \left[\frac{1}{12} N (N^2 - 1) \right]}{N} \\
 &= \frac{\pi^2 \delta f^2 (N^2 - 1)}{3}
 \end{aligned} \tag{2.53}$$

Resulting in a spatial uncertainty from (2.12) of

$$\sigma_x^2 \geq \frac{3c^2}{4 [\pi^2 \delta f^2 (N^2 - 1)] \text{SNR}} \tag{2.54}$$

which provides the same accuracy of the LFMW for $\delta f \sqrt{N^2 - 1} = BW$ where BW is the LFMW sweep bandwidth.

The spectral uncertainty can be calculated from the second moment of the rectangular pulse train used as a baseband modulation for this waveform such that

$$\begin{aligned}\zeta_t^2 &= \frac{\int (2\pi t)^2 |S(t)|^2 dt}{\int |S(t)|^2 dt} \\ &= \frac{\sum_{n=-\frac{N-1}{2}}^{\frac{N-1}{2}} \int (2\pi t)^2 \left| \text{rect} \left(\frac{t-nT_r}{T} \right) \right|^2 dt}{\sum_{n=-\frac{N-1}{2}}^{\frac{N-1}{2}} \int \left| \text{rect} \left(\frac{t-nT_r}{T} \right) \right|^2 dt}\end{aligned}\quad (2.55)$$

Applying the limits $[nT_r - \frac{T}{2}, nT_r + \frac{T}{2}]$ due to $\text{rect}(\cdot)$ being a time limited function

$$\begin{aligned}\zeta_t^2 &= \frac{\sum_{n=-\frac{N-1}{2}}^{\frac{N-1}{2}} \int_{nT_r - \frac{T}{2}}^{nT_r + \frac{T}{2}} (2\pi t)^2 dt}{\sum_{n=-\frac{N-1}{2}}^{\frac{N-1}{2}} \int_{nT_r - \frac{T}{2}}^{nT_r + \frac{T}{2}} dt} \\ &= \frac{\sum_{n=-\frac{N-1}{2}}^{\frac{N-1}{2}} 4\pi^2 \left[\left(nT_r + \frac{T}{2} \right)^3 - \left(nT_r - \frac{T}{2} \right)^3 \right]}{\sum_{n=-\frac{N-1}{2}}^{\frac{N-1}{2}} \left[\left(nT_r + \frac{T}{2} \right) - \left(nT_r - \frac{T}{2} \right) \right]} \\ &= \frac{\sum_{n=-\frac{N-1}{2}}^{\frac{N-1}{2}} 4\pi^2 \left[3n^2 T_r^2 T + \frac{T^3}{4} \right]}{NT} \\ &= \frac{4\pi^2 \left\{ 3T_r^2 T \left[\frac{1}{12} N (N^2 - 1) \right] + N \frac{T^3}{4} \right\}}{NT} \\ &= \pi^2 \left[T_r^2 (N^2 - 1) + T^2 \right]\end{aligned}\quad (2.56)$$

Resulting in an uncertainty in the velocity from (2.13) of

$$\sigma_v^2 \geq \frac{c^2}{4f_c^2 \pi^2 [T_r^2 (N^2 - 1) + T^2] \text{SNR}} \quad (2.57)$$

which decreases the uncertainty from a single rectangular pulse of duration T by spreading the temporal energy nonuniformly over the the time domain if the duty cycle is less than 100%.

2.2.3 Pulsed Two-Tone Waveform (PTTW)

The optimal performance of a time delay estimator maximizes the second moment of the frequency spectrum given by a waveform consisting of two frequencies at the opposite edges of the band of interest. In this case continuous wave waveform is needed due to the representation in the Fourier domain which results a delta function at the designated frequencies, yielding a perfect two-tone signal. In practice, it is necessary that the signal is time-limited due to system constraints. To assess the effects of this time limitation, a two-tone waveform modulated by a square temporal pulse is analyzed here. In the frequency domain, this creates $\text{sinc}(\cdot)$ functions at the designated two frequencies whose bandwidth is inversely proportional to the pulse duration. This results in a decrease of the mean squared bandwidth and in turn raises the minimum obtainable variance. As long as the pulse bandwidth is small compared to the frequency separation of the two tones, this reduction in accuracy has little effect on the variance.

The time domain representation of a pulsed two-tone waveform (PTTW) which can be expressed as

$$s(t) = \frac{1}{2} \text{rect}\left(\frac{t}{T}\right) \left(e^{-j\pi\Delta f t} + e^{j\pi\Delta f t} \right) \quad (2.58)$$

where $\text{rect}(\cdot)$ is the rectangular pulse function, T is the pulse duration, and Δf is the equivalent to the spectral separation between the two tones (i.e. $f_2 - f_1$) where f_2 and f_1 are the higher and lower frequency tones respectively. An image of an example of the PTTW can be seen in the time and frequency domains can be seen in Fig. 2.7. Here a baseband representation of the PTTW is represented therefore only the beat frequency between the two frequencies are present. If this waveform were to be upconverted to a carrier, a modulated sinusoid would be created.

The range and Doppler response of the PTTW can again be observed through inputting

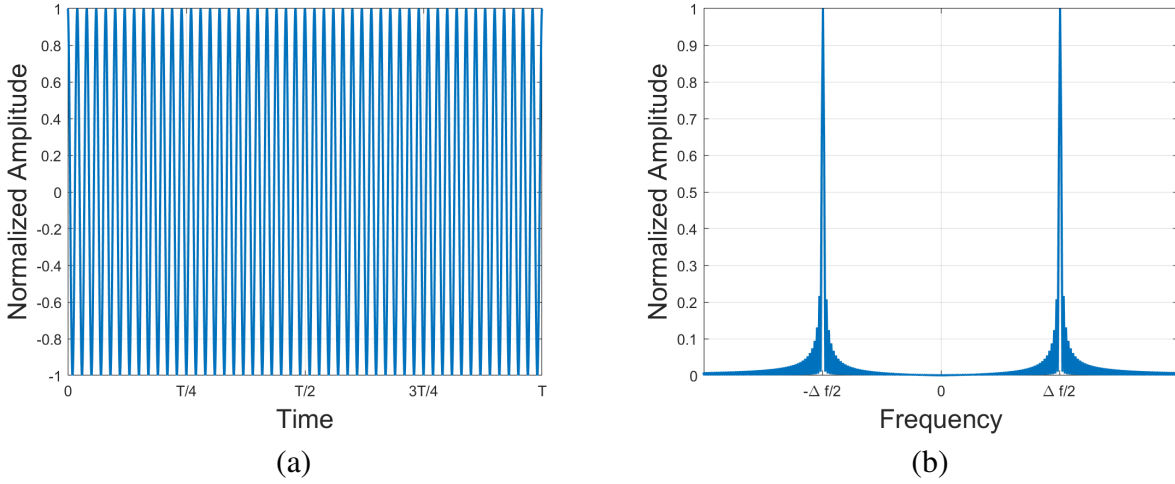


Figure 2.7: (a) The baseband PTTW in the time domain. (b) PTTW in the frequency domain.

the time domain representation of the PTTW from (2.58) into the ambiguity function (2.1)

$$\begin{aligned}
 AF(t, f_D) &= \frac{1}{4} \int_{-\infty}^{\infty} \text{rect}\left(\frac{\tau-t}{T}\right) \left(e^{j\pi\Delta f(\tau-t)} + e^{-j\pi\Delta f(\tau-t)} \right) \\
 &\quad \times \text{rect}\left(\frac{\tau}{T}\right) \left(e^{-j\pi\Delta f\tau} + e^{j\pi\Delta f\tau} \right) e^{j2\pi f_D\tau} d\tau
 \end{aligned} \tag{2.59}$$

Truncation of the integral can be performed due to $\text{rect}(\cdot)$ being a time limited function with the bounds $[-\frac{T}{2}, \frac{T}{2}]$

$$\begin{aligned}
 AF(t, f_D) &= \frac{1}{4} \int_{-\frac{T}{2}}^{t+\frac{T}{2}} \left(e^{-j\pi\Delta f t} + e^{j\pi\Delta f t} + e^{j\pi\Delta f(2\tau-t)} + e^{-j\pi\Delta f(2\tau-t)} \right) e^{j2\pi f_D\tau} d\tau \\
 &= \frac{e^{-j\pi\Delta f t} + e^{j\pi\Delta f t}}{j8\pi f_D} \left[e^{j2\pi f_D(t+\frac{T}{2})} - e^{-j\pi f_D T} \right] \\
 &\quad + \frac{e^{-j\pi\Delta f t}}{j8\pi(\Delta f + f_D)} \left[e^{j2\pi(\Delta f + f_D)(t+\frac{T}{2})} - e^{-j\pi(\Delta f + f_D)T} \right] \\
 &\quad + \frac{e^{j\pi\Delta f t}}{j8\pi(f_D - \Delta f)} \left[e^{j2\pi(f_D - \Delta f)(t+\frac{T}{2})} - e^{-j\pi(f_D - \Delta f)T} \right]
 \end{aligned} \tag{2.60}$$

Extracting a factor from each function so that every parenthesis contains a complex exponential

subtracted by its conjugate

$$\begin{aligned}
AF(t, f_D) &= \frac{(e^{-j\pi\Delta ft} + e^{j\pi\Delta ft}) e^{j\pi f_D t}}{j8\pi f_D} \left[e^{j\pi f_D(t+T)} - e^{-j\pi f_D(t+T)} \right] \\
&+ \frac{e^{-j\pi\Delta ft} e^{j\pi(\Delta f + f_D)t}}{j8\pi(\Delta f + f_D)} \left[e^{j\pi(\Delta f + f_D)(t+T)} - e^{-j\pi(\Delta f + f_D)(t+T)} \right] \\
&+ \frac{e^{j\pi\Delta ft} e^{j\pi(f_D - \Delta f)t}}{j8\pi(f_D - \Delta f)} \left[e^{j\pi(f_D - \Delta f)(t+T)} - e^{-j\pi(f_D - \Delta f)(t+T)} \right]
\end{aligned} \tag{2.61}$$

$e^{j\pi\Delta ft}$ cancels in the second and third terms and sinc functions can now be formed by multiplying each function by $\frac{t+T}{t+T}$ such that $\text{sinc}(\theta) = \frac{1}{j2\theta} (e^{j\theta} - e^{-j\theta})$

$$\begin{aligned}
AF(t, f_D) &= \frac{(e^{-j\pi\Delta ft} + e^{j\pi\Delta ft})}{4} e^{j\pi f_D t} (t+T) \text{sinc}(\pi f_D(t+T)) \\
&+ \frac{e^{j\pi f_D t}}{4} (t+T) \text{sinc}(\pi(\Delta f + f_D)(t+T)) \\
&+ \frac{e^{j\pi f_D t}}{4} (t+T) \text{sinc}(\pi(f_D - \Delta f)(t+T))
\end{aligned} \tag{2.62}$$

The terms $\frac{e^{j\pi f_D t}}{4}$ and $(t+T)$ can then be extracted from each term. This derivation shown above represents the case of $t < 0$ case but is symmetric for the case of $t > 0$. The general case of the derivation can be represented by

$$\begin{aligned}
AF(t, f_D) &= \frac{e^{j\pi f_D t} (T - |t|)}{4} \left[(e^{-j\pi\Delta ft} + e^{j\pi\Delta ft}) \text{sinc}(\pi f_D (T - |t|)) \right. \\
&+ \text{sinc}(\pi(\Delta f + f_D)(T - |t|)) \\
&+ \left. \text{sinc}(\pi(f_D - \Delta f)(T - |t|)) \right]
\end{aligned} \tag{2.63}$$

The magnitude of the ambiguity function can now be taken and like terms can be combined

$$\begin{aligned}
|AF(t, f_D)| &= \left| \frac{(T - |t|)}{4} \left[2 \text{sinc}(\pi f_D (T - |t|)) + \text{sinc}(\pi(\Delta f + f_D)(T - |t|)) \right. \right. \\
&+ \left. \left. \text{sinc}(\pi(f_D - \Delta f)(T - |t|)) \right] \right|
\end{aligned} \tag{2.64}$$

where the $|e^{j\pi f_D t}| = 1$ and $|e^{-j\pi\Delta ft} + e^{j\pi\Delta ft}| = 2$. An image of the ambiguity function for a PTTW can be seen in Fig. 2.8. From this image, it can be seen that there is a repeated lobing pattern in the time domain. This arises from the beat frequency between $-\frac{\Delta f}{2}$ and $\frac{\Delta f}{2}$. In the

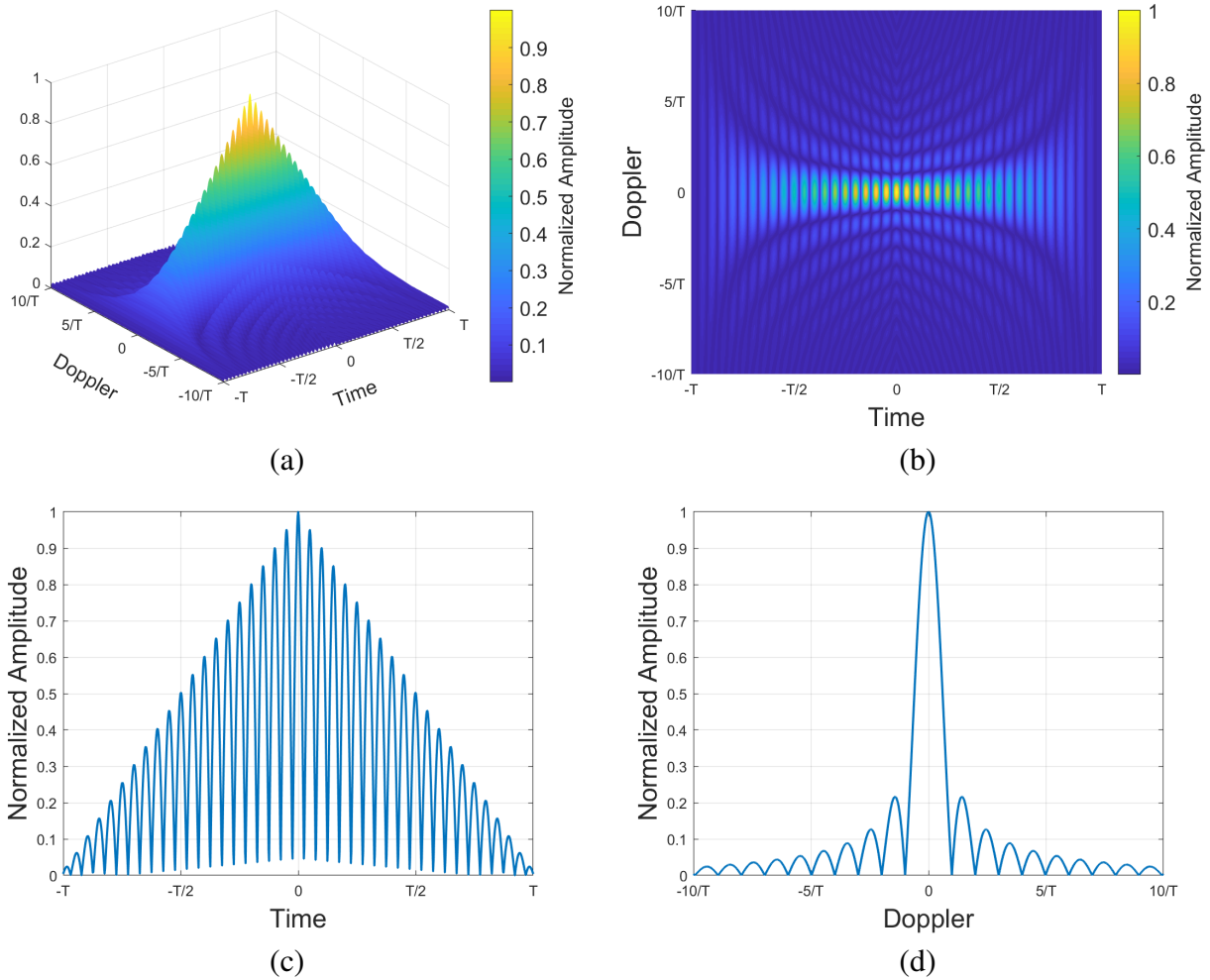


Figure 2.8: (a) Ambiguity function of the PTTW. (b) Intensity plot of the ambiguity function. (c) Matched filter of the PTTW (zero Doppler cut). (d) Doppler response of the PTTW (zero time cut).

frequency domain the response is a $\text{sinc}(\cdot)$ function which stems from the overlaying rectangular pulse modulation in the time domain.

While having the benefit of increased measurement accuracy, a PTTW waveform has a drawback which is that the measurement is highly ambiguous due to the large number of lobes in the temporal response. It is typically challenging to track the correct peak lobe especially in the presence of noise. Previous works have used an interleaved wideband pulse with bandwidth equal to $\frac{\Delta f}{4}$ to have effective peak tracking [86].

The uncertainty of the time and Doppler estimation are again measured through the tem-

poral and spectral uncertainty of the matched filter and Doppler cuts of the ambiguity function giving a measure of the stability of this waveform on a measurement by measurement basis. The calculation on of the CRLB, resulting from the first and second moment of the Fourier of the domain of interest, can be formulated solely from the second moment due to the PTTW inherently having a zero first moment $\mu_t = \mu_f = 0$. An approximation can be made for calculating the second moment of the of the frequency domain by using delta functions at each frequency $-\frac{\Delta f}{2}$ and $\frac{\Delta f}{2}$ where the assumption is made that the individual pulse bandwidth $\frac{1}{T}$ is much less than the overall bandwidth Δf . This insures that the modulation bandwidth stemming from the time limited aspect of the waveform has negligible degradation to the overall performance of the optimal continuous wave case. Calculation of the normalized mean squared bandwidth can be made using (2.5)

$$\begin{aligned}
\zeta_f^2 &= \frac{\int (2\pi f)^2 |S(f)|^2 df}{\int |S(f)|^2 df} \\
&= \frac{\int (2\pi f)^2 \left| \delta\left(f + \frac{\Delta f}{2}\right) + \delta\left(f - \frac{\Delta f}{2}\right) \right|^2 df}{\int \left| \delta\left(f + \frac{\Delta f}{2}\right) + \delta\left(f - \frac{\Delta f}{2}\right) \right|^2 df} \\
&= \frac{4\pi^2 \left[\left(\frac{\Delta f}{2}\right)^2 + \left(\frac{\Delta f}{2}\right)^2 \right]}{(1 + 1)} \\
&= \pi^2 \Delta f^2
\end{aligned} \tag{2.65}$$

The mean-squared bandwidth is maximized when the bandwidth, Δf , is also maximized and thus providing the minimum variance. This is the driving motivation behind spectrally sparse waveforms as a method for ranging. This results in a spatial uncertainty from (2.12) of [86]

$$\sigma_x^2 \geq \frac{c^2}{4(\pi^2 \Delta f^2) \text{SNR}} \tag{2.66}$$

providing an improvement of a factor of three from what can be achieved from the what can be seen by a waveform occupying the same bandwidth with equal spectral power at each frequency (i.e. LFMW with sweep bandwidth Δf).

The uncertainty of velocity (2.13) can be calculated from the spectral uncertainty (2.9) and (2.11) where the response is again linked to the rectangular modulation in the time domain.

Following the previous derivations

$$\sigma_v^2 \geq \frac{3c^2}{4f_c^2 (\pi^2 T^2) \text{SNR}} \quad (2.67)$$

which has the same Doppler uncertainty as the LFMW case for the same time duration T .

CHAPTER 3

WAVEFORMS DESIGNED FOR HIGH-ACCURACY RANGING FOR DISTRIBUTED BEAMFORMING ARRAYS

In this chapter I derive waveforms for range estimation, using the metrics discussed in the last chapter, to enable phase alignment of distributed beamforming. These waveforms are validated through experimentation. The waveforms in the previous chapter are used as a quality comparison for the new waveform designs. The specific waveforms I discuss in this chapter are: a waveform for near optimal estimation of position and velocity; a spectrally sparse waveform enabling joint frequency transfer and phase alignment; a method for using a standard communications waveform preamble to enable networked systems to perform position and velocity estimation without effecting the information throughput; and a pulse encoded dual-tone waveform for high-accuracy scalable range estimation. These waveform designs demonstrate different methods to address scalability for distributed systems that consist of more than two nodes, where multiple inter-node communication links are required. The advantages and disadvantages of time domain duplexing (TDD), frequency domain multiplexing (FDM), and pulse encoding for the purpose of scalability are discussed in this chapter.

3.1 Time Domain Duplex: Joint Range-Doppler Estimation Using Prolate Spheroidal Wave Functions (PSWF)

In this section a waveform design to provide near optimal performance as both a position and velocity estimator is presented. Prolate spheroidal wave functions (PSWF) are employed due to their unique ability to maximally concentrate signal energy into a finite time and bandwidth. Waveforms with finite durations reduce the spread of energy, in either temporal or spectral domains, resulting in an increase of the second moment of that respective domain and thereby an improvement of the theoretical estimation ability by reducing the CRLB. The PSWF presents a solution that is approximately finite in both domains and, therefore, is an optimal baseband wave-

form representation. Here an optimized mean squared duration and bandwidth are designed by concatenating two PSWFs to create a time envelope that is modulated by a two-tone signal. Due to this waveform's near maximum time and bandwidth occupancy, a time duplex method for scalability would need to be implemented where each primary to secondary connection of a distributed array would have individual time slots to perform their estimations.

3.1.1 Theory of Prolate Spheroidal Wave Functions

Since the early 1930 PSWFs have been known as the eigenfunctions to the Sturm-Liouville operators L_c given by

$$L_c(\psi) = (1 - x^2) \frac{d^2\psi}{dx^2} - 2x \frac{d\psi}{dx} - c^2 x^2 \psi \quad (3.1)$$

for any $c > 0$. This function arises from solving the Helmholtz equation $\Delta\Psi + k^2\Psi = 0$ over a prolate spheroid. Later in the 1960s Slepian, Pollak, and Landau arrived at the same function from the perspective of nonclassical versions of uncertainty principles [87–91]. Here they discovered the PSWFs to be the eigenfunctions of a self-adjoint integral operator defined by

$$\lambda_n \psi_n(t) = \int_{-\frac{T}{2}}^{\frac{T}{2}} \frac{\sin(2\pi W(t-s))}{\pi(t-s)} \psi_n(s) ds \quad n = 0, 1, 2, \dots \quad (3.2)$$

where λ_n are the eigenvalues, ψ_n are the PSWFs, W is bandwidth, and T is the time duration. The values of W and T are bound by the value $c = \pi TW$ known as the Slepian frequency.

For any given value such that $T > 0$ and $W > 0$ the PSWFs in (3.2) represent a countably infinite set of real functions which have the following properties:

1. $\psi_n(t)$ represent an orthonormal set of band-limited functions which for unit energy implies

$$\int_{-\infty}^{\infty} \psi_n(t) \psi_m(t) dt = \begin{cases} 0, & n \neq m \\ 1, & n = m \end{cases} \quad n, m = 0, 1, 2, 3, \dots$$

2. In the time interval $[-T/2, T/2]$ the values of $\psi_n(t)$ are also orthogonal yet do not contain the entire concentration of energy such that $\lambda_n \leq 1$.

$$\int_{-T/2}^{T/2} \psi_n(t)\psi_m(t)dt = \begin{cases} 0, & n \neq m \\ \lambda_n, & n = m \end{cases} \quad n, m = 0, 1, 2, 3 \dots$$

3. $\psi_n(t)$ is even or odd with even and odd values of n respectively.
4. There is exactly n zeros in the interval $[-T/2, T/2]$.

The functions $\psi_n(t)$ represent eigenfunctions to the equation in (3.2) where the values of λ_n represent the corresponding eigenvalues. Properties of the eigenvalues include the following:

1. They rank from largest to smallest values with the value of n such that

$$1 \geq \lambda_0 \geq \lambda_1 \geq \lambda_2 \geq \dots$$

2. They are the kernel of the sinc(\cdot) operator
3. They approach 0 as the value of n approaches infinity:

$$\lim_{n \rightarrow \infty} \lambda_n = 0$$

Slepian discovered that values of the eigenvalues are nearly 1 until $\frac{2c}{\pi}$ when at which they superexponentially approach 0 at a rate of approximately $\log(c)$ [92]. The transition point at which these values approach zero plays an important role by providing a truncation value to approximate the PSWFs.

3.1.2 Numerical Approximation of the PSWFs

There are many different methods to approximate these functions through numerical models, among them the quadrature method which uses the Gaussian quadrature formula [93–95] and the Whittaker-Shannon sampling theorem method [96, 97], but the classic method is the Bouwkamp

algorithm which uses the Legendre-Galerkin method [98, 99] and is the approach used in this dissertation. The Bouwkamp algorithm is based off of representing the PSWF as a set of normalized Legendre polynomials

$$\psi_n(t) = \sum_{k=0}^{\infty} \beta_{nk} \bar{P}_k(t) \quad (3.3)$$

where $\bar{P}_k(t)$ are the normalized Legendre polynomial and β_{nk} are the expansion coefficients. The Legendre polynomials are a set of orthogonal polynomials which satisfies the three-term recursion relation

$$P_{k+1}(t) = \frac{2k+1}{k+1}tP_k(t) - \frac{k}{k+1}P_{k-1}(t) \quad k \geq 1 \quad (3.4)$$

with the initial conditions

$$P_0(t) = 1 \quad (3.5)$$

$$P_1(t) = t$$

These Legendre polynomials are normalized to create an orthonormal basis set using the normalization factor

$$\bar{P}_k(t) = \sqrt{k + \frac{1}{2}} P_k(t) \quad (3.6)$$

The expansion coefficients β_{nk} present in (3.3) are calculated through an infinite symmetric pentadiagonal matrix \mathbf{A} [95, 100–102] known as the Galerkin matrix

$$\mathbf{A} = \begin{bmatrix} a_{0,0} & 0 & a_{0,2} & 0 & 0 & \cdots & 0 & 0 & 0 \\ 0 & a_{1,1} & 0 & a_{1,3} & 0 & \cdots & 0 & 0 & 0 \\ a_{2,0} & 0 & a_{2,2} & 0 & a_{2,4} & \cdots & 0 & 0 & 0 \\ \vdots & \vdots & \vdots & \vdots & \vdots & \ddots & \vdots & \vdots & \vdots \\ 0 & 0 & 0 & 0 & 0 & \cdots & a_{k,k-2} & 0 & a_{k,k} \end{bmatrix} \quad (3.7)$$

where the nonzero terms are defined as

$$a_{k,k} = k(k+1) + \frac{2k(k+1) - 1}{(2k+3)(2k-1)} c^2 \quad (3.8)$$

$$a_{k,k+2} = a_{k+2,k} = \frac{(k+1)(k+2)}{(2k+3)\sqrt{(2k+1)(2k+5)}} c^2$$

The eigenvalues and eigenvectors to this matrix \mathbf{A} can be solved by the eigen-problem

$$(\mathbf{A} - \chi_n \mathbf{I}) \boldsymbol{\beta}_n = \mathbf{0} \quad (3.9)$$

where χ_n are the eigenvalues and $\beta_n = (\beta_{n0}, \beta_{n1}, \beta_{n2}, \dots)$ is the eigenvector. From the orthogonality of Parseval's identity,

$$\sum_{k=0}^{\infty} |\beta_{nk}|^2 = 1 \quad \forall n \geq 0 \quad (3.10)$$

with the parity $\beta_{nk} = 0$ if $n + k$ is odd. In essence this states that if n is even only the even values of β_{nk} are used and similarly if n is odd only the odd values of β_{nk} are used.

To compute the series representation in (3.3) the values of k have to extend to infinity which is not feasible in any practical system. Instead an approximation is made by truncating the infinite sum such that

$$\psi_n(t) \approx \sum_{k=0}^M \beta_{nk} \bar{P}_k(t) \quad (3.11)$$

The truncation value is taken such that that $M > \frac{2c}{\pi}$ which is the limit after which the eigenvalues λ_n superexponentially approach zero [103].

It is also to be mentioned that this method only works for the bounds $[-1, 1]$ outside of which the result will experience extremely large errors. Values of $|t| \geq 1$ can be approximated by a series of Bessel functions [97] but for this dissertation I am only interested behavior of the function inside the bounds of $[-1, 1]$.

3.1.3 Range and Doppler Estimation Bounds

The bounds on spatial and spectral parameter estimation of the PSWFs can be calculated by the second moment of the Fourier of the parameter of interest due to the PSWF inherently having a zero first moment in both time and frequency. The joint measurement is fundamentally limited by the radar uncertainty principle

$$\sigma_t \sigma_f = \frac{1}{\pi \text{SNR}} \quad (3.12)$$

Due to nonexistence of a closed form solution to PSWFs, the bounds in (2.11) and (2.12) is solved numerically. Therefore, these bounds need to be calculated explicitly for the values of T and W on a case by case basis. A nominal value of $T = 10 \mu\text{s}$, which is indicative of the length of waveforms used in remote sensing, is chosen in this work. This results in bandwidth values of $W = 100 \text{ kHz}$,

$W = 400$ kHz, $W = 700$ kHz, and $W = 1$ MHz for the values of $c = \pi$, $c = 4\pi$, $c = 7\pi$, and $c = 10\pi$ respectively. For other values of T the estimation ability of the optimal, LFMW, and rectangular pulse cases scale proportionality providing the same conclusion but at a shifted value. Images of the calculated CRLBs for the baseband PSWFs as a time and frequency estimator can be seen in Fig. 3.1.

For the case of $c = \pi$ the bounds converge after $n = 1$ and provide no improvement with increasing order. This is due to the majority of the energy lying outside of the bounds in both time and frequency domains and thus poorly representing the signal, providing invalid estimation performance. As the value of c increases the concentration of energy within the given frequency window increases to become nearly maximum for all values of n and therefore improves the range accuracy. As for the frequency estimation, the performance slightly degrades as the value of c increases. This is due to the concentration of energy condensing to zero in the time domain. When comparing the performance of the baseband PSWFs to the optimal infinitesimally thin two tone and pulse waveforms and a classic LFMW that occupy the same time and bandwidth, it can be seen that the range estimation performance degrades as the value of c increases. This is again due the larger percentage of the energy concentration condensing to zero in both time and frequency leaving unused time and bandwidth at the edges of the windowed domains resulting in a reduction of the second moment in both time and frequency thereby reducing the obtainable estimation variance.

3.1.4 Remote Sensing Waveform Design Based on PSWF of the Zeroth Order

From the analysis in Section 2.2.3, the second moment of the frequency spectrum is maximized when the spectral energy is concentrated at two bifurcated frequencies at opposite ends of band of interest. By maximizing the second moment, the variance is minimized thus providing the most accurate estimation of the time delay. Similarly, from the mean squared duration (2.9) by separating the signal energy into two bifurcated temporal pulses at the ends of a time window, the second moment of the time domain is maximized and thus providing the most accurate estimation of frequency [86, 104]. In the time-frequency domain the optimal joint range-Doppler waveform

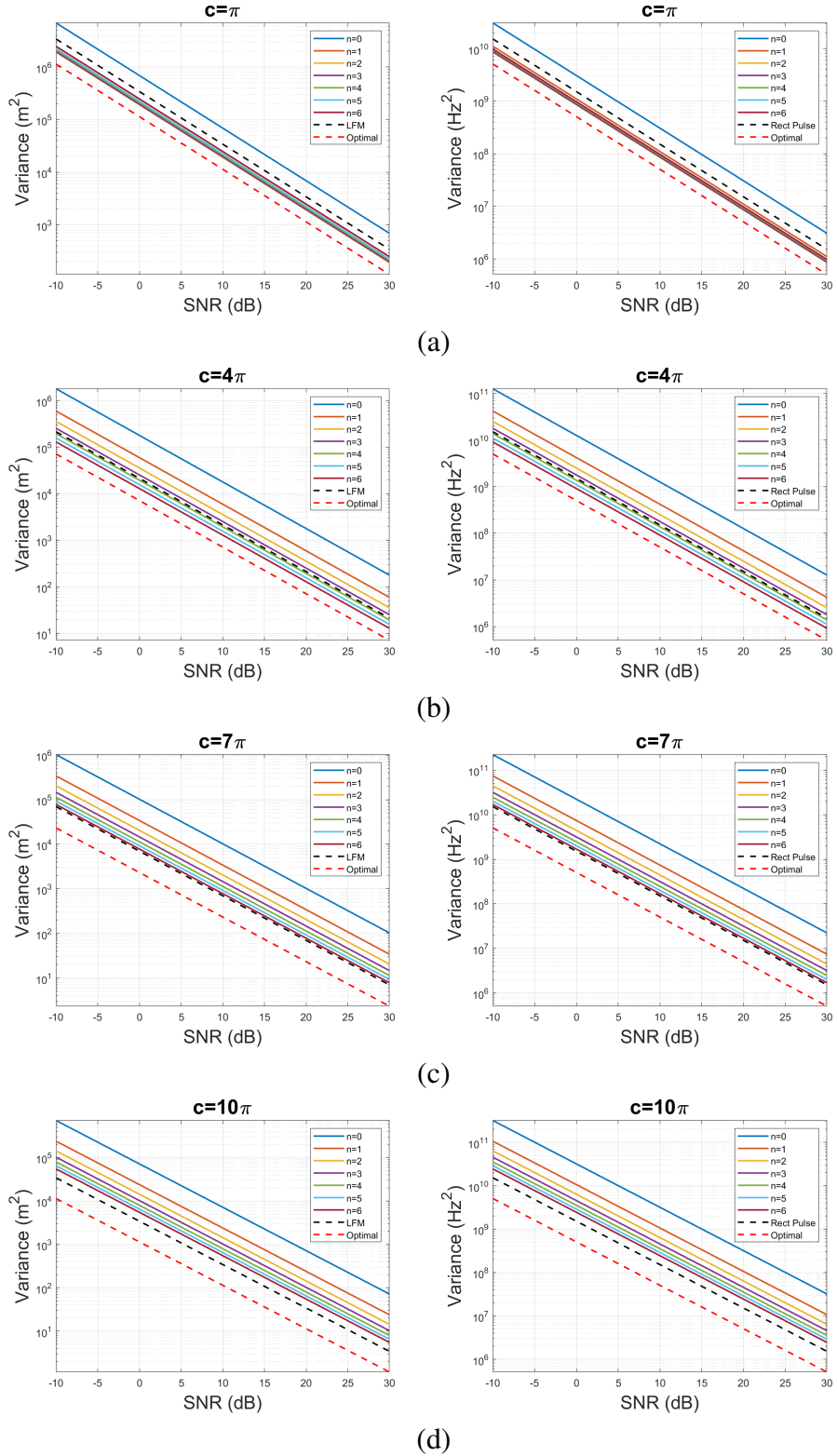


Figure 3.1: CRLB for Doppler (2.11) and range (2.12) of the baseband PSWFs for the cases of $c = \pi$ (a), $c = 4\pi$ (b), $c = 7\pi$ (c), and $c = 10\pi$ (d) on the right and left respectively.

would be represented by four delta functions at the four corners of the time-frequency window of interest.

Here each domain will be approached independently. In [104] the effects of temporally bifurcated rectangular pulses with varying bandwidth was explored. It was found from this study that pulses with higher instantaneous bandwidths have improved Doppler estimation performance over ones with low instantaneous bandwidth due to the shorter temporal duration and therefore the ability to achieve higher temporal second moments. Here I use a similar approach but instead of rectangular pulses, the PSWF of the 0^{th} order is used due to the maximal concentration of energy in both domains and, therefore, represents a nearly-optimal design approaching a delta function in both time and frequency. A depiction of the concatenated $n = 0$ PSWFs with various pulse bandwidths can be seen in Fig. 3.2 where the percentage in the legend refers to the ratio of the overall waveform bandwidth to the pulse instantaneous bandwidth such that $\frac{2T'}{T}$ where T' is the duration of the individual pulses. This waveform represents a baseband signal which can be used as an envelope for a frequency bifurcated signal (i.e. $f(t) = e^{j2\pi f_1 t} + e^{j2\pi f_2 t}$) the performance of which is inversely proportional the bandwidth $\sigma_t^2 \sim 1/(f_2 - f_1)^2$ as seen in Section 2.2.3. This dual pulse PSFW can be represented by

$$\begin{aligned} s(t) &= \left(\psi(t + t_0) + \psi(t - t_0) \right) \left(e^{-j\pi\Delta f t} + e^{j\pi\Delta f t} \right) \\ &= \sum_{k=0}^M \beta_{0k} \left(\overline{P}_k(t - t_0) + \overline{P}_k(t + t_0) \right) \left(e^{-j\pi\Delta f t} + e^{j\pi\Delta f t} \right) \end{aligned} \quad (3.13)$$

where $\psi(t)$ from (3.11) is shifted in time by t_0 and Δf is $f_2 - f_1$. The initial conditions to the shifted Legendre polynomials become

$$\begin{aligned} P_0(t \pm t_0) &= 1 \\ P_1(t \pm t_0) &= t \pm t_0 \end{aligned} \quad (3.14)$$

Applying these initial conditions to (3.13)

$$s(t) = 2 \sum_{k=0}^M \beta_{0k} \sqrt{k + \frac{1}{2}} \left(P_k(t) + t_0 \frac{2k + 1}{k + 1} \right) \left(e^{-j\pi\Delta f t} + e^{j\pi\Delta f t} \right) \quad (3.15)$$

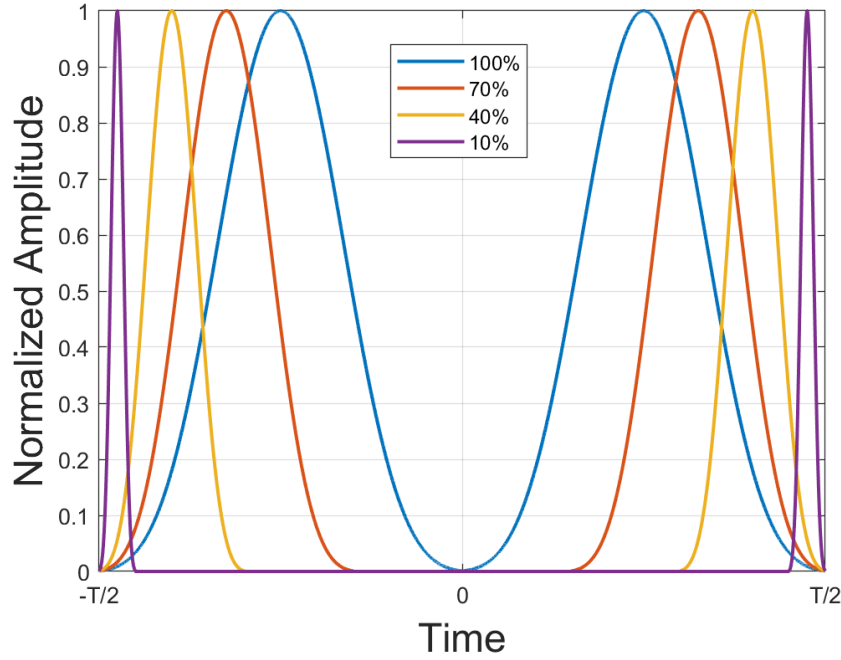
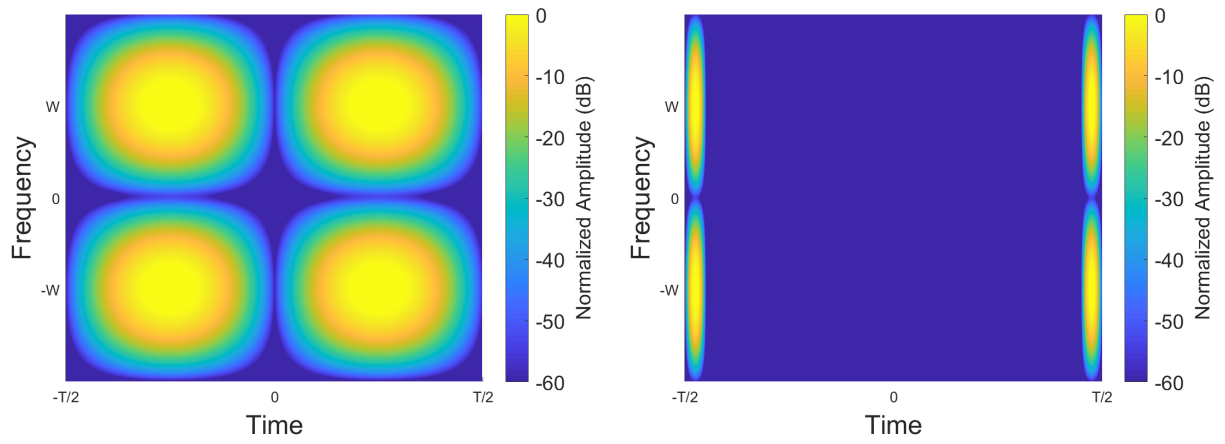


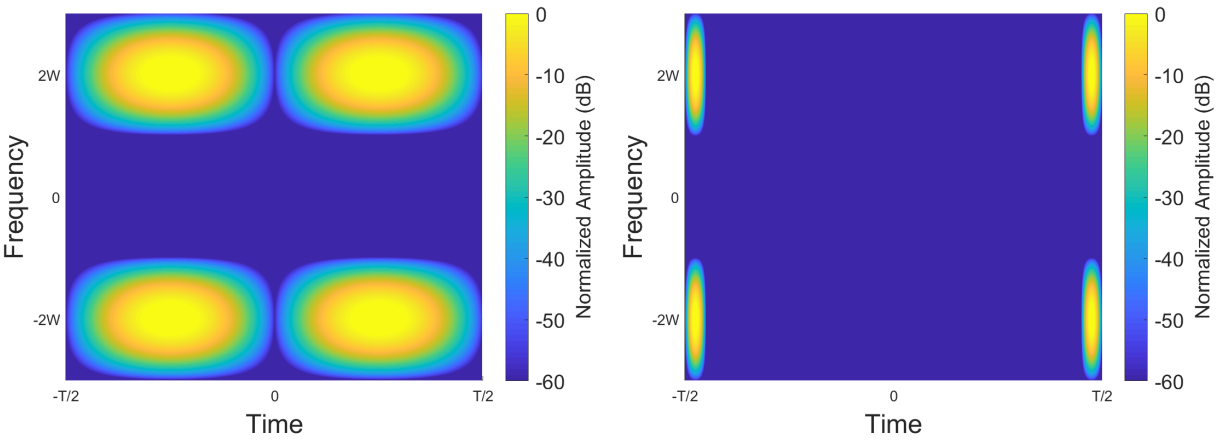
Figure 3.2: Time domain representation of the temporally bifurcated waveform formed from concatenating two $n = 0$ PSWFs. This example was taken at $c = 3\pi$.

The time-frequency plots of several examples of this time and frequency bifurcated waveform with various modulation percentages can be seen in Fig. 3.3.

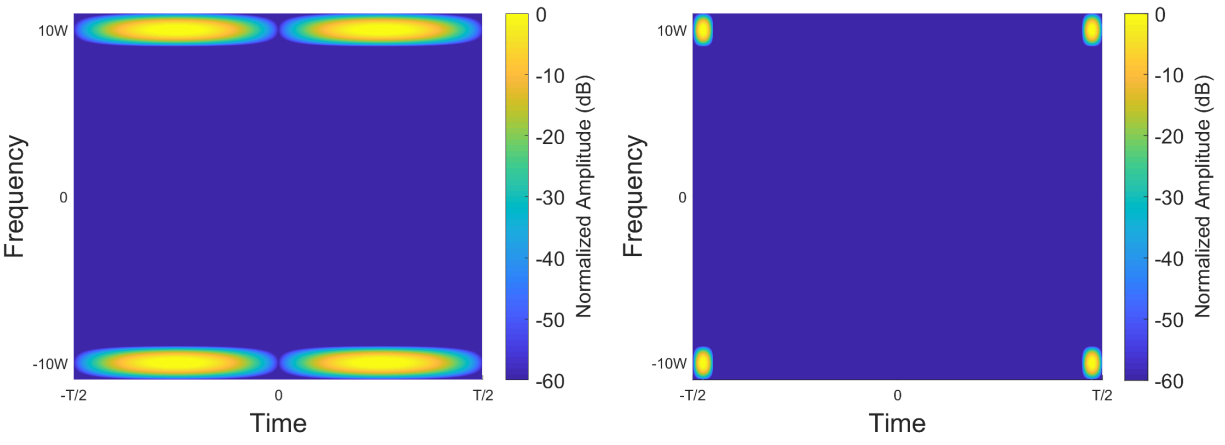
Time- and band-limited modulation of an optimal signal (i.e. four delta functions in the corners of the time-frequency window) results in a reduction of the mean-squared bandwidth/duration and degrades the performance of the parameter estimation ability. The effect of this degradation is dependent on the total bandwidth Δf and total duration T and therefore if the modulation represents a small portion of the overall domain the effect to the estimation performance is negligible. Here the effects of modulation on the estimation ability in both time (i.e. $\frac{2T'}{T}$) and frequency (i.e. $\frac{2W}{\Delta f}$) the results of which can be seen in Fig. 3.4 (a) and (b) for the spatial and spectral uncertainties respectively. From these plots it can be seen that the effects of the modulation decrease with percent coverage. For the case of the spatial bound, when $2W = \Delta f$ errors two orders of magnitude over the optimal can be expected. When the spectral bandwidth is reduced to $2W = 0.1\Delta f$ the estimation of spatial accuracy is nearly equivalent to the optimal. For the case of



(a)

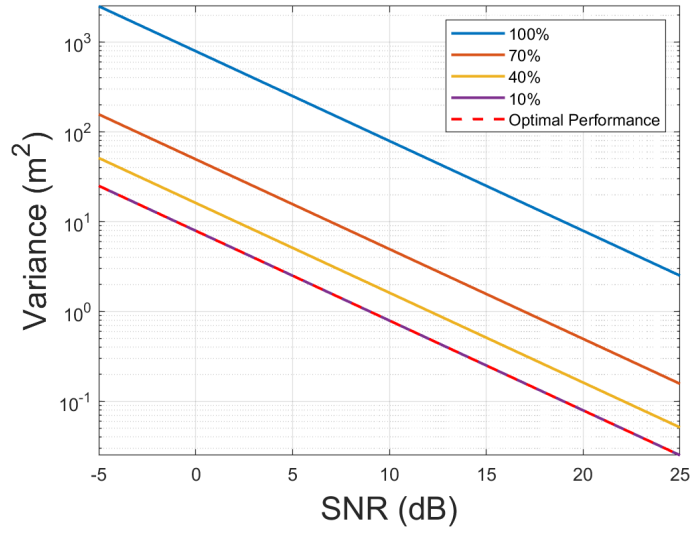


(b)

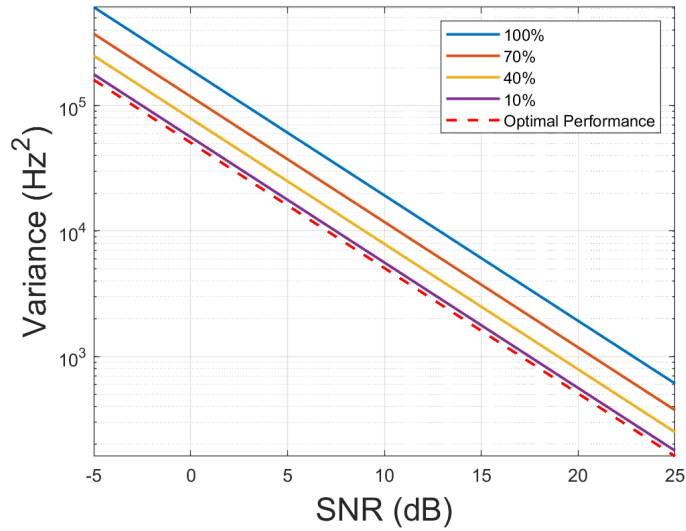


(c)

Figure 3.3: Time and frequency bifurcated waveform with 100% (left) and 10% (right) time modulation and 100% (a), 50% (b), and 10% (c) modulation in frequency.



(a)



(b)

Figure 3.4: (a) Comparison of the optimal CRLB to the CRLB of the spatial uncertainty of the dual pulse waveform with varying spectral bandwidth where the percentage refers to $\frac{2W}{\Delta f}$. (b) Comparison of the optimal CRLB to the CRLB of the frequency uncertainty of the dual pulse waveform with varying temporal instantaneous bandwidth where the percentage refers to $\frac{2T'}{T}$.

the spectral bound, when $2T' = T$ errors of roughly half an order of magnitude above the optimal can be expected. When the temporal bandwidth is reduced to $2T' = 0.1T$ the estimation ability is within 90% of the optimal error. It is to be noted that these bounds can be further improved to more closely represent the optimal result by further reducing the modulation percentage in the

respective domain and therefore, more closely representing a delta functions.

The ambiguity function for the dual PSWF can be calculated by inputting the time domain representation of the waveform (3.15) into the the ambiguity function equation (2.1), yielding

$$\begin{aligned}
AF(t, f_D) = & \int_{-\infty}^{\infty} 2 \sum_{q=0}^Q \beta_{0q} \sqrt{q + \frac{1}{2}} \left(P_q(t - \tau) + t_0 \frac{2q + 1}{q + 1} \right) \left(e^{j\pi\Delta f(t-\tau)} + e^{-j\pi\Delta f(t-\tau)} \right) \\
& \times 2 \sum_{k=0}^M \beta_{0k} \sqrt{k + \frac{1}{2}} \left(P_k(\tau) + t_0 \frac{2k + 1}{k + 1} \right) \left(e^{-j\pi\Delta f\tau} + e^{j\pi\Delta f\tau} \right) e^{j2\pi f_D \tau} d\tau
\end{aligned} \tag{3.16}$$

Due to the orthogonality principle of Legendre polynomials $k \neq q = 0$ reduces (3.16) to

$$\begin{aligned}
AF(t, f_D) = & 4 \int_{-\infty}^{\infty} \sum_{k=0}^M \beta_{0k}^2 \left(k + \frac{1}{2} \right) \left(P_k(t - \tau) + t_0 \frac{2k + 1}{k + 1} \right) \left(e^{j\pi\Delta f(t-\tau)} + e^{-j\pi\Delta f(t-\tau)} \right) \\
& \times \left(P_k(\tau) + t_0 \frac{2k + 1}{k + 1} \right) \left(e^{-j\pi\Delta f\tau} + e^{j\pi\Delta f\tau} \right) e^{j2\pi f_D \tau} d\tau
\end{aligned} \tag{3.17}$$

From here the calculation of the ambiguity function is less tractable to be analyzed analytically due to the recursion properties of the Legendre polynomials. At this point the rest of the calculation is carried out numerically and can be seen in Fig. 3.5. Here we can see the ambiguous nature of this waveform. From the zoomed in portion of the center of the intensity plot in Fig 3.5(d) the spectral and temporal ambiguities of the underlying beat pattern in time, resulting from the two frequencies, and Doppler, from the two temporal pulses, can be seen. As for the zoomed in portion on the far left, ambiguities in time are present as only one temporal pulse has been correlated at this point.

To disambiguate this waveform two approaches can be made: the use of a waveform representing a square domain in time and frequency given by pseudo-random white noise; and a waveform representing a sloped domain in time and frequency given by an LFMW. The amount of time and bandwidth allocated to the disambiguation waveform dictate the performance. Examples of using pseudo-random white noise and an LFMW to disambiguate can be seen in Fig. 3.6 and Fig. 3.7 respectively. This method of disambiguation represents a time-duplexed scheme where the measurement waveform and disambiguation waveform are sent in separate time slots as to not

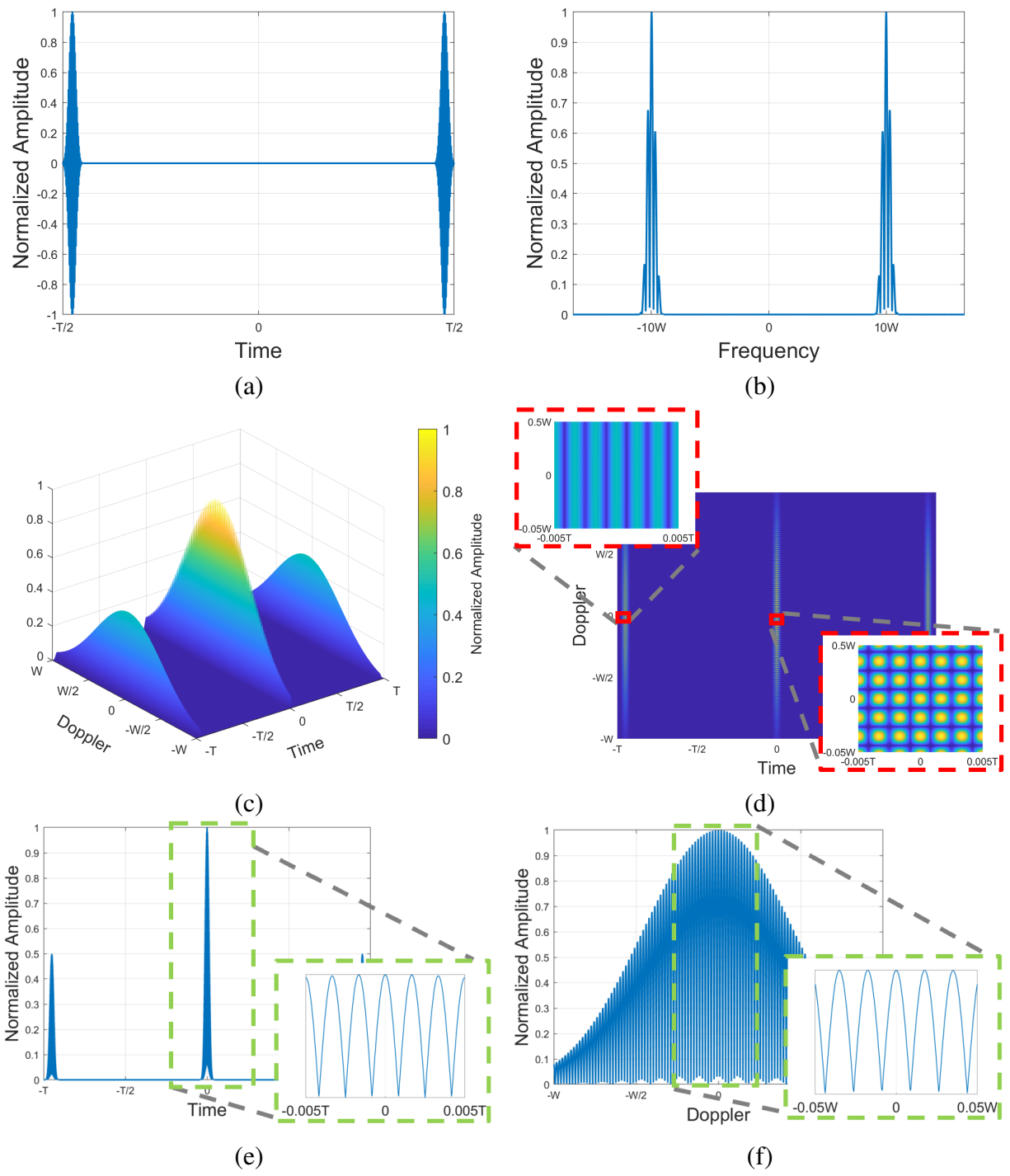


Figure 3.5: (a) Time representation of the waveform with 10% modulation. (b) Spectral representation with 10% modulation. (c) Ambiguity function of the dual pulse PSWF. (d) Intensity plot of the ambiguity function showing ambiguous nature in both time and frequency. (e) Matched filter of the dual pulse PSWF (zero Doppler cut). (f) Doppler response of the dual pulse PSWF (zero time cut).

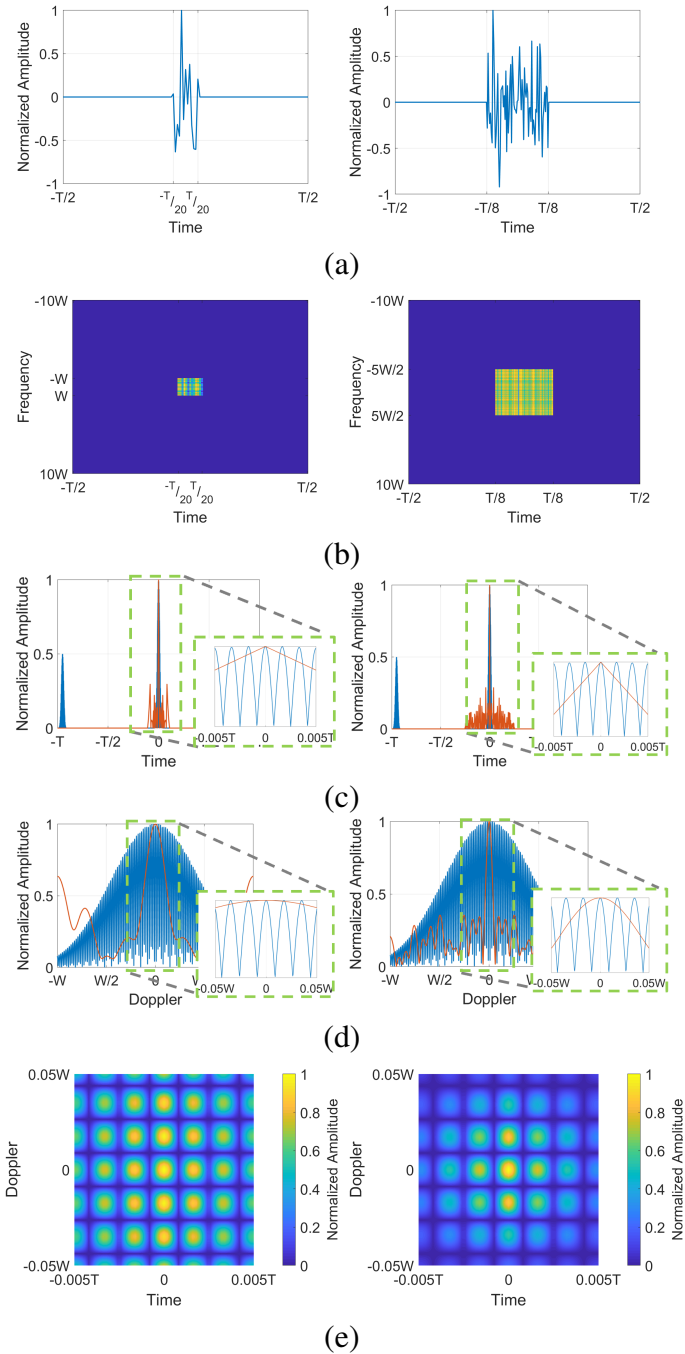


Figure 3.6: Pseudo-random white noise for disambiguation for 10% occupation of both time and frequency, relative to the measurement waveform (left), and 25% occupancy in time and frequency (right). (a) Pseudo-random white noise in the time domain. (b) Time-frequency plot of the pseudo-random white noise. (c) Matched filter response for the measurement waveform (blue) and disambiguation (red). (d) Doppler response of the measurement waveform (blue) and disambiguation (red). (e) Combined ambiguity function of measurement waveform and disambiguation demonstrating suppression of sidelobes in both time and Doppler.

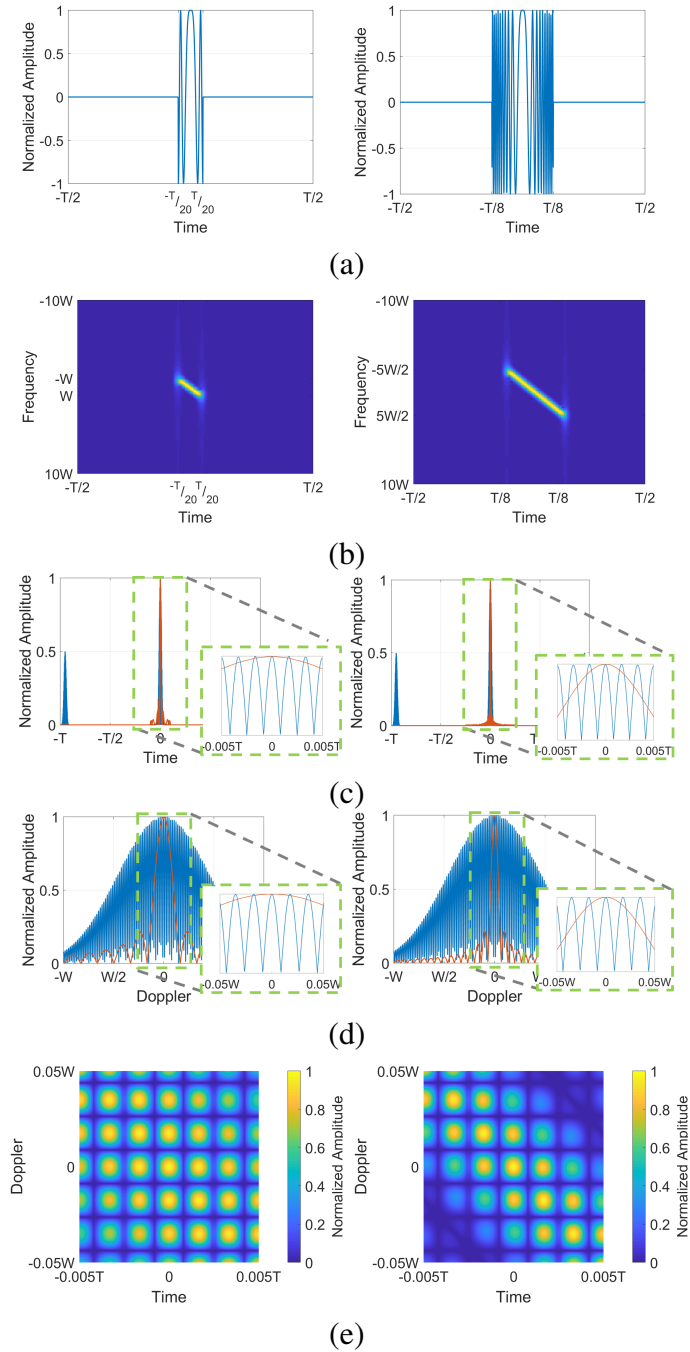


Figure 3.7: LFMW for disambiguation for 10% occupancy of both time and frequency, relative to the measurement waveform (left), and 25% occupancy in time and frequency (right). (a) LFMW in the time domain. (b) Time-frequency plot of the LFMW. (c) Matched filter response for the measurement waveform (blue) and disambiguation (red). (d) Doppler response of the measurement waveform (blue) and disambiguation (red). (e) Combined ambiguity function of measurement waveform and disambiguation demonstrating suppression of sidelobes in both time and Doppler.

interfere with the measurement ability of the derived dual PSWF. An alternative method could be used, due to the dual PSWF sparsity in both time and frequency, where the disambiguation pulse is embedded between the two PSWF pulses. This method would save time, as only one time slot is required rather than two, and reduce computational complexity as the calculation of a single matched filter and Doppler response would be required. However, embedding the disambiguation method would reduce that second moment in both time and frequency domains and therefore reduce the obtainable measurement accuracy where the impact in both disambiguation ability and degradation of the accuracy depends on the energy and occupational time and bandwidth allocated to the disambiguation pulse.

3.1.4.1 Simulation

To evaluate the estimation ability of this waveform in comparison to the derived bounds, a simulation is conducted in MATLAB. The waveform parameters that are considered consist of a temporal bifurcation of $\frac{2T'}{T} = 10\%$ where $T = 10 \mu\text{s}$ and a frequency bifurcation of $\frac{2W}{\Delta f} = 10\%$ where $W = 6 \text{ MHz}$. An image of the waveform for the time and frequency domain can be seen in Fig. 3.5(a). This waveform is then corrupted with AWGN so that the estimation performance at multiple SNR levels can be evaluated. The SNR of the signal is evaluated using an eigenvalue decomposition method from Section 2.1.4.

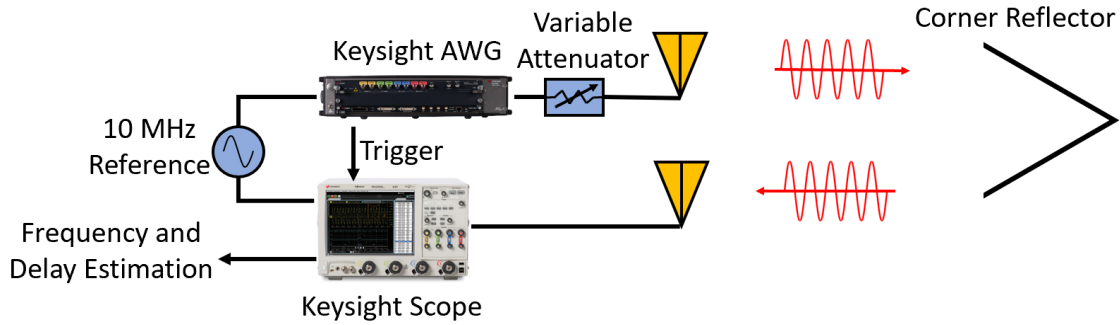
The positional uncertainty, again solved using (2.12), is calculated from the time of flight temporal uncertainty. An estimation of time of flight of the received signal can be evaluated from the peak value of a matched filtering process. An image of the matched filter output can be seen in Fig. 3.5(e). The peak value was then interpolated using a built-in MATLAB spline interpolator by 1000 points to improve the measurement estimation and avoid binning around the peak. The waveform variance is then calculated from these 1000 peak values. The matched filter process also maximizes the SNR of the signal by providing an additional processing gain equivalent to the time-bandwidth product where the time component is the time duration T and the bandwidth is the receiver bandwidth which is linked to the sample rate and filtering of the signal.

The estimation of the frequency was performed by evaluating the one-sided frequency spectrum of the matched filter autocorrelation function and taking the peak value. An image of the Doppler response of the dual pulse waveform can be seen in Fig. 3.5(f) where the lobing structure appears from the interference of the overlapping instantaneous bandwidths of the temporal pulses and is concurrent with the findings in [104]. The peak frequency of the spectrum was interpolated by 1000 points using MATLAB's build-in spline function and the variance was taken over the 1000 Monte Carlo iterations.

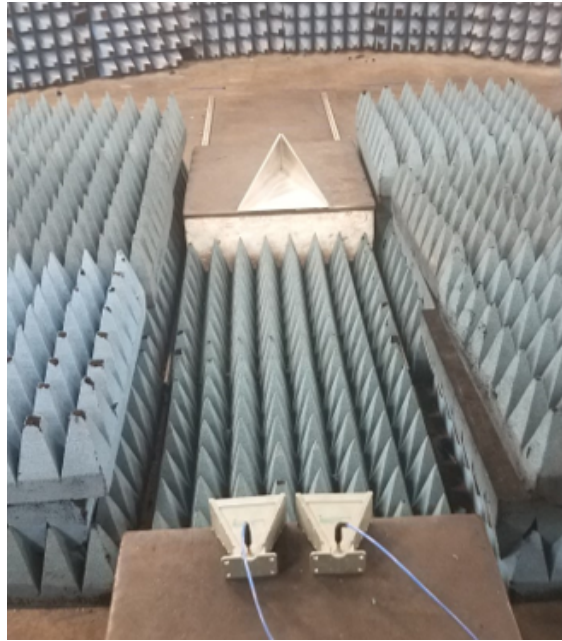
3.1.4.2 Measurements

Wireless measurements are performed in a semi-enclosed arch range using a two standard gain 2 – 12 GHz wideband horn antennas oriented in a quasi monostatic fashion at the edge of the range. A corner reflector is placed at the center of the range approximately 1.25 m from the transmitter and receiver. The signal is generated at the RF level with a center frequency of 3 GHz using a M8190A 12 GSa/s Keysight arbitrary waveform generator (AWG). Variable attenuation is applied to the output of the AWG so that multiple SNR levels could be evaluated. The receiving antenna is connected to a MSO-X 92004A Keysight Infiniium High-Performance Oscilloscope. The scope captures are triggered using a threshold detection on a rectangular pulse provided by the AWG. Both the AWG and the scope's local oscillators are locked using an external 10 MHz source provided by an Agilent MXG Analog Signal Generator. 1000 observations are recorded on the scope and processed offline in MATLAB where digital down conversion to baseband was performed and a low pass filter with a cutoff frequency of 100 MHz is applied. The estimation process is performed in the same way as the simulation which was conducted for 1000 Monte Carlo iterations to provide statistical relevance comparatively to the measured data. A block diagram of the experimental setup along with an image of the setup in the arch range can be seen in Fig. 4.6(a) and (b) respectively.

An image of a measured waveform in the time-frequency domain where $T = 10 \mu\text{s}$ and $W = 6 \text{ MHz}$ can be seen in Fig. 3.9(a). The results of both spatial and frequency estimation



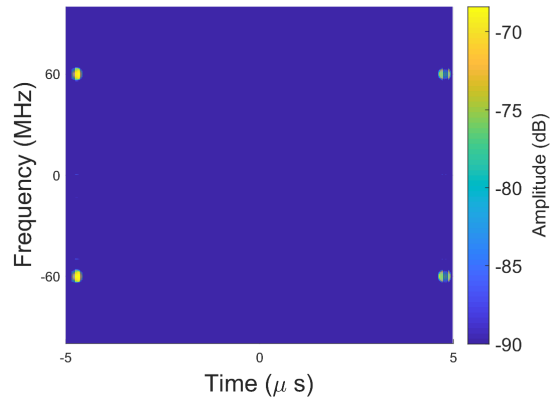
(a)



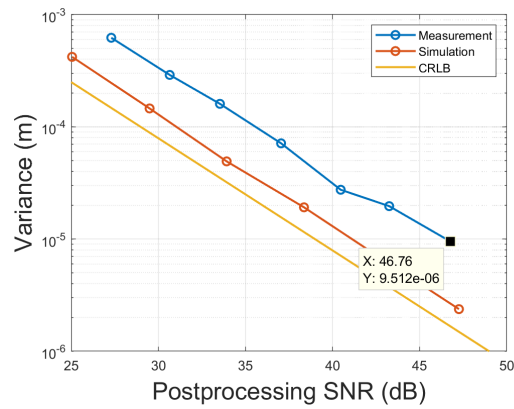
(b)

Figure 3.8: (a) Block diagram of the wireless experimental setup. (b) Image of experimental setup in the semi-enclosed arch range.

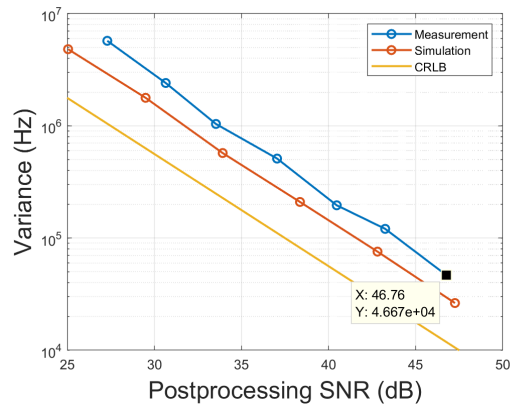
for both simulation and measurements compared to the calculated bounds can be seen in Fig. 3.9(b) and (c) respectively. From this plot it can be seen that measurements closely match the simulation and the calculated bounds providing a near-optimal estimation in both temporal and spectral domains. At the highest performing point, measured accuracies of $\sigma_m = 3.1$ mm and $\sigma_f = 216$ Hz are obtained at 13 dB preprocessing SNR with 33 dB of processing gain. This enables a beamforming frequency of 6.45 GHz with an accuracy of $\frac{\lambda}{15}$.



(a)



(b)



(c)

Figure 3.9: (a) Time-frequency plot of a measured waveform with $T = 10 \mu\text{s}$ and $W = 6 \text{ MHz}$. (b) Comparison of measured results, simulation, and CRLB for the dual pulse PSWF as a spatial estimator. (c) Comparison of measured results, simulation, and CRLB for the dual pulse PSWF as a frequency estimator.

3.2 Time Domain Duplex: Joint Phase Alignment and Frequency Transfer for Wideband Systems

In this section I address a waveform used for inter-node coordination to jointly enable the measurement of the range between platforms, while simultaneously transferring a frequency reference in a stable manner such that the frequency can be used to discipline a local oscillator. Here the waveforms used to enable estimation of delay (which yields an estimate of the range) as well as estimation of the frequency reference, which would be input to a PLL to align the oscillator of the receiving node to that of the transmitting node are described. These waveforms are based on the spectrally sparse model of the PTTW which uses a large portion of the system bandwidth. For this reason, like the dual PSFW, this method represents a time duplex scheme for scalability where each node has a specific time slot to perform its measurement to acquire both a range estimation and the frequency reference.

3.2.1 Waveform Design

In the prior chapter, the use of the two-tone continuous wave (TTCW) signal for optimal ranging accuracy was described, but is generally not obtainable due to system constraints, leading to the PTTW from Section 2.2.3. Due to the high-accuracy capability of the PTTW signal, it is used as the base for the joint ranging and frequency transfer waveform in this work. A frequency reference, which is chosen to be 10 MHz, clock signal is modulated onto the lower of the two tones, and the phase error is measured to assess the stability of a frequency alignment process. The normalized PTTW signal is given by

$$s_1(t) = \frac{1}{2} \text{rect} \left(\frac{t}{T} \right) \left(e^{-j\pi\Delta ft} + e^{j\pi\Delta ft} \right) \quad (3.18)$$

where Δf is the frequency difference between the two frequencies of the two-tone waveform. Three different types of modulation schemes are implemented for the frequency reference f_m : single sideband, double sideband, and amplitude modulation, shown respectively in the following:

$$s_2(t) = \frac{1}{2} \text{rect} \left(\frac{t}{T} \right) \left(\mathbf{H}[\cos(2\pi f_m t)] e^{-j\pi\Delta ft} + e^{j\pi\Delta ft} \right) \quad (3.19)$$

$$s_3(t) = \frac{1}{2} \text{rect} \left(\frac{t}{T} \right) \left(\cos(2\pi f_m t) e^{-j\pi \Delta f t} + e^{j\pi \Delta f t} \right) \quad (3.20)$$

$$s_4(t) = \frac{1}{3} \text{rect} \left(\frac{t}{T} \right) \left\{ \left[1 + \sin(2\pi f_m t) \right] e^{-j\pi \Delta f t} + e^{j\pi \Delta f t} \right\} \quad (3.21)$$

where \mathbf{H} is the Hilbert transform. Fig. 3.10 shows these waveforms simulated in MATLAB and measured using an M8190A 12 GSa/s AWG. Here the baseline PTTW waveform uses a 150 MHz tone separation, the lower of the two tones is then modulated with a 10 MHz frequency reference signal.

The above expressions can be evaluated to determine the theoretical performance of each waveform in terms of delay estimation and frequency estimation. The error in estimating the delay can be determined by evaluating each of the three waveforms using (2.5) and (2.12). To make the analysis more general, the signals s_i above can be rewritten in their baseband forms as

$$s_2(t) = \frac{1}{2} \text{rect} \left(\frac{t}{T} \right) \left(e^{j\pi(-\Delta f + 2f_m)t} + e^{j\pi \Delta f t} \right) \quad (3.22)$$

$$s_3(t) = \frac{1}{3} \text{rect} \left(\frac{t}{T} \right) \left(e^{-j2\pi(\Delta f + 2f_m)t} + e^{j\pi(-\Delta f + 2f_m)t} + e^{j\pi \Delta f t} \right) \quad (3.23)$$

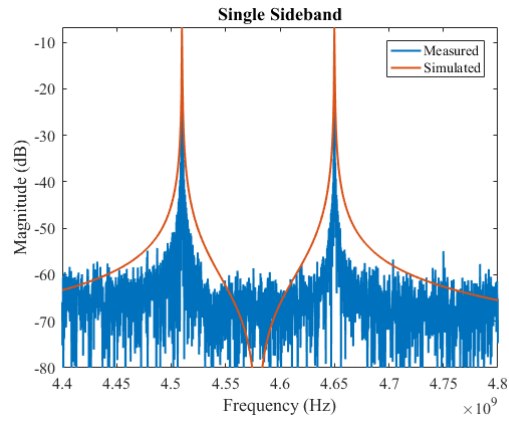
$$s_4(t) = \frac{1}{4} \text{rect} \left(\frac{t}{T} \right) \left(e^{-j\pi(\Delta f + 2f_m)t} + e^{-j\pi \Delta f t} + e^{j\pi(-\Delta f + 2f_m)t} + e^{j\pi \Delta f t} \right) \quad (3.24)$$

The above formulation takes a more general approach to the location of the tones in terms of their relative separations.

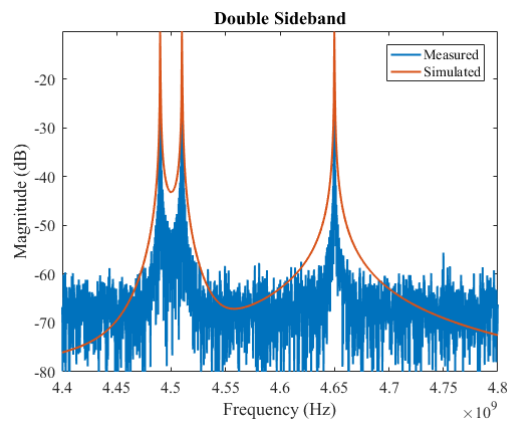
3.2.1.1 Ambiguity Function

The response of the PTTW using single sideband modulation to estimate time delay and Doppler is given by the ambiguity function (2.1) with the model of the time domain waveform from (3.22)

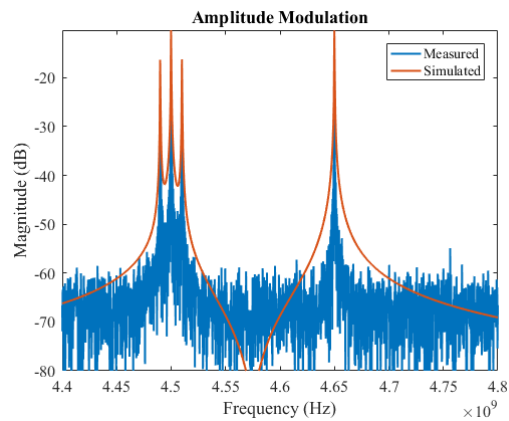
$$\begin{aligned} AF_2(t, f_D) = & \frac{1}{4} \int_{-\infty}^{\infty} \text{rect} \left(\frac{\tau - t}{T} \right) \left(e^{j\pi(\Delta f - 2f_m)(\tau - t)} + e^{-j\pi \Delta f(\tau - t)} \right) \\ & \times \text{rect} \left(\frac{\tau}{T} \right) \left(e^{-j\pi(\Delta f - 2f_m)\tau} + e^{j\pi \Delta f \tau} \right) e^{j2\pi f_D \tau} d\tau \end{aligned} \quad (3.25)$$



(a)



(b)



(c)

Figure 3.10: Ranging is based on widely-spaced two-tone signal with 100 MHz of bandwidth, with the lower tone modulated by a 10 MHz frequency reference. (a) Spectrum of the joint ranging and frequency transfer signal using single-sideband modulation. (b) Spectrum of the joint ranging and frequency transfer signal using double-sideband modulation. (c) Spectrum of the joint ranging and frequency transfer signal using amplitude modulation.

Truncation of the integral can be performed due to time domain rectangular envelope, $\text{rect}(\cdot)$, being a time limited function with the bounds $[-\frac{T}{2}, \frac{T}{2}]$, yielding

$$\begin{aligned}
AF_2(t, f_D) &= \frac{1}{4} \int_{-\frac{T}{2}}^{t+\frac{T}{2}} \left(e^{-j\pi(\Delta f-2f_m)t} + e^{j\pi\Delta ft} + e^{j\pi[(\Delta f-2f_m)(\tau-t)+\Delta f\tau]} \right. \\
&\quad \left. + e^{-j\pi[(2\Delta f-2f_m)\tau-\Delta ft]} \right) e^{j2\pi f_D \tau} d\tau \\
AF_2(t, f_D) &= \frac{e^{-j\pi(\Delta f-2f_m)t} + e^{j\pi\Delta ft}}{j8\pi f_D} \left[e^{j2\pi f_D \left(t+\frac{T}{2}\right)} - e^{-j\pi f_D T} \right] \\
&\quad + \frac{e^{-j\pi(\Delta f-2f_m)t}}{j8\pi(\Delta f - f_m + f_D)} \left[e^{j2\pi(\Delta f - f_m + f_D) \left(t+\frac{T}{2}\right)} - e^{-j\pi(\Delta f - f_m + f_D)T} \right] \\
&\quad + \frac{e^{j\pi\Delta ft}}{j8\pi(f_D - \Delta f + f_m)} \left[e^{j2\pi(f_D - \Delta f + f_m) \left(t+\frac{T}{2}\right)} - e^{-j\pi(f_D - \Delta f + f_m)T} \right]
\end{aligned} \tag{3.26}$$

Extracting a factor from each function so that every parenthesis contains a complex exponential subtracted by its conjugate

$$\begin{aligned}
AF_2(t, f_D) &= \frac{\left(e^{-j\pi(\Delta f-2f_m)t} + e^{j\pi\Delta ft} \right) e^{j\pi f_D t}}{j8\pi f_D} \left[e^{j\pi f_D (t+T)} - e^{-j\pi f_D (t+T)} \right] \\
&\quad + \frac{e^{-j\pi(\Delta f-2f_m)t} e^{j\pi(\Delta f - f_m + f_D)t}}{j8\pi(\Delta f - f_m + f_D)} \left[e^{j\pi(\Delta f - f_m + f_D)(t+T)} - e^{-j\pi(\Delta f - f_m + f_D)(t+T)} \right] \\
&\quad + \frac{e^{j\pi\Delta ft} e^{j\pi(f_D - \Delta f + f_m)t}}{j8\pi(f_D - \Delta f + f_m)} \left[e^{j\pi(f_D - \Delta f + f_m)(t+T)} - e^{-j\pi(f_D - \Delta f + f_m)(t+T)} \right]
\end{aligned} \tag{3.27}$$

$e^{j\pi\Delta ft}$ cancels in the second and third terms and sinc functions can now be formed by multiplying each function by $\frac{t+T}{t+T}$ such that $\text{sinc}(\theta) = \frac{1}{j2\theta} (e^{j\theta} - e^{-j\theta})$

$$\begin{aligned}
AF_2(t, f_D) &= \frac{\left(e^{-j\pi(\Delta f-2f_m)t} + e^{j\pi\Delta ft} \right)}{4} e^{j\pi f_D t} (t+T) \text{sinc} \left(\pi f_D (t+T) \right) \\
&\quad + \frac{e^{j\pi(f_m+f_D)t}}{4} (t+T) \text{sinc} \left(\pi (\Delta f - f_m + f_D) (t+T) \right) \\
&\quad + \frac{e^{j\pi(f_m+f_D)t}}{4} (t+T) \text{sinc} \left(\pi (f_D - \Delta f + f_m) (t+T) \right)
\end{aligned} \tag{3.28}$$

The terms $\frac{e^{j\pi f_D t}}{4}$ and $(t+T)$ can then be extracted from each term. This derivation shown above represents the case of $t < 0$ case but is symmetric for the case of $t > 0$. The general case of the

derivation can be represented by

$$\begin{aligned}
AF_2(t, f_D) = \frac{e^{j\pi f_D t} (T - |t|)}{4} & \left[\left(e^{-j\pi(\Delta f - 2f_m)t} + e^{j\pi\Delta f t} \right) \text{sinc} \left(\pi f_D (T - |t|) \right) \right. \\
& + e^{j\pi f_m t} \text{sinc} \left(\pi (\Delta f - f_m + f_D) (T - |t|) \right) \\
& \left. + e^{j\pi f_m t} \text{sinc} \left(\pi (f_D - \Delta f + f_m) (T - |t|) \right) \right] \quad (3.29)
\end{aligned}$$

The magnitude of the ambiguity function can now be taken

$$\begin{aligned}
|AF_2(t, f_D)| = \left| \frac{(T - |t|)}{4} \right. & \left[2 \text{sinc} \left(\pi f_D (T - |t|) \right) + \text{sinc} \left(\pi (\Delta f - f_m + f_D) (T - |t|) \right) \right. \\
& \left. \left. + \text{sinc} \left(\pi (f_D - \Delta f + f_m) (T - |t|) \right) \right] \right| \quad (3.30)
\end{aligned}$$

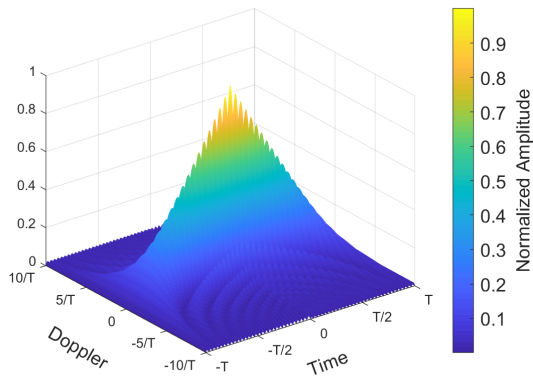
where the $|e^{j\pi f_D t}| = 1$, $|e^{j\pi f_m t}| = 1$, and $|e^{-j\pi(\Delta f - 2f_m)t} + e^{j\pi\Delta f t}| = 2$. An image of the ambiguity function of single sideband modulation with $\Delta f = 50$ MHz and $f_m = 10$ MHz along with the matched filter and Doppler response can be seen in Fig. 3.11. This figure resembles the ambiguity function of the PTTW due to single sideband modulation containing two frequencies.

The ambiguity function of the PTTW using double sideband modulation with the model of the time domain waveform from (3.23)

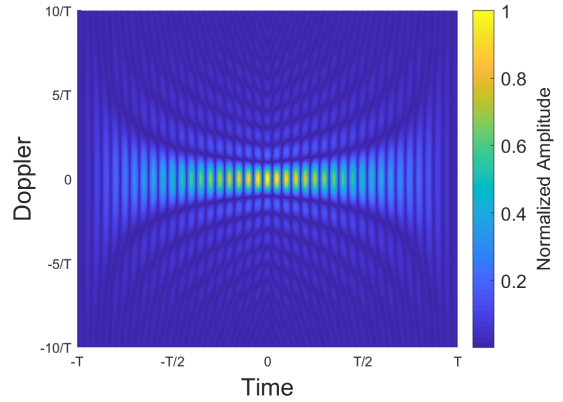
$$\begin{aligned}
AF_3(t, f_D) = \frac{1}{9} \int_{-\infty}^{\infty} \text{rect} \left(\frac{\tau - t}{T} \right) & \left(e^{j\pi(\Delta f - 2f_m)(\tau - t)} + e^{j\pi(\Delta f + 2f_m)(\tau - t)} + e^{-j\pi\Delta f(\tau - t)} \right) \\
& \times \text{rect} \left(\frac{\tau}{T} \right) \left(e^{-j\pi(\Delta f - 2f_m)\tau} + e^{-j\pi(\Delta f + 2f_m)\tau} + e^{j\pi\Delta f\tau} \right) e^{j2\pi f_D \tau} d\tau \quad (3.31)
\end{aligned}$$

Truncation of the integral due to $\text{rect}(\cdot)$ envelope

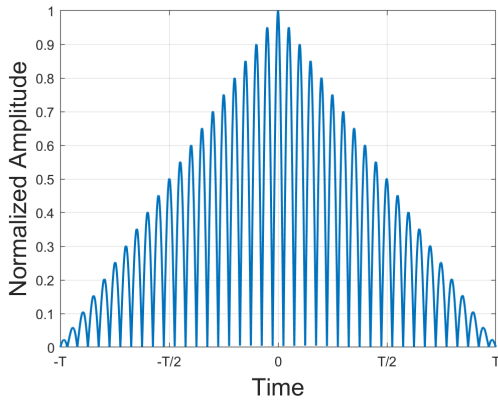
$$\begin{aligned}
AF_3(t, f_D) = \frac{1}{9} \int_{-\frac{T}{2}}^{t + \frac{T}{2}} & \left(e^{-j\pi(\Delta f - 2f_m)t} + e^{j\pi[4f_m\tau - (\Delta f + 2f_m)t]} + e^{-j\pi[(2\Delta f - 2f_m)\tau - \Delta f t]} \right. \\
& + e^{-j\pi(\Delta f + 2f_m)t} + e^{-j\pi[4f_m\tau + (\Delta f - 2f_m)t]} + e^{-j\pi[(2\Delta f + 2f_m)\tau - \Delta f t]} \\
& \left. + e^{j\pi\Delta f t} + e^{j\pi[(\Delta f - 2f_m)(\tau - t) + \Delta f \tau]} + e^{j\pi[(\Delta f + 2f_m)(\tau - t) + \Delta f \tau]} \right) e^{j2\pi f_D \tau} d\tau \quad (3.32)
\end{aligned}$$



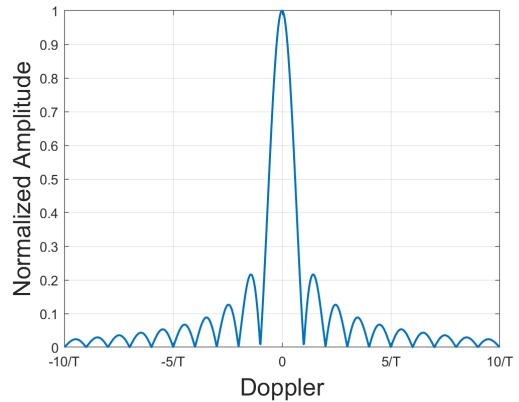
(a)



(b)



(c)



(d)

Figure 3.11: (a) Ambiguity function of the PTTW with single sideband modulation. (b) Intensity plot of the ambiguity function. (c) Matched filter of single sideband modulation (zero Doppler cut). (d) Doppler response of the single sideband modulation (zero time cut).

$$\begin{aligned}
AF_3(t, f_D) = & \frac{e^{-j\pi(\Delta f - 2f_m)t} + e^{-j\pi(\Delta f + 2f_m)t} + e^{j\pi\Delta ft}}{j18\pi f_D} \left[e^{j2\pi f_D \left(t + \frac{T}{2}\right)} - e^{-j\pi f_D T} \right] \\
& + \frac{e^{-j\pi(\Delta f + 2f_m)t}}{j18\pi(2f_m + f_D)} \left[e^{j2\pi(2f_m + f_D) \left(t + \frac{T}{2}\right)} - e^{-j\pi(2f_m + f_D)T} \right] \\
& + \frac{e^{j\pi\Delta ft}}{j18\pi(f_D - \Delta f + f_m)} \left[e^{j2\pi(f_D - \Delta f + f_m) \left(t + \frac{T}{2}\right)} - e^{-j\pi(f_D - \Delta f + f_m)T} \right] \\
& + \frac{e^{-j\pi(\Delta f - 2f_m)t}}{j18\pi(f_D - 2f_m)} \left[e^{j2\pi(f_D - 2f_m) \left(t + \frac{T}{2}\right)} - e^{-j\pi(f_D - 2f_m)T} \right] \\
& + \frac{e^{j\pi\Delta ft}}{j18\pi(f_D - \Delta f - f_m)} \left[e^{j2\pi(f_D - \Delta f - f_m) \left(t + \frac{T}{2}\right)} - e^{-j\pi(f_D - \Delta f - f_m)T} \right] \\
& + \frac{e^{-j\pi(\Delta f - 2f_m)t}}{j18\pi(f_D + \Delta f - f_m)} \left[e^{j2\pi(f_D + \Delta f - f_m) \left(t + \frac{T}{2}\right)} - e^{-j\pi(f_D + \Delta f - f_m)T} \right] \\
& + \frac{e^{-j\pi(\Delta f + 2f_m)t}}{j18\pi(f_D + \Delta f + f_m)} \left[e^{j2\pi(f_D + \Delta f + f_m) \left(t + \frac{T}{2}\right)} - e^{-j\pi(f_D + \Delta f + f_m)T} \right]
\end{aligned} \tag{3.33}$$

Creating a complex exponential subtracted by its conjugate can be made by extracting a factor in

each parenthesis

$$\begin{aligned}
AF_3(t, f_D) = & \frac{\left(e^{-j\pi(\Delta f - 2f_m)t} + e^{-j\pi(\Delta f + 2f_m)t} + e^{j\pi\Delta ft} \right) e^{j\pi f_D t}}{j18\pi f_D} \\
& \times \left[e^{j\pi f_D(t+T)} - e^{-j\pi f_D(t+T)} \right] \\
& + \frac{e^{-j\pi(\Delta f + 2f_m)t} e^{j\pi(2f_m + f_D)t}}{j18\pi(2f_m + f_D)} \left[e^{j\pi(2f_m + f_D)(t+T)} - e^{-j\pi(2f_m + f_D)(t+T)} \right] \\
& + \frac{e^{j\pi\Delta ft} e^{j\pi(f_D - \Delta f + f_m)t}}{j18\pi(f_D - \Delta f + f_m)} \left[e^{j\pi(f_D - \Delta f + f_m)(t+T)} - e^{-j\pi(f_D - \Delta f + f_m)(t+T)} \right] \\
& + \frac{e^{-j\pi(\Delta f - 2f_m)t} e^{j\pi(f_D - 2f_m)t}}{j18\pi(f_D - 2f_m)} \left[e^{j\pi(f_D - 2f_m)(t+T)} - e^{-j\pi(f_D - 2f_m)(t+T)} \right] \\
& + \frac{e^{j\pi\Delta ft} e^{j\pi(f_D - \Delta f - f_m)t}}{j18\pi(f_D - \Delta f - f_m)} \left[e^{j\pi(f_D - \Delta f - f_m)(t+T)} - e^{-j\pi(f_D - \Delta f - f_m)(t+T)} \right] \\
& + \frac{e^{-j\pi(\Delta f - 2f_m)t} e^{j\pi(f_D + \Delta f - f_m)t}}{j18\pi(f_D + \Delta f - f_m)} \left[e^{j\pi(f_D + \Delta f - f_m)(t+T)} - e^{-j\pi(f_D + \Delta f - f_m)(t+T)} \right] \\
& + \frac{e^{-j\pi(\Delta f + 2f_m)t} e^{j\pi(f_D + \Delta f + f_m)t}}{j18\pi(f_D + \Delta f + f_m)} \left[e^{j\pi(f_D + \Delta f + f_m)(t+T)} - e^{-j\pi(f_D + \Delta f + f_m)(t+T)} \right]
\end{aligned} \tag{3.34}$$

$e^{j\pi\Delta ft}$ cancels in the third, fifth, sixth, and seventh terms and the $e^{j2\pi f_m t}$ cancel in the second and fourth terms. Sinc functions can now be formed by multiplying each function by $\frac{t+T}{t}$ such

that $\text{sinc}(\theta) = \frac{1}{j2\theta} (e^{j\theta} - e^{-j\theta})$

$$\begin{aligned}
AF_3(t, f_D) = & \frac{\left(e^{-j\pi(\Delta f - 2f_m)t} + e^{-j\pi(\Delta f + 2f_m)t} + e^{j\pi\Delta ft} \right) e^{j\pi f_D t}}{9} (t + T) \\
& \times \text{sinc} \left(\pi f_D (t + T) \right) \\
& + \frac{e^{j\pi(f_D - \Delta f)t}}{9} (t + T) \text{sinc} \left(\pi (2f_m + f_D) (t + T) \right) \\
& + \frac{e^{j\pi(f_D + f_m)t}}{9} (t + T) \text{sinc} \left(\pi (f_D - \Delta f + f_m) (t + T) \right) \\
& + \frac{e^{j\pi(f_D - \Delta f)t}}{9} (t + T) \text{sinc} \left(\pi (f_D - 2f_m) (t + T) \right) \\
& + \frac{e^{j\pi(f_D - f_m)t}}{9} (t + T) \text{sinc} \left(\pi (f_D - \Delta f - f_m) (t + T) \right) \\
& + \frac{e^{j\pi(f_D + f_m)t}}{9} (t + T) \text{sinc} \left(\pi (f_D + \Delta f - f_m) (t + T) \right) \\
& + \frac{e^{j\pi(f_D - f_m)t}}{9} (t + T) \text{sinc} \left(\pi (f_D + \Delta f + f_m) (t + T) \right)
\end{aligned} \tag{3.35}$$

The terms $\frac{e^{j\pi f_D t}}{9}$ and $(t + T)$ can then be extracted from each term. This derivation shown above represents the case of $t < 0$ case but is symmetric for the case of $t > 0$. The general case is given represented by

$$\begin{aligned}
AF_3(t, f_D) = & \frac{e^{j\pi f_D t} (T - |t|)}{9} \left[\left(e^{-j\pi(\Delta f - 2f_m)t} + e^{-j\pi(\Delta f + 2f_m)t} + e^{j\pi\Delta ft} \right) \right. \\
& \times \text{sinc} \left(\pi f_D (T - |t|) \right) \\
& + e^{-j\pi\Delta ft} \text{sinc} \left(\pi (2f_m + f_D) (T - |t|) \right) + e^{j\pi f_m t} \text{sinc} \left(\pi (f_D - \Delta f + f_m) (T - |t|) \right) \\
& + e^{-j\pi\Delta ft} \text{sinc} \left(\pi (f_D - 2f_m) (T - |t|) \right) + e^{-j\pi f_m t} \text{sinc} \left(\pi (f_D - \Delta f - f_m) (T - |t|) \right) \\
& \left. + e^{j\pi f_m t} \text{sinc} \left(\pi (f_D + \Delta f - f_m) (T - |t|) \right) + e^{-j\pi f_m t} \text{sinc} \left(\pi (f_D + \Delta f + f_m) (T - |t|) \right) \right]
\end{aligned} \tag{3.36}$$

The magnitude of the ambiguity function can now be taken and like terms can be combined

$$\begin{aligned}
|AF_3(t, f_D)| = & \left| \frac{(T - |t|)}{9} \left[3 \operatorname{sinc} \left(\pi f_D (T - |t|) \right) + \operatorname{sinc} \left(\pi (2f_m + f_D) (T - |t|) \right) \right. \right. \\
& + \operatorname{sinc} \left(\pi (f_D - \Delta f + f_m) (T - |t|) \right) + \operatorname{sinc} \left(\pi (f_D - 2f_m) (T - |t|) \right) \\
& + \operatorname{sinc} \left(\pi (f_D - \Delta f - f_m) (T - |t|) \right) + \operatorname{sinc} \left(\pi (f_D + \Delta f - f_m) (T - |t|) \right) \\
& \left. \left. + \operatorname{sinc} \left(\pi (f_D + \Delta f + f_m) (T - |t|) \right) \right] \right|
\end{aligned} \tag{3.37}$$

where the magnitude of exponential terms $|e^{j\pi f_D t}| = 1$, $|e^{\pm j\pi f_m t}| = 1$, $|e^{-j\pi \Delta f t}| = 1$, and $|e^{-j\pi(\Delta f - 2f_m)t} + e^{-j\pi(\Delta f + 2f_m)t} + e^{j\pi \Delta f t}| = 3$. An image of the ambiguity function of double sideband modulation with $\Delta f = 50$ MHz and $f_m = 10$ MHz along with the matched filter and Doppler response can be seen in Fig. 3.12.

Finally, the ambiguity function of the PTTW using amplitude modulation with the model of the time domain waveform from (3.24)

$$\begin{aligned}
AF_4(t, f_D) = & \frac{1}{16} \int_{-\infty}^{\infty} \operatorname{rect} \left(\frac{\tau - t}{T} \right) \left(e^{j\pi(\Delta f - 2f_m)(\tau - t)} + e^{j\pi \Delta f(\tau - t)} + e^{j\pi(\Delta f + 2f_m)(\tau - t)} \right. \\
& \left. + e^{-j\pi \Delta f(\tau - t)} \right) \\
& \times \operatorname{rect} \left(\frac{\tau}{T} \right) \left(e^{-j\pi(\Delta f - 2f_m)\tau} + e^{-j\pi \Delta f \tau} + e^{-j\pi(\Delta f + 2f_m)\tau} + e^{j\pi \Delta f \tau} \right) e^{j2\pi f_D \tau} d\tau
\end{aligned} \tag{3.38}$$

The integral can be truncated due to $\operatorname{rect}(\cdot)$ envelope such that

$$\begin{aligned}
AF_4(t, f_D) = & \frac{1}{16} \int_{-\frac{T}{2}}^{t + \frac{T}{2}} \left(e^{-j\pi(\Delta f - 2f_m)t} + e^{-j\pi[(\Delta f - 2f_m)t + 2f_m\tau]} + e^{-j\pi[(\Delta f - 2f_m)t + 4f_m\tau]} \right. \\
& + e^{j\pi[(\Delta f - 2f_m)(\tau - t) + \Delta f \tau]} + e^{j\pi[2f_m\tau - \Delta f t]} + e^{-j\pi \Delta f t} + e^{-j\pi[\Delta f t + 2f_m\tau]} \\
& + e^{j\pi \Delta f(2\tau - t)} + e^{j\pi[4f_m\tau - (\Delta f + 2f_m)t]} + e^{j\pi[2f_m\tau - (\Delta f + 2f_m)t]} + e^{-j\pi(\Delta f + 2f_m)t} \\
& + e^{j\pi[(\Delta f + 2f_m)(\tau - t) + \Delta f \tau]} + e^{j\pi[\Delta f t - (2\Delta f - 2f_m)\tau]} + e^{-j\pi \Delta f(2\tau - t)} + e^{j\pi[\Delta f t - (2\Delta f + 2f_m)\tau]} \\
& \left. + e^{j\pi \Delta f t} \right) e^{j2\pi f_D \tau} d\tau
\end{aligned} \tag{3.39}$$

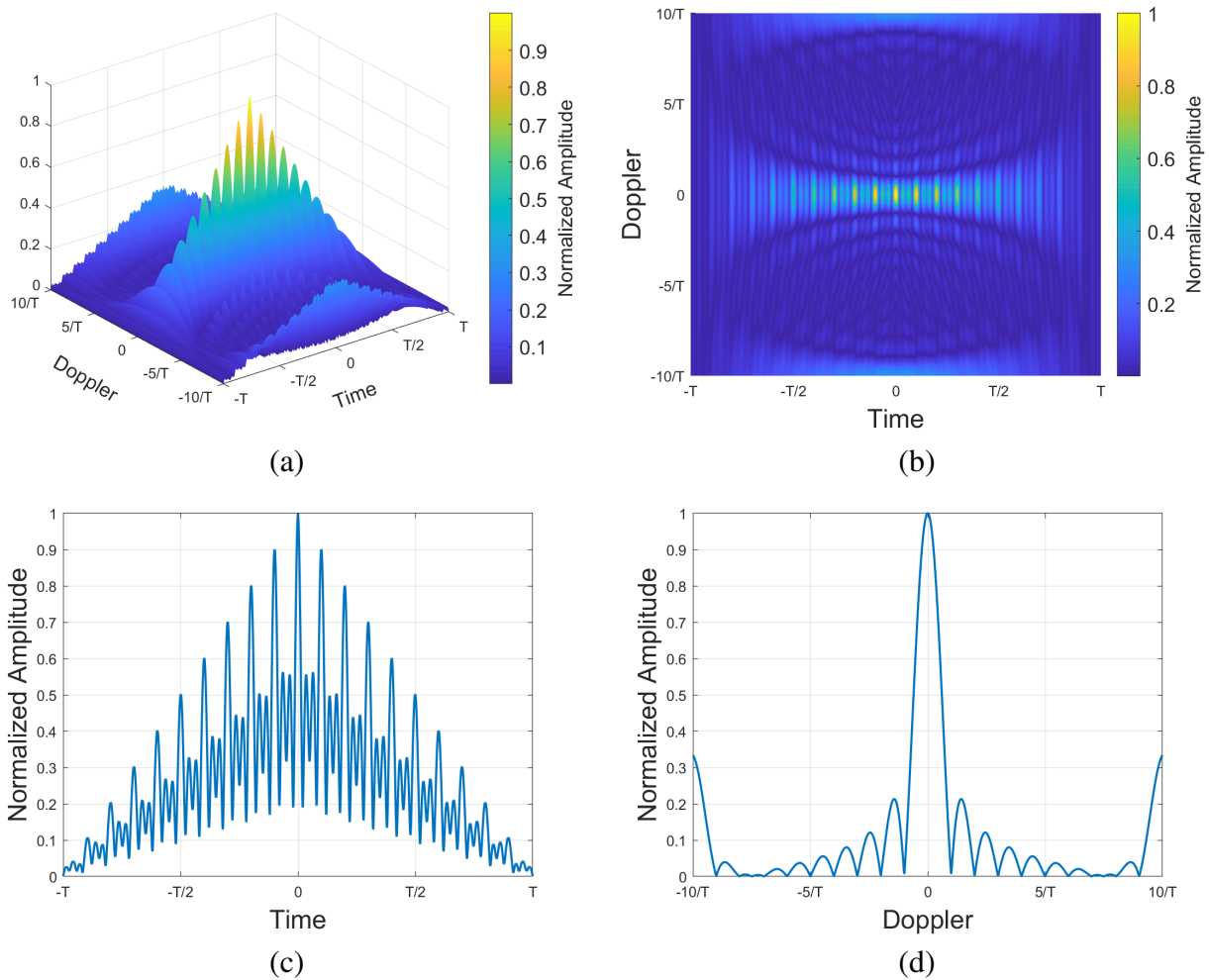


Figure 3.12: (a) Ambiguity function of the PTTW with double sideband modulation. (b) Intensity plot of the ambiguity function. (c) Matched filter of double sideband modulation (zero Doppler cut). (d) Doppler response of the double sideband modulation (zero time cut).

$$\begin{aligned}
AF_4(t, f_D) = & \frac{e^{-j\pi(\Delta f - 2f_m)t} + e^{-j\pi(\Delta f + 2f_m)t} + e^{j\pi\Delta ft} + e^{-j\pi\Delta ft}}{j32\pi f_D} \\
& \times \left[e^{j2\pi f_D \left(t + \frac{T}{2}\right)} - e^{-j\pi f_D T} \right] \\
& + \frac{e^{-j\pi(\Delta f - 2f_m)t} + e^{-j\pi\Delta ft}}{j32\pi (f_D - f_m)} \left[e^{j2\pi (f_D - f_m) \left(t + \frac{T}{2}\right)} - e^{-j\pi (f_D - f_m) T} \right] \\
& + \frac{e^{-j\pi(\Delta f - 2f_m)t}}{j32\pi (f_D - 2f_m)} \left[e^{j2\pi (f_D - 2f_m) \left(t + \frac{T}{2}\right)} - e^{-j\pi (f_D - 2f_m) T} \right] \\
& + \frac{e^{-j\pi(\Delta f - 2f_m)t}}{j32\pi (f_D + \Delta f - f_m)} \left[e^{j2\pi (f_D + \Delta f - f_m) \left(t + \frac{T}{2}\right)} - e^{-j\pi (f_D + \Delta f - f_m) T} \right] \\
& + \frac{e^{-j\pi\Delta ft} + e^{-j\pi(\Delta f + 2f_m)t}}{j32\pi (f_D + f_m)} \left[e^{j2\pi (f_D + f_m) \left(t + \frac{T}{2}\right)} - e^{-j\pi (f_D + f_m) T} \right] \\
& + \frac{e^{-j\pi\Delta ft}}{j32\pi (f_D + \Delta f)} \left[e^{j2\pi (f_D + \Delta f) \left(t + \frac{T}{2}\right)} - e^{-j\pi (f_D + \Delta f) T} \right] \\
& + \frac{e^{-j\pi(\Delta f + 2f_m)t}}{j32\pi (f_D + 2f_m)} \left[e^{j2\pi (f_D + 2f_m) \left(t + \frac{T}{2}\right)} - e^{-j\pi (f_D + 2f_m) T} \right] \\
& + \frac{e^{-j\pi(\Delta f + 2f_m)t}}{j32\pi (f_D + \Delta f + f_m)} \left[e^{j2\pi (f_D + \Delta f + f_m) \left(t + \frac{T}{2}\right)} - e^{-j\pi (f_D + \Delta f + f_m) T} \right] \\
& + \frac{e^{j\pi\Delta ft}}{j32\pi (f_D - \Delta f + f_m)} \left[e^{j2\pi (f_D - \Delta f + f_m) \left(t + \frac{T}{2}\right)} - e^{-j\pi (f_D - \Delta f + f_m) T} \right] \\
& + \frac{e^{j\pi\Delta ft}}{j32\pi (f_D - \Delta f)} \left[e^{j2\pi (f_D - \Delta f) \left(t + \frac{T}{2}\right)} - e^{-j\pi (f_D - \Delta f) T} \right] \\
& + \frac{e^{j\pi\Delta ft}}{j32\pi (f_D - \Delta f - f_m)} \left[e^{j2\pi (f_D - \Delta f - f_m) \left(t + \frac{T}{2}\right)} - e^{-j\pi (f_D - \Delta f - f_m) T} \right]
\end{aligned} \tag{3.40}$$

Extracting a factor from each function so that every parenthesis contains a complex exponential

subtracted by its conjugate

$$\begin{aligned}
AF_4(t, f_D) = & \frac{e^{-j\pi(\Delta f - 2f_m)t} + e^{-j\pi(\Delta f + 2f_m)t} + e^{j\pi\Delta ft} + e^{-j\pi\Delta ft}}{j32\pi f_D e^{-j\pi f_D t}} \\
& \times \left[e^{j\pi f_D(t+T)} - e^{-j\pi f_D(t+T)} \right] \\
& + \frac{\left(e^{-j\pi(\Delta f - 2f_m)t} + e^{-j\pi\Delta ft} \right) e^{j\pi(f_D - f_m)t}}{j32\pi(f_D - f_m)} \left[e^{j\pi(f_D - f_m)(t+T)} - e^{-j\pi(f_D - f_m)(t+T)} \right] \\
& + \frac{e^{-j\pi(\Delta f - 2f_m)t} e^{j\pi(f_D - 2f_m)t}}{j32\pi(f_D - 2f_m)} \left[e^{j\pi(f_D - 2f_m)(t+T)} - e^{-j\pi(f_D - 2f_m)(t+T)} \right] \\
& + \frac{e^{-j\pi(\Delta f - 2f_m)t} e^{j\pi(f_D + \Delta f - f_m)t}}{j32\pi(f_D + \Delta f - f_m)} \left[e^{j\pi(f_D + \Delta f - f_m)(t+T)} - e^{-j\pi(f_D + \Delta f - f_m)(t+T)} \right] \\
& + \frac{\left(e^{-j\pi\Delta ft} + e^{-j\pi(\Delta f + 2f_m)t} \right) e^{j\pi(f_D + f_m)t}}{j32\pi(f_D + f_m)} \left[e^{j\pi(f_D + f_m)(t+T)} - e^{-j\pi(f_D + f_m)(t+T)} \right] \\
& + \frac{e^{-j\pi\Delta ft} e^{j\pi(f_D + \Delta f)t}}{j32\pi(f_D + \Delta f)} \left[e^{j\pi(f_D + \Delta f)(t+T)} - e^{-j\pi(f_D + \Delta f)(t+T)} \right] \\
& + \frac{e^{-j\pi(\Delta f + 2f_m)t} e^{j\pi(f_D + 2f_m)t}}{j32\pi(f_D + 2f_m)} \left[e^{j\pi(f_D + 2f_m)(t+T)} - e^{-j\pi(f_D + 2f_m)(t+T)} \right] \\
& + \frac{e^{-j\pi(\Delta f + 2f_m)t} e^{j\pi(f_D + \Delta f + f_m)t}}{j32\pi(f_D + \Delta f + f_m)} \left[e^{j\pi(f_D + \Delta f + f_m)(t+T)} - e^{-j\pi(f_D + \Delta f + f_m)(t+T)} \right] \\
& + \frac{e^{j\pi\Delta ft} e^{j\pi(f_D - \Delta f + f_m)t}}{j32\pi(f_D - \Delta f + f_m)} \left[e^{j\pi(f_D - \Delta f + f_m)(t+T)} - e^{-j\pi(f_D - \Delta f + f_m)(t+T)} \right] \\
& + \frac{e^{j\pi\Delta ft} e^{j\pi(f_D - \Delta f)t}}{j32\pi(f_D - \Delta f)} \left[e^{j\pi(f_D - \Delta f)(t+T)} - e^{-j\pi(f_D - \Delta f)(t+T)} \right] \\
& + \frac{e^{j\pi\Delta ft} e^{j\pi(f_D - \Delta f - f_m)t}}{j32\pi(f_D - \Delta f - f_m)} \left[e^{j\pi(f_D - \Delta f - f_m)(t+T)} - e^{-j\pi(f_D - \Delta f - f_m)(t+T)} \right]
\end{aligned} \tag{3.41}$$

Sinc functions can now be formed by multiplying each function by $\frac{t+T}{t+T}$ such that

$\text{sinc}(\theta) = \frac{1}{j2\theta} \left(e^{j\theta} - e^{-j\theta} \right)$ yielding

$$\begin{aligned}
AF_4(t, f_D) = & \frac{e^{-j\pi(\Delta f - 2f_m)t} + e^{-j\pi(\Delta f + 2f_m)t} + e^{j\pi\Delta ft} + e^{-j\pi\Delta ft}}{16e^{-j\pi f_D t}} \\
& \times (t + T) \text{sinc} \left(\pi f_D (t + T) \right) \\
& + \frac{\left(e^{-j\pi(\Delta f - 2f_m)t} + e^{-j\pi\Delta ft} \right) e^{j\pi(f_D - f_m)t}}{16} (t + T) \text{sinc} \left(\pi (f_D - f_m) (t + T) \right) \\
& \quad + \frac{e^{j\pi(f_D - \Delta f)t}}{16} (t + T) \text{sinc} \left(\pi (f_D - 2f_m) (t + T) \right) \\
& \quad + \frac{e^{j\pi(f_D + f_m)t}}{16} (t + T) \text{sinc} \left(\pi (f_D + \Delta f - f_m) (t + T) \right) \\
& + \frac{\left(e^{-j\pi\Delta ft} + e^{-j\pi(\Delta f + 2f_m)t} \right) e^{j\pi(f_D + f_m)t}}{16} (t + T) \text{sinc} \left(\pi (f_D + f_m) (t + T) \right) \\
& \quad + \frac{e^{j\pi f_D t}}{16} (t + T) \text{sinc} \left(\pi (f_D + \Delta f) (t + T) \right) \\
& \quad + \frac{e^{j\pi(f_D - \Delta f)t}}{16} (t + T) \text{sinc} \left(\pi (f_D + 2f_m) (t + T) \right) \\
& + \frac{e^{j\pi(f_D - f_m)t}}{16} (t + T) \text{sinc} \left(\pi (f_D + \Delta f + f_m) (t + T) \right) \\
& + \frac{e^{j\pi(f_D + f_m)t}}{16} (t + T) \text{sinc} \left(\pi (f_D - \Delta f + f_m) (t + T) \right) \\
& \quad + \frac{e^{j\pi f_D t}}{16} (t + T) \text{sinc} \left(\pi (f_D - \Delta f) (t + T) \right) \\
& + \frac{e^{j\pi(f_D - f_m)t}}{16} (t + T) \text{sinc} \left(\pi (f_D - \Delta f - f_m) (t + T) \right)
\end{aligned} \tag{3.42}$$

The terms $\frac{e^{j\pi f_D t}}{16}$ and $(t + T)$ can then be extracted from each term. This derivation shown above represents the case of $t < 0$ case but is symmetric for the case of $t > 0$. The general case of the

derivation can be represented by

$$\begin{aligned}
AF_4(t, f_D) = & \frac{(T - |t|)}{16e^{-j\pi f_D t}} \left(e^{-j\pi(\Delta f - 2f_m)t} + e^{-j\pi(\Delta f + 2f_m)t} + e^{j\pi\Delta f t} + e^{-j\pi\Delta f t} \right) \\
& \times \text{sinc} \left(\pi f_D (T - |t|) \right) \\
& + \left(e^{-j\pi(\Delta f - 2f_m)t} + e^{-j\pi\Delta f t} \right) e^{-j\pi f_m t} \text{sinc} \left(\pi (f_D - f_m) (T - |t|) \right) \\
& + e^{-j\pi\Delta f t} \text{sinc} \left(\pi (f_D - 2f_m) (T - |t|) \right) + e^{j\pi f_m t} \text{sinc} \left(\pi (f_D + \Delta f - f_m) (T - |t|) \right) \\
& + \left(e^{-j\pi\Delta f t} + e^{-j\pi(\Delta f + 2f_m)t} \right) e^{j\pi f_m t} \text{sinc} \left(\pi (f_D + f_m) (T - |t|) \right) \\
& + \text{sinc} \left(\pi (f_D + \Delta f) (T - |t|) \right) + e^{-j\pi\Delta f t} \text{sinc} \left(\pi (f_D + 2f_m) (T - |t|) \right) \\
& + e^{-j\pi f_m t} \text{sinc} \left(\pi (f_D + \Delta f + f_m) (T - |t|) \right) + e^{j\pi f_m t} \text{sinc} \left(\pi (f_D - \Delta f + f_m) (T - |t|) \right) \\
& + \text{sinc} \left(\pi (f_D - \Delta f) (T - |t|) \right) + e^{-j\pi f_m t} \text{sinc} \left(\pi (f_D - \Delta f - f_m) (T - |t|) \right)
\end{aligned} \tag{3.43}$$

The magnitude of the ambiguity function can now be taken and like terms can be combined

$$\begin{aligned}
|AF_4(t, f_D)| = & \left| \frac{(T - |t|)}{16} \left[4 \text{sinc} \left(\pi f_D (T - |t|) \right) + 2 \text{sinc} \left(\pi (f_D - f_m) (T - |t|) \right) \right. \right. \\
& + \text{sinc} \left(\pi (f_D - 2f_m) (T - |t|) \right) + \text{sinc} \left(\pi (f_D + \Delta f - f_m) (T - |t|) \right) \\
& + 2 \text{sinc} \left(\pi (f_D + f_m) (T - |t|) \right) + \text{sinc} \left(\pi (f_D + \Delta f) (T - |t|) \right) \\
& + \text{sinc} \left(\pi (f_D + 2f_m) (T - |t|) \right) + \text{sinc} \left(\pi (f_D + \Delta f + f_m) (T - |t|) \right) \\
& + \text{sinc} \left(\pi (f_D - \Delta f + f_m) (T - |t|) \right) + \text{sinc} \left(\pi (f_D - \Delta f) (T - |t|) \right) \\
& \left. \left. + \text{sinc} \left(\pi (f_D - \Delta f - f_m) (T - |t|) \right) \right] \right|
\end{aligned} \tag{3.44}$$

An image of the ambiguity function of amplitude modulation format with $\Delta f = 50$ MHz and $f_m = 10$ MHz along with the matched filter and Doppler response can be seen in Fig. 3.13.

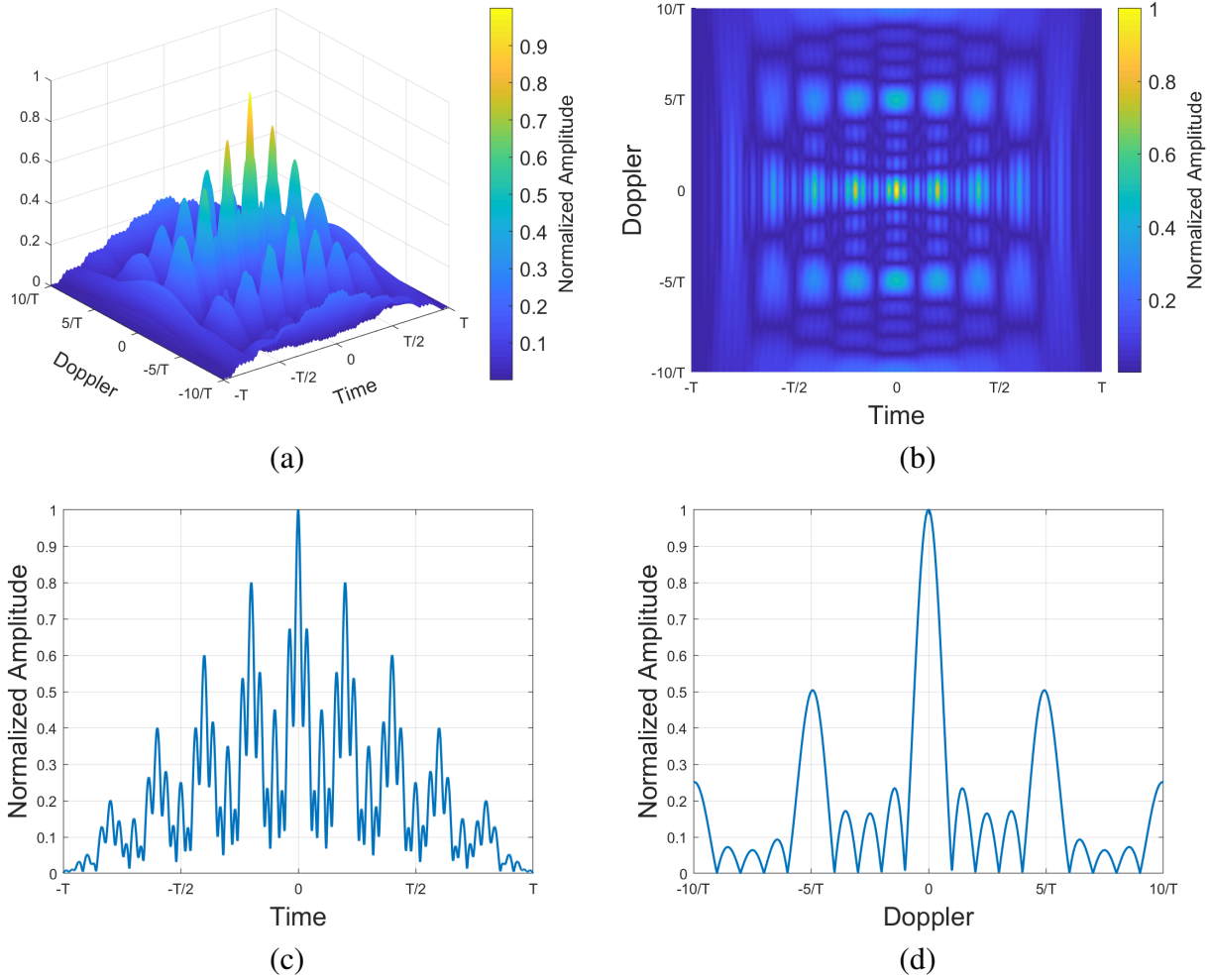


Figure 3.13: (a) Ambiguity function of the PTTW with amplitude modulation. (b) Intensity plot of the ambiguity function. (c) Matched filter of amplitude modulation (zero Doppler cut). (d) Doppler response of the amplitude modulation (zero time cut).

3.2.1.2 Range Estimation Lower Bounds

The spatial estimation ability from (2.12) for the PTTW signal with the frequency reference f_m modulated on the lower of the two tones can be approximated by delta functions in the frequency domain. While the first moment for these waveforms is not entirely negligible, the modulated tone f_m is assumed to be small compared to the overall total waveform bandwidth Δf . Therefore, the spatial estimation can be approximated by the second moment of the frequency spectrum (2.5).

The second moment using single sideband modulation (3.22) is given by

$$\begin{aligned}
\zeta_{f,2}^2 &= \frac{\int (2\pi f)^2 |S_2(f)|^2 df}{\int |S_2(f)|^2 df} \\
&= \frac{\int (2\pi f)^2 \left| \delta \left[f + \left(\frac{\Delta f}{2} - f_m \right) \right] + \delta \left[f - \frac{\Delta f}{2} \right] \right|^2 df}{\int \left| \delta \left[f + \left(\frac{\Delta f}{2} - f_m \right) \right] + \delta \left[f - \frac{\Delta f}{2} \right] \right|^2 df} \\
&= \frac{4\pi^2 \left[\left(\frac{\Delta f}{2} - f_m \right)^2 + \left(\frac{\Delta f}{2} \right)^2 \right]}{1 + 1} \\
&= \frac{4\pi^2 \left[\frac{\Delta f^2}{2} - f_m \Delta f + f_m^2 \right]}{1 + 1} \\
&= 2\pi^2 \left[\frac{\Delta f^2}{2} - f_m \Delta f + f_m^2 \right]
\end{aligned} \tag{3.45}$$

This gives a positional uncertainty form of

$$\sigma_{x,2}^2 \geq \frac{c^2}{4\pi^2 \left[\Delta f^2 - 2f_m \Delta f + 2f_m^2 \right] \text{SNR}} \tag{3.46}$$

Similarly, for modulation using double sideband modulation (3.23) the positional uncertainty can be derived by the second moment

$$\begin{aligned}
\zeta_{f,3}^3 &= \frac{\int (2\pi f)^2 |S_3(f)|^2 df}{\int |S_3(f)|^2 df} \\
&= \frac{\int (2\pi f)^2 \left| \delta \left[f + \left(\frac{\Delta f}{2} + f_m \right) \right] + \delta \left[f + \left(\frac{\Delta f}{2} - f_m \right) \right] + \delta \left[f - \frac{\Delta f}{2} \right] \right|^2 df}{\int \left| \delta \left[f + \left(\frac{\Delta f}{2} + f_m \right) \right] + \delta \left[f + \left(\frac{\Delta f}{2} - f_m \right) \right] + \delta \left[f - \frac{\Delta f}{2} \right] \right|^2 df} \\
&= \frac{4\pi^2 \left[\left(\frac{\Delta f}{2} + f_m \right)^2 + \left(\frac{\Delta f}{2} - f_m \right)^2 + \left(\frac{\Delta f}{2} \right)^2 \right]}{1 + 1 + 1} \\
&= \frac{4\pi^2 \left[\frac{3\Delta f^2}{4} + 2f_m^2 \right]}{3} \\
&= \pi^2 \left[\Delta f^2 + \frac{8f_m^2}{3} \right]
\end{aligned} \tag{3.47}$$

Resulting in a positional uncertainty of

$$\sigma_{x,3}^2 \geq \frac{c^2}{4\pi^2 \left[\Delta f^2 + \frac{8f_m^2}{3} \right] \text{SNR}} \tag{3.48}$$

Finally, adding the frequency reference to the PTTW signal using amplitude modulation (3.24) is similar to double-sideband modulation, except that the carrier tone at the lower frequency is not suppressed, resulting in four frequency tones. The positional uncertainty can be derived from the second moment

$$\begin{aligned}
\zeta_{f,4}^3 &= \frac{\int (2\pi f)^2 |S_4(f)|^2 df}{\int |S_4(f)|^2 df} \\
&= \frac{\int (2\pi f)^2 \left| \delta \left[f + \left(\frac{\Delta f}{2} + f_m \right) \right] + \delta \left[f + \frac{\Delta f}{2} \right] + \delta \left[f + \left(\frac{\Delta f}{2} - f_m \right) \right] + \delta \left[f - \frac{\Delta f}{2} \right] \right|^2 df}{\int \left| \delta \left[f + \left(\frac{\Delta f}{2} + f_m \right) \right] + \delta \left[f + \frac{\Delta f}{2} \right] + \delta \left[f + \left(\frac{\Delta f}{2} - f_m \right) \right] + \delta \left[f - \frac{\Delta f}{2} \right] \right|^2 df} \\
&= \frac{4\pi^2 \left[\left(\frac{\Delta f}{2} + f_m \right)^2 + \left(\frac{\Delta f}{2} \right)^2 + \left(\frac{\Delta f}{2} - f_m \right)^2 + \left(\frac{\Delta f}{2} \right)^2 \right]}{1 + 1 + 1 + 1} \\
&= \pi^2 \left[\Delta f^2 + 2f_m^2 \right]
\end{aligned} \tag{3.49}$$

Resulting in a positional uncertainty of

$$\sigma_{x,4}^2 \geq \frac{c^2}{4\pi^2 \left[\Delta f^2 + 2f_m^2 \right] \text{SNR}} \tag{3.50}$$

From the equations formed for the three modulation formats in (3.46), (3.48), and (3.50) it can be noticed that the bounds are only a function of PTTW tone separation and modulation bandwidth.

3.2.1.3 Frequency Estimation Lower Bound

Estimation of the frequency of a signal is dependent on the duration over which the signal is observed. In particular, the accuracy in estimating the frequency of a signal is inversely dependent on the mean-square duration of the signal (2.9). Calculating this error for the three waveforms analyzed here is generally complicated due to the fact that the signals vary in amplitude as a function of time. However, the objective is not to estimate the frequency of the entire signal, but only of the frequency reference signal modulated onto the waveform. To accomplish this, the signal is first demodulated from the PTTW signal, recovering only the frequency reference f_m . For such a waveform with a rectangular envelope of duration T , the mean-square duration is given

by [105]

$$\zeta_t^2 = \frac{(\pi T)^2}{3} \quad (3.51)$$

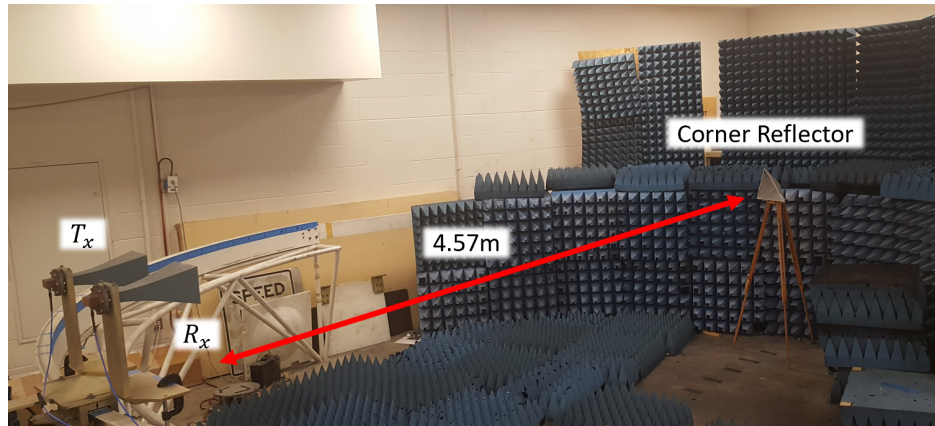
yielding a frequency estimation error from (2.11) of

$$\sigma_f^2 \geq \frac{3}{(\pi T)^2 \text{SNR}} \quad (3.52)$$

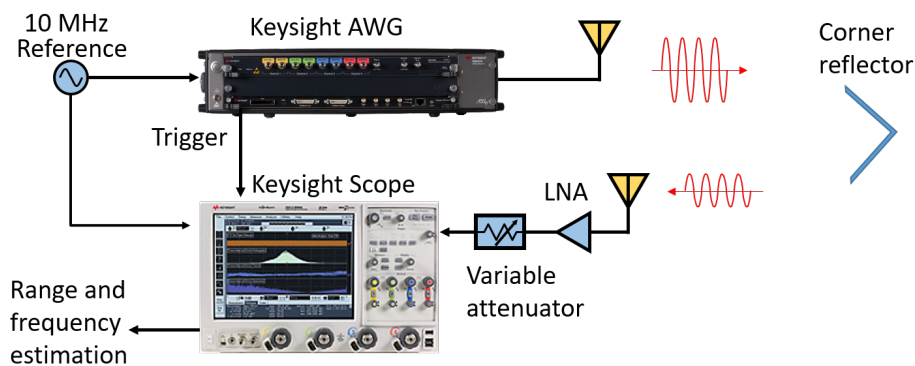
which is the same for all three modulated waveforms and provides the same performance as the LFMW and PTTW.

3.2.2 Experimental Setup and Signal Processing

An experimental ranging system is designed to test the accuracy of estimating the range and frequency using the above waveforms. The transmit antenna is connected to a Keysight M8191 AWG which is used to generate the various waveforms. The waveforms are transmitted through a standard gain 3.95 – 5.85 GHz horn antenna and reflected off of a corner reflector that was placed at the center of a wireless test range 4.57 m from the transmitter (see Fig. 3.14(a)). The received signal is then captured using a MSO-X 92004A Keysight Infiniium High-Performance Oscilloscope. The trigger signal, which consisted of the pulse envelope of the transmitted waveform, is sent from the AWG to the oscilloscope, where an internal threshold detector is used to trigger the waveform capture. The Oscilloscope and AWG reference clocks are locked to a master 10 MHz reference produced by a Agilent MXG Analog Signal Generator. The received waveform amplitude levels are changed using different combinations of attenuators equaling 6, 9, 15, 20, and 30 dB reductions from the maximum signal strength so that the performance could be evaluated over different SNR levels. A 20 dB gain low noise amplifier (LNA) is used preceding the attenuators. The attenuators and amplifier are placed on the receive side to effect total signal amplitude including noise from the transmitter and from the receiver hardware. A block diagram of the measurement system can be seen in Fig. 3.14(b).



(a)



(b)

Figure 3.14: (a) Image of the joint ranging and frequency transfer system experimental setup in an indoor wireless test range. The distance between the transceiver and the corner reflector was 4.57 m.(b) Block diagram of measurement system used in the experiments. The transmitter, represented by the Arbitrary Waveform Generator (AWG) generates the multi-tone signal, and the oscilloscope samples the received signals.

3.2.2.1 Waveform Processing

The delay, and thus the range, is measured by processing the received signal with a matched filter using an analytic copy of the transmitted signal and estimating the time of the peak in the filter output. Each captured measurement is a triggered $5 \mu\text{s}$ segment which contains a $2 \mu\text{s}$ pulse of the modulated signal surrounded by noise. Each capture is digitally filtered 10 MHz above and below the frequency band of interest. 500 of these captures are collected per waveform, per tone separation, and per SNR. A manual disambiguation process is performed by choosing the maximum of the first matched filter output then, for all following matched filter outputs, the nearest peak to

the first matched filter maximum. This approach allows appropriate estimation of the accuracy without requiring consideration of ambiguities. Spline interpolation is performed around the 10 points nearest to the estimated peak to alleviate quantization issues and improve the estimator performance. The processing gain resulting from the matched filter where BW_r is the filtered receiver bandwidth yields the gains given in Table 3.1.

Table 3.1: Processing Gain

Tone Separation	50 MHz	100 MHz	150 MHz	200 MHz
Processing Gain	22.04 dB	24.15 dB	25.6 dB	26.6 dB

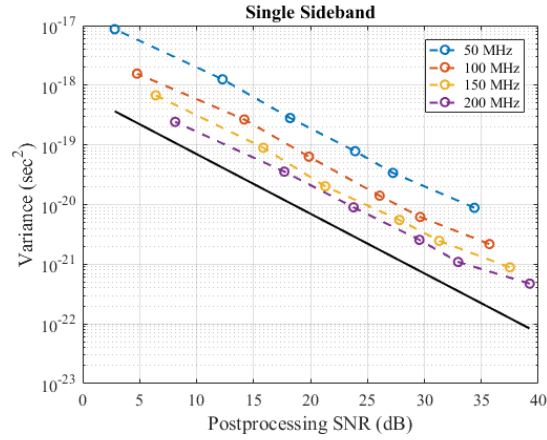
Frequency estimation is achieved by demodulating the 10 MHz reference signal from the PTTW signal. The received waveforms are downconverted using the frequency of lower tone of the PTTW. Once the signals are downconverted digital low-pass filtering with a 20 MHz cutoff frequency is applied to filter out higher signals and harmonics. Amplitude modulation requires an additional high-pass filter with a 5 MHz cutoff frequency to filter out additional lower frequency signals resulting from the four tone modulation format. Each capture is processed only around the $2 \mu s$ waveform duration. The frequency estimator is implemented by measuring the zero-crossings of the 10 MHz signal which is done by rectifying the signal and calculating the temporal differences in the minima of the rectified signal. The standard deviation of the zero crossings are taken for each capture, from which the overall mean was calculated. The exact modulated frequency is detected and the standard deviation is converted to an angular variation versus this frequency, yielding the total phase error due to frequency mismatch.

3.2.2.2 Experimental Results

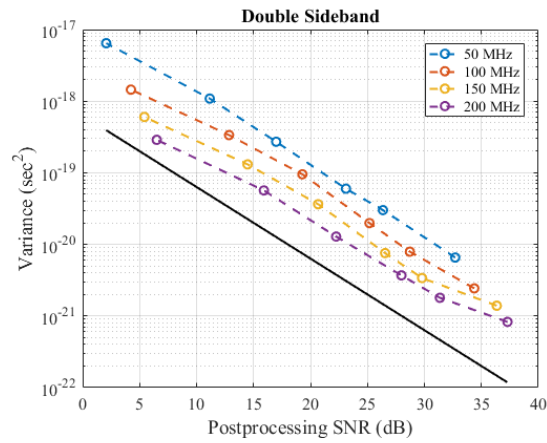
The delay estimation error for the three modulation formats is shown in Fig. 3.15, along with the theoretical lower bounds for 200 MHz tone separation calculated from (3.46), (3.48), and (3.50). The variance is expected to decrease with tone separation, since increasing the tone separation serves to increase the mean-square bandwidth. It is clear that the delay estimation performance

tracks precisely as predicted versus SNR and tone separation, despite the presence of the 10 MHz frequency reference modulated onto the lower tone. A comparison of the performance of all three modulation formats is shown in Fig. 3.16. Effectively, the mean-square bandwidth of the signal is largely unchanged in the presence of the frequency reference, leading to consistent delay estimates. In each case, the 200 MHz tone separation achieves a delay accuracy on the order of 10^{-21} s², or a range accuracy of 4.7 mm, supporting coherent operations in arrays operating at frequencies up to 4.2 GHz with degradation of less than 0.5 dB (i.e. $\frac{\lambda}{15}$).

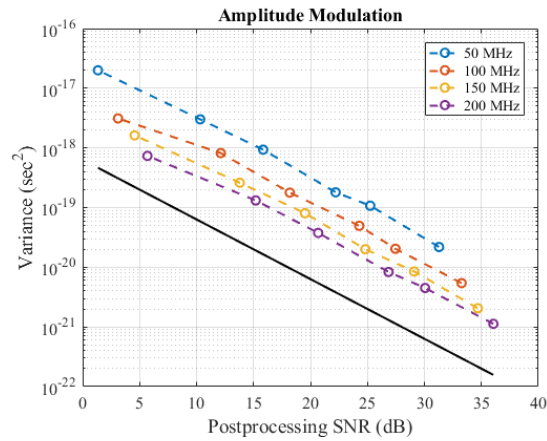
The measured error in the frequency estimation of each of the modulation types, along with the theoretical lower bound, is shown in Fig. 3.17. The performance is dependent on SNR as predicted, but is largely independent of the tone separation. The frequency of the higher tone is arbitrary as long as it is above the filter cutoff, however any remaining residual signal can degrade the estimation performance. In order to ensure that the coherent beam degrades by less than 0.5 dB compared to ideal coherent gain, frequency estimation of less than 18° (i.e. $\frac{\lambda}{20}$) is required, which is represented by the dashed red line. The results indicate that this metric is achievable for all modulation formats with reasonable SNR.



(a)



(b)



(c)

Figure 3.15: Measured delay estimation accuracy versus SNR with the frequency reference included using (a) single-sideband, (b) double-sideband, and (c) amplitude modulation. The separation of the ranging tones is given in the legend, with the CRB for the 200 MHz tone separation from (3.46), (3.48), and (3.50) for (a), (b), and (c) respectively plotted as the solid line.

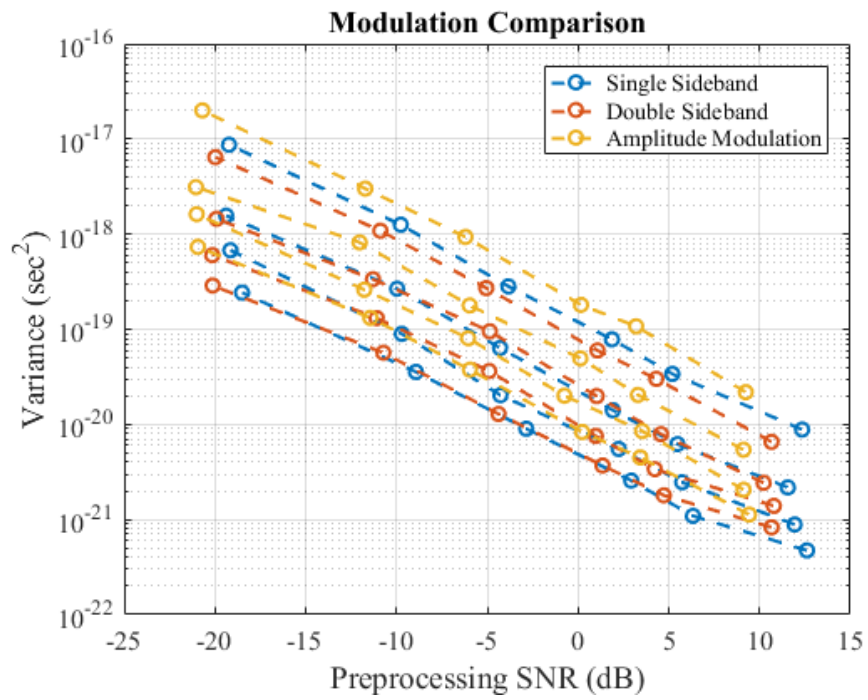
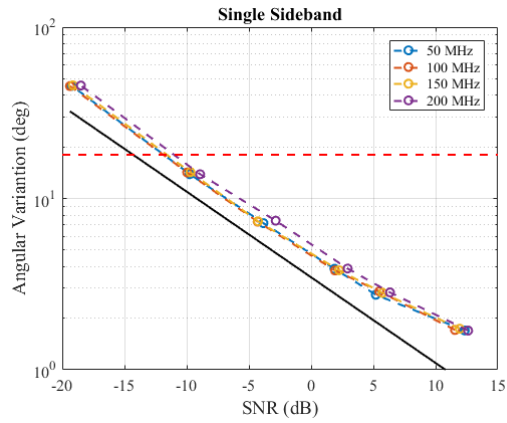
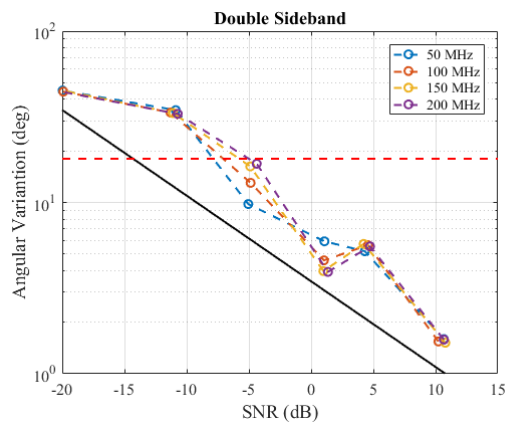


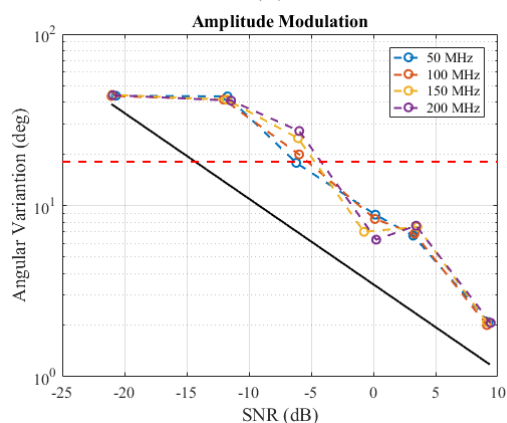
Figure 3.16: Comparison of all three modulation formats showing consistent performance regardless of the modulation format.



(a)



(b)



(c)

Figure 3.17: Variance on the estimate of the 10 MHz frequency reference versus SNR using (a) single-sideband modulation, (b) double-sideband modulation, and (c) amplitude modulation. The separation of the ranging tones is given in the legend. The red dashed line indicates the 18° requirement to ensure $P(G_c \geq 0.9) \approx 1$ for large arrays. The CRB given by (3.52) is shown in the solid line.

3.3 Frequency Division: Phase Alignment for Networked Systems

A common application of interest for distributed systems is communication in which information is sent from point A to point B . This section discusses the use of distributed systems that are acting as a communication system in a dual radar-comm approach to the range estimation. Many current communication systems utilize an orthogonal frequency division multiplexing (OFDM) methodology for information transfer [84, 106–109] where a deterministic preamble precedes the modulated information for synchronization purposes. These preambles present a unique set of orthogonal frequency bands for each user in the system and present a solution to simultaneous internode measurements without the time delays needed for a time duplex scheme. This is a method to address distributed scalability without interfering with information transfer.

3.3.1 Orthogonal Frequency Division Multiplexing (OFDM)

Coherent distributed arrays consisting of large numbers of nodes generally necessitate some multiplexing approach to enable internode ranging between multiple node pairs. While this may be accomplished using time-domain multiplexing, where the range between each node is done in sequence, with mobile nodes there is inherently some time limitations after which the motion of the nodes, either from intentional movement or inherent platform vibration, causes the measurement to no longer be sufficiently accurate. It is thus preferable to begin with a orthogonal frequency division multiplexing (OFDM) approach where multiple measurements can be accomplished simultaneously, after which additional time-multiplexing may be included.

OFDM contains some inherent time-domain information, since the bandwidth of the channels used for each node pair dictates limits on the waveform length. If a half-duplex system is available then there is a limitation on the minimum detectable time delay that can be measured due to bandwidth constraints such that $T_{min} = \frac{2}{BW}$ where BW is the total available bandwidth. With this minimum available time the minimum detectable range can be calculated as $R_{min} = T_{min}c$ where c is the speed of light. This T_{min} is now the lower limit of the pulse length for a half duplex

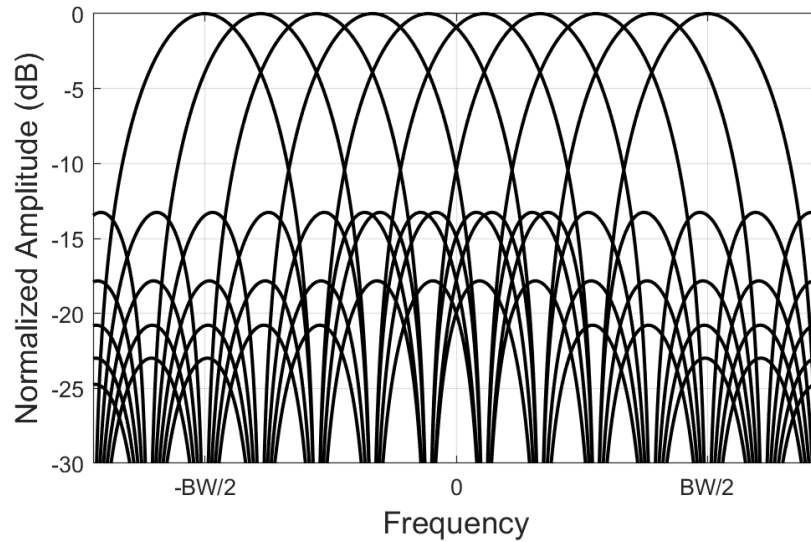


Figure 3.18: Channel splitting using an FDM method where the $\text{sinc}(\cdot)$ representation comes from the Fourier of a rectangular time domain envelope. The spacing of each channel is equivalent to $1/T$ to ensure that the peak is at a null of all of the other $\text{sinc}(\cdot)$ functions.

system. For a full duplex system there is no minimum range limitation due to the ability to transmit and receive simultaneously. The dwell time for each transmission measurement is at least $2T$ where T is the pulse length which is fixed to the max dimension of the array such that $T = \frac{R_{max}}{c}$ so there is sufficient time for the signal to travel the full extent of the array. Therefore the minimum waveform length is defined by the type of system that is available and by the dimensions of the array. It is to be noted that these are minimum temporal limits and in practice waveforms are much longer than this mostly due to hardware limitations.

3.3.2 IEEE 802.11 Standards and Legacy Preamble Format

Here IEEE 802.11a/g/n/ac/ax standards are considered due to their general ubiquity in wireless systems. These standards utilize an OFDM architecture to modulate information onto carriers at frequencies of 2.4 GHz or 5 GHz, with bandwidths of 20 MHz, 40 MHz, 80 MHz, or 160 MHz, depending on the standard [110]. As with any WiFi format, each packet of data is preceded by a preamble to help synchronize the receiver, reduce channel noise, and reduce errors. All of the

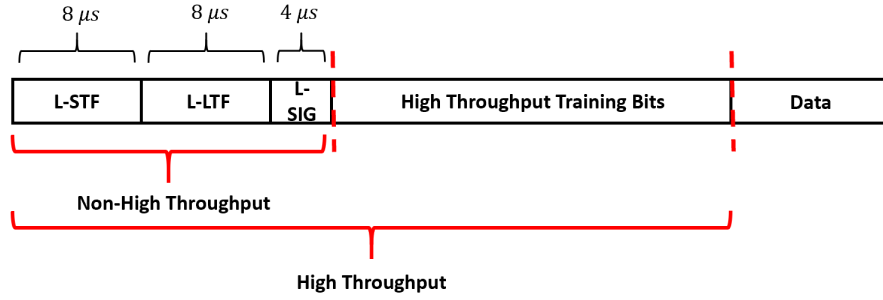


Figure 3.19: Visualization of Legacy preamble.

standards have the same format type known as Legacy. A visualization of the packet format using a Legacy preamble can be seen in Fig. 3.19. Synchronization of the carrier frequencies, which is performed in both non-high throughput and high throughput cases, is accomplished by the transmitter simultaneously bursting a symbol consisting of the set of sub-carriers that are used in the following message. This is known as the training field which can either be short or long lasting $8 \mu\text{s}$ or $16 \mu\text{s}$ and is denoted by Legacy short training field (L-STF) and Legacy long training field (L-LTF) respectively. The Legacy preamble training fields can be represented generally by

$$s_{\text{Legacy}}(t) = \frac{1}{\sqrt{N}} \sum_{n=-\frac{N-1}{2}}^{\frac{N-1}{2}} \text{rect}\left(\frac{t}{T}\right) e^{j2\pi n\delta f t} \quad (3.53)$$

where N is the number of sub-carriers, T is the total waveform duration, and δf is the separation between the carrier tones. These training fields are present in each packet sent from the transmitter and therefore are a reliable source for measurement repeatability within a short time frame, assuming a consistent stream of information is being sent. Therefore, the training field will be used for the basis to obtain a range measurement.

The time and Doppler response of using the legacy preamble for radar measurements can be observed through the ambiguity function (2.1) by

$$AF(t, f_D) = \frac{1}{N} \int_{-\infty}^{\infty} \sum_{n=-\frac{N-1}{2}}^{\frac{N-1}{2}} \text{rect}\left(\frac{\tau-t}{T}\right) e^{-j2\pi n\delta f(\tau-t)} \text{rect}\left(\frac{\tau}{T}\right) e^{j2\pi n\delta f\tau} e^{j2\pi f_D\tau} d\tau \quad (3.54)$$

The summation and integral are linear processes therefore the integration can be brought inside the summation

$$AF(t, f_D) = \frac{1}{N} \sum_{n=-\frac{N-1}{2}}^{\frac{N-1}{2}} e^{j2\pi n\delta ft} \int_{-\infty}^{\infty} \text{rect}\left(\frac{\tau-t}{T}\right) \text{rect}\left(\frac{\tau}{T}\right) e^{j2\pi f_D\tau} d\tau \quad (3.55)$$

The integral, due to the rectangular time domain envelope, can be truncated due to the time limited nature of the $\text{rect}(\cdot)$ function with bounds $[-\frac{T}{2}, \frac{T}{2}]$, yielding

$$\begin{aligned} AF(t, f_D) &= \frac{1}{N} \sum_{n=-\frac{N-1}{2}}^{\frac{N-1}{2}} e^{j2\pi n\delta ft} \int_{-\frac{T}{2}}^{t+\frac{T}{2}} e^{j2\pi f_D\tau} d\tau \\ &= \frac{1}{N} \sum_{n=-\frac{N-1}{2}}^{\frac{N-1}{2}} e^{j2\pi n\delta ft} \left[\frac{1}{j2\pi f_D} \left(e^{j2\pi f_D(t+\frac{T}{2})} - e^{-j\pi f_D T} \right) \right] \end{aligned} \quad (3.56)$$

Extracting a factor of $e^{j\pi f_D t}$ so the function in the parenthesis contains a complex exponential subtracted by its conjugate

$$AF(t, f_D) = \frac{1}{N} \sum_{n=-\frac{N-1}{2}}^{\frac{N-1}{2}} e^{j2\pi n\delta ft} \left[\frac{e^{j\pi f_D t}}{j2\pi f_D} \left(e^{j\pi f_D(t+T)} - e^{-j\pi f_D(t+T)} \right) \right] \quad (3.57)$$

A $\text{sinc}(\cdot)$ function can now be formed by multiplying by $\frac{t+T}{t+T}$ such that $\text{sinc} \theta = \frac{1}{j2\theta} (e^{j\theta} - e^{-j\theta})$

$$AF(t, f_D) = \frac{1}{N} \sum_{n=-\frac{N-1}{2}}^{\frac{N-1}{2}} e^{j2\pi n\delta ft} \left[e^{j\pi f_D t} (t+T) \text{sinc} \left(\pi f_D (t+T) \right) \right] \quad (3.58)$$

This derivation shown above represents the case of $t < 0$ case but is symmetric for the case of $t > 0$. The general case of the derivation can be represented by

$$AF(t, f_D) = \frac{1}{N} \left[e^{j\pi f_D t} (T - |t|) \text{sinc} \left(\pi f_D (T - |t|) \right) \right] \sum_{n=-\frac{N-1}{2}}^{\frac{N-1}{2}} e^{j2\pi n\delta ft} \quad (3.59)$$

The summation of the complex exponentials containing the index of summation follow the same approach as the SFW in Section 2.2.2

$$S_{sum} = \sum_{n=-\frac{N-1}{2}}^{\frac{N-1}{2}} e^{j2\pi n\delta ft} = \frac{\sin(\pi N\delta ft)}{\sin(\pi\delta ft)} \quad (3.60)$$

Plugging (3.60) back into (3.59)

$$AF(t, f_D) = \frac{1}{N} e^{j\pi f_D t} (T - |t|) \text{sinc}\left(\pi f_D (T - |t|)\right) \frac{\sin(\pi N\delta ft)}{\sin(\pi\delta ft)} \quad (3.61)$$

The magnitude can now be taken where $|e^{j\pi f_D t}| = 1$ resulting in [85]

$$|AF(t, f_D)| = \left| \frac{1}{N} (T - |t|) \text{sinc}\left(\pi f_D (T - |t|)\right) \frac{\sin(\pi N\delta ft)}{\sin(\pi\delta ft)} \right| \quad (3.62)$$

An image of an example of the legacy preamble ambiguity function along with the matched filter and Doppler responses can be seen in Fig. 3.20.

3.3.3 Theoretical ranging Accuracy of the Legacy Preamble and the Stepped-Frequency Waveform

The SFW, from Section 2.2.2, is a commonly-used radar waveform. The SFW is again represented by

$$s(t) = \frac{1}{\sqrt{N}} \sum_{n=-\frac{N-1}{2}}^{\frac{N-1}{2}} \text{rect}\left(\frac{t - nT_r}{T}\right) e^{j2\pi n\delta ft} \quad (3.63)$$

where T_r is the period between pulses, N is the number of pulses, and δf is the frequency step for every consecutive pulse. This is very similar to the model of the L-STF and L-LTF but in this case the sub-carriers are transmitted all at once rather than at different times. A time frequency plot comparing the formulation of the training field to the SFW can be seen in Fig. 3.21.

The positional and velocity estimation accuracy of this waveform is given by the CRLBs in (2.12) and (2.13) respectively where the estimation ability is again solely dependent on the

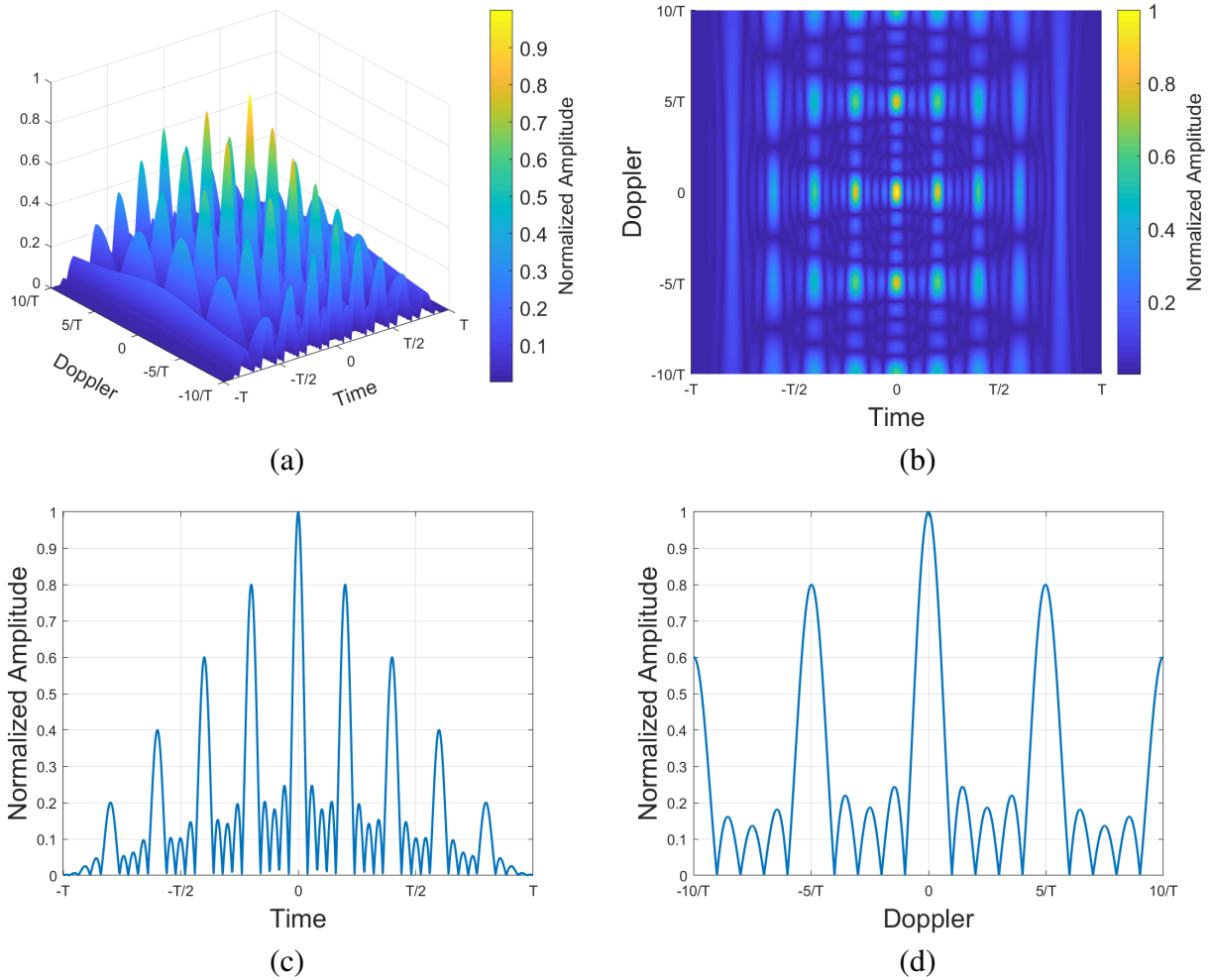


Figure 3.20: (a) Ambiguity function of the Legacy preamble. (b) Intensity plot of the ambiguity function. (c) Matched filter of the Legacy preamble (zero Doppler cut). (d) Doppler response of the Legacy preamble (zero time cut).

second moments due to preamble format being zero mean time and frequency, $\mu_f = \mu_t = 0$. The second moment of the frequency spectrum (2.5) can be approximated by delta functions in the the

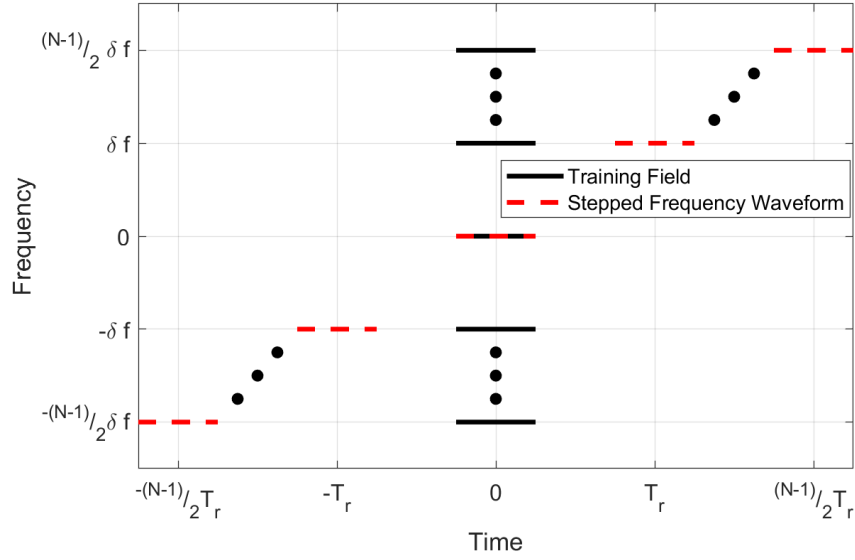


Figure 3.21: Time-frequency plot of the Legacy preamble training field and SFW with a 50% duty cycle.

frequency domain by

$$\begin{aligned}
 \zeta_f^2 &= \frac{\int (2\pi f)^2 |S(f)|^2 df}{\int |S(f)|^2 df} \\
 &= \frac{\sum_{n=-\frac{N-1}{2}}^{\frac{N-1}{2}} \int (2\pi f)^2 |\delta(f - n\delta f)|^2 df}{\sum_{n=-\frac{N-1}{2}}^{\frac{N-1}{2}} \int |\delta(f - n\delta f)|^2 df} \\
 &= \frac{4\pi^2 \left(\sum_{n=-\frac{N-1}{2}}^{\frac{N-1}{2}} (n\delta f)^2 \right)}{N} \\
 &= \frac{4\pi^2 \delta f^2 \left[\frac{1}{12} N (N^2 - 1) \right]}{N} \\
 &= \frac{\pi^2 \delta f^2 (N^2 - 1)}{3}
 \end{aligned} \tag{3.64}$$

Resulting in a positional uncertainty of

$$\sigma_x^2 \geq \frac{3c^2}{4 [\pi^2 \delta f^2 (N^2 - 1)] \text{SNR}} \tag{3.65}$$

The spectrum of the SFW, given the appropriate T , δf , and N , is thus identical to the spectrum of the Legacy preamble, and therefore the mean-squared bandwidth of the Legacy preamble is equal to that of the SFW,

$$\zeta_f^2|_{\text{Legacy}} = \zeta_f^2|_{\text{SFW}}. \quad (3.66)$$

Thus the performance of a Legacy preamble as a delay (and therefore ranging) estimator is equal to that of the SFW for an equivalent SNR.

The uncertainty in velocity can be solved for by (2.13) and (2.9)

$$\begin{aligned} \zeta_t^2 &= \frac{\int (2\pi t)^2 |s(t)|^2 dt}{\int |s(t)|^2 dt} \\ &= \frac{\int (2\pi t)^2 |\text{rect}(\frac{t}{T})|^2 dt}{\int |\text{rect}(\frac{t}{T})|^2 dt} \\ &= \frac{\int_{-T/2}^{T/2} (2\pi t)^2 dt}{\int_{-T/2}^{T/2} dt} \\ &= \frac{\frac{4\pi^2}{3} \left[\left(\frac{T}{2}\right)^3 - \left(-\frac{T}{2}\right)^3 \right]}{\frac{T}{2} + \frac{T}{2}} \\ &= \frac{\pi^2 T^2}{3} \end{aligned} \quad (3.67)$$

Giving a uncertainty in velocity of

$$\sigma_v^2 \geq \frac{3c^2}{4f_c^2 (\pi^2 T^2) \text{SNR}} \quad (3.68)$$

This has the same performance as the LFMW and PTTW for the same duration T . Comparing (3.67) to (2.56) the Legacy preamble has reduced performance in velocity estimation relative to the SFW due to the uniform distribution of energy over the time domain.

To demonstrate the similarities of the ranging performance of the Legacy preamble and the SFW, a simulation of these two waveforms are shown in Fig. 3.22 where in Fig. 3.22(a) there is an example of an 802.11n waveform with 20 MHz of bandwidth and data on sub-carriers ± 4 , ± 8 , ± 12 , ± 16 , ± 20 , and ± 24 . This is then modeled as a SFW in Fig. 3.22(b) where $N = 12$, $T = 8 \mu\text{s}$, and $\delta f = 1.25 \text{ MHz}$ ($4 * 312.5 \text{ kHz}$) where 312.5 kHz is the standard 802.11n channel

bandwidth and the center frequency (DC at baseband after demodulation) is neglected. Both the corresponding spectrum of the L-STF and the SFW are given in Fig. 3.22(c). The normalized matched filter output can be seen in Fig. 3.22(d) for both waveforms. The matched filter produces the same output shape for both the L-STF and the SFW which, therefore, reinforces the conclusion that they provide the same accuracy as a time delay estimator.

Using the Legacy preamble over the SFW as an estimator entails a processing gain reduction by a factor of N due to the reduction in time-bandwidth product. However, it should be noted that temporal pulse compression of multitone signals is not classically done in radar systems. Phase-modulated waveforms are prevalent in radar, since such signals can be implemented with constant amplitude, and transmitters can then be operated at a maximum power level at all times (typically near the 1 – dB compression point where efficiency is high), yielding optimal sensitivity. Multitone signals, however, are amplitude modulated, which necessitates operating transmitters below the compression point. Communications systems commonly operate in this region due to the use of signals such as quadrature amplitude modulation (QAM), thus pulse compression of Legacy preambles is feasible when implemented in communications systems.

3.3.4 Experimental Validation

To measure the variance of the Legacy preamble as a range estimator, a wireless experiment is conducted in a semi-enclosed antenna range. The 802.11 waveform is produced using MATLAB's WLAN toolbox on a host computer connected to a Keysight M8191 AWG and is received by a Keysight MSO-X 92004A Oscilloscope. Taking into consideration the memory depth of the scope, the 802.11 waveform with the shortest time duration is chosen for this ranging experiment. This correlates to the standard that supports the largest bandwidth of 160 MHz and therefore 802.11ac is chosen and given a simple payload of [1 0 0 1]. For other formats of 802.11 with the Legacy preamble, the results scale proportionally with the supported bandwidth as the method of information modulation does not interfere with the range estimation process. An image of the time and frequency domain representations of the waveform used for the ranging experiment can be seen in

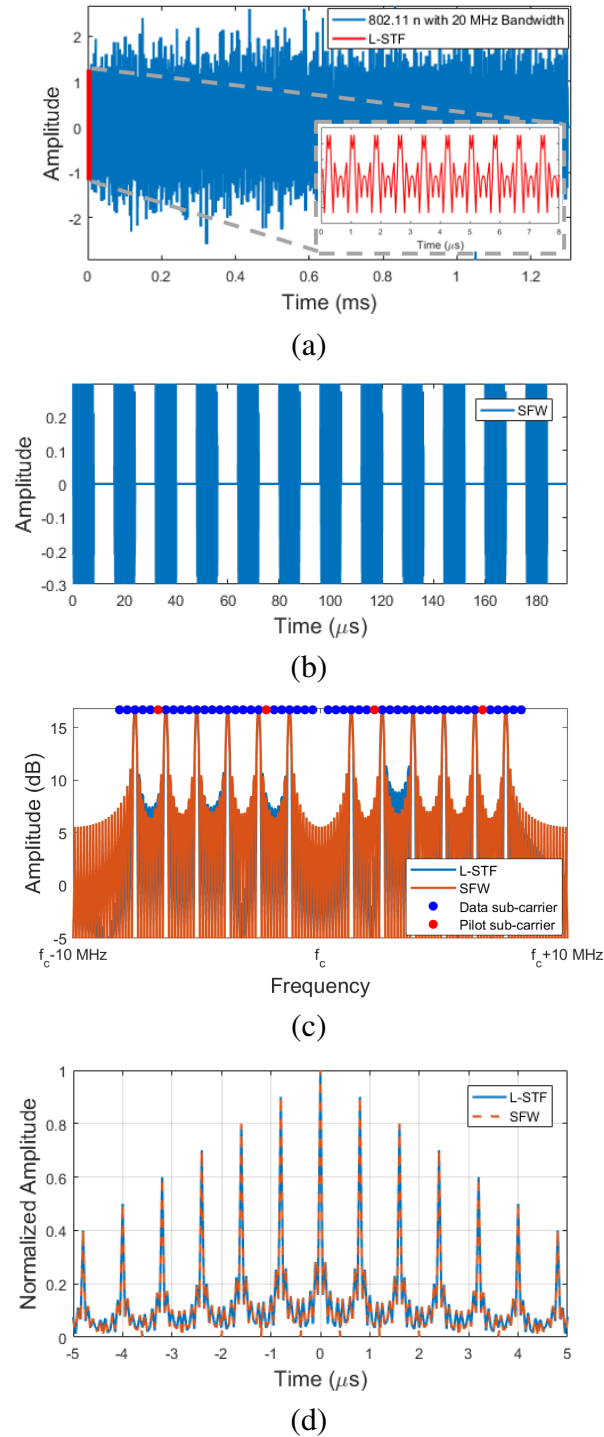
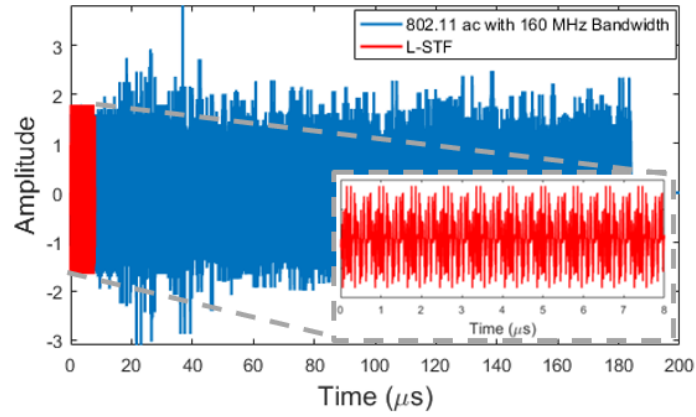


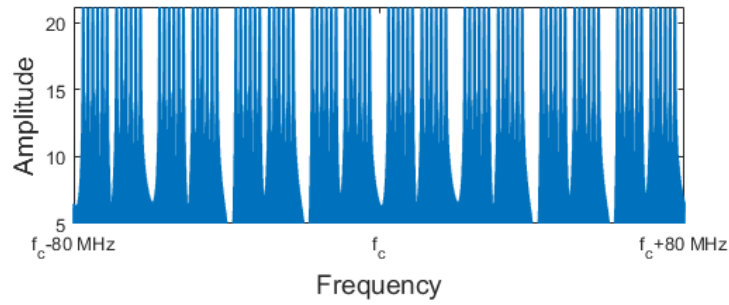
Figure 3.22: (a) Simulated IEEE 802.11n waveform with 20 MHz bandwidth with payload (blue) and L-STF preamble (red). (b) SFW with $T_r = 8 \mu s$ with a 50% duty cycle and containing the 12 data sub-carriers present in the L-STF. (c) Spectrum of both the 802.11n L-STF and the SFW. (d) Normalized zero time delay matched filter output for both L-STF and SFW demonstrating the similarities in the temporal waveform shapes.

Figs. 3.23(a) and 3.23(b) respectively along with the resulting matched filter output in Fig. 3.23(c). There are only two channels in the 802.11ac format that support 160 MHz bandwidth operation, channels 50 and 114 centered at 5.25 GHz and 5.57 GHz respectively. Channel 50 is chosen for this experiment. The baseband signal is upconverted to a RF carrier using a double balanced mixer with 10 dB insertion loss. The LO signal was generated by a Agilent MXG Analog signal generator. To counteract the loss of the mixer, the RF signal is amplified on both of the transmit and receive ends by a 22 dB power amplifier and a 17 dB LNA respectively. The internal clock frequencies of the AWG, scope, and signal generator are all connected via SMA cables to ensure that all operations are derived from the same reference signal.

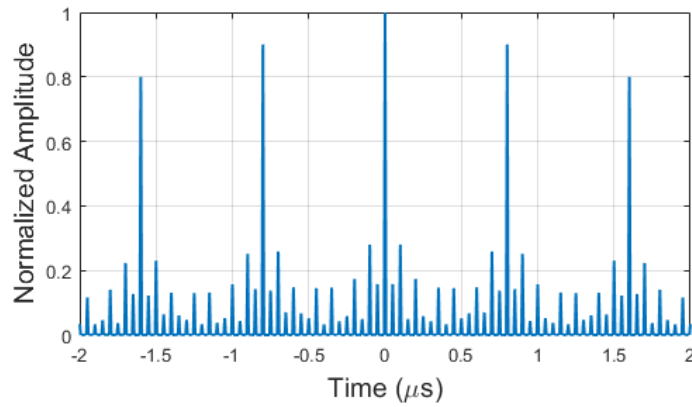
The transmit and receive antennas are two standard gain 3.95 – 5.85 GHz horn antennas that are placed close together in a quasi-monostatic fashion at the edge of the semi-enclosed arch range. A corner reflector was placed in the center of the range at approximately 1.5 m distance from the ranging system. An image of the block diagram of the setup along with an image of the experimental setup in the semi-enclosed arch range can be seen in Figs. 3.24(a) and 3.24(b) respectively. The SNR of the received signal is changed using attenuators on the input to the scope. The scope capture is triggered by an internal threshold detection from a rectangular pulse sent by AWG and the received waveform is downloaded to MATLAB where the matched filter and range estimation processing is implemented offline. The peak of each matched filter output is upsampled by 1000 points using spline interpolation. At each attenuation level the variance of 100 estimated values are calculated, and the SNR is estimated using the eigenvalue decomposition process from Section 2.1.4. The resulting measured variances, simulations of the performance of the 802.11ac waveform along with the corresponding SFW, and the theoretical bound can be seen in Fig. 3.24(c). At all SNR values the SFW and Legacy preamble achieved similar ranging performance in simulation, supporting the use of the Legacy preamble as a ranging waveform. The measured Legacy preamble ranging performance closely matches the simulation, and is comparable to the lower bound. At 50 dB postprocessing SNR (19 dB preprocessing SNR and 31 dB of processing gain determined from the time-bandwidth product) the Legacy preamble was able to obtain a two-way ranging error



(a)



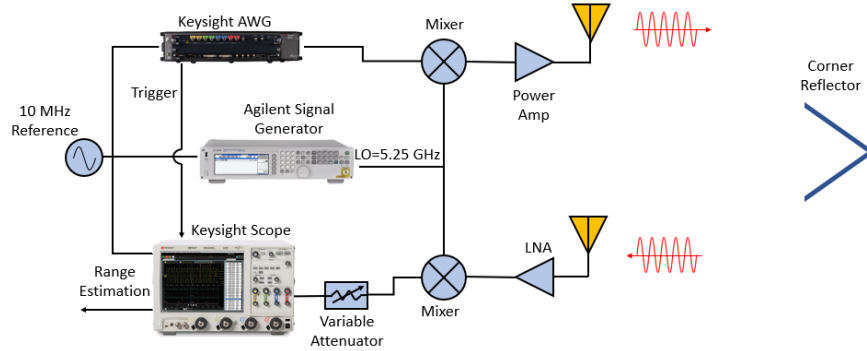
(b)



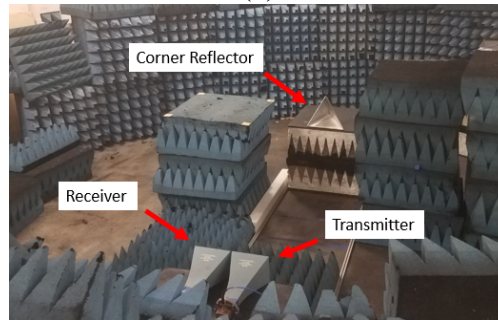
(c)

Figure 3.23: (a) Measured IEEE 802.11ac waveform with 160 MHz bandwidth. (b) Measured spectrum of the waveform. (c) Measured matched filter output.

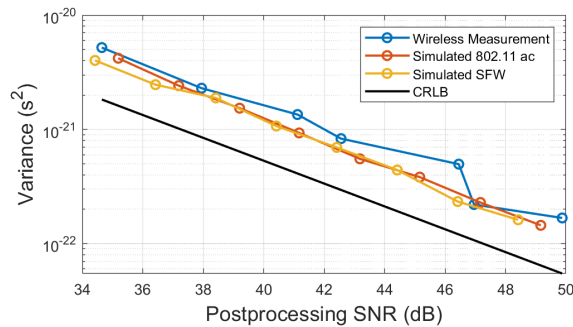
of $\sigma_x = 1.9$ mm providing a maximum beamforming frequency of 10.5 GHz with the accuracy of $\frac{\lambda}{15}$ of the coherent transmitted signal.



(a)



(b)



(c)

Figure 3.24: (a) Block diagram of the ranging experiment (AWG = arbitrary waveform generator, LNA = low-noise amplifier). The corner reflector was placed a distance of 1.5 m from the ranging system. Delay estimation processing was implemented offline in MATLAB. (b) Image of experimental setup up in the semi-enclosed arch range. (c) Measurement variances along with simulated data for 1000 Monte Carlo iterations over various SNR values. The simulated performance of the SFW and Legacy preamble waveforms yielded nearly identical delay estimation, verifying the theoretical similarities of the lower bounds described earlier. The measured performance of the Legacy preamble waveform was close to the simulated performance and comparable to the lower bound (CRLB). The Legacy preamble waveform achieved a lowest ranging error of 1.9mm with a preprocessing SNR of 19 dB combined with 31 dB of processing gain for a total SNR of 50 dB.

3.4 Pulse Encoding: Two-Tone Stepped Frequency Waveform (TTSFW)

This section I analyze another method of using frequency division to provide simultaneous high accuracy range measurements between multiple nodes for a distributed array. Here

a pulse encoded waveform, based off of the spectrally sparse PTTW from Section 2.2.3 and the disambiguation properties of the SFW from Section 2.2.2, is implemented in a one, two, and three node system. It is shown that this waveform has scalability potential of $N!$ where N is the number of pulses providing each unique primary to secondary node connection with a unique pulse structure to look for on return utilizing the same pulse structure and supporting simultaneous range measurements with equivalent accuracy to multiple node pairs without the use of time scheduling.

3.4.1 Frequency Domain Multiplexing (FDM) Approach

Similar to the networked system, this method uses a frequency division method but here the domain is split in two to accommodate the structure of the PTTW. Once the limit on temporal length, T , of the waveform is determined, the bandwidth that each pulse occupies can be estimated as $f_{ch} = \frac{1}{T}$. Using frequency domain multiplexing (FDM) the number of simultaneous connections can be estimated as $m = \frac{BW}{f_{ch}}$ where BW is the total waveform bandwidth [111]. It can now be assumed that m connections can be made in $2T$ accounting for two way propagation. Given metrics relative to the coherence time of the channel between the elements, such as the vibration profile of the platforms, a desired update rate Δt can be chosen. The total number of connectable nodes can then be derived from the number of m connections that can be made in Δt . An estimation of this number can be expressed as

$$N = \frac{BW \Delta t}{2} \quad (3.69)$$

Once the domain is divided into bands, two bands are designated for a given node pair to form a channel. Channels are given two bands to support the spectral sparsity of the two-tone structure of this waveform, as described in this section. To prevent measurement bias, the channels are sequentially organized such that the tone separation of each channel remains constant (see Fig. 3.25).

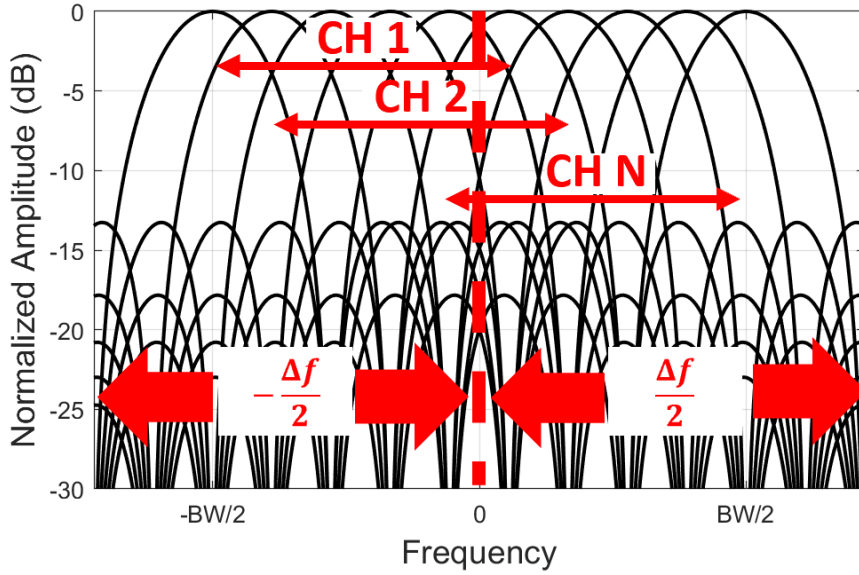


Figure 3.25: Channel splitting using an FDM method for a two-tone system where half of the bandwidth is allocated to the first tone, $-\frac{\Delta f}{2}$, of the N channels and the second half is allocated to the upper tone, $\frac{\Delta f}{2}$.

3.4.2 Waveform Design

The multi-node high-accuracy ranging waveform is based on a spectrally-sparse, two-tone waveform. In this section, the multi-node stepped-frequency waveform is derived and discussed. To combine the advantage of both the resolution of the PTTW and the disambiguation ability of the SFW, a two-tone stepped-frequency waveform (TTSFW) is developed. This is done by first choosing the individual pulse bandwidth, Δf , then monotonically increasing these frequencies by δf keeping the bandwidth of every pulse the same.

This waveform can be scaled similarly to that of the PTTW but instead of having only one pulse, here the waveform includes an arbitrary N pulses, essentially stitching N different PTTW pulses into one waveform. Since more resources are being used per node connection it is intuitive that the scalability would decrease, however this is not the case. In fact the same waveform with N pulses can be used to service $N!$ connections. This is done by shifting the order of pulses (frequency steps) so that there are $N!$ unique waveforms utilizing the same pulses, each

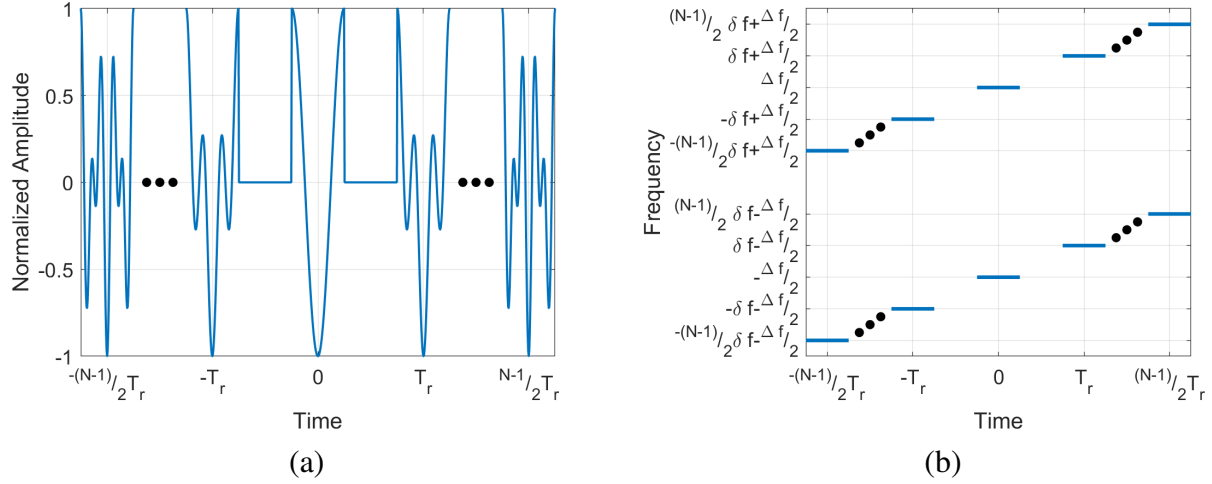


Figure 3.26: (a) Two-tone stepped-frequency waveform in the time domain. (a) TTSFW in the time-frequency domain

in a different order. The baseband TTSFW signal can be modeled as

$$s(t) = \frac{1}{2\sqrt{N}} \sum_{n=-\frac{N-1}{2}}^{\frac{N-1}{2}} \text{rect}\left(\frac{t-nT_r}{T}\right) \left(e^{-j\pi\Delta f t} + e^{j\pi\Delta f t}\right) e^{j2\pi n\delta f t} \quad (3.70)$$

Using the scalability approach described above, the frequency step and pulse bandwidth can be expressed in terms of the full system bandwidth as $\delta f = \frac{BW}{2N-1}$ and $\Delta f = N\delta f = \frac{NBW}{2N-1}$. An image of the time frequency spectrum along with the waveform in the time domain can be seen in Fig. 3.26.

The disambiguation properties of the waveform, along with its response to both time delay and Doppler, can be observed from the ambiguity function of the TTSFW. Inputting the time domain representation of the TTSFW in (3.70) into the ambiguity function in (2.1)

$$AF(t, f_D) = \frac{1}{4N} \int_{-\infty}^{\infty} \sum_{n=-\frac{N-1}{2}}^{\frac{N-1}{2}} \text{rect}\left(\frac{\tau-t-nT_r}{T}\right) \left(e^{j\pi\Delta f(\tau-t)} + e^{-j\pi\Delta f(\tau-t)}\right) \times e^{-j2\pi n\delta f(\tau-t)} \times \text{rect}\left(\frac{\tau-nT_r}{T}\right) \left(e^{-j\pi\Delta f\tau} + e^{j\pi\Delta f\tau}\right) e^{j2\pi n\delta f\tau} e^{j2\pi f_D\tau} d\tau \quad (3.71)$$

The summation and integral are linear processes therefore the integration can be brought inside the summation

$$\begin{aligned}
AF(t, f_D) &= \frac{1}{4N} \sum_{n=-\frac{N-1}{2}}^{\frac{N-1}{2}} e^{j2\pi n\delta ft} \int_{-\infty}^{\infty} \text{rect}\left(\frac{\tau - t - nT_r}{T}\right) \left(e^{j\pi\Delta f(\tau-t)} + e^{-j\pi\Delta f(\tau-t)} \right) \\
&\quad \times \text{rect}\left(\frac{\tau - nT_r}{T}\right) \left(e^{-j\pi\Delta f\tau} + e^{j\pi\Delta f\tau} \right) e^{j2\pi f_D\tau} d\tau
\end{aligned} \tag{3.72}$$

A substitution can be made such that $\hat{\tau} = \tau - nT_r$

$$\begin{aligned}
AF(t, f_D) &= \frac{1}{4N} \sum_{n=-\frac{N-1}{2}}^{\frac{N-1}{2}} e^{j2\pi n\delta ft} \int_{-\infty}^{\infty} \text{rect}\left(\frac{\hat{\tau} - t}{T}\right) \left(e^{j\pi\Delta f(\hat{\tau}+nT_r-t)} + e^{-j\pi\Delta f(\hat{\tau}+nT_r-t)} \right) \\
&\quad \times \text{rect}\left(\frac{\hat{\tau}}{T}\right) \left(e^{-j\pi\Delta f(\hat{\tau}+nT_r)} + e^{j\pi\Delta f(\hat{\tau}+nT_r)} \right) e^{j2\pi f_D(\hat{\tau}+nT_r)} d\hat{\tau}
\end{aligned} \tag{3.73}$$

Truncation of the integral around $[-\frac{T}{2}, \frac{T}{2}]$ can be performed time limited nature of the $\text{rect}(\cdot)$ envelope, yielding

$$\begin{aligned}
AF(t, f_D) &= \frac{1}{4N} \sum_{n=-\frac{N-1}{2}}^{\frac{N-1}{2}} e^{j2\pi n(\delta ft + f_D T_r)} \int_{-\frac{T}{2}}^{t+\frac{T}{2}} \left[e^{-j\pi\Delta f t} + e^{j\pi\Delta f t} + e^{j\pi\Delta f[2(\hat{\tau}+nT_r)-t]} \right. \\
&\quad \left. + e^{-j\pi\Delta f[2(\hat{\tau}+nT_r)-t]} \right] e^{j2\pi f_D \hat{\tau}} d\hat{\tau} \\
&= \frac{1}{4N} \sum_{n=-\frac{N-1}{2}}^{\frac{N-1}{2}} e^{j2\pi n(\delta ft + f_D T_r)} \left[\frac{e^{-j\pi\Delta f t} + e^{j\pi\Delta f t}}{j2\pi f_D} \left(e^{j2\pi f_D(t+\frac{T}{2})} - e^{-j\pi f_D T} \right) \right. \\
&\quad + \frac{e^{j\pi\Delta f(2nT_r-t)}}{j2\pi(\Delta f + f_D)} \left(e^{j2\pi(\Delta f + f_D)(t+\frac{T}{2})} - e^{-j\pi(\Delta f + f_D)T} \right) \\
&\quad \left. + \frac{e^{j\pi\Delta f(t-2nT_r)}}{j2\pi(f_D - \Delta f)} \left(e^{j2\pi(f_D - \Delta f)(t+\frac{T}{2})} - e^{-j\pi(f_D - \Delta f)T} \right) \right]
\end{aligned} \tag{3.74}$$

Extracting a factor from each function so that every parenthesis contains a complex exponential subtracted by its conjugate

$$\begin{aligned}
AF(t, f_D) = \frac{1}{4N} \sum_{n=-\frac{N-1}{2}}^{\frac{N-1}{2}} e^{j2\pi n(\delta f t + f_D T r)} & \left[\frac{\left(e^{-j\pi \Delta f t} + e^{j\pi \Delta f t} \right) e^{j\pi f_D t}}{j2\pi f_D} \right. \\
& \times \left(e^{j\pi f_D(t+T)} - e^{-j\pi f_D(t+T)} \right) \\
& + \frac{e^{j\pi \Delta f(2nT r - t)} e^{j\pi(\Delta f + f_D)t}}{j2\pi(\Delta f + f_D)} \left(e^{j\pi(\Delta f + f_D)(t+T)} - e^{-j\pi(\Delta f + f_D)(t+T)} \right) \\
& \left. + \frac{e^{j\pi \Delta f(t-2nT r)} e^{j\pi(f_D - \Delta f)t}}{j2\pi(f_D - \Delta f)} \left(e^{j\pi(f_D - \Delta f)(t+T)} - e^{-j\pi(f_D - \Delta f)(t+T)} \right) \right]
\end{aligned} \tag{3.75}$$

$e^{j\pi \Delta f t}$ cancels in the second and third terms and sinc functions can now be formed by multiplying each function by $\frac{t+T}{t+T}$ such that $\text{sinc}(\theta) = \frac{1}{j2\theta} (e^{j\theta} - e^{-j\theta})$

$$\begin{aligned}
AF(t, f_D) = \frac{1}{4N} \sum_{n=-\frac{N-1}{2}}^{\frac{N-1}{2}} e^{j2\pi n(\delta f t + f_D T r)} & \left[\left(e^{-j\pi \Delta f t} + e^{j\pi \Delta f t} \right) \right. \\
& \times e^{j\pi f_D t} (t+T) \text{sinc} \left(\pi f_D (t+T) \right) \\
& + e^{j\pi(f_D t + 2nT r)} (t+T) \text{sinc} \left(\pi (\Delta f + f_D) (t+T) \right) \\
& \left. + e^{j\pi(f_D t - 2nT r)} (t+T) \text{sinc} \left(\pi (f_D - \Delta f) (t+T) \right) \right]
\end{aligned} \tag{3.76}$$

The terms $e^{j\pi f_D t}$ and $(t+T)$ can then be extracted from each term.

$$\begin{aligned}
AF(t, f_D) = \frac{e^{j\pi f_D t} (t+T)}{4N} \sum_{n=-\frac{N-1}{2}}^{\frac{N-1}{2}} e^{j2\pi n(\delta f t + f_D T r)} & \left[\left(e^{-j\pi \Delta f t} + e^{j\pi \Delta f t} \right) \right. \\
& \times \text{sinc} \left(\pi f_D (t+T) \right) \\
& + e^{j2\pi n T r} \text{sinc} \left(\pi (\Delta f + f_D) (t+T) \right) \\
& \left. + e^{-j2\pi n T r} \text{sinc} \left(\pi (f_D - \Delta f) (t+T) \right) \right]
\end{aligned} \tag{3.77}$$

The summations of the complex exponentials containing the index of summation follow the same approach as the SFW in Section 2.2.2 where

$$S_{sum} = \sum_{n=-\frac{N-1}{2}}^{\frac{N-1}{2}} e^{j2\pi n(\delta ft + f_D T_r)} = \frac{\sin\left(\pi N(\delta ft + f_D T_r)\right)}{\sin\left(\pi(\delta ft + f_D T_r)\right)} \quad (3.78)$$

$$S_{sum} = \sum_{n=-\frac{N-1}{2}}^{\frac{N-1}{2}} e^{\pm j2\pi n T_r} = \frac{\sin\left(\pi N T_r\right)}{\sin\left(\pi T_r\right)}$$

Plugging these values of the summations back into (3.77)

$$AF(t, f_D) = \frac{e^{j\pi f_D t} (t + T)}{4N} \frac{\sin\left(\pi N(\delta ft + f_D T_r)\right)}{\sin\left(\pi(\delta ft + f_D T_r)\right)} \left\{ \left(e^{-j\pi \Delta f t} + e^{j\pi \Delta f t} \right) \right. \\ \left. \times \operatorname{sinc}\left(\pi f_D (t + T)\right) \right. \\ \left. + \frac{\sin\left(\pi N T_r\right)}{\sin\left(\pi T_r\right)} \left[\operatorname{sinc}\left(\pi(\Delta f + f_D)(t + T)\right) + \operatorname{sinc}\left(\pi(f_D - \Delta f)(t + T)\right) \right] \right\} \quad (3.79)$$

This derivation shown above represents the case of $t < 0$ case but is symmetric for the case of $t > 0$. The general case of the magnitude derivation can be represented by

$$|AF(t, f_D)| = \left| \frac{(T - |t|)}{4N} \frac{\sin\left(\pi N(\delta ft + f_D T_r)\right)}{\sin\left(\pi(\delta ft + f_D T_r)\right)} \left\{ 2 \operatorname{sinc}\left(\pi f_D (T - |t|)\right) \right. \right. \\ \left. \left. + \frac{\sin\left(\pi N T_r\right)}{\sin\left(\pi T_r\right)} \left[\operatorname{sinc}\left(\pi(\Delta f + f_D)(T - |t|)\right) + \operatorname{sinc}\left(\pi(f_D - \Delta f)(T - |t|)\right) \right] \right\} \right| \quad (3.80)$$

where $\left| e^{j\pi f_D t} \right| = 1$ and $\left| e^{-j\pi \Delta f} + e^{j\pi \Delta f} \right| = 2$. A plot of this function can be seen in Fig. 3.27. Looking at the $f_D = 0$ cut of the ambiguity function, this function is maximized at every $t = \frac{nN}{\Delta f}$. Since the lobing pattern of the PTTW occurs at every $t = \frac{n}{\Delta f}$ the disambiguation properties of this waveform are now apparent: for an N pulse system, there is $N - 1$ consecutive lobes notched out of the matched filter output of the PTTW with the same Δf . It is important to note, however,

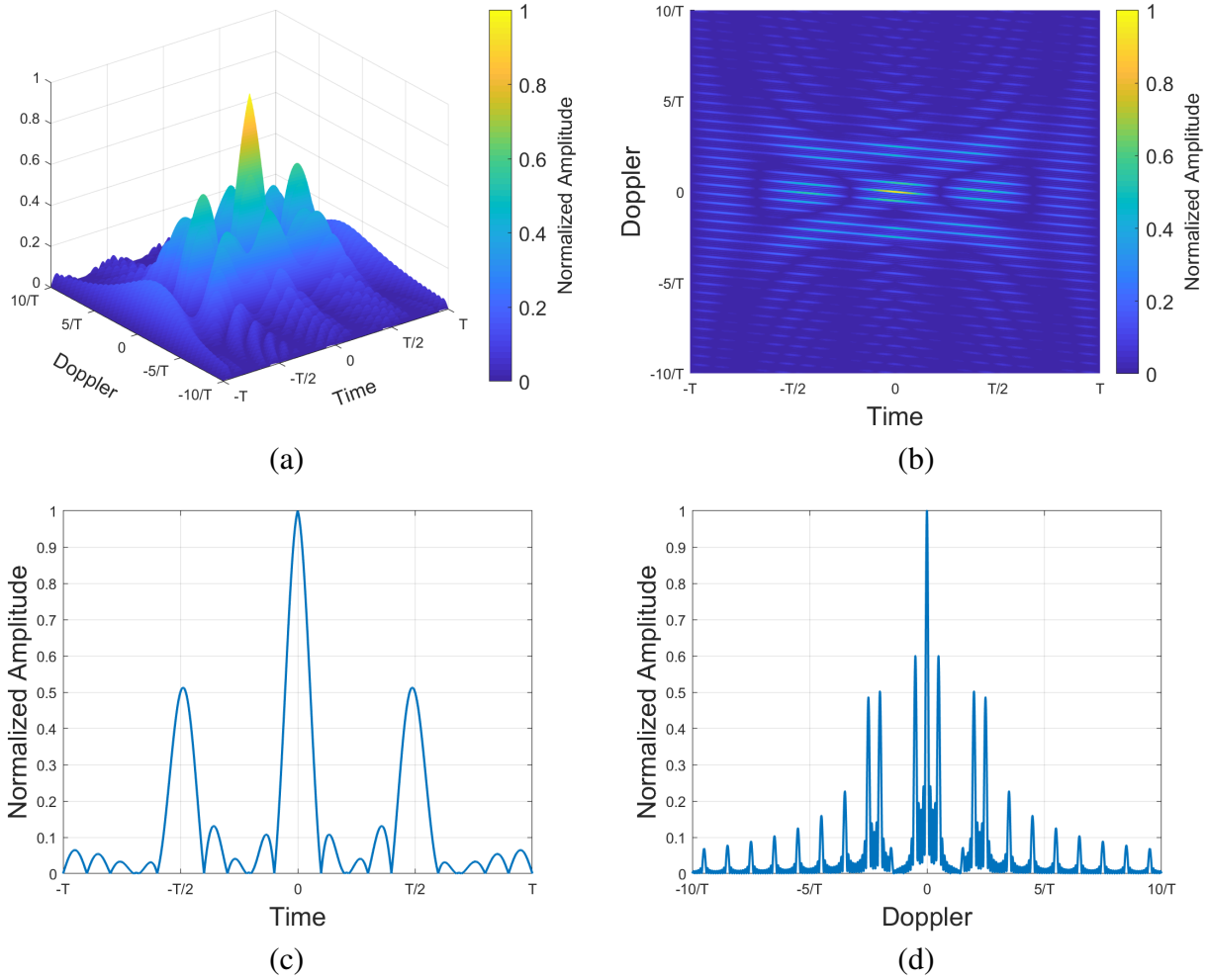


Figure 3.27: (a) Ambiguity function of the TTSFW. (b) Intensity plot of the ambiguity function. (c) Matched filter of the TTSFW (zero Doppler cut). (d) Doppler response of TTSFW (zero time cut).

that the spectrally sparse nature of the TTSFW waveform, along with the ability to simultaneously transmit multiple waveforms simultaneously, makes the TTSFW more beneficial to implement than a traditional LFMW.

The uncertainty of the estimation ability of the TTSFW can be derived using (2.12) and (2.13), where again this waveform is fundamentally zero mean frequency and zero mean time duration, $\mu_t = \mu_f = 0$, making the CRLB solely dependent on the second moment. The mean-squared bandwidth, for the uncertainty in position, can be solved for by making the approximation that the spectrum of each pulse of the TTSFW consists of two delta functions at $-\frac{\Delta f}{2} + n\delta f$ and

$\frac{\Delta f}{2} + n\delta f$ such that

$$\begin{aligned}
\zeta_f^2 &= \frac{\int (2\pi f)^2 |S(f)|^2 df}{\int |S(f)|^2 df} \\
&= \frac{\sum_{n=0}^{N-1} \int (2\pi f)^2 \left| \delta \left[f + \left(\frac{\Delta f}{2} - n\delta f \right) \right] + \delta \left[f - \left(\frac{\Delta f}{2} + n\delta f \right) \right] \right| df}{\sum_{n=0}^{N-1} \int \left| \delta \left[f + \left(\frac{\Delta f}{2} - n\delta f \right) \right] + \delta \left[f - \left(\frac{\Delta f}{2} + n\delta f \right) \right] \right| df} \\
&= \frac{4\pi^2 \sum_{n=0}^{N-1} \left(\frac{\Delta f}{2} - n\delta f \right)^2 + \left(\frac{\Delta f}{2} + n\delta f \right)^2}{\sum_{n=0}^{N-1} (1+1)} \\
&= \frac{8\pi^2 \sum_{n=0}^{N-1} \left(\frac{\Delta f}{2} \right)^2 + (n\delta f)^2}{2N} \\
&= \pi^2 \Delta f^2 + \frac{(2\pi\delta f)^2}{N} \left[\frac{1}{12} N (N^2 - 1) \right] \\
&= \pi^2 \Delta f^2 + \frac{(\pi\delta f)^2 (N^2 - 1)}{3}
\end{aligned} \tag{3.81}$$

The definitions for $\Delta f = N\delta f = \frac{NBW}{2N-1} = \frac{BW}{2-\frac{1}{N}}$ and $\delta f = \frac{BW}{2N-1}$ can now be applied. Plugging these into the mean squared bandwidth

$$\zeta_f^2 = \pi^2 \left(\frac{BW}{2 - \frac{1}{N}} \right)^2 + \frac{(\pi BW)^2 (N^2 - 1)}{3(4N^2 + 4N + 1)} \tag{3.82}$$

This gives a positional uncertainty of from (2.12) as

$$\sigma_x^2 \geq \frac{c^2}{4 \left[\pi^2 \left(\frac{BW}{2 - \frac{1}{N}} \right)^2 + \frac{(\pi BW)^2 (N^2 - 1)}{3(4N^2 + 4N + 1)} \right]^2 \text{SNR}} \tag{3.83}$$

Looking at the limits of the mean-squared bandwidth, if $N = 1$ then the second term becomes zero and the first term becomes $\pi^2 BW^2$. This is exactly the result found in (2.65) in the two-tone case which is to be expected since when $N = 1$ the TTFSW reduces to a two-tone waveform. Looking at the opposite bound, when $N = \infty$, the the first term approaches

$$\lim_{N \rightarrow \infty} \left[\pi^2 \left(\frac{BW}{2 - \frac{1}{N}} \right)^2 \right] = \frac{(\pi BW)^2}{4} \tag{3.84}$$

and the second term

$$(\pi BW)^2 \lim_{N \rightarrow \infty} \left[\frac{(N^2 - 1)}{3(4N^2 + 4N + 1)} \right] = \frac{(\pi BW)^2}{3} \quad (3.85)$$

The term in (3.84) is the two tone case when the individual pulse bandwidth is $\frac{BW}{2}$. This follows the scalability approach described previously for a large number N (see Fig. 3.25). The term in (3.85) is exactly the bound that is obtained by using a LFMW signal with equal amplitude across the frequency band BW [105]. This is again to be expected due to the equal distribution of power over the spectrum emulating the approximation used to derive the mean-squared bandwidth of the LFMW (i.e. a rectangular function bounded by $[-\frac{BW}{2}, \frac{BW}{2}]$). It can be deduced that the first term in (3.82) is a measure of the mean squared bandwidth of the individual pulses and the second term is a measure of the mean squared bandwidth of the overall waveform. A plot of the TTSFW's accuracy vs. number of pulses used can be seen in Fig. 3.28(a). From this figure, the best obtainable bound is for when $N = 1$ which is the two-tone case. The value of the mean-squared bandwidth then increases in a logarithmic fashion until the upper bound of $\frac{7(\pi BW)^2}{12}$ is reached at approximately $N = 20$. To test the robustness of the waveform as the number of pulses increases, 1000 Monte Carlo simulations are performed with 4 MHz of total bandwidth at approximately 30 dB preprocessing SNR and duration of 500 μs sampled at 25 MHz. This is to emulate what is achievable by the measurements in the following section. The simulated results as a function of the number of pulses, N , can also be seen on the Fig. 3.28(a) while a plot of the simulation with a fixed N and variable SNR can be seen in Fig. 3.28(b).

The uncertainty in velocity follows the same derivation in Section 2.2.2 where the time characteristics of a rectangular pulse train used as an envelope are the same as the SFW and results in

$$\sigma_v^2 \geq \frac{c^2}{4f_c^2 \pi^2 [T_r^2 (N^2 - 1) + T^2]} \text{SNR} \quad (3.86)$$

A comparison of the beneficial attributes of the TTSFW in comparison to the waveforms derived in Chapter 2 can be seen in Table 3.2.

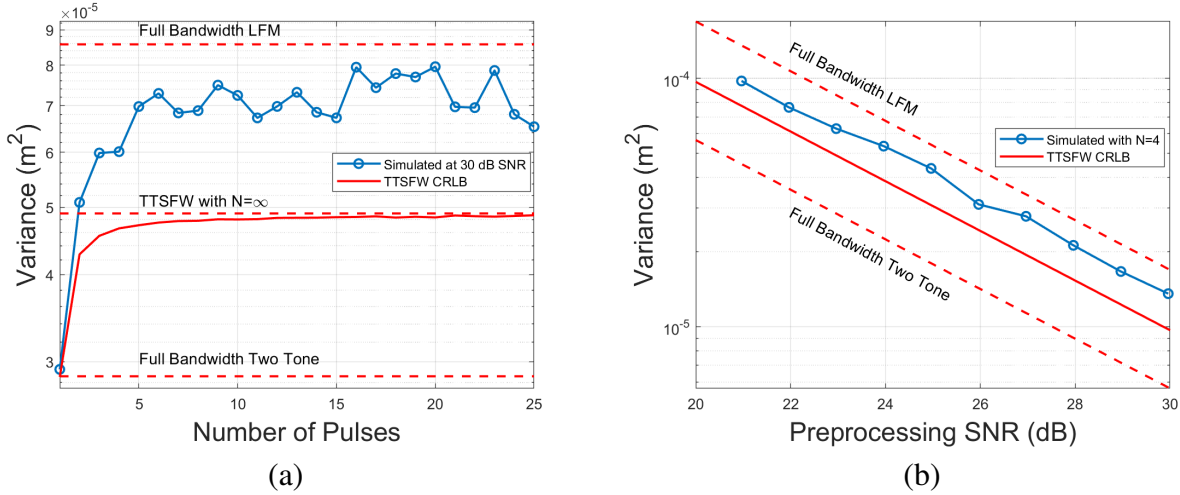


Figure 3.28: (a) The bounds and simulation of TTSFW vs. number of pulse with 4 MHz of bandwidth total bandwidth and 30 dB preprocessing SNR. (b) The bounds and simulation of TTSFW vs. SNR with the pulse number fixed to $N = 4$.

Table 3.2: Comparison of discussed waveform attributes

Rank based on CRLB (lowest to highest)	Waveform	Scalable	Unambiguous
1	Full Bandwidth Two Tone	No	No
2	TTSFW	Yes	Yes
3	PTTW	Yes	No
4	Full Bandwidth LFMW	No	Yes

3.4.3 Measurements

3.4.3.1 Waveform Properties

A comparison test for the accuracy of the TTSFW and the PTTW was performed using an Ettus X310 software defined radio (SDR) which has an operational bandwidth of 10 MHz – 6 GHz, and an instantaneous bandwidth of 160 MHz. The SDR interfaces with a host computer through a 10 GHz Ethernet cable and is processed using LabView. Due to processing rate limitations the sampling rate of the SDR is confined to 25 MHz. To ensure that the resulting matched filter digitization is too coarse, both waveforms are taken to have equivalent pulse bandwidth Δf to be

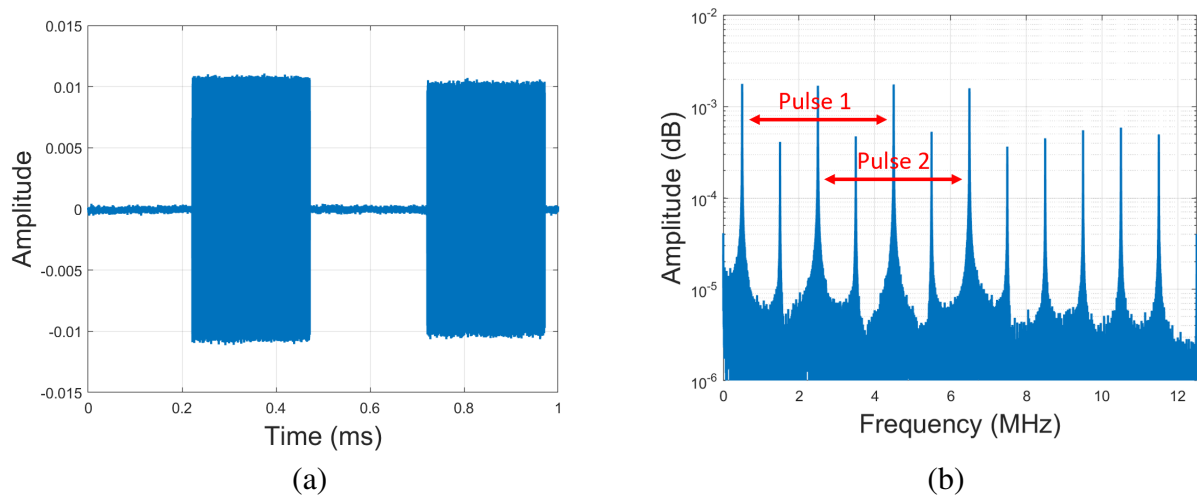


Figure 3.29: (a) Measured two pulse TTSFW in time domain. (b) Two pulse TTSFW in the frequency domain.

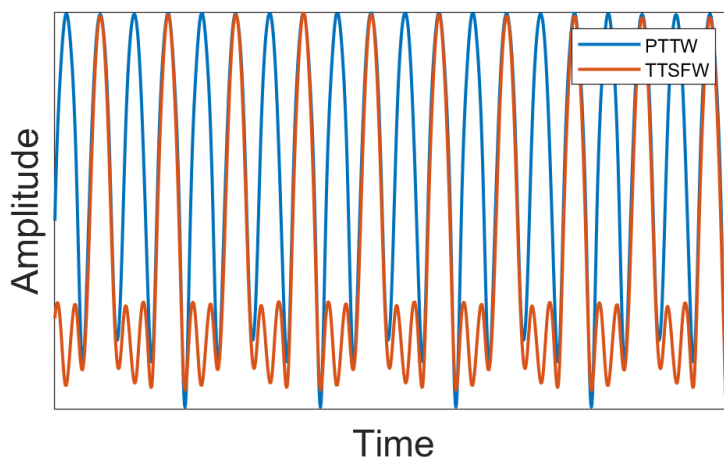


Figure 3.30: Measured matched filter output of the PTTW and TTSFW waveforms produced on the X310 using two pulses

4 MHz and a pulse duration of 1 ms with duty cycle of 50%. To confirm that both waveforms have the same integration time of 0.5 ms, the time is split into two equal 0.25 ms pulses of the TTSFW. The corresponding bandwidth Δf for the TTSFW is 2 MHz which means that every other lobe of the the PTTW is notched out. An image of the TTSFW in the time domain and in the frequency domain can be seen in Fig. 3.29 and an image of the comparison of the matched filter outputs of the TTSFW and PTTW can be seen in Fig. 3.30.

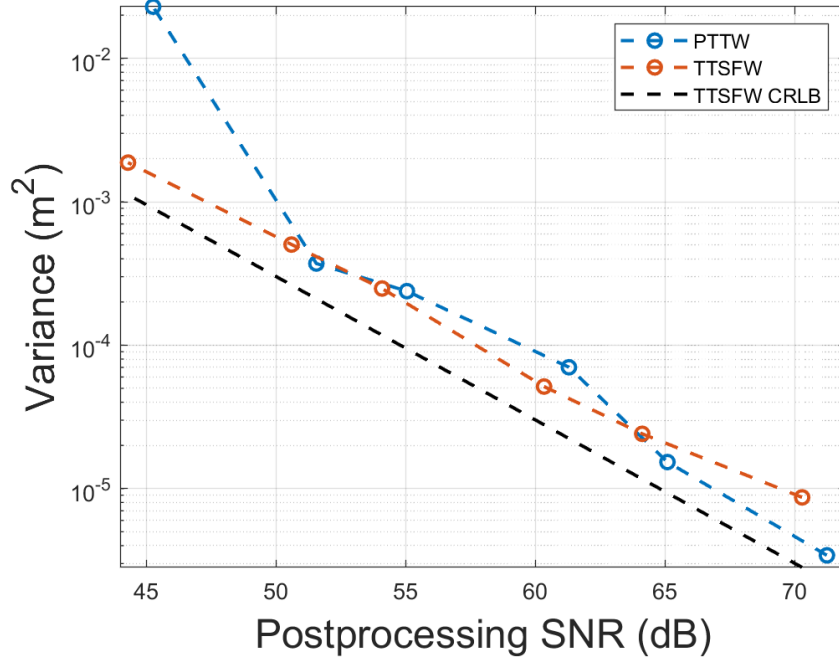


Figure 3.31: Comparison of variance of PTTW and TTSFW with equal Δf to the CRLB of the TTSFW.

Measurements are taken using a loopback architecture, where the transmit channel on the SDR is connected directly to the receive channel via a SMA cable. The received waveform is passed through a matched filter and then interpolated eight times using a built-in LabView spline function to improve the accuracy of the measurement. The interpolation was limited to 8 due to processing limitations and the desire to keep the processing running real-time. Increased latencies resulted in dropped packets, leads to incorrect measurements. The peak of 100 matched filter outputs are recorded and averaged together. The received signal SNR is estimated using the eigenvalue decomposition approach for Section 2.1.4. The processing gain resulting from using the matched filter for the case of $T = 0.5$ ms and a receiver bandwidth of $BW_r = 12.5$ MHz is 38 dB. A comparison of the variance of the two pulse TTSFW and a PTTW with equivalent Δf vs the derived CRLB for the TTSFW in (3.83) can be seen in Fig. 3.31. The variances are comparable indicating that the accuracy obtained by the TTSFW is equivalent to that of the PTTW with equal Δf .

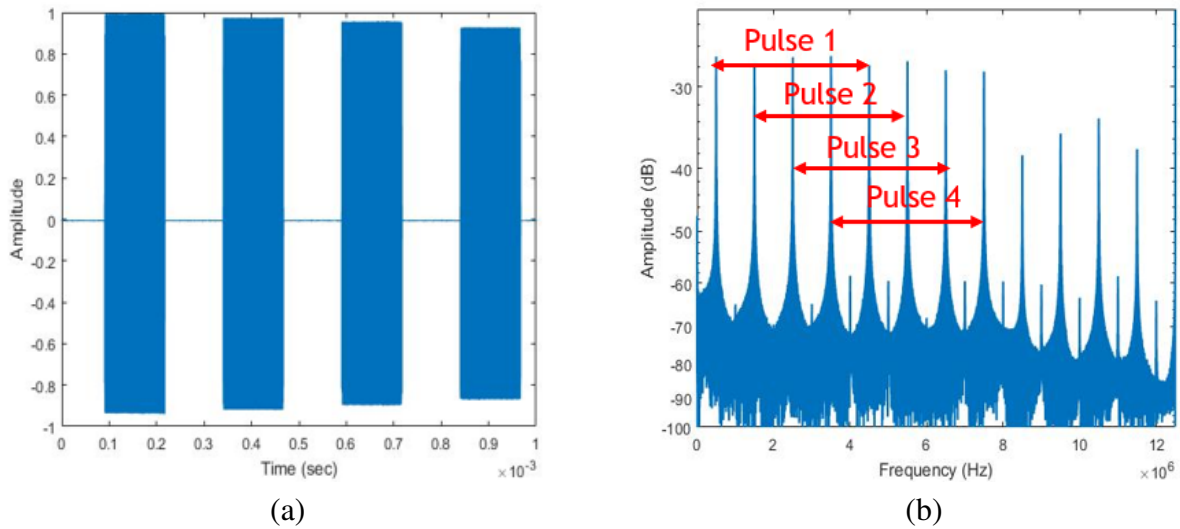


Figure 3.32: (a) Measured four pulse TTSFW in time domain. (b) Four pulse TTSFW in the frequency domain.

3.4.3.2 Wireless Ranging Measurements

Wireless ranging measurements are taken on a 24 ft semi-enclosed arch range with a corner reflector or an SDR-based active repeater placed in the middle of the range. Horn antennas are placed on the edge of the arch using a wideband (2 – 12 GHz) standard gain horn antenna as the transmitter and a narrowband (3.5 – 5.5 GHz) standard gain horn antenna as the receiver. An Ettus X310 SDR is used to create the TTSFW. The horn antenna have greater directivity at higher frequencies which helps with multipath error from the lab environment. For this reason the center frequency is chosen to be 5.25 GHz due to the limiting bandwidth of the narrowband horns.

The ranging waveform consists of a four-pulse TTSFW with each pulse bandwidth equal to $\Delta f = 4$ MHz and increasing $\delta f = 1$ MHz with every consecutive pulse. The sampling frequency is chosen to be 25 MHz which is the highest obtainable stable sample rate with the equipment setup. The total waveform duration is 1 ms, in which each pulse has a duration of $250 \mu\text{s}$ and a duty cycle of 50%. These waveforms have a preprocessing SNR of approximately 30 dB. An image of the waveform in the time domain and frequency domain can be seen in Fig. 4.1. The disambiguation properties of the four pulse waveform can be seen in Fig. 3.33.

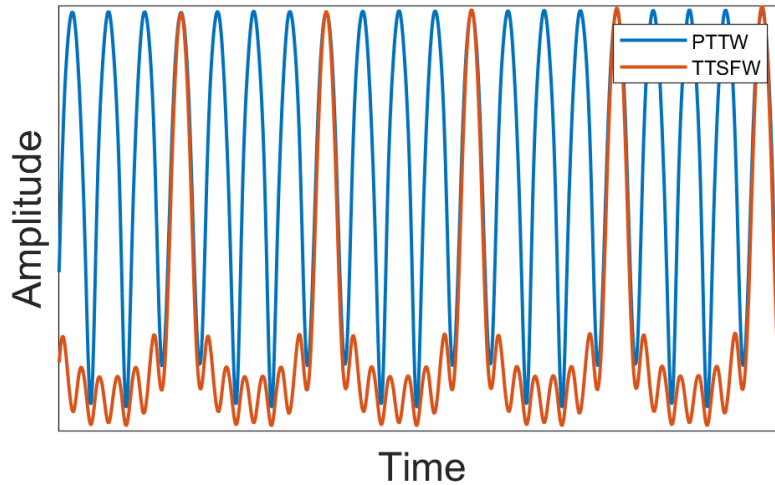
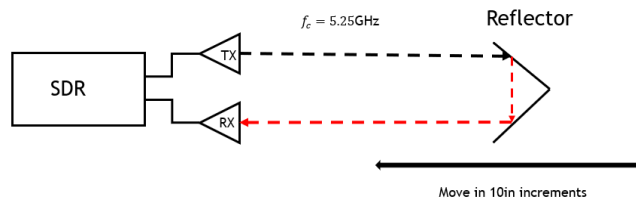


Figure 3.33: Measured matched filter output of the PTTW and TTSFW waveforms produced on the X310 using four pulses.

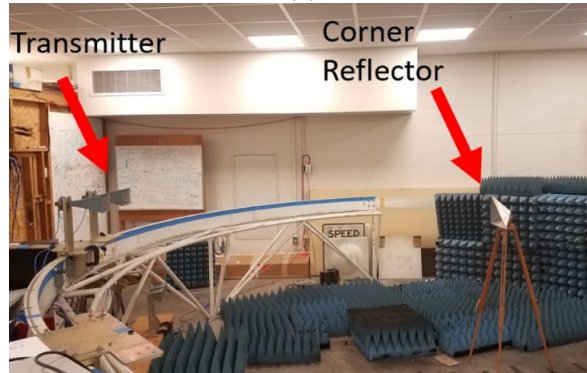
The first measurement is taken using a single SDR transmitting to a corner reflector. This experiment is representative of a single secondary node where a secondary node determines its relative range to a single point in the array. The corner reflector is placed at the far end of the range (15 ft from the transmitter) and moved 10 ft towards the transmitter in 10 in increments. The return waveform is then passed through the matched filter and interpolated 8 times to improve the accuracy. The peak of the matched filter is then selected by using a simple peak finding operation since the properties of the TTSFW take care of the disambiguation. At each distance 100 matched filter peaks are averaged together.

After the measurement is taken and the position values are computed, a simple post-processing calibration procedure is implemented to account for any static delays that are inherent to the system. The calibration procedure is performed by taking the average of the differences between the expected value and the measured value at each point and subtracting this average from all points. An image of the performance of a single SDR can be seen in Fig. 3.34.

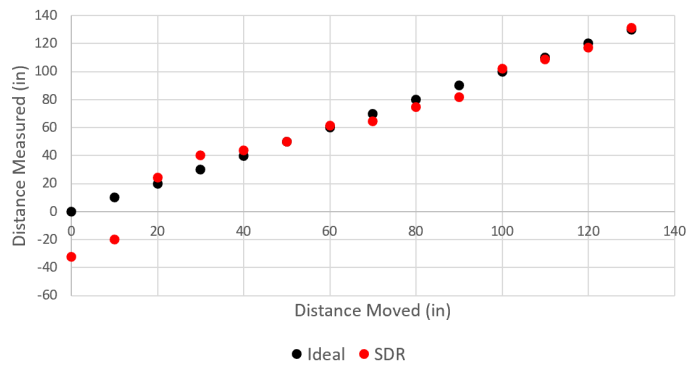
The second measurement is to test the performance of multiple SDRs ranging to a corner reflector simultaneously. This experiment is representative of two secondary nodes performing simultaneous ranging. To do this measurement, all of the experiment parameters from the single



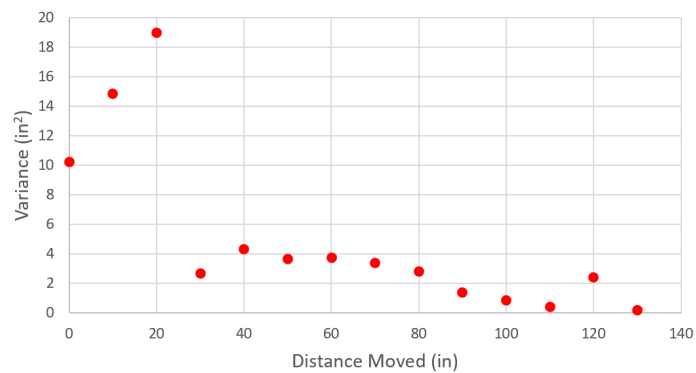
(a)



(b)



(c)

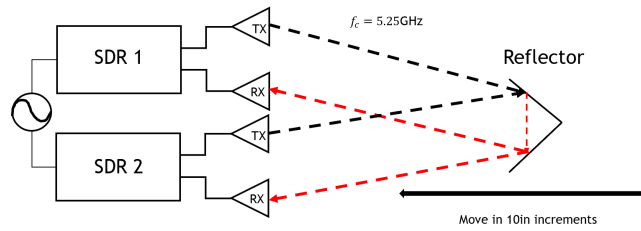


(d)

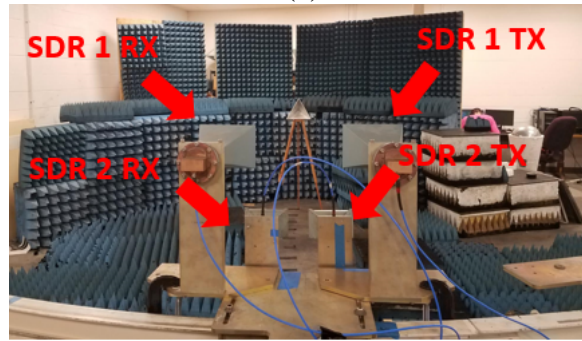
Figure 3.34: (a) Schematic of single SDR in the arch range. (b) Image of experimental setup. (c) Range Measurement results. (d) Variance of measurement.

SDR case remained the same, however two separate SDRs and sets of horn antennas are used. The reference oscillators of the two SDRs are locked via cable; in future work this will be implemented with a wireless link. The two sets of antennas are placed in the same area at different elevations. The waveforms used by two SDRs contains the same set of frequencies but where the first SDR steps up in frequency, the second steps down in frequency, implementing the different step cycles mentioned in the previous section. This results in no interference between the waveforms, and in turn allows for no needed coordination of the waveform start times between the SDRs. An image of the performance of both SDRs can be seen in Fig. 3.35.

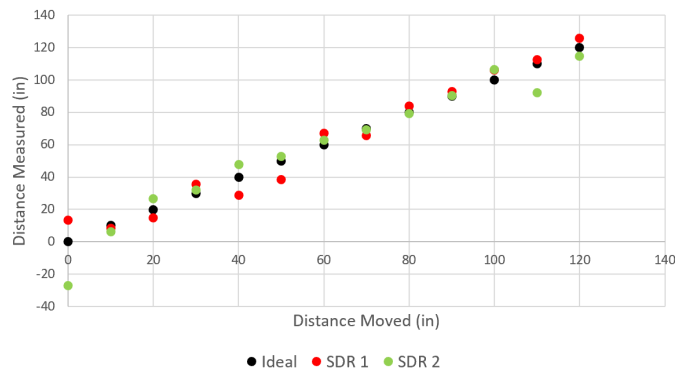
The third measurement is conducted to demonstrate the scalability of the waveform to three separate SDRs. The corner reflector is removed from the setup and replaced by an SDR acting as an active repeater that captures the incoming signals and retransmits them with increased gain. This helps to increase the SNR of the received signals by changing the signal decay from $\frac{1}{r^4}$ to $\frac{1}{r^2}$ due to the retransmit gain, and further reduce the effects of multipath. This experiment is representative of two secondary nodes ranging to a primary node which here is given by the repeater. In a fully distributed array this primary node would be sending out the reference beamforming signal in which the secondary nodes, now with knowledge of the distance to the primary, phase adjust their output creating a coherent system. The center frequencies of transmit and receive are separated to also help with multipath issues. The two SDRs on the side of the range are transmitting at 5 GHz and the repeater responds at 5.25 GHz. The performance at each distance can be seen in Fig. 3.36. Clearly, the ranging waveform produces accurate range measurements, below 1 in² variance for multiple nodes simultaneously. The achieved ranging accuracy of $\sigma_x = 8.03$ mm (or 0.1 in²) enables coherent transmission up to 2.49 GHz in a two-way ranging measurement, following from the requirement that the error is within $\frac{\lambda}{15}$ of the coherent transmission signal.



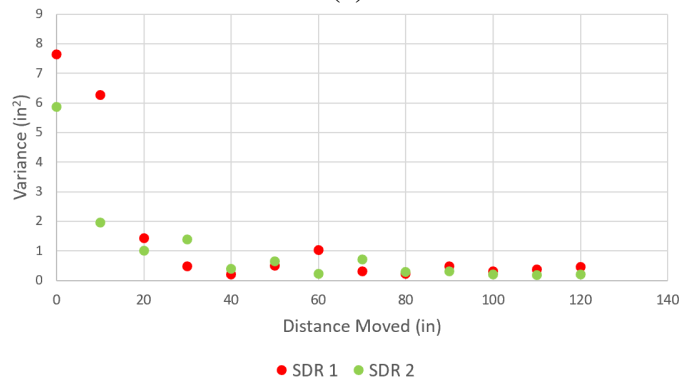
(a)



(b)

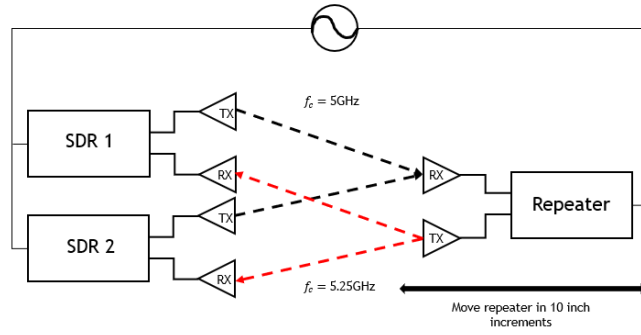


(c)

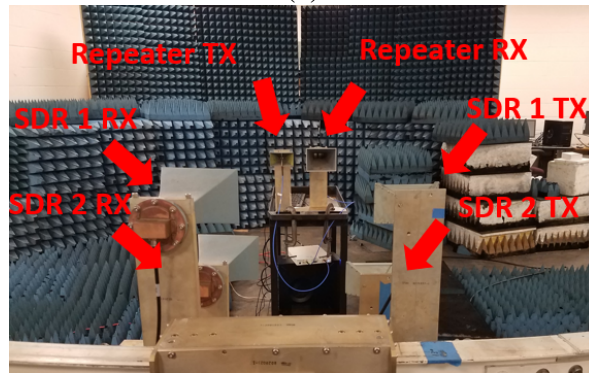


(d)

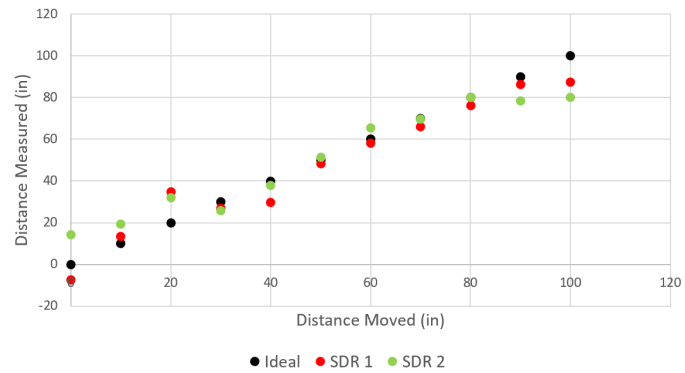
Figure 3.35: (a) Schematic of two SDRs in the arch range. (b) Image of experimental setup. (c) Range Measurement results. (d) Variance of measurement.



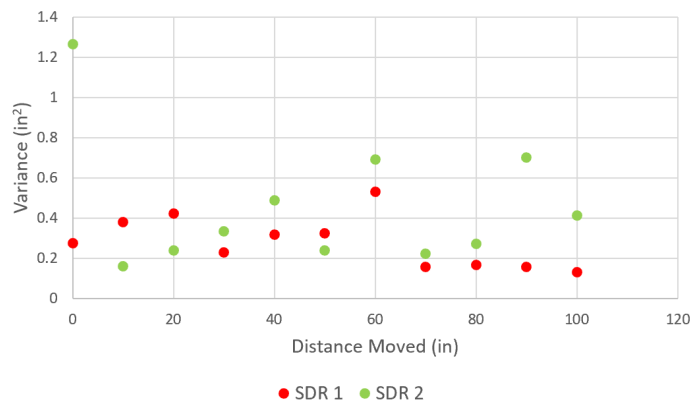
(a)



(b)



(c)



(d)

Figure 3.36: (a) Schematic of three SDRs in the arch range. (b) Image of experimental setup. (c) Range Measurement results. (d) Variance of measurement.

3.5 Comparison to Traditional Wideband Ranging Methods

Traditional hardware-based approaches to high-accuracy ranging entail the use of wideband waveforms such as frequency modulated continuous wave (FMCW) waveforms or pulsed LFMW. The accuracy of the estimate of the delay (range) does scale inversely with increasing bandwidth, as indicated by (2.12) and (2.11), however the waveforms typically used for millimeter-scale ranging use bandwidths of hundreds of MHz or even GHz, which generally increase cost and can lead to non-idealities such as passband ripple or increased insertion loss from wideband impedance matching. In contrast, spectrally-sparse waveforms like those demonstrated herein can be implemented with individually narrow-band hardware channels, easing cost and reducing some of the undesirable hardware imperfections of wideband systems. The receiver hardware can also be simplified by leveraging the spectrally sparse nature of the waveforms; the ability to subsample spectrally sparse signals with a low-rate digitizer and digitally reconstruct the waveform to achieve sub-mm ranging accuracy has been previously demonstrated [52].

High-accuracy ranging is typically approached by using wideband waveforms which achieve both good resolution and good accuracy. While resolution is dependent on overall bandwidth, the accuracy is dependent on the mean-square bandwidth as shown earlier, and as such the accuracy can be improved with spectrally-sparse waveforms [86]. Commonly used waveforms include FMCW and ultra-wideband (UWB) waveforms. A one-dimensional high-accuracy ranging system was developed using FMCW waveform in [112] with a ranging standard deviation of 0.1 mm. The waveform had 2 GHz bandwidth with 2 ms sweep time at a center frequency of 75 GHz, with range estimates averaged over 2000 samples, increasing the SNR by 16.5 dB. This system was tested for a distance up to 1.43 m in an anechoic chamber. Three-dimensional ranging was implemented in [113] using UWB waveforms with a frequency range of 5.4 to 10.6 GHz, demonstrating dynamic tracking with a root mean square error (RMSE) of 5.24 mm, and static positioning RMSE of 1.98 mm using averaging over 106 samples. An accuracy of 0.1 mm was also reported for other short-range localization radars [114, 115]. Other radars using smaller bandwidths yielded less accurate measurements, e.g. in [116] a waveform with 500 MHz bandwidth

was used on a center frequency of 23.75 GHz to achieve a range resolution of 30 cm.

Compared to traditional ranging methods, the use of spectrally-sparse waveforms has benefits not only in terms of accuracy, but also hardware implementation; as described later, the challenge of implementing instantaneously wideband signals in hardware is alleviated with the use of only a few frequency tones. In particular, the basic two-tone ranging approach enables direct scalability, by changing the separation of the two signal tones. Previously, the ability to estimate range with 0.3 mm accuracy using only two frequency tones separated by up to 4 GHz was demonstrated [117]. A comparison of the results of my approaches with the literature using a figure of merit (FOM) aimed at including the benefits of spectral sparsity and ranging accuracy. The FOM is defined as the *accuracy per unit occupied bandwidth*, or the product of the waveform bandwidth, spectral occupancy (the fraction of the total bandwidth occupied by the waveform), and ranging accuracy. The FOM and other parameters are compared in Table 3.3. The spectral occupancy is calculated by the fraction of the bandwidth of the waveform tones relative to the total bandwidth (i.e. $\frac{1}{T}$).

Table 3.3: Comparison of Waveform Performance

Ref.	Waveform	Bandwidth (MHz)	Spectral Occupancy (%)	Range Accuracy (mm)	FOM ^a (mm/MHz)
[112]	FMCW	2000	100	0.1	200
[113]	UWB	5200	100	5.24	27,248
[114]	FMCW	2000	100	0.1	200
[115]	Spread Spectrum	3120	100	0.1	312
[116]	FMCW	500	100	300	150,000
S. M. Ellison	Range-Doppler	120	0.83	3.1	3
S. M. Ellison	Joint Range-Frequency	200	0.75	4.7	7
S. M. Ellison	Rad-Comm	160	18.75	1.9	57
S. M. Ellison	TTSFW	6	0.27	8.03	0.13

^aFOM = bandwidth × spectral occupancy × range accuracy

CHAPTER 4

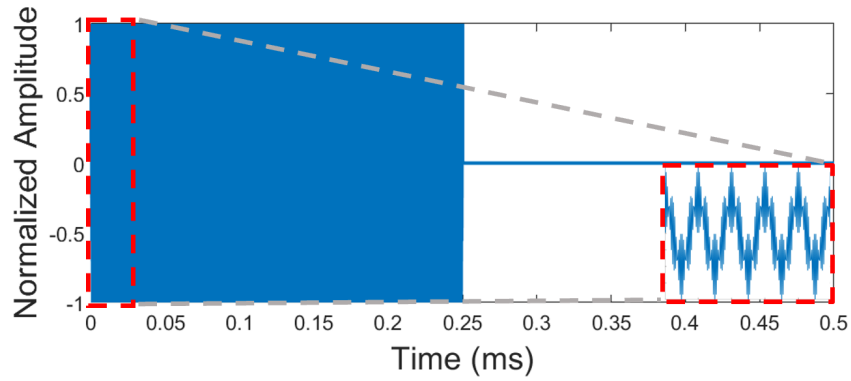
DEMONSTRATION OF WIRELESS PHASE ALIGNMENT IN DISTRIBUTED BEAMFORMING

In this chapter I demonstrate a two- and three-node open-loop coherent distributed beamforming system consisting of one primary node and one to two secondary nodes. To estimate the internode ranging (i.e. the term d in (2.15)) in the Section 2.2.3, I investigated the use of spectrally-sparse waveforms for high-accuracy ranging, showing that a two-tone waveform obtains near-optimal ranging accuracy. Addressing the ambiguity and scalability challenges that arise with a simple two-tone waveform, I developed a TTFSW in Section 3.4. This chapter expands on the prior derived waveform, TTFSW, to enable arbitrary beamforming in an distributed open-loop sense by implementing the range estimations to maintain phase alignment for a dynamic array operating with a continuous wave beamforming signal at 1.5 GHz.

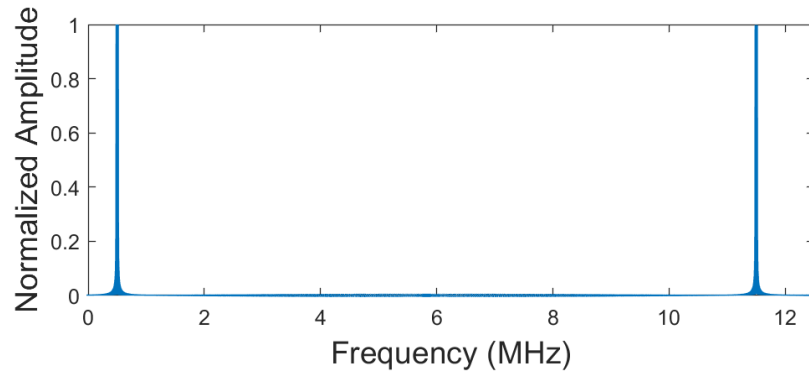
4.1 Range Estimation Waveform

Due to the need for scalability the TTFSW is used. In the case of a two-node array, consisting of a primary node and a single secondary node, only a single pulse $N = 1$ is required since only a single unique connection is made. Fig. 4.1 shows an example implementation of this waveform in the time and frequency domains. For this case the baseband waveform has a duration of 1 ms with a 50% duty cycle and frequencies $f_1 = 500$ kHz and $f_2 = 11.5$ MHz, which matches the bandwidth that has been demonstrated to obtain high ranging accuracy from Section 3.4.

In the case of a three-node array, consisting of a primary node and two secondary nodes, there are two unique connections and therefore a multipulse waveform is required such that $N \geq 2$. I demonstrate here a waveform supporting more than three nodes, with $N = 5$ to illustrate the scalability. An image of the waveform in the time domain and frequency domain can be seen in Fig. 4.2. The time duration of the baseband waveform was $200 \mu\text{s}$ per pulse with a 50% duty cycle, frequencies $f_1 = 500$ kHz and $f_2 = 5.5$ MHz, and a step size of $\delta f = 1$ MHz. To ensure that



(a)



(b)

Figure 4.1: Measured waveform supporting ranging between two nodes: (a) time domain; (b) frequency domain.

each connection has a unique pulse signature, one secondary node begins its waveform with the pulse containing the lowest frequency pair of tones and increases the frequency by the frequency step, while the second secondary node begins with the pulse with the highest frequency pair and decreases the frequency by the frequency step; this approach to unique pulse-to-pulse signatures per node is easily extendable. The pulse labels in Fig. 4.2(b) given by Pulse $a - b$ indicate the pulse order relative to the secondary such that the index a is associated with secondary node one while b is associated with secondary node two.

4.2 Ranging Requirements for Open-Loop Distributed Beamforming

Inherent uncertainty is present in any system that attempts to estimate a parameter due to the presence of random noise. A measure of the variance or stability of an estimate of a random

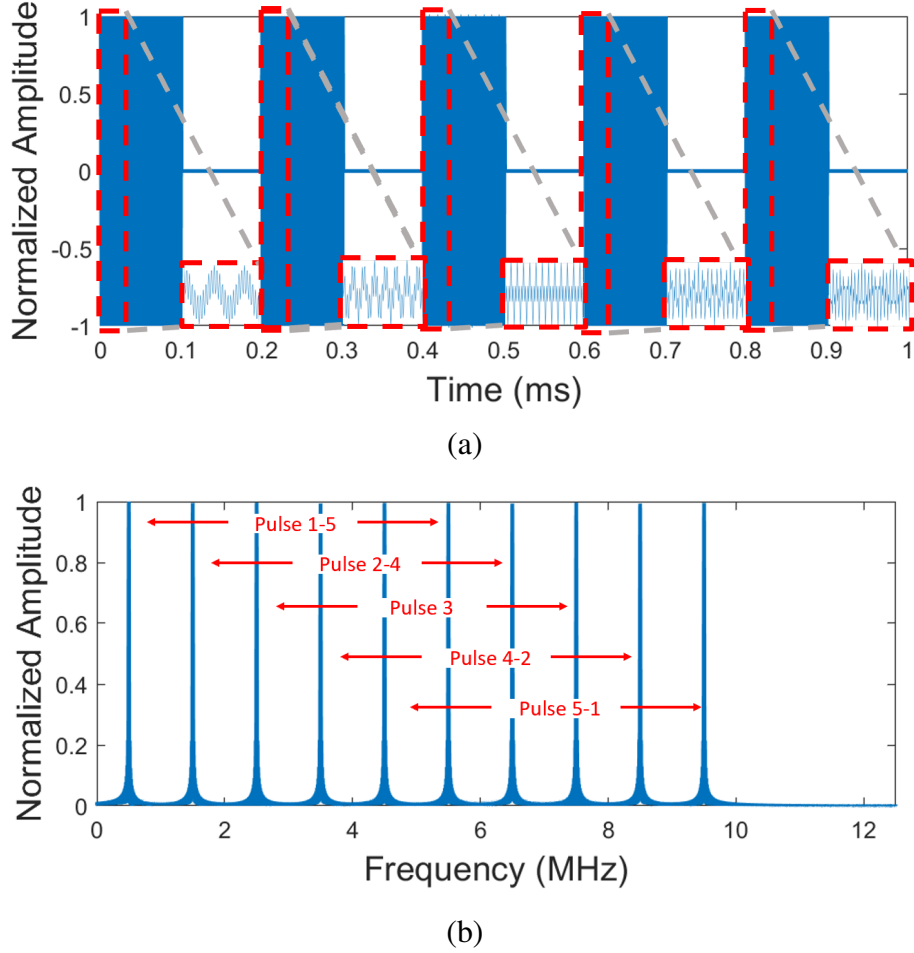


Figure 4.2: Measured waveform supporting ranging between five nodes: (a) time domain; (b) frequency domain.

variable is given by the CRLB, which for position estimation is given by (2.12). The mean-square bandwidth for the two waveforms, which will dictate the CRLB due to this waveform inherently having a zero first moment in both domains, with the aforementioned parameters yields

$$\zeta_{f,2 \text{ node}}^2 \Big|_{N=1} = \pi^2 BW^2 = 1.942 \times 10^{15}$$

$$\zeta_{f,3 \text{ node}}^2 \Big|_{N=5} = \frac{507\pi^2 BW^2}{1000} = 6.0547 \times 10^{14}$$

The lower bound on delay estimation for the two waveforms can now be evaluated considering an SNR of 30 dB; this closely matches that can be obtained in typical cooperative ranging techniques. Note that, unlike a traditional radar ranging measurement which undergoes propagation losses in both directions, the cooperative ranging only suffers losses in one direction, with the

primary node repeating the signal with added gain. Thus, relatively high SNR values are feasible. The processing gain resulting from the matched filter process is equivalent to the time-bandwidth product of $NTBW_r$, where T is the non-zero time duration of the pulse, N is the number of pulses, and BW_r is the receiver noise bandwidth which for this work, since no additional filtering outside the analog bandwidth of the system is used, is equal to the sampling bandwidth of 12.5 MHz.

For the two node experiment, $T = 250 \mu\text{s}$, thus the processing gain is 35 dB resulting in a post processing SNR of 65 dB. Using (2.12) the bound on the accuracy of a two-way measurement is $\sigma_x = 2.44 \text{ mm}$. The distance uncertainty sets the maximum operation frequency that can be achieved by

$$f \leq \frac{c}{20\sigma_x} \quad (4.1)$$

where σ_x is the standard deviation of the two way distance measurement and the factor of 20 derives from the coherent gain statistical analysis for the end-fire array configuration for Section 2.1.3. For this case the resulting maximum frequency is limited to $f_{2 \text{ node}} \leq 6.14 \text{ GHz}$.

For the three node experiment, NT resulting from the summation of all the pulses was equal to $500 \mu\text{s}$, yielding a processing gain of 38 dB resulting in a post processing SNR of 68 dB. The distance estimation accuracy can then be calculated using (2.12) and is equal to $\sigma_x = 2.42 \text{ mm}$. The maximum operational frequency for the three node is thus derived to be $f_{3 \text{ node}} \leq 6.18 \text{ GHz}$.

4.3 Range Estimation Refinement for Node Motion

Phase alignment of the beamforming signals to produce a phase coherent system at the target destination is performed by estimating the range between the primary node and the corresponding secondary node and applying the appropriate phase shift. For this experiment, the ranging signal is transmitted from the secondary node(s) to the primary node where a repeater captures the signals and retransmits. Thereby, the propagation losses are proportional to $\frac{1}{r^2}$ rather than $\frac{1}{r^4}$ which is seen by typical radar measurements. The center frequencies of the transmit and receive of the repeater are separated by 1 GHz. This ensures that the desired signal dominate any

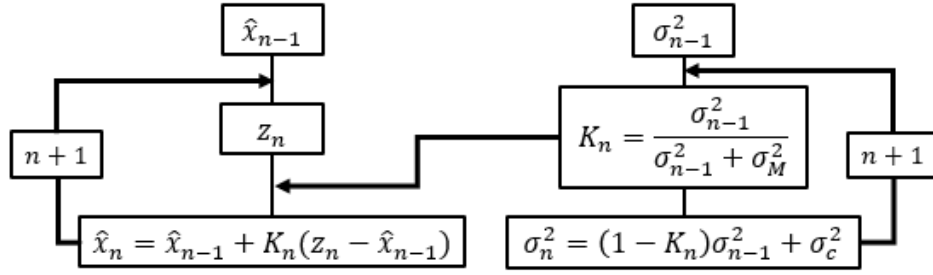


Figure 4.3: Block diagram of the Kalman filter used for range estimation refinement with moving nodes.

multipath and any crosstalk can be neglected. After the signal is received, the secondary node estimates the time of flight by matched filtering the return signal. The peak of the matched filter is spline interpolated in real-time in LabView with 1000 points to avoid discretization errors.

The matched filter output peak value is tracked using a 1-D Kalman filter. A Kalman filter gives the optimal state estimation for linear systems in the presence of Gaussian noise [118]. The model of the filter, shown in Fig. 4.3, is

$$\hat{x}_n = \hat{x}_{n-1} + K_n(z_n - \hat{x}_{n-1}) \quad (4.2)$$

where \hat{x}_n is the prediction of the current state, \hat{x}_{n-1} is the prediction of the previous state, z_n is the measurement at the current state, and K_n is the current state Kalman gain given by

$$K_n = \frac{\sigma_{n-1}^2}{\sigma_{n-1}^2 + \sigma_M^2} \quad (4.3)$$

where σ_{n-1}^2 is the previous state uncertainty and the measurement variance $\sigma_M^2 = 3 \times 10^{-5}$ is determined by measuring the variance of 1000 peak values. The current state uncertainty is then updated by

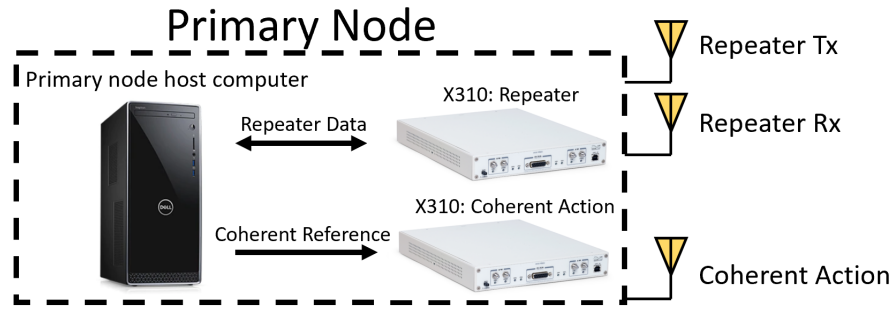
$$\sigma_n^2 = (1 - K_n)\sigma_{n-1}^2 + \sigma_c^2 \quad (4.4)$$

where an additional constant uncertainty of $\sigma_c^2 = 5 \times 10^{-6}$ is added to model the array dynamics. This added uncertainty is used to model the internode range of the system as a constant value with a small, random perturbation to account for both positive and negative radial motion. The

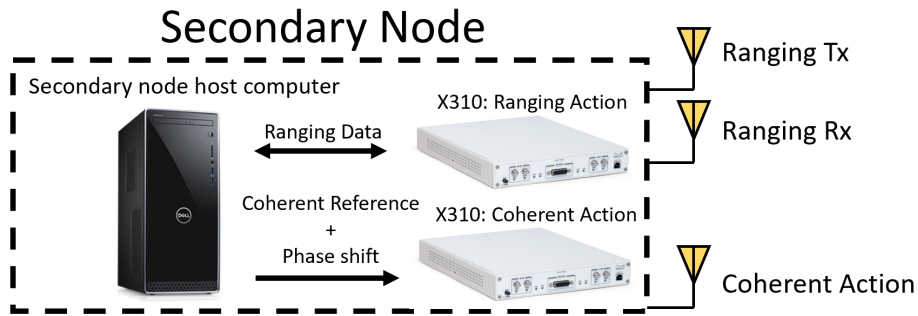
experiments in the following section have induced motion that is proportional to the coherent frequency wavelength of the 1.5 GHz (20 cm), which is roughly 2% of the sampling interval of the matched filter at 25 MHz (12 m). Since this induced motion is very small compared to the discretization of the matched filter, this motion acts like a fluctuation on an otherwise constant value and therefore a 1-D Kalman filter is sufficient. However, if the motion is much larger than a fraction of the matched filter sampling rate, resulting in discontinuities in the matched filter output, the Kalman filter will diverge. If this is the case, other techniques such as a higher dimensional Kalman filter, such as an EKF [119–121] to linearize the discontinuities or an unscented Kalman filter (UKF) [122–124], may be needed. The time delay estimate found from the output of the Kalman filter is then converted to a phase shift of the operational frequency. This phase shift is then applied to the beamforming carrier signal on the secondary node. Thus, as the primary and secondary change their relative positions, the outputs remain phase locked at the target location.

4.4 Distributed Antenna Array and Open-Loop Distributed Beamforming Experiments

The architecture investigated in this work is based on a single primary node and multiple secondary nodes. As the objective is to demonstrate the ability to simultaneously measure internode range between multiple nodes with sufficient accuracy to support beamforming, a continuous-wave transmitted signals is used, and the reference oscillators are locked via cable. Wireless frequency alignment can be implemented in various ways for a fully wireless system including: an adjunct self-mixing circuit [34, 125]; two-way time transfer [126, 127]; reference broadcast synchronization [128]; timing synch protocol for sensor networks [129]; flooding time synch protocol [130]; and ultra wideband pulse time of arrival [131–133]. An image of the block diagram of the primary and secondary nodes can be seen in Fig. 4.4 (a) and (b) respectively. Each node consisted of two Ettus X310 SDRs, each of which are connected to one host computer running Windows 7 with 32 GB of RAM via 10 GB Ethernet cables. The X310s utilize two UBX 160 daughterboards which have operational bandwidths from DC to 6 GHz with an instantaneous



(a)



(b)

Figure 4.4: Block diagrams of the nodes.

bandwidth of up to 160 MHz. These daughterboards support complex up- and down-conversion for in-phase and quadrature mixing as well as internal amplification equivalent to 30 dB and 33.5 dB for the transmit and receive sides, respectively. A block diagram of the X310 RF chain can be seen in Fig. 4.5. The SDRs interface with the host computer using LabVIEW 2018 where a maximum sampling rate of 25 MHz is possible and is limited by the data throughput between LabVIEW and the SDRs, restricting the maximum achievable instantaneous bandwidth to 12.5 MHz.

One SDR on each node transmits the beamforming signal while the second SDR is used to either implement ranging to the primary node, or to capture and retransmit any incoming ranging signals from the secondary nodes. Each secondary node transmits a version of the ranging waveform with a distinct stepped-frequency pattern. The primary node repeats any incoming signals in a continuous manner (i.e. no time scheduling was required). Each secondary node then processes the received signal via matched filter followed by the Kalman filter refinement step. Both of the two

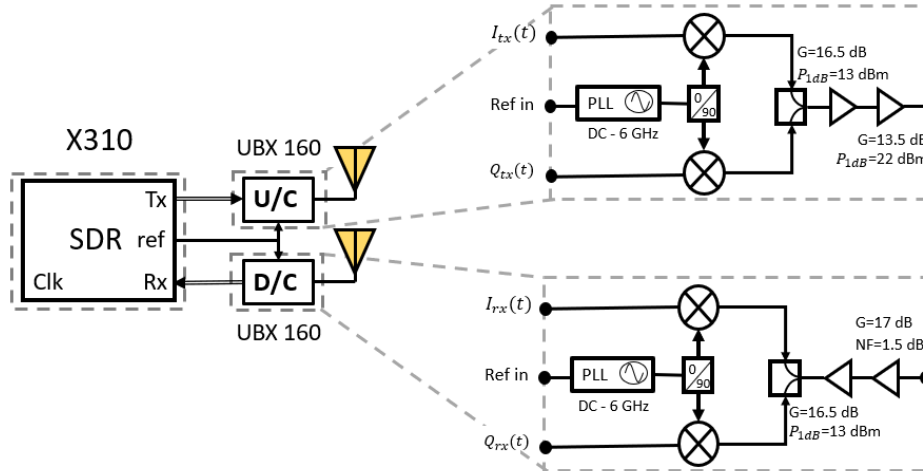


Figure 4.5: RF chain internal to each of the X310 SDRs.

and three node experiments described below yields SNR values of approximately 30 dB, which are determined using an eigenvalue decomposition approach from Section 2.1.4. The secondary nodes then calculate the range, from which the relative phase of the beamforming carrier signal is updated based on the measured range estimation.

The beamforming signals are transmitted from each node at a carrier frequency of 1.5 GHz using 1.35 – 9.5 GHz ultra wideband log periodic antennas. Transmission of the ranging signals from the secondary nodes are implemented at a carrier frequency of 4.25 GHz and, after reception at the primary node, are retransmitted at a carrier frequency of 5.25 GHz, providing frequency diversity to mitigate crosstalk and multipath. The beamformed signals are captured on a Keysight MSO-X 92004A oscilloscope. The power levels of the individual signals are also recorded at each location by selectively turning on individual transmitters.

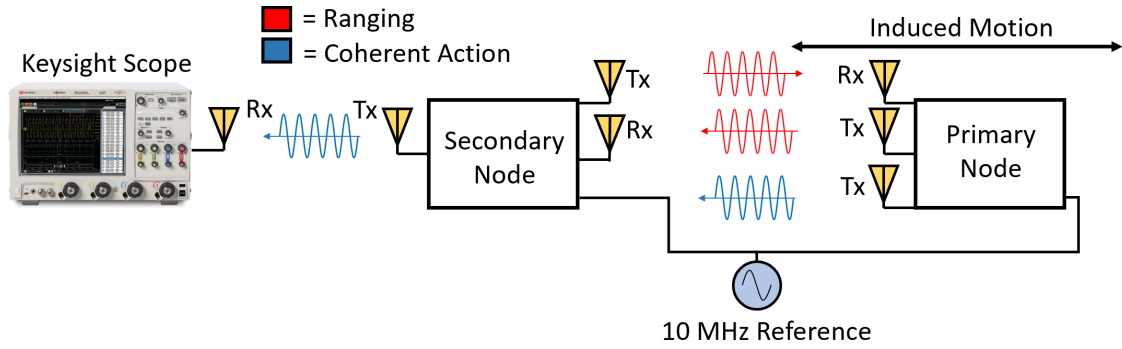
4.5 Two-Node Experiment

Two experiments are conducted, one with two transmitting nodes and one with three transmitting nodes. In both cases the arrays are steering to the end-fire direction. The primary node is moved in both experiments, inducing relative phase errors between all nodes that is corrected via range estimation. An initial calibration procedure is implemented by adjusting the phases of

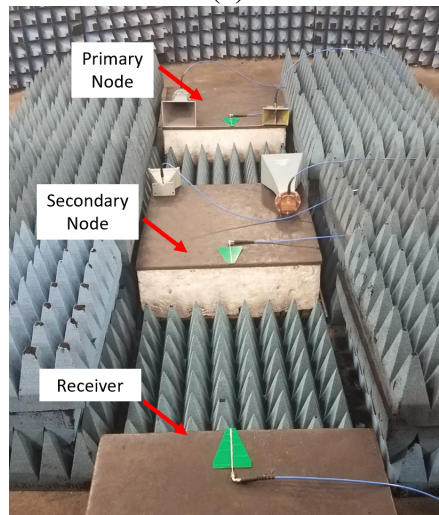
the transmitted signals until maximum gain is obtained; after this point no adjustment is performed aside from that implemented by the ranging system. The calibration procedure effectively amounts to calibration of the phase delays present in each node, and can reasonably be implemented without monitoring the received power by using, e.g., power couplers at the transmitter outputs.

The two-node distributed array consists of a primary node and a single secondary node separated initially by a distance of 1.5 m. The receiving antenna at the destination is located at a distance of 1.5 m from the secondary node, and 3 m from the initial position of the primary node. The diagram of the setup is shown in Fig. 4.6(a), where the red colored signals indicate the ranging and the blue signals represent beamforming. Fig. 4.6(b) shows the experimental system in a semi-enclosed arch range in the laboratory. The beamforming and ranging antennas are set on foam blocks that are easily repositioned by manually sliding to different positions. Absorber is used to mitigate reflections from nearby objects that are not fully shielded by the mounted absorber in the range. The primary node is moved by hand in approximately 2 cm increments towards the secondary to simulate motion in the array for a total of 20 cm, equal to the wavelength of the beamforming frequency. At each distance 100 snapshots containing 15 cycles of the 1.5 GHz signal are captured on the scope. The resulting 1,500 peak values are averaged to give the measured amplitude at each distance.

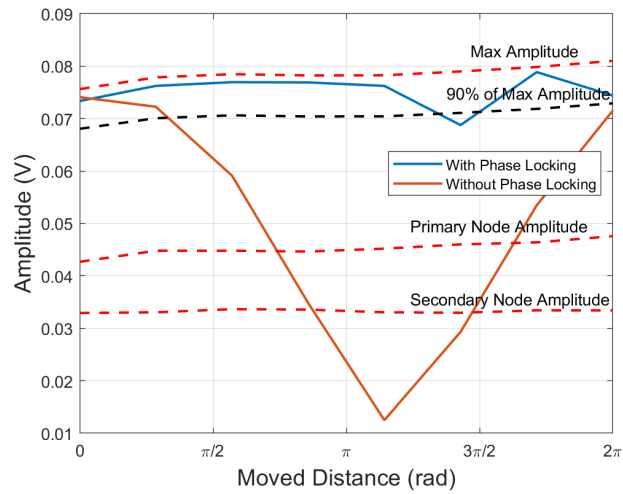
Fig. 4.6(c) shows the measured results of the beamforming experiment. The red dashed lines show the individual amplitudes of the two transmitters, as well as the ideal summation of the two signal, denoted as max amplitude, which represents the maximum possible beamformed amplitude that can be achieved with error-free phase correction. The black dashed line indicates the 90% coherent gain threshold. Two beamforming measurements are represented in the plot. The first is an uncorrected beamforming experiment where the ranging system is not utilized to update the transmission phase of the secondary node, represented by the orange curve. The signal begins initially at a high coherent amplitude value, before decreasing to a null and finally increasing again to a high amplitude value, clearly showing the constructive and destructive interference expected when no phase correction is implemented. The blue line shows the result of performing the same



(a)



(b)



(c)

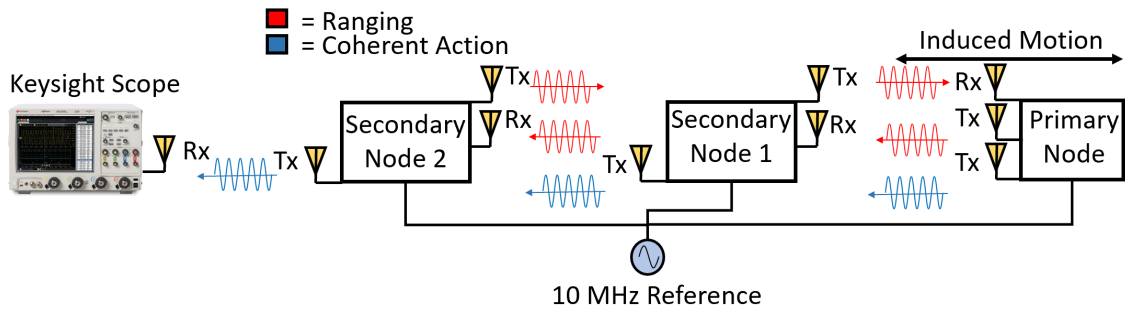
Figure 4.6: (a) Block diagram of the distributed two-node experiment. (b) Image of the experimental setup in the semi-enclosed arch range. (c) Measured results of coherent gain with and without performing range-based phase correction.

measurement with the ranging system automatically updating the phase of the beamforming signal. The phase corrected beamforming signal amplitude is close to the ideal level for the majority of the test, indicating successful beamforming when the nodes undergo relative motion.

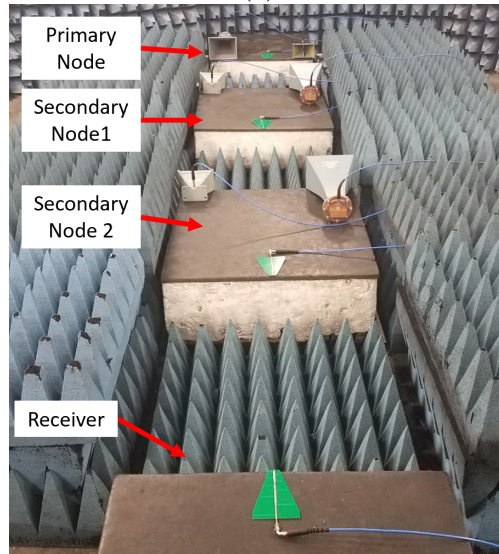
4.6 Three-Node Experiment

The two-node system is expanded upon to create a three-node open-loop beamforming system. The array is oriented in an end-fire configuration, again to demonstrate the most challenging beamforming case. A diagram of the setup is shown in Fig. 4.7(a), where the red colored signals indicate ranging and the blue signals represent beamforming. Fig. 4.7(b) shows the experimental system in a semi-enclosed arch range in the laboratory. The two secondary nodes are separated by 0.6 m, with first secondary node a distance of 1 m from the receiving antenna. The primary node starts at a distance of 1 m from the second secondary node. The two secondary nodes remain stationary, and range to the primary node, which captures and retransmits both signals. No time scheduling is used for individual measurements; the TTSFW supports simultaneous multi-node operation thus no scheduling is required. The primary node is again moved in 2 cm increments for a total of 20 cm. In the same way as the two-node experiment, at each distance 100 snapshots containing fifteen cycles of the 1.5 GHz signal are captured. The resulting 1,500 peak values are again averaged to give the measured amplitude at each distance.

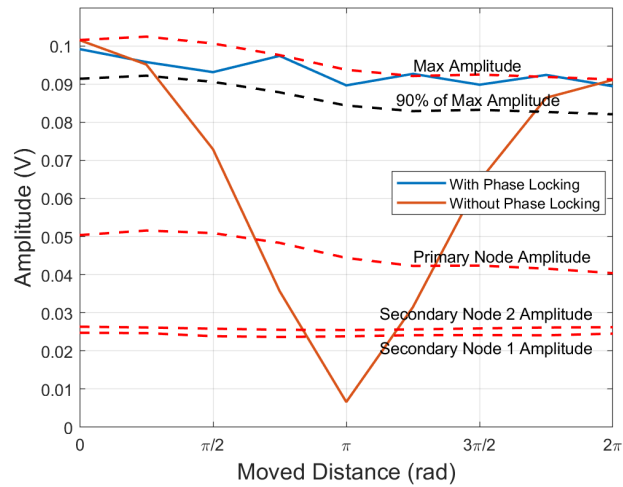
The measured results of the three-node experiment are shown in Fig. 4.7(c). Here the two secondary node individual powers are again constant resulting from their stationary positions. The uncorrected beamforming measurement showed a clear null, dropping to 7% of the available total power when the primary node location causes destructive interference. When the ranging system is utilized, the system maintains a high-gain beamforming signal, achieving a coherent power level consistently above the 90% threshold. The amplitude of the beamforming signal closely matches the ideal level, indicating successful beamforming of a three node system when undergoing relative node motion.



(a)



(b)



(c)

Figure 4.7: (a) Block diagram of the distributed three-node experiment. (b) Image of the experimental setup in the semi-enclosed arch range. (c) Measured results of coherent gain with and without performing range-based phase correction.

CHAPTER 5

APPLICATION OF PHASE ALIGNED COHERENT DISTRIBUTED ARRAYS

Phases arrays have advantageous properties when it comes to communication, namely they maximize power transfer in a desired direction. However, traditional phased array architectures also transmit power, and therefore information, to undesired directions through sidelobes. This information can be recovered by an eavesdropper with a sufficiently sensitive receiver. The array sidelobes are inherent to the system and created through the array design. Past works have addressed the mitigation of sidelobe energy with unique array configurations designed through numerical optimization. However, this technique has limited functionality due to the inability to fully eliminate sidelobe energy, and therefore the information can still be recovered by eavesdroppers. To combat the drawbacks faced by traditional phased arrays, time modulated arrays are designed to change array characteristics over time, which provides another degree of freedom. These arrays present a method for improved communication security as well as the ability to provide multiple independent data streams to different locations enabling signals utilizing on-off keying [134], frequency shift keying [135], pulse-position modulation [136], or amplitude- and phase-based modulations [69, 70]. Types of time modulated arrays include: parasitic arrays where driven elements are loaded by switching parasitic elements which modulate the amplitude and phase of signals to create a distinct symbol constellation in the direction of the desired receiver and different characteristics in undesired locations [69–71]; periodically switched arrays in which elements of the array are switched on or off to synthetically change the electrical baselines of elements in the array causing the radiation pattern to change and thus change the locations of sidelobes [72–74]; and directional modulation where the driven elements are given additional baseband phase shifts creating unique modulation constellations which can be demodulated at the intended receiver but creates distortion at undesired directions making information unrecoverable [75–78]. A significant drawback to all these methods is a reduction in mainbeam power, and therefore impose a trade-off for secure communications: in switching arrays, elements are selectively turned off, effectively

reducing the total possible output power; parasitic arrays trade radiated power to power parasitic elements and require extensive trial-and-error analysis to obtain the desired effects; and directional modulation imparts the change of element weights to alter the sidelobes, which also results in a reduced mainbeam gain.

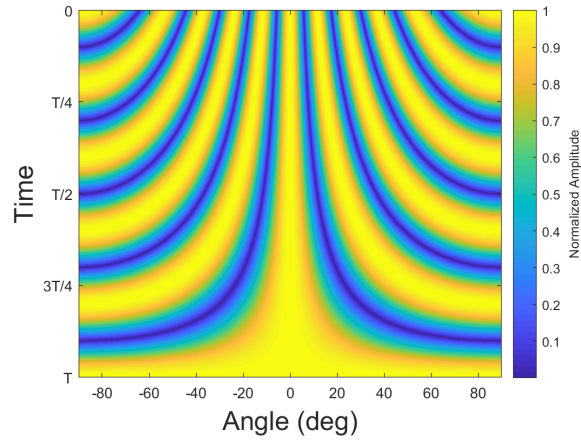
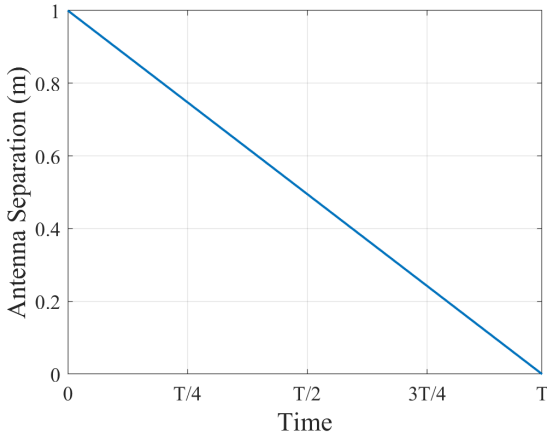
CDA's present a viable solution to both secure communications and maximum power transfer. Distributed arrays are unique in the fact that they operate similar to phased arrays but consist of several elements physically distributed in space, which enables spatial position to be used as another degree of freedom. When elements of an array move physical position relative to each other, the electrical baselines of the array are also changed and thus so are the locations of sidelobes. This is similar to the effects of the periodic switching arrays but, whereas periodic switching arrays suffer from reduced power due to unused elements, CDA's do not reduce power levels, as the mainbeam power can remain unaltered as the elements physically move.

5.1 Antenna Array Dynamics and Impacts on Wireless Communication

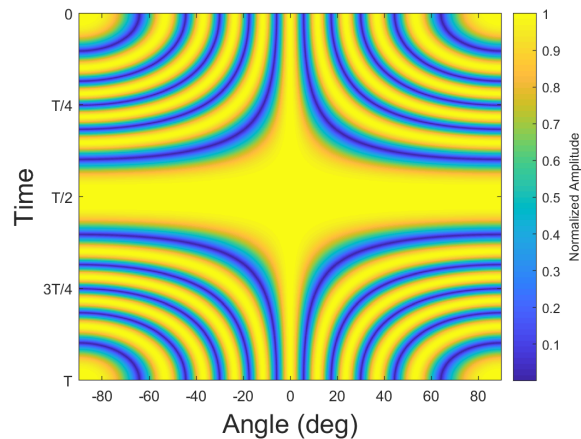
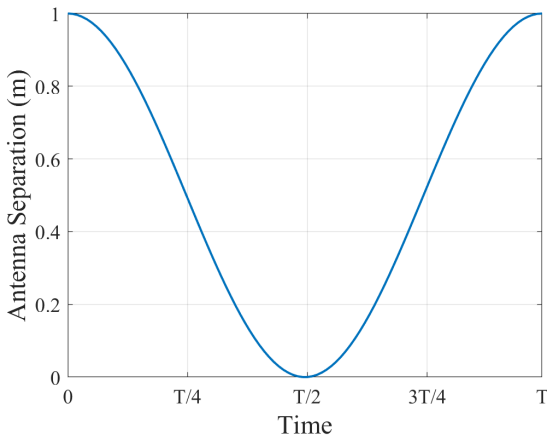
The energy radiated from multiple antennas that work together in a cooperative array add constructively and destructively at different points in space. The radiation pattern of a static antenna array can be calculated by the array factor [137] given by

$$AF(\theta, \phi) = \sum_{n=1}^N I_n(\theta, \phi) e^{jk(\mathbf{r}_n \cdot \hat{\mathbf{r}})} \quad (5.1)$$

where $I_n(\theta, \phi)$ is the element pattern of the n^{th} element, \mathbf{r}_n is the location of the n^{th} element, $\hat{\mathbf{r}}$ is the unit vector in the direction of \mathbf{r}_n , and $k = \frac{2\pi}{\lambda}$ is the wave number where λ is the wavelength of the beamforming frequency. The position of the elements, given a constant beamforming frequency, dictate aspects of the radiation pattern such as mainbeam width as well as location and number of sidelobes. In a dynamic array, elements change their physical position, and therefore the radiation pattern characteristics are dynamic with time. However, as long as coherence is maintained, the power delivered in the mainbeam remains unchanged. This can be demonstrated through a simple two element array where two different flight paths as well as their subsequent radiation patterns over time can be seen in Fig. 5.1. From this image it can be seen that as the spatial



(a)



(b)

Figure 5.1: Flight paths are taken over a 1 m extent at a 1.5 GHz beamforming frequency assuming a dipole transmitter and broadside beamforming direction. (a) Linear flight path (left) and resulting array radiation pattern over time (right). (b) Sinusoidal flight path (left) and resulting array radiation pattern over time (right).

location changes with time, so does the location and intensity of sidelobes. This is the key to this method of masking the information sent or filtering received information to/from a single location other than the desired one.

The ability to change the location and intensity of radiated sidelobes aid in the security of wireless systems for both transmit and receive operations. In a transmit system, the relocation of sidelobe energy results in signal amplitude and phase fluctuations at off angle directions making it increasingly difficult to accurately demodulate a received signal and thus challenging for an eavesdropper to recover transmitted information over an extended period of time. In a receive

system, the change in location and intensity of sidelobes energy makes it difficult to jam as the effectiveness of the addition of uncorrelated signals fluctuate over an extend period of time. In addition to this, if a location of a jammer or eavesdropper can be estimated, a flight path can be designed such that a null is steered to that specific direction while maintaining the variation in sidelobe characteristics in all other directions.

5.1.1 Estimation of Bit-Error-Rate of Communications Signals

Many applications can benefit from increased transmission security including radar, remote sensing, and imaging; but one of the most prominent impacts is in the area of communication. Here I demonstrate the degradation of reliable signal information at angles outside of the mainbeam through determination of the bit-error-ratio (BER) of the communication signal. The probability of bit error in a phase-based symbol modulation is calculated through the complimentary Gaussian error function [75, 138] and is defined as

$$P_b(error) = \frac{1}{2} \operatorname{erfc} \left(\sqrt{\frac{E_b}{N_0}} \right) \quad (5.2)$$

where E_b is the bit energy and $\frac{N_0}{2}$ is the noise power spectral density. For a binary phase shift key (BPSK) signal $E_b = E_s$ where E_s is the symbol energy. The symbol energy is calculated through the power of the radiation pattern over a set of angles.

To account for element motion of dynamic arrays, \mathbf{r}_n with time, I define the *average radiation pattern* as the weighted integration of the array factor over the total flight path in all space. Here the integral weight is the spatial probability density function (PDF) of the path. Without loss of generality, the position is calculated in Cartesian coordinates $(\hat{x}, \hat{y}, \hat{z})$ and is expressed as

$$\overline{AF(\theta, \phi)} = \sum_{n=1}^N I_n \int_{r_{n,\in\{\hat{x},\hat{y},\hat{z}\},min}}^{r_{n,\in\{\hat{x},\hat{y},\hat{z}\},max}} \iiint p(r_{n,\hat{x},\hat{y},\hat{z}}) e^{jk(r_{n,\hat{x},\hat{y},\hat{z}} \cdot \hat{r})} dx dy dz \quad (5.3)$$

where $p(r_{n,\hat{x},\hat{y},\hat{z}})$ is the spatial PDF of the flight trajectory. From this it can be seen that to estimate the BER the exact flight path does not need to be known, only the distribution over space is required.

Therefore, if a vibration profile of a mobile platform or deviation from a preset flight path is known, the BER can be estimated through the PDF alone. Here I consider the example of two-element linear array lying on the x axis, from which (5.3) reduces to

$$\overline{AF(\theta)} = 1 + \int_{r_{\hat{x},min}}^{r_{\hat{x},max}} p(r_{\hat{x}}) e^{jkr_{\hat{x}} \sin \theta} dr_{\hat{x}} \quad (5.4)$$

The PDF of the linear flight path, shown in Fig. 5.1, can be solved for by

$$p(r_{\hat{x}}) = \frac{1}{r_{\hat{x},max} - r_{\hat{x},min}} \quad (5.5)$$

as it has a uniform distribution over space. The sinusoidal path can be solved for by

$$p(r_{\hat{x}}) = \frac{1}{\pi \sqrt{1 - \left(\frac{2x - r_{\hat{x},max} - r_{\hat{x},min}}{r_{\hat{x},max} - r_{\hat{x},min}} \right)^2}} \quad (5.6)$$

and is defined over the extent $[0, \pi]$ where symmetry exists for $[\pi, 2\pi]$ assuming a uniform sampling rate, or data rate, over the entire path. In addition to this, if nonuniform sampling is performed such that the data is pulsed at different locations along the flight path, unique radiation patterns can be designed depending on the desired goal of the user. The BER of a nonuniform data rate can be estimated using the above process as well, assuming that the spatial probability is known.

It is to be noted here that (5.3) is a calculation of the average radiation pattern, and provides an estimation of the BER of a dynamic CDA rather than a lower bound. This is due to time instances where off angle directions have improved or reduced performance relative to the mean depending on the current state of the array. A demonstration of the improved BER performance that CDAs can provide can be seen in Fig. 5.2 where the two designated flight paths from Fig. 5.1 are compared a static two-element array with 1 m of separation. This example was taken at a beamforming frequency of 1.5 GHz and a SNR, given by $\frac{E_b}{N_0/2}$, of 12 dB. From this figure it can be seen that the reliability of information at broadside is maintained while reducing the performance at off angle directions up to a two orders of magnitude, therefore improving the transmission security and reducing the chance of recoverable information for an eavesdropper.

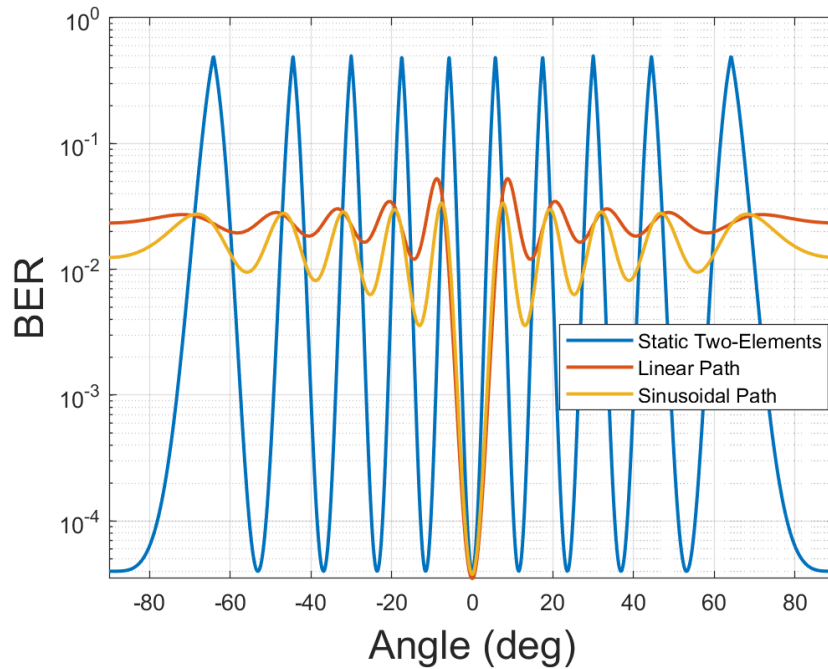
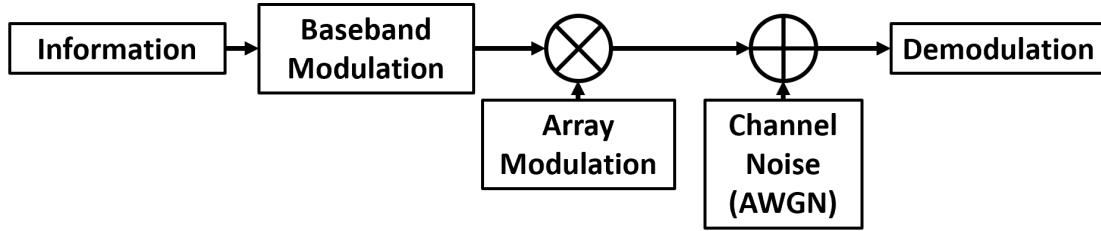


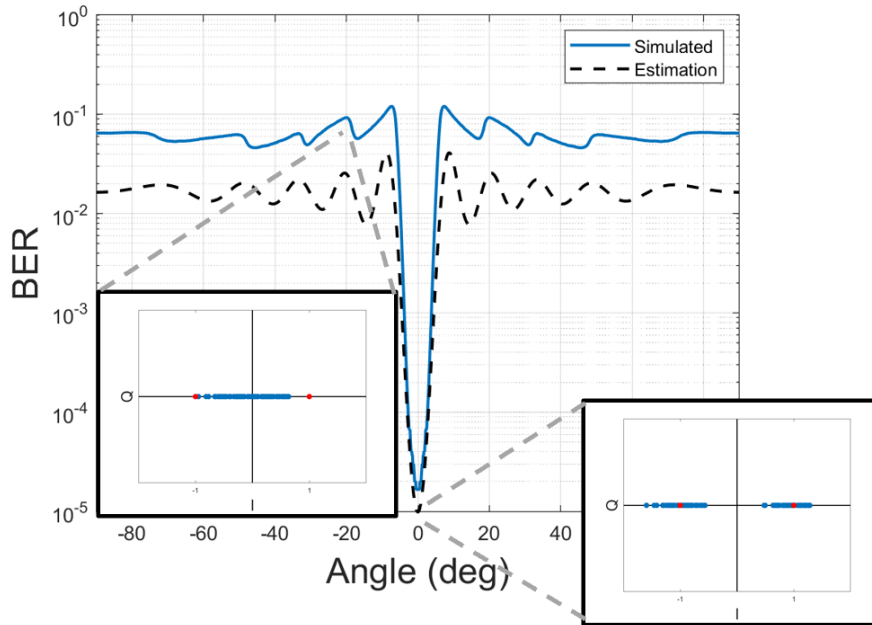
Figure 5.2: Comparison of BER performance of a static case of two dipoles at 1 m separation, and the estimated performance of the two designated flight paths at 1.5 GHz and 12 dB of SNR.

5.1.2 Simulation

The effectiveness of this method is verified through simulation by calculating the array pattern (5.4) over a 90° to 90° domain for a time T . The array pattern is then used to modulate the amplitude of a pseudo-random bit sequence (PRBS) of 300 kbits. AWGN is then applied to the bit sequence to create an SNR of 12 dB in the mainbeam, oriented at broadside, and a constant noise power-spectral density is maintained at all angles. The demodulation process is performed by mapping the bit plus noise by its Euclidean distance to the nearest constellation point. The demodulated data is then compared to the original PRBS and the BER is calculated at each angle. A block diagram of this process can be seen in Fig. 5.3(a) along with an example of the the simulation results in comparison to the calculated estimation in Fig. 5.3(b). Here the disruption of the demodulated data (blue) in comparison to the correct constellation points (red) in off angle directions can be seen.



(a)



(b)

Figure 5.3: (a) Block diagram of the simulation. (b) Simulated BER over -90° to 90° domain compared to calculated estimation for the linear case. The snapshots of data show the 100 points of demodulated data (blue) and the location of the constellation points (red) at angles -20° and 0° .

5.2 Dynamic Distributed Antenna Array Design and implementation

In this chapter an open-loop CDA, where information is sent from two different elements, is implemented. The fundamental electrical states that must be coordinated are phase and, since pulsed information is to be sent, time. Time alignment is performed by a preamble consisting of a high-amplitude pulse that is sent initially for calibration; time alignment is relatively stationary after this initial calibration, but long-term systems would require periodic recalibration using the same approach. Phase alignment must be performed continually due to the motion of the platforms,

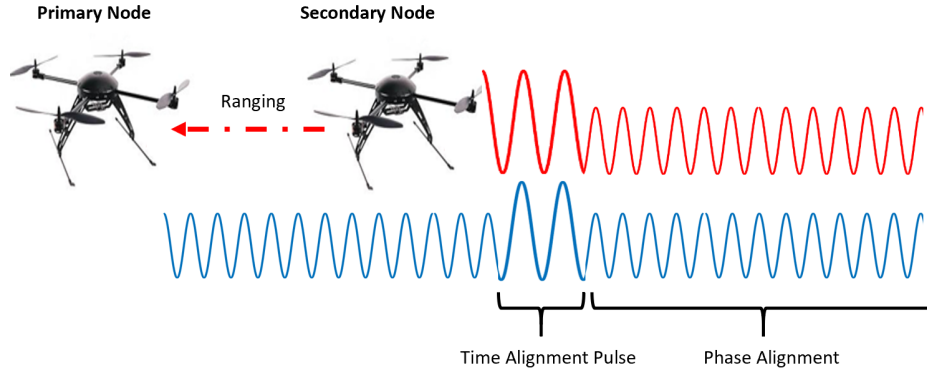


Figure 5.4: Method of performing alignment of electrical states of time, through high amplitude preamble, and phase, range estimation between primary and secondary elements.

and is implemented through a range estimation between elements. Static phase offsets which do not change during the course of the operation, such as static phase delays through the electronic systems, and are calibrated prior to operation.

The structure of the dynamic distributed array follows the structure described in Chapter 4 and is achieved using a hierarchical centralized architecture consisting of a single primary element and one subsequent secondary element. An image depicting this method of time alignment, through a high amplitude preamble, and phase alignment, through a range estimation, can be seen in Fig. 5.4.

5.2.1 Ranging Waveform

The ranging waveform used for this work is the TTSFW from Section 3.4. This waveform is generated on an Ettus X310 SDR which is connected to a host computer via 10 GB Ethernet cable and interfaced with using LabView 2018. The achievable sampling rate using this setup is 20 MHz, where the limiting factor is LabView processing speed, providing an instantaneous bandwidth of 10 MHz. For this experiment, which consists of two elements, only one unique connection is made and, therefore, only a single pulse of the TTSFW is required. The remaining parameters are chosen to be $\Delta f = 6$ MHz and $T_r = 500 \mu s$ with a 50% duty cycle. An image of the TTSFW used in this experiment for both time and frequency can be seen in Fig. 5.5.

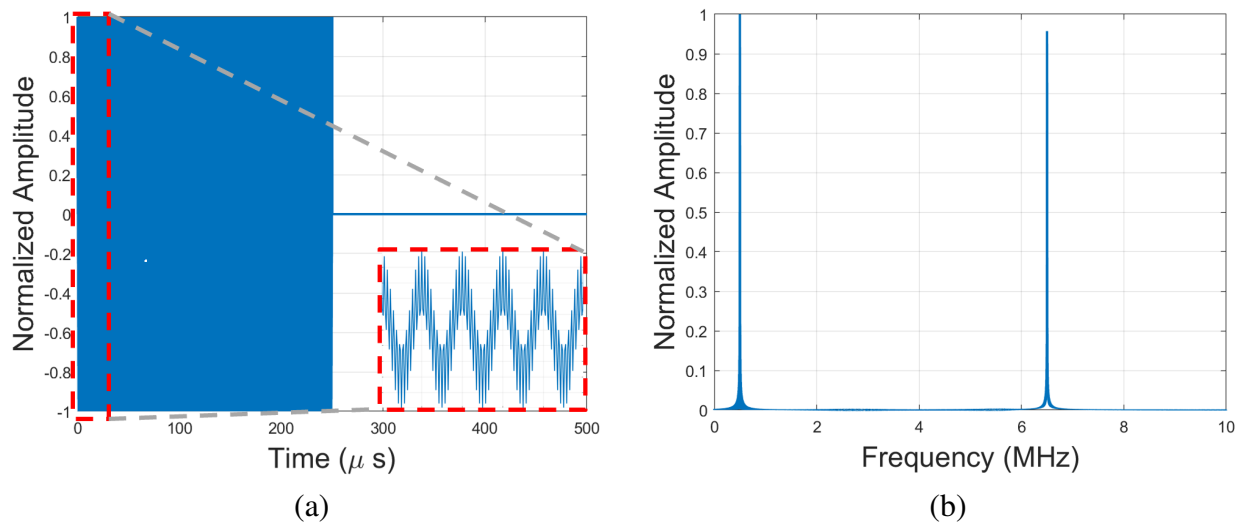


Figure 5.5: (a) Ranging waveform in the time domain. (b) Ranging waveform in the frequency domain.

5.2.2 Estimation Ability

The estimation ability of the TTTSFW, given by (3.83), is again dictated by the mean-squared bandwidth of the signal which is given by (3.82) which for the aforementioned waveform parameters is derived as

$$\zeta_f^2 \Big|_{N=1} = \pi^2 BW^2 = 3.5531 \times 10^{14} \quad (5.7)$$

The CRLB for the TTTSFW, (3.83), can be evaluated at an SNR of 24 dB which represents the worst case scenario seen from the measured data and is estimated through a eigenvalue decomposition method described in Section 2.1.4.

The processing gain from the matched filter process, given by TBW_r , where $T = 250 \mu$ s and BW_r is the receiver noise bandwidth which, since no filter is being used, is 10 MHz. The processing gain is equivalent to 34 dB giving a total post processing SNR of 58 dB. The maximum theoretical positional accuracy, given these parameters, can be found to be $\sigma_x = 1$ cm. The relative ranging accuracy for broadside beamforming must be known within $\frac{\lambda}{15}$, unlike end-fire that requires $\frac{\lambda}{20}$, to have a high probability of achieving 90%

$$f \leq \frac{c}{15\sigma_x} \quad (5.8)$$

with provides an obtainable beamforming frequency of $f \leq 1.9964$ GHz. To stay close to this limit, the beamforming frequency for the experiment is chosen to be 1.5 GHz.

To ensure that the range estimation provides an estimate of the beamforming phase before the elements move out of coherent range with a degradation of 10%, the maximum velocity of the element relative motion can be calculated as

$$v = \frac{\lambda}{15T_{update}} \quad (5.9)$$

where v is the maximum velocity, λ is the wavelength of the beamforming frequency, and T_{update} is the update rate. The ranging process on the host computer of the secondary element is measured to have an average processing time of 60 ms. This leads to a maximum tolerable velocity of 0.2 m/s to ensure a coherent gain of approximately 80% where 10% degradation comes from the uncertainty in the ranging process and 10% from the motion of the elements moving out of relative coherence before a new phase update is available.

5.3 Experimental Validation of Secure Communication

Wireless measurements are conducted in a semi-enclosed arch range where the receiver consists of a 0.5–6 GHz horn antenna mounded along the outer rail of the range and a two element open-loop CDA is mounted on a linear actuator in the middle of the range 3.05 m away from the receiver. The receiving antenna is rotated around the outer rail of the range on a movable platform in 10° increments to evaluate the performance of the array at angles off of broadside. The received signals are captured on an Ettus X310 SDR where signals are downconverted to baseband using the internal local oscillator (LO), which is frequency locked to the elements within the array to emulate worst case scenario of an eavesdropper having perfect clocking information. The baseband waveform is then off-boarded to MATLAB for processing. The primary and secondary elements of the CDA are each equipped with a 0.698 – 2.69 GHz dipole antenna for beamforming and two 1.3 – 9.5 GHz ultra wideband log periodic antenna for ranging. Beamforming operation takes place at 1.5 GHz while the ranging is performed at 4 GHz and 5.5 GHz for transmit and receive respectively. The separation of ranging center frequencies is to avoid cross talk, and chosen such

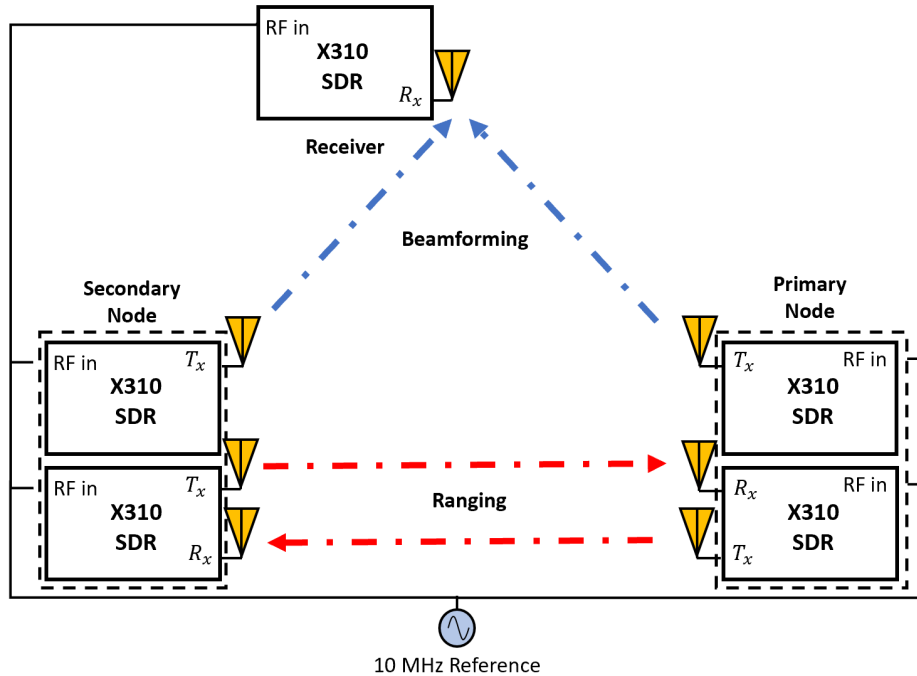


Figure 5.6: Block diagram of the experimental setup

that they lie far outside the instantaneous bandwidths achievable on each radio. Due to the linear actuator only having a single moving platform, the primary element is mounted stationary on the end while the secondary element is mounted to the movable platform, therefore, all of the array's motion is done solely by the secondary element. A block diagram of the experimental setup can be seen in Fig. 5.6 where the red arrowed lines represent the internode ranging while the blue arrowed lines represent beamforming. An image of the the experimental setup in the range can be seen in Fig. 5.7(a) along with the antenna configuration on each element can in Fig. 5.7(b).

The full extent that the linear actuator can achieve is 1 m but due to the antenna mounting structure the motion of the array is limited 0.744 m. The farthest separation of the elements is limited to 0.934 m and the closest range the elements achieve is 0.196 m to avoid collision of the log periodic antennas. The element positions for these two limiting factors can be seeing in Fig. 5.7(c) and (d) for the cases of farthest and closest extents respectively. The simulation was run with these range limits and a comparison to the true flight path, taken from the linear actuator data, can be seen in Fig. 5.8. The RMSE of the deviation of the actual path from the simulated path is 4.7 mm and 1.16 cm for the linear and sinusoidal cases respectively. It should be noted

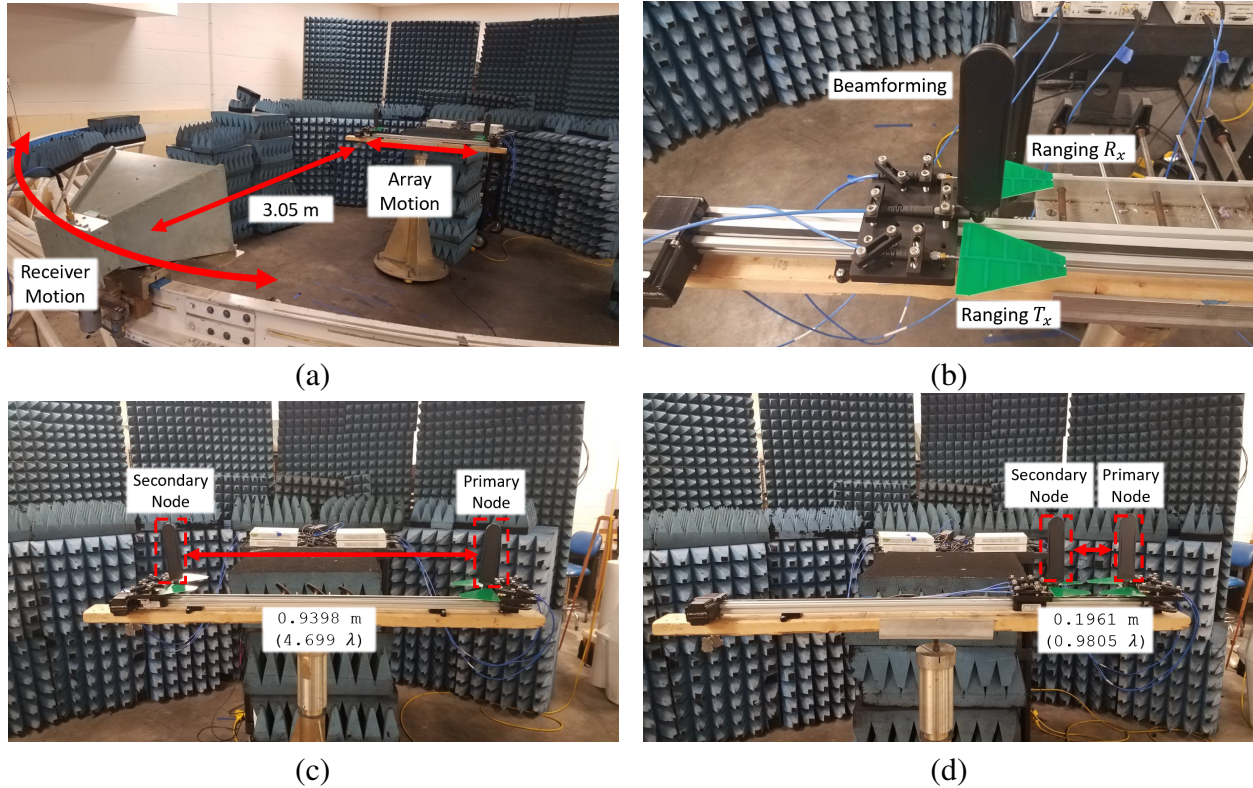


Figure 5.7: (a) Image of the experimental setup in the semi-enclosed arch range. (b) Image of the antenna setup for ranging and beamforming on each element. (c) Farthest separation of the elements mounted on the linear actuator. (d) Closest separation of the elements mounted on the linear actuator.

here that the sinusoidal case is only captured from $[0, \pi]$ due to memory depth constraints of the saving process. This limited path will have no effect the resulting BER, as the probability in (5.4) is symmetric around π . The maximum velocity of the relative motion between the elements is measured to be 0.1923 m/s which is below the limit of 0.2 m/s required for 10% degradation of the coherent signal. The coherent gain for these two flight paths is measured by comparing the coherent sum of the two elements to the sum of the two elements radiating independently and is found to be 79.9% and 78.78% (~ 1 dB degradation) for the linear and sinusoidal case respectively. Higher levels of coherence can be achieved by one of the following ways: lowering the beamforming frequency; increasing the ranging waveform bandwidth to lower the positional uncertainty; reducing the processing overhead to provide a quicker update to the beamforming phase; or reducing the velocity of the relative motion between the elements.

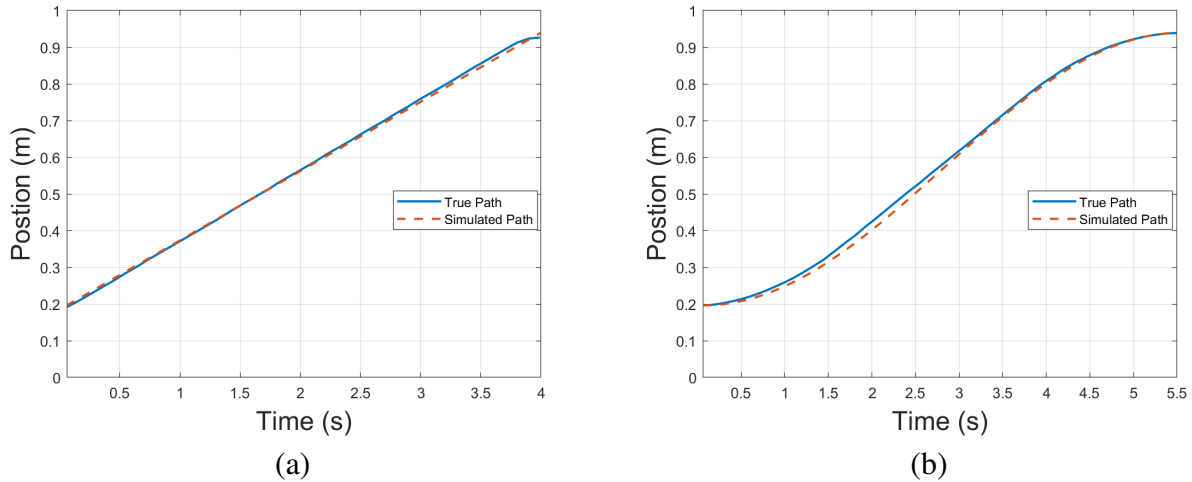
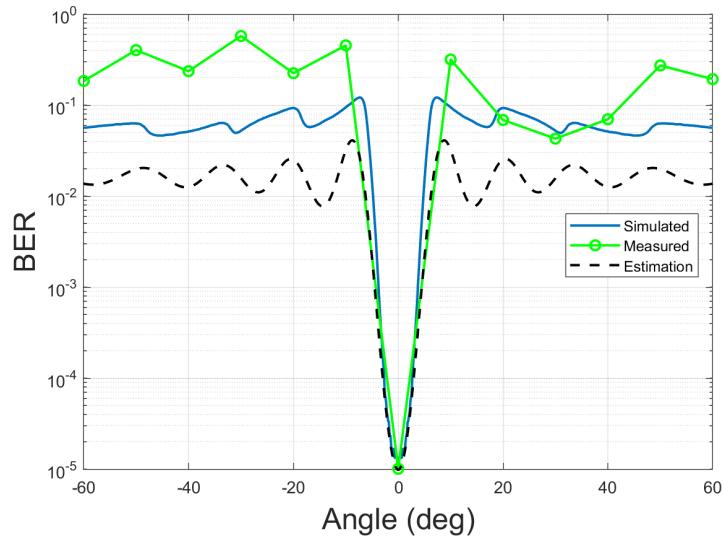


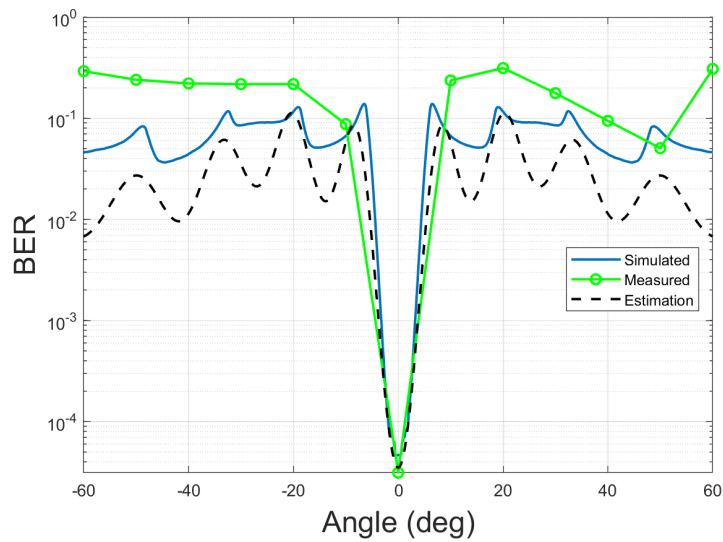
Figure 5.8: (a) Comparison of simulated and actual flight path for the linear case. (b) Comparison of simulated and actual flight path for the sinusoidal case.

Calibration of the data is performed prior to operation by placing the array in a static state at the farthest extent of the linear actuator and the receiving horn, oriented at the desired beamforming direction, is connected to a MSO-X 92004A Keysight Infiniium High-Performance Oscilloscope. The timing on the output of the secondary element is altered until sufficient overlap with the primary element the high amplitude time alignment pulse is achieved. Once time alignment is complete, phase alignment is accomplished by alternating the output phase of the secondary element until a maximum amplitude of the beamforming signal can be seen on the scope. After calibration is performed the receiving antenna is then connected to a X310 SDR for capture where data is collected at a bit rate of 100 kbits/s. The PRBS is generated using a built-in LabView maximum length sequence (MLS) block for the time durations depicted in Fig. 5.8. The linear actuator motion is then started and the array is set in constant relative motion. Once the data is collected and off-boarded to MATLAB, processing is performed by first stripping off the time alignment pulse. The data is demodulated by averaging the samples of each bit plus noise and mapping this mean value to a constellation point by the Euclidean distance. Measurements are taken at 12.85 dB and 12.05 dB SNR determined by an eigenvalue decomposition method, from Section 2.1.4, for the linear and sinusoidal paths respectively. The measured results of a -60° to 60° extent measured in 10° increments can be seen in Fig. 5.9(a) and (b) for the linear and sinusoidal cases

respectively and are compared to simulation and estimation value of the BER. It can be noticed from these results that the positive angles have improved performance compared to the negative angles where the result is expected to be symmetric around 0° . The analysis for the estimation, as well as the simulation, assume far field operation and symmetric motion between both elements. For this experimental setup, this is not the case. The primary element remains stationary relative to the positive angles while the secondary element performs the motion towards the negative angles. Although this mismatch is present, a relatively good matching between measured, simulated, and estimated results can be seen providing approximately a BER of 10^{-5} at broadside and roughly 0.5 at off angle directions and therefore, proves that CDAs present a viable solution to secure sensing while maintaining near maximum power transfer.



(a)



(b)

Figure 5.9: (a) Comparison of simulated, measured, and calculated estimation of the BER for the linear case. (b) Comparison of simulated, measured, and calculated estimation of the BER for the sinusoidal case.

CHAPTER 6

CONCLUSION

In this work I have designed and experimentally validated a method to perform phase alignment that is more conducive to scalability, simpler system implementation, lower cost, and distributed beamforming applications than what has been demonstrated in the literature. To overcome the lack of positional information inherent in closed-loop and retrodirective methods, the use of internode range to enable phase-based beamsteering operation is implemented. I derived and experimentally evaluated novel ranging waveforms utilizing time domain duxplexing, frequency division multiplexing, and pulse encoding scalability approaches to operate with a variety of distributed systems and applications including remote sensing as well as communication. These waveforms include: a near optimal range and velocity estimation waveform; a waveform to perform joint ranging and frequency transfer; a ranging waveform using existing IEEE 802.11 preamble formats; and highly scalable pulse encoded waveform based on a spectrally-sparse two-tone waveform that monochromatically increases its frequency on pulse by pulse basis.

Using the range estimations provided from the TTFSW waveform, an experimental demonstration of phase alignment supporting up to 120 nodes with three nodes transmitting in a dynamic open-loop distributed beamforming array with greater than 90% coherent gain using the primary-secondary hierarchical topology was presented. Beamforming in the L-band region was proven to be obtainable with no more than 12.5 MHz bandwidth allocated to the range estimation waveform making applications such as L-band SAR for vegetation and forestry measurements as well communications at the L-band frequency range obtainable using off-the-shelf equipment. Furthermore, this method is directly scalable to larger arrays.

I demonstrated an implementation of distributed beamforming phase alignment of a dynamic coherent open-loop CDA with designated element flight paths to improve the security of wireless operations. A wireless beamforming experiment was shown to have approximately 80% maximum power transfer, which can be improved upon by allocating more bandwidth to the esti-

mation process or alternate flight paths, while corrupting data to the point of becoming unrecoverable at off-angle directions. This method has applications that are resistant to eavesdropping on transmit and resistant to jamming on receive. This is made possible by the dynamics of the array changing the electrical baselines of the synthesized array and thus changing the locations of constructive interference in space while maintaining coherence at the desired target destination.

This dissertation has thus laid the ground work for open-loop distributed beamforming applications by addressing the most challenging coordination aspect to enable open-loop distributed beamforming, phase alignment of the beamforming signals. As many wireless distributed systems require flexibility to support various applications, I have addressed phase alignment in a highly scalable manor for a variety of applications and, due to the pairwise structure of the primary-secondary topology, total system failure can be avoided from individual element failure. Wireless coherent beamforming operations in the microwave region were performed with relatively low cost off-the-shelf equipment making this method highly repeatable and easily implemented for future works in distributed beamforming from aerial platforms. The introduction of array dynamics, shown in this work, make applications consisting of mobile nodes such as drone swarms or satellite constellations performing coherent operations feasible using this technique for application spaces of communication and remote sensing, which has previously been unobtainable for closed-loop architectures.

APPENDICES

APPENDIX A

MATLAB FORMULATION OF BASEBAND PSWF

```
clear all
close all
clc
%%%%%%%%%%%%%%%%%%%%%%%%%%%%%%%%%%%%%%%%%%%%%%%%%%%%%%%%%%%%%%%%%%%%%%%%
c=3*pi;
order=0:7;
M=ceil(1.1*c+max(order)+100);
for i_ord=1:length(order)
%%%%%%%%%%%%%%%%%%%%%%%%%%%%%%%%%%%%%%%%%%%%%%%%%%%%%%%%%%%%%%%%%%%%%%%%
%%%%%%%%%%%%%%%%%%%%%%%%%%%%%%%%%%%%%%%%%%%%%%%%%%%%%%%%%%%%%%%%%%%%%%%%
%A matrix
A=zeros(M,M);
for i_N=1:M
    A(i_N,i_N)=(i_N-1)*((i_N-1)+1)+(2*(i_N-1)*((i_N-1)+1)-1)...
        /((2*(i_N-1)+3)*(2*(i_N-1)-1))*c^2;
    if i_N+1<M
        A(i_N,i_N+2)=((i_N-1)+2)*((i_N-1)+1)/((2*(i_N-1)+3)...
            *sqrt((2*(i_N-1)+1)*(2*(i_N-1)+5)))*c^2;
        A(i_N+2,i_N)=((i_N-1)+2)*((i_N-1)+1)/((2*(i_N-1)+3)...
            *sqrt((2*(i_N-1)+1)*(2*(i_N-1)+5)))*c^2;
    end
end
end
```

```

A_even=A(1:2:M,1:2:M);
A_odd=A(2:2:M,2:2:M);

[B_even,~]=eig(A_even);
[B_odd,~]=eig(A_odd);

B(1:2:M)=B_even(:,ceil((order(i_ord)+1)/2));
B(2:2:M)=B_odd(:,ceil((order(i_ord)+1)/2));

for i_M=1:M
    if mod(order(i_ord)+i_M-1,2)==1
        B(i_M)=0;
    end
end

sum(abs(B).^2)

%Legrange Polynomial
t=linspace(-1,1,10000);
P=[ones(1,length(t)); t];
for i_N=2:M
    P(i_N+1,:)=(2*(i_N-1)+1)/((i_N-1)+1)*t.*P(i_N,:)+...
        -(i_N-1)/((i_N-1)+1)*P(i_N-1,:);
end

%normalized Legrange Polynomial
for i_P=1:length(P(:,1))

```

```

        P(i_P ,:)=P(i_P ,:)* sqrt ((i_P -1)+0.5);
    end
%%%%%%%%%%
%%%%%%%%%%
    %calculate PSWF
    PSFW=zeros (1 , length ( t ));
    for i_M=1:M
        PSFW=B(i_M)*P(i_M ,:)+PSFW;
    end
    if ( order ( i_ ord )==2)||( order ( i_ ord )==6)
        PSFW=-(PSFW);
    end
    if ( order ( i_ ord )==3)||( order ( i_ ord )==7)
        PSFW=-(PSFW);
    end
    PSFW=(-1)^(c / pi +1)*PSFW;
    PSFWs(i_ ord ,:)=PSFW;

    if mod( order ( i_ ord )+i_M-1,2)==1
        figure (1)
        subplot (1 ,2 ,1)
        plot ( t ,PSFW, ' Linewidth ' ,1.5)
        grid on
        hold on
        xlabel ( ' Time ' , ' Fontsize ' ,14)
        ylabel ( ' Amplitude ' , ' Fontsize ' ,14)
        legend ( ' n=0 ' , ' n=2 ' , ' n=4 ' , ' n=6 ' )
    end

```

```

xticks([-1 0 1])
xticklabels({'-T/2','0','T/2'})
title('c=4\pi','FontSize',18)
else
subplot(1,2,2)
plot(t,PSFW,'Linewidth',1.5)
hold on
grid on
legend('n=1','n=3','n=5')
xlabel('Time','FontSize',14)
ylabel('Amplitude','FontSize',14)
xticks([-1 0 1])
xticklabels({'-T/2','0','T/2'})
title('c=4\pi','FontSize',18)
end

clear PSFW

end

% save(['c=' num2str(c/pi) 'pi.mat'], 'PSFWs', 't')
save(['c=10pi.mat'], 'PSFWs', 't')

```

APPENDIX B

MATLAB FORMULATION OF DUAL PULSE PSWF

```
% clear all
close all
clc
%%%%%%%%%%%%%%%%%%%%%%%%%%%%%%%%%%%%%%%%%%%%%%%%%%%%%%%%%%%%%%%%%%%%%%%%
load c=10pi.mat
wf=PSFWs(1,:);
clear t
%%%%%%%%%%%%%%%%%%%%%%%%%%%%%%%%%%%%%%%%%%%%%%%%%%%%%%%%%%%%%%%%%%%%%%%%
mod=10/100;
len=10e-6;
%%%%%%%%%%%%%%%%%%%%%%%%%%%%%%%%%%%%%%%%%%%%%%%%%%%%%%%%%%%%%%%%%%%%%%%%
snr=linspace(-5,85);
SNR=10.^(snr/10);
interp=0;
%%%%%%%%%%%%%%%%%%%%%%%%%%%%%%%%%%%%%%%%%%%%%%%%%%%%%%%%%%%%%%%%%%%%%%%%
for i_mod=1:length(mod)
    t=linspace(-len/4*mod(i_mod),len/4*mod(i_mod),length(wf));
    smpps=1/(t(2)-t(1));
    t1=-len/2:1/smpps:len/2;

    W=3/(len/2*mod(i_mod));

    waveform=zeros(1,length(t1));
```



```
save('for_plots.mat', 'waveform', 't1', 'wf2')
```

```
save('opt_wf.mat', 'opt_wf', 't1', 'crlb_t', 'crlb_f', 'snr', 't')
```

APPENDIX C

MATLAB PSWF SIMULATION

```
clear all
close all
clc
%%%%%%%%%%%%%%%%%%%%%%%%%%%%%%%%%%%%%%%%%%%%%%%%%%%%%%%%%%%%%%%%%%%%%%%%
load opt_wf.mat
waveform=opt_wf;
waveform=10*waveform ./ max(abs(waveform));
%%%%%%%%%%%%%%%%%%%%%%%%%%%%%%%%%%%%%%%%%%%%%%%%%%%%%%%%%%%%%%%%%%%%%%%%
MC=1000;
smpps=1/(t1(2)-t1(1));
dB=linspace(-30,20,10);
interp=25;
%%%%%%%%%%%%%%%%%%%%%%%%%%%%%%%%%%%%%%%%%%%%%%%%%%%%%%%%%%%%%%%%%%%%%%%%
for i_dB=1:length(dB)
    disp(i_dB)
    for i_MC=1:MC
        disp(i_MC)

        sig(:,i_MC)=waveform+wgn(1,length(waveform),-dB(i_dB));

        [corr,lag]=xcorr(waveform,sig(:,i_MC));
        [~,lms]=findpeaks(abs(corr),'SortStr','descend');
        [~,pp]=min(abs(lag(lms)/smpps-0));
```

```

%         figure ()
%         plot ( lag / smpps , abs ( corr ) )
%         return

%%-----
%interp
    intrp =3;
    redic =10000;
    newtau=lag ( lmxs ( pp )- intrp ) / smpps : 1 / ...
        ( smpps * redic ) : lag ( lmxs ( pp )+ intrp ) / smpps ;
    Vs=interp1 ( lag ( ( lmxs ( pp )- intrp ) : ( lmxs ( pp )+ intrp ) ) ...
        / smpps , abs ( corr ( ( lmxs ( pp )- intrp ) : ( lmxs ( pp )+ intrp ) ) ) ...
        , newtau , ' spline ' );

    [ ~ , I1 ] = max ( Vs );
    tops_t ( i_MC ) = newtau ( I1 ( 1 ) );

%%-----
    temp = [ corr zeros ( 1 , interp * length ( corr ) ) ];
    Y = fft ( temp );
    L = length ( Y );
    P2 = abs ( Y / L );
    P1 = P2 ( 1 : L / 2 + 1 );
    P1 ( 2 : end - 1 ) = 2 * P1 ( 2 : end - 1 );
    fs = linspace ( 0 , smpps / 2 , L / 2 + 1 );

    [ ~ , lmxs ] = findpeaks ( P1 , ' SortStr ' , ' descend ' );

```

```

[~,pp]=min(abs(fs(lmxs)-60e6));
%
    pp=1;

%
    figure()
%
    plot(fs/1e6,P1./max(abs(P1)),'Linewidth',1.5)
%
    set(gca,'FontSize',22)
% %
    axis([5.75 6.25 0 1])
%
    grid on
%
    xticks([6])
%
    xticklabels({'10W'})
%
    xlabel('Frequency','FontSize',28)
%
    ylabel('Normalized Amplitude','FontSize',28)
%
    return

%
    figure()
%
    plot(lag/smpps*1e3,abs(corr)./max(abs(corr))...
        ,'Linewidth',1.5)
%
    xticks([-1 0 1])
%
    grid on
%
    axis([-1 1 0 1])
%
    xlabel('Time','FontSize',28)
%
    xticklabels({'-T','0','T'})
%
    ylabel('Normalized Amplitude','FontSize',28)
%
    set(gca,'FontSize',22)

%
    figure()

```

```

%      plot(t1*1e3, waveform, 'Linewidth', 1.5)
%      xlabel('Time', 'FontSize', 28)
%      ylabel('Normalized Amplitude', 'FontSize', 28)
%      set(gca, 'FontSize', 22)
%      xticks([-0.5 0 0.5])
%      xticklabels({'-T/2', '0', 'T/2'})
%      grid on
%
%      figure()
%      plot(linspace(-smpps/2, smpps/2, length(P1))/1e6, ...
%           P1./max(abs(P1)), 'Linewidth', 1.5)
%      axis([-7 7 0 1])
%      grid on
%      xlabel('Frequency', 'FontSize', 28)
%      ylabel('Normalized Amplitude', 'FontSize', 28)
%      set(gca, 'FontSize', 22)
%      xticks([-6 0 6])
%      xticklabels({'-10W', '0', '10W'})
% return
%%-----
%interp
    intrp=4;
    redic=10000;
    newtau=fs(lmxs(pp)-intrp):(fs(2)-fs(1))...
           /redic:fs(lmxs(pp)+intrp);
    Vs=interp1(fs((lmxs(pp)-intrp):(lmxs(pp)+intrp))...
              ,P1((lmxs(pp)-intrp):(lmxs(pp)+intrp))...

```

```

        ,newtau , ' spline ' );

%       figure ( )
%       plot ( newtau , Vs )
%       return
        [ ~ , I1 ] = max ( Vs );
        tops_f ( i_MC ) = newtau ( I1 ( 1 ) );

end
top = ( mean ( tops_t ) + 2 * std ( tops_t ) );
bot = ( mean ( tops_t ) - 2 * std ( tops_t ) );

tops_t ( top < tops_t ) = [];
tops_t ( bot > tops_t ) = [];

top = ( mean ( tops_f ) + 2 * std ( tops_f ) );
bot = ( mean ( tops_f ) - 2 * std ( tops_f ) );

tops_f ( top < tops_f ) = [];
tops_f ( bot > tops_f ) = [];

data_t ( i_dB ) = var ( tops_t );
data_f ( i_dB ) = var ( tops_f );

temp = sort ( eig ( cov ( sig ) ) , ' descend ' );
sig_w = mean ( temp ( 5 : MC ) );
Ps = 1 / MC * ( temp ( 1 ) - sig_w );

```

```

snr_t(i_dB)=10*log10(abs(Ps/sig_w))+10*log10(smpps*10e-6);
snr_f(i_dB)=10*log10(abs(Ps/sig_w));

%     temp=sort(eig(cov(sig_f)), 'descend');
%     sig_w=mean(temp(5:MC));
%     Ps=1/MC*(temp(1)-sig_w);
%     snr_f(i_dB)=10*log10(abs(Ps/sig_w));
%
    clc
end

figure()
semilogy(snr_t,(3e8)^2/4*data_t,'-o','Linewidth',1.5)
hold on
semilogy(snr,crlb_t,'Linewidth',1.5)
grid on
% axis([45 85 2.5e-8 0.5e-3])
xlabel('Postprocessing SNR (dB)','FontSize',18)
ylabel('Variance (m^2)','FontSize',18)
legend('Simulation','CRLB')

figure()
semilogy(snr_t,data_f,'-o','Linewidth',1.5)
hold on
semilogy(snr,crlb_f,'Linewidth',1.5)
grid on
% axis([-5 35 0.5e2 1e6])

```

```
xlabel('SNR (dB)', 'FontSize', 18)
ylabel('Variance (Hz^2)', 'FontSize', 18)
legend('Simulation', 'CRLB')

save('simulation_results.mat', 'data_f', 'data_t', 'snr_t', 'snr_f')
```

APPENDIX D

MATLAB PSWF MEASUREMENT PROCESSING

```
clear all
close all
clc
%%%%%%%%%%%%%%%%%%%%%%%%%%%%%%%%%%%%%%%%%%%%%%%%%%%%%%%%%%%%%%%%%%%%%%%%
load opt_wf.mat
template=opt_wf;
%%%%%%%%%%%%%%%%%%%%%%%%%%%%%%%%%%%%%%%%%%%%%%%%%%%%%%%%%%%%%%%%%%%%%%%%
dB=[0 3 6 10 13 16 20];
filt=100e6;
MC=1000;
%%%%%%%%%%%%%%%%%%%%%%%%%%%%%%%%%%%%%%%%%%%%%%%%%%%%%%%%%%%%%%%%%%%%%%%%
for i_dB=1:length(dB)
    disp(i_dB)
    load([num2str(dB(i_dB)) '_dB.mat'])
    ind=1;
    for i_MC=1:MC
        disp(i_MC)
        t1=linspace(0,10e-6,length(waveform(:,i_MC)));

        temp_wf=waveform(:,i_MC)'.*exp(j*2*pi*3e9*t1);
        smpps=1/(t1(2)-t1(1));

        waveform1(:,i_MC)=lowpass(temp_wf,filt,smpps);
    end
end
```

```

%       waveform1 (: ,i_MC)=temp_wf;
%       t1=t1 (1:50:end);
%       return
%       P1=abs ( fftshift ( fft ( waveform1 (: ,i_MC) ) ) );
%       fs=linspace ( -smpps/2 , smpps/2 , length ( P1 ) );
%       figure ()
%       plot ( fs , P1 )
%       return

%       figure ()
%       subplot ( 2 , 1 , 1 )
%       plot ( t1 , waveform1 (: ,i_MC) )
%       subplot ( 2 , 1 , 2 )
%       plot ( t1 , template )
%       return

[ corr , lag ]=xcorr ( temp_wf , template );
%       [ ~ , lmxs ]=findpeaks ( abs ( corr ( floor ( 0.25 * length ( corr ) ) ...
%       : floor ( 0.75 * length ( corr ) ) ) ) , ' SortStr ' , ' descend ' );
%       figure ()
%       plot ( lag / smpps , abs ( corr ) )
%       return
%       waveform2 (: ,i_MC)=corr ;

[ ~ , lmxs ]=findpeaks ( abs ( corr ) , ' SortStr ' , ' descend ' );

```

```

if i_MC==1
    [~,pp]=min(abs(lag(lmxs)/smpps-3.87e-8));
else
    [~,pp]=min(abs(lag(lmxs)/smpps-tops_t(1)));
end

%%-----

%interp
intrp=3;
redic=10000;
newtau=lag(lmxs(pp)-intrp)/smpps:1/(smpps*redic)...
        :lag(lmxs(pp)+intrp)/smpps;
Vs=interp1(lag((lmxs(pp)-intrp):(lmxs(pp)+intrp))...
            /smpps,abs(corr((lmxs(pp)-intrp):(lmxs(pp)+intrp)))...
            ,newtau,'spline');

[~,I1]=max(Vs);
tops_t(i_MC)=newtau(I1(1));

%    figure()
%    plot(lag/smpps,abs(corr))
%    hold on
%    scatter(tops_t,max(abs(corr)))
%    scatter(lag(2002)/smpps,max(abs(corr)))

%    return
%%-----

```

```

%      Y = fft([corr zeros(1,10*length(corr))]);
Y = fft(corr);
%      Y = fft(waveform(:,i_MC));
L = length(Y);
P2 = abs(Y/L);
P1 = P2(1:L/2+1);
P1(2:end-1) = 2*P1(2:end-1);
fs = linspace(0,smpps/2,L/2+1);

%      figure()
%      plot(fs,P1)
%      return

[~,lmxs]=findpeaks(P1,'SortStr','descend');

if i_MC==1
    [~,pp]=min(abs(fs(lmxs)-59.2e6));
else
    [~,pp]=min(abs(fs(lmxs)-tops_f(1)));
end

%%-----
%interp
intrp=3;
redic=1000;
newtau=fs(lmxs(pp)-intrp):(fs(2)-fs(1))...
    /redic:fs(lmxs(pp)+intrp);
Vs=interp1(fs((lmxs(pp)-intrp):(lmxs(pp)+intrp))...

```

```

        ,P1((lmsx(pp)-intrp):(lmsx(pp)+intrp))...
        ,newtau,'spline');

%       figure()
%       plot(newtau,Vs)
%       return
    [~,I1]=max(Vs);
    tops_f(i_MC)=newtau(I1(1));

%       scatter(1:i_MC,tops_f)
%       hold on

end

top=(mean(tops_t)+2*std(tops_t));
bot=(mean(tops_t)-2*std(tops_t));

temp1=find(top<tops_t);
if ~isempty(temp1)
    tops_t(temp1)=[];
    tops_f(temp1)=[];
    waveform(:,temp1)=[];
end

temp2=find(bot>tops_t);
if ~isempty(temp2)
    tops_t(temp2)=[];

```

```

        tops_f(temp2)=[];
        waveform(:,temp2)=[];
    end

    clear temp1 temp2

    top=(mean(tops_f)+2*std(tops_f));
    bot=(mean(tops_f)-2*std(tops_f));

    temp1=find(top<tops_f);
    if ~isempty(temp1)
        tops_f(temp1)=[];
        tops_t(temp1)=[];
        waveform(:,temp1)=[];
    end

    temp2=find(bot>tops_f);
    if ~isempty(temp2)
        tops_f(temp2)=[];
        tops_t(temp2)=[];
        waveform(:,temp2)=[];
    end

    end

%
%     figure()
%     scatter(1:length(tops_t),tops_t)
%     return

```

```

data_t(i_dB)=var(tops_t);
data_f(i_dB)=var(tops_f);

clc

temp=sort(eig(cov(waveform1)),'descend');
sig_w=mean(temp(2:length(waveform1(1,:))));
Ps=1/length(waveform1(1,:))*(temp(1)-sig_w);
snr_t(i_dB)=10*log10(abs(Ps/sig_w))+10*log10(2*filt*10e-6);
snr_f(i_dB)=10*log10(abs(Ps/sig_w));

end
%%%%%%%%%%%%%%%%%%%%%%%%%%%%%%%%%%%%%%%%%%%%%%%%%%%%%%%%%%%%%%%%%%%%%%%%%
figure()
semilogy(snr_t,(3e8)^2/4*data_t,'-o','Linewidth',1.5)
hold on
semilogy(snr,crlb_t,'Linewidth',1.5)
grid on
% axis([45 85 2.5e-8 0.5e-3])
xlabel('Attenuation (dB)','FontSize',18)
ylabel('Variance (m^2)','FontSize',18)
% legend('Simulation','CRLB')

figure()
semilogy(snr_t,data_f,'-o','Linewidth',1.5)
hold on
semilogy(snr,crlb_f,'Linewidth',1.5)
grid on

```

```
% axis([-5 35 0.5e2 1e6])
xlabel('Attenuation (dB)', 'FontSize', 18)
ylabel('Variance (Hz^2)', 'FontSize', 18)
% legend('Simulation', 'CRLB')

save('results.mat', 'data_f', 'data_t', 'snr_t')
```

APPENDIX E

MATLAB NETWORK SYSTEM SIMULATION

```
clear all
close all
clc
%%%%%%%%%%%%%%%%%%%%%%%%%%%%%%%%%%%%%%%%%%%%%%%%%%%%%%%%%%%%%%%%%%%%%%%%
fs=160e6;
dB=0:2:15;
MC=1000;
%%-----
    %vht (ac)
load 160MHz_SFW.mat
preamble=SFW;
%%-----
% t = ((0:length(vhtWaveform)-1)/fs);
t = ((0:length(preamble)-1)/fs);
% preamble=vhtWaveform(1:(fs*8e-6));
% t1 = ((0:length(preamble)-1)/(fs));
%%%%%%%%%%%%%%%%%%%%%%%%%%%%%%%%%%%%%%%%%%%%%%%%%%%%%%%%%%%%%%%%%%%%%%%%
% preamble_interp=[preamble; zeros(2*length(preamble),1)];
% yy=fftshift(10*log10(abs(fft(preamble_interp))));
% ff=fs*(0:length(yy)-1)/length(yy);
%%-----
for i_dB=1:length(dB)
    disp(i_dB)
```


APPENDIX F

MATLAB NETWORK SYSTEM MEASUREMENT PROCESSING

```
clear all
close all
clc
load vht_160.mat
cd 11_18_19
cd 160MHz_2
%%-----
    %802.11ac
fs =160e6; % Set sampling frequency = channel bandwidth
smpps=500e6;
dB=[0 3 6 10 13 16 20];
% dB=[16 20 26 30 36 40 46 50];
%%-----
% cfgVHT = wlanVHTConfig;
% cfgVHT.ChannelBandwidth=[ 'CBW' num2str( fs / 1e6 )];
% bits = [1;0;0;1;1];
% vhtWaveform = wlanWaveformGenerator( bits ,cfgVHT, ...
%     'NumPackets',1,'IdleTime',20e-6);
%%-----
t = ((0:length(vhtWaveform)-1)/fs);
t1=0:1/smpps:max(t);
vhtWaveform=interp1(t,vhtWaveform,t1);
preamble=vhtWaveform(1:(smpps*8e-6)+1);
```

```

[B,A]=butter(10,(80e6)/(smpps/2));
preamble=filter(B,A,preamble);
preamble=preamble-mean(preamble);

% preamble_interp=[preamble];
% y=fft(preamble_interp);
% L=length(preamble_interp);
%
% P2=10*log10(abs(y/L));
% P1=P2(1:(L/2)+1);
% P1(2:end-1)=2*P1(2:end-1);
% ff=smpps*(0:(L/2))/L;
%
% figure()
% plot(ff,P1)
% return

for i_dB=1:length(dB)
    disp(i_dB)
    load([num2str(dB(i_dB)) 'dB.mat'])
%     figure()
%     plot((1:length(waveform(:,1)))/smpps, waveform(:,1))
%     hold on
%     plot(t1, preamble_interp)
%     return
%     y=fft(waveform(:,1));

```

```

%     L=length ( waveform (: , 1 ) );
%
%     P2=10*log10 ( abs ( y / L ) );
%     P1=P2 ( 1 : ( L / 2 ) + 1 );
%     P1 ( 2 : end - 1 ) = 2 * P1 ( 2 : end - 1 );
%     ff=2*fs *( 0 : ( L / 2 ) ) / L;

%     figure ( )
%     plot ( ff , P1 )
%     return
for it=1:100
    disp ( it )
    waveform (: , it ) = filter ( B , A , waveform (: , it ) );
    waveform (: , it ) = waveform (: , it ) - mean ( waveform (: , it ) );

    [ Xs , lag ] = xcorr ( waveform (: , it ) , preamble );

%     figure ( )
%     plot ( lag / smpps , abs ( Xs ) )
%
%     return

[ ~ , lmxs ] = findpeaks ( abs ( Xs ) , ' SortStr ' , ' descend ' );
pp=1;
if it > 1
    [ ~ , pp ] = min ( abs ( lag ( lmxs ) / smpps - tops ( 1 ) ) );
end

%%-----

```



```
measured_variance=variance;  
measured_snr=snr;  
cd ..  
% cd ..  
% save('ac_160_data.mat','measured_variance','measured_snr')  
  
figure()  
semilogy(snr, variance, '-o')  
  
figure()  
semilogy(dB, variance)
```

APPENDIX G

MATLAB TTSFW SIMULATION

```
clear all
close all
clc
%%-----
BW=5e6;
NN=1:25;
fs=25e6;
MC=1000;
%%-----
    %waveform
for i_NN=1:length(NN)
    disp(i_NN)
    N=NN(i_NN);
    t=0:1/fs:1e-3/(2*N);

    waveform=0;
    for i_N=1:N
        df=BW/(2*N-1);
        Df=N*df;

        S=[exp(j*2*pi*(1e6+(i_N-1)*df)*t)+exp(j*2*pi*...
            (1e6+Df+(i_N-1)*df)*t) zeros(1,length(t))];
        waveform=cat(2, waveform, S);
    end
end
```



```

%      tt_std=std ( tops );
%      tt_mean=mean ( tops );
%      tops ( tops <( tt_mean -2* tt_std ) )= [];
%      tops ( tops >( tt_mean+2* tt_std ) )= [];

variance ( i_NN)= var ( tops );

temp=sort ( eig ( cov ( sing ) ) , ' descend ' );
sig_w=mean ( temp ( 5 : 1000 ) );
Ps = 1/995 * ( temp ( 1 ) - sig_w );
snr ( i_NN)= ( abs ( Ps / sig_w ) ) * 10 ^ ( 3 / 10 ) * ( 0.5 e - 3 * 12.5 e 6 );

TTSF_var ( i_NN)= 1 ./ ( 4 * snr ( i_NN ) * ( pi ^ 2 .* Df ^ 2 + ...
    ( 2 .* pi .* df ) ^ 2 ./ N .* ( N * ( 2 * N ^ 2 - 3 * N + 1 ) / 6 ) ) );

TT_var ( i_NN)= 1 ./ ( 4 * snr ( i_NN ) * ( pi ^ 2 .* Df ^ 2 ) );
TT_var ( i_NN)= 1 ./ ( 4 * snr ( i_NN ) * ( pi ^ 2 .* BW ^ 2 ) / 3 );
clear sing
clc

end

figure ()
plot ( lag , abs ( Xs ) )
%%-----
%Fourier
% y=fft ( waveform );
% P2=10*log10 ( abs ( y / length ( waveform ) ) );

```

```

% P1=P2(1:(length(waveform)/2)+1);
% P1(2:end-1)=2*P1(2:end-1);
% f=fs*(0:(length(waveform)/2))/length(waveform);
%%-----
% figure()
% plot(1:length(waveform), waveform)

% figure()
% plot(f, P1)

figure()
semilogy(NN, variance)
hold on
plot(NN, TTsf_var)

```

APPENDIX H

MATLAB DISTRIBUTED BEAMFORMING MEASUREMENT PROCESSING

```
clear all
close all
clc
%%%%%%%%%%%%%%%%%%%%%%%%%%%%%%%%%%%%%%%%%%%%%%%%%%%%%%%%%%%%%%%%%%%%%%%%%
step=1:9;

for i_step=1:length(step)
    load(['step_' num2str(step(i_step)) '.mat'])

    ch1=0;
    ch2=0;
    comb=0;
    for i=1:100
        temp1=findpeaks(waveform(:,i));

        ch1=[ch1 temp1'];
    end
    ch1_mean(i_step)=mean(ch1(2:end));
end
% cd ..
% lock_ch1=ch1_mean;
% lock_ch2=ch2_mean;
% lock_comb=comb_mean;
```


APPENDIX I

MATLAB SECURE TRANSMISSION SIMULATION FOR THE LINEAR CASE

```
clear all
close all
clc
%%%%%%%%%%%%%%%%%%%%%%%%%%%%%%%%%%%%%%%%%%%%%%%%%%%%%%%%%%%%%%%%%%%%%%%%
ang=pi/180*(-90:0.1:90);
lambda_f=0.9398/0.2;
lambda_n=0.1961/0.2;
num_bits=300000;
SNR=12.6;

AP=zeros(num_bits,length(ang));
%%%%%%%%%%%%%%%%%%%%%%%%%%%%%%%%%%%%%%%%%%%%%%%%%%%%%%%%%%%%%%%%%%%%%%%%
    %linear motion
d=fliplr(linspace(lambda_n,lambda_f,num_bits));
%%%%%%%%%%%%%%%%%%%%%%%%%%%%%%%%%%%%%%%%%%%%%%%%%%%%%%%%%%%%%%%%%%%%%%%%
%%%%%%%%%%%%%%%%%%%%%%%%%%%%%%%%%%%%%%%%%%%%%%%%%%%%%%%%%%%%%%%%%%%%%%%%
    %array pattern
for i_d=1:length(d)
    disp(i_d)

    AP(i_d,:)=1+exp(j*2*pi*d(i_d)*sin(ang));
end
AP=AP./max(max(abs(AP)));
```

```

clc

%data

bits_clean=randsample([-1 1],num_bits,'true');
% noise=wgn(1,num_bits,-SNR);
noise=awgn(AP(:,901),SNR)-AP(:,901);

%noise PSD
N = length(noise);
xdft = fftshift(fft(noise));
psdx = (1/(num_bits*N)) * (abs(xdft).^2);
noise_energy=sum(psdx);

%radiated data
for i_ap=1:length(AP(1,:))
    data=abs(AP(:,i_ap)).* bits_clean'+noise;

    if ang(i_ap)==pi/180*-20
        figure()
        plot([-2 2],[0 0],'k','Linewidth',1.5)
        hold on
        plot([0 0],[-2 2],'k','Linewidth',1.5)
        axis([-2 2 -2 2])
        scatter(data(1:500),zeros(1,500),60,'Filled')
        scatter([-1 1],zeros(1,2),60,'r','Filled')
    end
end

```

```

xlabel('I', 'FontSize', 22)
ylabel('Q', 'FontSize', 22)
xticks([-1 1])
yticks([])
elseif ang(i_ap)==0
figure()
plot([-2 2],[0 0], 'k', 'Linewidth', 1.5)
hold on
plot([0 0],[-2 2], 'k', 'Linewidth', 1.5)
scatter(data(1:500), zeros(1,500), 60, 'Filled')
scatter([-1 1], zeros(1,2), 60, 'r', 'Filled')
xlabel('I', 'FontSize', 22)
ylabel('Q', 'FontSize', 22)
axis([-2 2 -2 2])
xticks([-1 1])
yticks([])
elseif ang(i_ap)==pi/180*60
figure()
plot([-2 2],[0 0], 'k', 'Linewidth', 1.5)
hold on
plot([0 0],[-2 2], 'k', 'Linewidth', 1.5)
scatter(data(1:500), zeros(1,500), 60, 'Filled')
scatter([-1 1], zeros(1,2), 60, 'r', 'Filled')
xlabel('I', 'FontSize', 22)
ylabel('Q', 'FontSize', 22)
axis([-2 2 -2 2])
xticks([-1 1])

```



```

AP_mean=mean(AP);

BER_thry1=1/2*erfc(sqrt(abs(AP_mean).^2/(2*noise_energy)));
%
%
angl=ang;

%figures
figure()
semilogy(angl*180/pi,BER,'Linewidth',1.5)
hold on

% clear BER angl
% load results.mat
%
% semilogy(ang(1:13),BER(1:13),'g-o','Linewidth',1.5)
semilogy(angl*180/pi,BER_thry1,'--k','Linewidth',1.5)
axis([-90 90 -inf 1])
xlabel('Angle (deg)','FontSize',18)
ylabel('BER','FontSize',18)
grid on
% legend('Simulated','Measured','Estimation')
legend('Simulated','Estimation')

```

APPENDIX J

MATLAB SECURE TRANSMISSION MEASUREMENT PROCESSING FOR THE LINEAR CASE

```
clear all
close all
clc
%
ang = -60:10:60;
template = load('mls.txt');
%
for i_ang = 1:length(ang)
    disp(i_ang)
    temp = load(['waveform_' num2str(ang(i_ang)) '.txt']);

    temp = temp((end-4000):end, :);

    temp1 = max(max(temp));
    temp2 = min(min(temp));
    if abs(temp1) < abs(temp2)
        temp = -temp;
    end
    [row, col] = find(temp == max(abs([temp1 temp2])));
    [~, loc] = find(temp(row, :) > max(abs([temp1 temp2]))/2);
    temp = [temp(:, loc(1)+1+10:end) temp(:, 1:loc(1))];

%    figure()
```

```

%      plot(1:length(temp(1,:)),temp(row,:))
%      return

for i_it=1:length(temp(:,1))
    disp(i_it)

    place=5:10:length(temp(i_it,:));
    for i_demod=1:length(place)
        wf_demod(i_demod)=mean(temp(i_it,place(i_demod)...
            -4:place(i_demod)+4));
    end
    wf_demod(wf_demod>0)=1;
    wf_demod(wf_demod<1)=-1;

%      if ang(i_ang)==0
%          wf_demod(1)=-wf_demod(1);
%      end

    temp_BER(i_it)=sum(abs(wf_demod'-template(2:end))/2)...
        /(length(template)-1);
end
BER(i_ang)=mean(temp_BER);

temp=sort(eig(cov(temp')), 'descend');
sig_w=mean(temp(2:length(temp(:,1))));
Ps=1/length(temp(:,1))*(temp(1)-sig_w);

```

```
snr(i_ang)=10*log10(abs(Ps/sig_w));

clear temp
clc
end

figure()
semilogy(ang,BER)

save('results.mat','BER','ang')
```

APPENDIX K

MATLAB SECURE TRANSMISSION SIMULATION FOR THE SINUSOIDAL CASE

```
clear all
close all
clc
%%%%%%%%%%%%%%%%%%%%%%%%%%%%%%%%%%%%%%%%%%%%%%%%%%%%%%%%%%%%%%%%%%%%%%%%
ang=pi/180*(-90:0.1:90);
lambda_f=0.9398/0.2;
lambda_n=0.1961/0.2;
num_bits=300000;
SNR=12;

AP=zeros(num_bits,length(ang));
%%%%%%%%%%%%%%%%%%%%%%%%%%%%%%%%%%%%%%%%%%%%%%%%%%%%%%%%%%%%%%%%%%%%%%%%
    %sinusoidal motion
d=cos(linspace(0,2*pi,2*num_bits))*(lambda_f-lambda_n)/2...
    +(lambda_n+lambda_f)/2;
d=d(num_bits+1:end);

% figure()
% plot(1:num_bits,0.2*d)
% return
%%%%%%%%%%%%%%%%%%%%%%%%%%%%%%%%%%%%%%%%%%%%%%%%%%%%%%%%%%%%%%%%%%%%%%%%
%%%%%%%%%%%%%%%%%%%%%%%%%%%%%%%%%%%%%%%%%%%%%%%%%%%%%%%%%%%%%%%%%%%%%%%%
    %array pattern
```

```

for i_d=1:length(d)
    disp(i_d)

    AP(i_d,:)=1+exp(j*2*pi*d(i_d)*sin(ang));
end
AP=AP./max(max(abs(AP)));

clc

%data
bits_clean=randsample([-1 1],num_bits,'true');
% noise=wgn(1,num_bits,-SNR);
noise=awgn(AP(:,901),SNR)-AP(:,901);

%noise PSD
N = length(noise);
xdft = fftshift(fft(noise));
psdx = (1/(num_bits*N)) * (abs(xdft).^2);
noise_energy=sum(psdx);

%radiated data
for i_ap=1:length(AP(1,:))
    data=abs(AP(:,i_ap)).* bits_clean'+noise;

    bit_energy(i_ap)=abs(mean(AP(:,i_ap)))^2;

```



```

%figures
figure()
semilogy(ang1*180/pi,BER,'Linewidth',1.5)
hold on

clear BER ang
load results.mat

semilogy(ang(1:13),BER(1:13),'g-o','Linewidth',1.5)
semilogy(ang1*180/pi,BER_thry1,'--k','Linewidth',1.5)
axis([-90 90 -inf 1])
xlabel('Angle (deg)','FontSize',18)
ylabel('BER','FontSize',18)
grid on
legend('Simulated','Measured','Estimation')

```

APPENDIX L

MATLAB SECURE TRANSMISSION MEASUREMENT PROCESSING FOR THE SINUSOIDAL CASE

```
clear all
close all
clc
%
ang = -60:10:60;
template = load('mls.txt');
%
for i_ang = 1:length(ang)
    disp(i_ang)
    temp = load(['waveform_' num2str(ang(i_ang)) '.txt']);

    temp = temp((end - 5500):end, :);

    temp1 = max(max(temp));
    temp2 = min(min(temp));
    if abs(temp1) < abs(temp2)
        temp = -temp;
    end
    [row, col] = find(temp == max(abs([temp1 temp2])));
    [~, loc] = find(temp(row, :) > max(abs([temp1 temp2]))/2);
    temp = [temp(:, loc(1)+1+10:end) temp(:, 1:loc(1))];

%    figure()
```

```

%      plot(1:length(temp(1,:)),temp(row,:))
%      return

for i_it=1:length(temp(:,1))
    disp(i_it)

    place=5:10:length(temp(i_it,:));
    for i_demod=1:length(place)
        wf_demod(i_demod)=mean(temp(i_it,place(i_demod)...
            -4:place(i_demod)+4));
    end
    wf_demod(wf_demod>0)=1;
    wf_demod(wf_demod<1)=-1;

%      if ang(i_ang)==0
%          wf_demod(1)=-wf_demod(1);
%      end

    temp_BER(i_it)=sum(abs(wf_demod'-template(2:end))/2)...
        /(length(template)-1);
end
BER(i_ang)=mean(temp_BER);

temp=sort(eig(cov(temp')), 'descend');
sig_w=mean(temp(2:length(temp(:,1))));
Ps=1/length(temp(:,1))*(temp(1)-sig_w);

```

```
snr(i_ang)=10*log10(abs(Ps/sig_w));

clear temp
clc
end

figure()
semilogy(ang,BER)

save('results.mat','BER','ang')
```

BIBLIOGRAPHY

BIBLIOGRAPHY

- [1] P. Bidigare, M. Oyarzyn, D. Raeman, D. Chang, D. Cousins, R. O'Donnell, C. Obranovich, and D. R. Brown. Implementation and demonstration of receiver-coordinated distributed transmit beamforming across an ad-hoc radio network. In *2012 Conference Record of the Forty Sixth Asilomar Conference on Signals, Systems and Computers (ASILOMAR)*, pages 222–226, Nov 2012.
- [2] R. Mudumbai, J. Hespanha, U. Madhow, and G. Barriac. Scalable feedback control for distributed beamforming in sensor networks. In *Proceedings. International Symposium on Information Theory, 2005. ISIT 2005.*, pages 137–141, 2005.
- [3] D. R. Brown III and H. V. Poor. Time-slotted round-trip carrier synchronization for distributed beamforming. *IEEE Transactions on Signal Processing*, 56(11):5630–5643, Nov 2008.
- [4] B. Peiffer, R. Mudumbai, A. Kruger, A. Kumar, and S. Dasgupta. Experimental demonstration of a distributed antenna array pre-synchronized for retrodirective transmission. In *2016 Annual Conference on Information Science and Systems (CISS)*, pages 460–465, March 2016.
- [5] R. Mudumbai, G. Barriac, and U. Madhow. On the feasibility of distributed beamforming in wireless networks. *IEEE Transactions on Wireless Communications*, 6(5):1754–1763, May 2007.
- [6] S. Prager, M. S. Haynes, and M. Moghaddam. Wireless subnanosecond rf synchronization for distributed ultrawideband software-defined radar networks. *IEEE Transactions on Microwave Theory and Techniques*, 68(11):4787–4804, 2020.
- [7] G. Barriac, R. Mudumbai, and U. Madhow. Distributed beamforming for information transfer in sensor networks. In *Third International Symposium on Information Processing in Sensor Networks, 2004. IPSN 2004*, pages 81–88, April 2004.
- [8] J. A. Nanzer, R. L. Schmid, T. M. Comberiate, and J. E. Hodkin. Open-loop coherent distributed arrays. *IEEE Transactions on Microwave Theory and Techniques*, 65(5):1662–1672, May 2017.
- [9] A. I. Zaghroui, O. Kilic, L. Q. Sun, and M. Lieberman. Distributed aperture design for low profile earth station antennas. In *IEEE Antennas and Propagation Society International Symposium. 1999 Digest. Held in conjunction with: USNC/URSI National Radio Science Meeting (Cat. No.99CH37010)*, volume 3, pages 2088–2091 vol.3, July 1999.
- [10] P. Benthem and G. W. Kant. Embrace: Results from an aperture array for radio astronomy. In *2012 6th European Conference on Antennas and Propagation (EUCAP)*, pages 629–633, March 2012.

- [11] F. K. Sharifabad, M. A. Jensen, and A. L. Anderson. Array beamforming synthesis for point-to-point mimo communication. *IEEE Trans. Antennas Propag.*, 63(9):3878–3886, Sep. 2015.
- [12] M. A. Jensen and J. W. Wallace. A review of antennas and propagation for mimo wireless communications. *IEEE Trans. Antennas Propag.*, 52(11):2810–2824, Nov 2004.
- [13] M. D. Migliore. On the role of the number of degrees of freedom of the field in mimo channels. *IEEE Trans. Antennas Propag.*, 54(2):620–628, Feb 2006.
- [14] F. K. Sharifabad, M. A. Jensen, J. Medbo, and J. Furuskog. Measurement-based performance analysis of cooperative mimo beamforming. *IEEE Antennas Wireless Propag. Lett.*, 11:1394–1397, 2012.
- [15] S. Jayaprakasam, S. K. Abdul Rahim, C. Y. Leow, T. O. Ting, and A. A. Eteng. Multi-objective beam pattern optimization in collaborative beamforming via nsga-ii with selective distance. *IEEE Trans. Antennas Propag.*, 65(5):2348–2357, May 2017.
- [16] D. C. Jenn. Transmission equation for multiple cooperative transmitters and collective beamforming. *IEEE Antennas Wireless Propag. Lett.*, 7:606–608, 2008.
- [17] Y. Fan, Y. Zhou, D. He, and W. Xia. Fast transmit beamforming with distributed antennas. *IEEE Antennas Wireless Propag. Lett.*, 16:121–124, 2017.
- [18] S. Goguri, D. Ogbe, S. Dasgupta, R. Mudumbai, D. R. Brown, D. J. Love, and U. Madhow. Optimal precoder design for distributed transmit beamforming over frequency-selective channels. *IEEE Trans. Wireless Commun.*, 17(11):7759–7773, Nov 2018.
- [19] M. Rossi, A. M. Haimovich, and Y. C. Eldar. Spatial compressive sensing for mimo radar. *IEEE Trans. Signal Process.*, 62(2):419–430, Jan 2014.
- [20] MK Arti and Manav R Bhatnagar. Beamforming and combining in hybrid satellite-terrestrial cooperative systems. *IEEE Communications Letters*, 18(3):483–486, 2014.
- [21] Minseok Kim, Jun-ichi Takada, and Yohei Konishi. Novel scalable mimo channel sounding technique and measurement accuracy evaluation with transceiver impairments. *IEEE Transactions on Instrumentation and Measurement*, 61(12):3185–3197, 2012.
- [22] Geoffrey F Edelmann and Charles F Gaumond. Beamforming using compressive sensing. *The Journal of the Acoustical Society of America*, 130(4):EL232–EL237, 2011.
- [23] Y. Buchris, A. Amar, J. Benesty, and I. Cohen. Incoherent synthesis of sparse arrays for frequency-invariant beamforming. *IEEE/ACM Transactions on Audio, Speech, and Language Processing*, 27(3):482–495, 2019.
- [24] Steven J Gibbons, Frode Ringdal, and Tormod Kværna. Detection and characterization of seismic phases using continuous spectral estimation on incoherent and partially coherent arrays. *Geophysical Journal International*, 172(1):405–421, 2008.

- [25] Seth S Kessler, Eric B Flynn, and Michael D Todd. Hybrid coherent/incoherent beam forming diagnostic approach to naval assets. In *Proceedings of the 8th International Workshop on Structural Health Monitoring*, volume 2, pages 1839–1846, 2011.
- [26] C. Chen, C. Tseng, J. Denis, and C. Lin. Adaptive distributed beamforming for amplify-and-forward relay networks: Convergence analysis. *IEEE Transactions on Wireless Communications*, 13(8):4167–4178, Aug 2014.
- [27] Raghuraman Mudumbai, D Richard Brown Iii, Upamanyu Madhow, and H Vincent Poor. Distributed transmit beamforming: challenges and recent progress. *IEEE Communications Magazine*, 47(2):102–110, 2009.
- [28] R. L. Schmid, S. M. Ellison, T. M. Comberiate, J. E. Hodkin, and J. A. Nanzer. Microwave wireless coordination technologies for coherent distributed maritime radar. In *2017 IEEE MTT-S International Microwave Symposium (IMS)*, pages 884–887, June 2017.
- [29] Wei-Hao Chiu, Yu-Hsiang Huang, and Tsung-Hsien Lin. A dynamic phase error compensation technique for fast-locking phase-locked loops. *IEEE Journal of Solid-State Circuits*, 45(6):1137–1149, 2010.
- [30] Thomas Musch, Michael Gerding, and Burkhard Schiek. A phase-locked-loop concept for the generation of two rf-signals with a small frequency offset. *IEEE transactions on instrumentation and measurement*, 54(2):709–712, 2005.
- [31] H. Ouassal, T. Rocco, M. Yan, and J. A. Nanzer. Decentralized frequency synchronization in distributed antenna arrays with quantized frequency states and directed communications. *IEEE Transactions on Antennas and Propagation*, pages 1–1, 2020.
- [32] T. Musch, M. Gerding, and B. Schiek. A phase-locked-loop concept for the generation of two rf-signals with a small frequency offset. *IEEE Transactions on Instrumentation and Measurement*, 54(2):709–712, April 2005.
- [33] W. Chiu, Y. Huang, and T. Lin. A dynamic phase error compensation technique for fast-locking phase-locked loops. *IEEE Journal of Solid-State Circuits*, 45(6):1137–1149, June 2010.
- [34] S. Mghabghab, H. Ouassal, and J. A. Nanzer. Wireless frequency synchronization for coherent distributed antenna arrays. In *2019 IEEE International Symposium on Antennas and Propagation and USNC-URSI Radio Science Meeting*, pages 1575–1576, July 2019.
- [35] Pratik Chatterjee and Jeffrey A Nanzer. Effects of time alignment errors in coherent distributed radar. In *Radar Conference (RadarConf18), 2018 IEEE*, pages 0727–0731. IEEE, 2018.
- [36] C Shen and H Yu. Time-delay alignment technique for a randomly distributed sensor array. *IET communications*, 5(8):1068–1072, 2011.
- [37] P. Yin, X. Yang, T. Zeng, and X. Hu. Robust time synchronization method based on step frequency signal for wideband distributed coherent aperture radar. In *2013 IEEE International Symposium on Phased Array Systems and Technology*, pages 383–388, Oct 2013.

- [38] A. Tashlinskiy and M. Tsarev. An algorithm for time shift estimation of radio pulses received by spatially distributed sensors. In *2015 International Siberian Conference on Control and Communications (SIBCON)*, pages 1–4, May 2015.
- [39] C. Shen and H. Yu. Time-delay alignment technique for a randomly distributed sensor array. *IET Communications*, 5(8):1068–1072, May 2011.
- [40] P. Chatterjee and J. A. Nanzer. Effects of time alignment errors in coherent distributed radar. In *2018 IEEE Radar Conference (RadarConf18)*, pages 0727–0731, April 2018.
- [41] P. Chatterjee and J. A. Nanzer. Sdr-based wireless time alignment for coherent distributed beamforming. In *2019 USNC-URSI Radio Science Meeting*, July 2019.
- [42] R. Mudumbai, D. R. Brown Iii, U. Madhow, and H. V. Poor. Distributed transmit beamforming: challenges and recent progress. *IEEE Communications Magazine*, 47(2):102–110, February 2009.
- [43] D. R. Brown, G. B. Prince, and J. A. McNeill. A method for carrier frequency and phase synchronization of two autonomous cooperative transmitters. In *IEEE 6th Workshop on Signal Processing Advances in Wireless Communications, 2005.*, pages 260–264, 2005.
- [44] Raghuraman Mudumbai, Ben Wild, Upamanyu Madhow, and Kannan Ramchandran. Distributed beamforming using 1 bit feedback: from concept to realization. In *Proceedings of the 44th Allerton conference on communication, control and computation*, volume 8, pages 1020–1027, 2006.
- [45] W. Tushar and D. B. Smith. Distributed transmit beamforming based on a 3-bit feedback system. In *2010 IEEE 11th International Workshop on Signal Processing Advances in Wireless Communications (SPAWC)*, pages 1–5, June 2010.
- [46] R. D. Preuss and D. R. Brown, III. Two-way synchronization for coordinated multicell retrodirective downlink beamforming. *IEEE Transactions on Signal Processing*, 59(11):5415–5427, Nov 2011.
- [47] R. D. Preuss and D. R. Brown. Retrodirective distributed transmit beamforming with two-way source synchronization. In *2010 44th Annual Conference on Information Sciences and Systems (CISS)*, pages 1–6, 2010.
- [48] B. Peiffer, R. Mudumbai, S. Goguri, A. Kruger, and S. Dasgupta. Experimental demonstration of retrodirective beamforming from a fully wireless distributed array. In *MILCOM 2016 - 2016 IEEE Military Communications Conference*, pages 442–447, 2016.
- [49] Walter Christoph Haggmann. Network synchronization techniques for satellite communication systems. 1982.
- [50] J. L. Wang, S. Y. Huang, and C. S. Liao. Time and frequency transfer system using gnss receiver. *Radio Science*, 49(12):1171–1182, Dec 2014.

- [51] WQ Wang, CB Ding, and XD Liang. Time and phase synchronisation via direct-path signal for bistatic synthetic aperture radar systems. *IET Radar, Sonar & Navigation*, 2(1):1–11, 2008.
- [52] T. M. Comberiate, R. L. Schmid, J. E. Hodkin, M. D. Sharp, and J. A. Nanzer. A bandpass sampling receiver for wide-bandwidth, spectrally-sparse waveforms for high-accuracy range measurements. *IEEE Microwave and Wireless Components Letters*, 27(1):88–90, Jan 2017.
- [53] L. Hu, S. Zhang, and G. Lu. Observation-to-track pairing using electro-optical(eo) systems. In *2006 International Conference on Mechatronics and Automation*, pages 589–594, June 2006.
- [54] S. C. Taylor. High-precision tracking: an essential component of the optical multiple access (oma) system. In *IEE Colloquium on Optical Intersatellite Links and On-Board Techniques*, pages 12/1–12/7, Jan 1990.
- [55] J. R. Klauder, A. C. Price, S. Darlington, and W. J. Albersheim. The theory and design of chirp radars. *The Bell System Technical Journal*, 39(4):745–808, July 1960.
- [56] B. L. Lewis and F. F. Kretschmer. Linear frequency modulation derived polyphase pulse compression codes. *IEEE Transactions on Aerospace and Electronic Systems*, AES-18(5):637–641, 1982.
- [57] Ran Tao, Nan Zhang, and Yue Wang. Analysing and compensating the effects of range and doppler frequency migrations in linear frequency modulation pulse compression radar. *IET radar, sonar & navigation*, 5(1):12–22, 2011.
- [58] Nicolas Grein and Hermann Winner. Fmcw radar system with linear frequency modulation, October 12 1993. US Patent 5,252,981.
- [59] R. Li-xiang and M. Er-ke. Study on hprf pulsed doppler stepped frequency radar system. In *2006 CIE International Conference on Radar*, pages 1–4, Oct 2006.
- [60] Irina Gladkova. Analysis of stepped-frequency pulse train design. *IEEE Transactions on Aerospace and Electronic Systems*, 45(4):1251–1261, 2009.
- [61] Andrew J Wilkinson, Richard T Lord, and Michael R Inggs. Stepped-frequency processing by reconstruction of target reflectivity spectrum. In *Proceedings of the 1998 South African Symposium on Communications and Signal Processing-COMSIG'98 (Cat. No. 98EX214)*, pages 101–104. IEEE, 1998.
- [62] Lei Zhang, Zhi-jun Qiao, Mengdao Xing, Yachao Li, and Zheng Bao. High-resolution isar imaging with sparse stepped-frequency waveforms. *IEEE Transactions on Geoscience and Remote Sensing*, 49(11):4630–4651, 2011.
- [63] John C Curlander and Robert N McDonough. *Synthetic aperture radar*, volume 11. Wiley, New York, 1991.
- [64] Mehrdad Soumekh. *Synthetic aperture radar signal processing*, volume 7. New York: Wiley, 1999.

- [65] J Patrick Fitch. *Synthetic aperture radar*. Springer Science & Business Media, 2012.
- [66] Giorgio Franceschetti and Riccardo Lanari. *Synthetic aperture radar processing*. CRC press, 1999.
- [67] Ettien Kpré, Cyril Decroze, Moctar Mouhamadou, and Thomas Fromenteze. Computational imaging for compressive synthetic aperture interferometric radiometer. *IEEE Transactions on Antennas and Propagation*, 66(10):5546–5557, 2018.
- [68] A Richard Thompson, James M Moran, and George W Swenson Jr. *Interferometry and synthesis in radio astronomy*. Springer Nature, 2017.
- [69] A. Babakhani, D. B. Rutledge, and A. Hajimiri. Transmitter architectures based on near-field direct antenna modulation. *IEEE Journal of Solid-State Circuits*, 43(12):2674–2692, 2008.
- [70] A. Babakhani, D. B. Rutledge, and A. Hajimiri. A near-field modulation technique using antenna reflector switching. In *2008 IEEE International Solid-State Circuits Conference - Digest of Technical Papers*, pages 188–605, 2008.
- [71] A. H. Chang, A. Babakhani, and A. Hajimiri. Near-field direct antenna modulation (nf-dam) transmitter at 2.4ghz. In *2009 IEEE Antennas and Propagation Society International Symposium*, pages 1–4, 2009.
- [72] W. Kummer, A. Villeneuve, T. Fong, and F. Terrio. Ultra-low sidelobes from time-modulated arrays. *IEEE Transactions on Antennas and Propagation*, 11(6):633–639, 1963.
- [73] B. Lewis and J. Evins. A new technique for reducing radar response to signals entering antenna sidelobes. *IEEE Transactions on Antennas and Propagation*, 31(6):993–996, 1983.
- [74] Shiwen Yang, Y. . Gan, and Peng Khiang Tan. Linear antenna arrays with bidirectional phase center motion. *IEEE Transactions on Antennas and Propagation*, 53(5):1829–1835, 2005.
- [75] M. P. Daly and J. T. Bernhard. Directional modulation technique for phased arrays. *IEEE Transactions on Antennas and Propagation*, 57(9):2633–2640, 2009.
- [76] M. P. Daly, E. L. Daly, and J. T. Bernhard. Demonstration of directional modulation using a phased array. *IEEE Transactions on Antennas and Propagation*, 58(5):1545–1550, 2010.
- [77] M. P. Daly and J. T. Bernhard. Beamsteering in pattern reconfigurable arrays using directional modulation. *IEEE Transactions on Antennas and Propagation*, 58(7):2259–2265, 2010.
- [78] M. P. Daly and J. T. Bernhard. Directional modulation and coding in arrays. In *2011 IEEE International Symposium on Antennas and Propagation (APSURSI)*, pages 1984–1987, 2011.
- [79] Merrill Ivan Skolnik et al. *Introduction to radar systems*, volume 3. McGraw-hill New York, 1980.

- [80] Mark A Richards, Jim Scheer, William A Holm, and William L Melvin. *Principles of modern radar*. Citeseer, 2010.
- [81] B Roy Frieden. *Science from Fisher information*. 2004.
- [82] H.L. Van Trees. *Detection, Estimation, and Modulation Theory, Part I: Detection, Estimation, and Linear Modulation Theory*. Number pt. 1. Wiley, 2004.
- [83] M. Hamid, N. Björnell, and S. Ben Slimane. Sample covariance matrix eigenvalues based blind snr estimation. In *2014 IEEE International Instrumentation and Measurement Technology Conference (I2MTC) Proceedings*, pages 718–722, May 2014.
- [84] G. Lellouch, R. Pribic, and P. van Genderen. Frequency agile stepped ofdm waveform for hrr. In *2009 International Waveform Diversity and Design Conference*, pages 90–93, Feb 2009.
- [85] G. S. Gill and Jen-Chih Huang. The ambiguity function of the step frequency radar signal processor. In *Proceedings of International Radar Conference*, pages 375–380, Oct 1996.
- [86] J. A. Nanzer and M. D. Sharp. On the estimation of angle rate in radar. *IEEE Transactions on Antennas and Propagation*, 65(3):1339–1348, March 2017.
- [87] David Slepian and Henry Pollak. Prolate spheroidal wave functions, fourier analysis and uncertainty—i. *Bell System Technical Journal*, 40(1):43–63, 1961.
- [88] Henry Landau and Henry Pollak. Prolate spheroidal wave functions, fourier analysis and uncertainty—ii. *Bell System Technical Journal*, 40(1):65–84, 1961.
- [89] Henry Landau and Henry Pollak. Prolate spheroidal wave functions, fourier analysis and uncertainty—iii: the dimension of the space of essentially time-and band-limited signals. *Bell System Technical Journal*, 41(4):1295–1336, 1962.
- [90] David Slepian. Prolate spheroidal wave functions, fourier analysis and uncertainty—iv: extensions to many dimensions; generalized prolate spheroidal functions. *Bell System Technical Journal*, 43(6):3009–3057, 1964.
- [91] David Slepian. Prolate spheroidal wave functions, fourier analysis, and uncertainty—v: The discrete case. *Bell System Technical Journal*, 57(5):1371–1430, 1978.
- [92] David Slepian. Some comments on fourier analysis, uncertainty and modeling. *SIAM review*, 25(3):379–393, 1983.
- [93] A Karoui. High frequency classical and circular prolate spheroidal wave functions and approximation of almost band-limited functions. *preprint*, 2008.
- [94] Gregory Beylkin and Lucas Monzon. On generalized gaussian quadratures for exponentials and their applications. *Applied and Computational Harmonic Analysis*, 12(3):332–373, 2002.

- [95] Hong Xiao, Vladimir Rokhlin, and Norman Yarvin. Prolate spheroidal wavefunctions, quadrature and interpolation. *Inverse problems*, 17(4):805, 2001.
- [96] Kedar Khare and Nicholas George. Sampling theory approach to prolate spheroidal wavefunctions. *Journal of Physics A: Mathematical and General*, 36(39):10011, 2003.
- [97] G Walter and T Soleski. A new friendly method of computing prolate spheroidal wave functions and wavelets. *Applied and Computational Harmonic Analysis*, 19(3):432–443, 2005.
- [98] CJ Bouwkamp. On spheroidal wave functions of order zero. *Journal of Mathematics and Physics*, 26(1-4):79–92, 1947.
- [99] Carson Flammer. *Spheroidal wave functions*. Courier Corporation, 2014.
- [100] Li-Lian Wang. A review of prolate spheroidal wave functions from the perspective of spectral methods. *J. Math. Study*, 50(2):101–143, 2017.
- [101] Julien Barral and Stéphane Seuret. *Recent developments in fractals and related fields*. Springer, 2010.
- [102] Vladimir Rokhlin and Hong Xiao. Approximate formulae for certain prolate spheroidal wave functions valid for large values of both order and band-limit. *Applied and Computational Harmonic Analysis*, 22(1):105–123, 2007.
- [103] Qian-Yong Chen, David Gottlieb, and Jan S HeSthaven. Spectral methods based on prolate spheroidal wave functions for hyperbolic pdes. *SIAM Journal on Numerical Analysis*, 43(5):1912–1933, 2005.
- [104] S. M. Ellison and J. A. Nanzer. Waveform design for improved doppler accuracy. In *2018 USNC-URSI Radio Science Meeting (Joint with AP-S Symposium)*, pages 11–12, July 2018.
- [105] M. I. Skolnik. *Introduction to Radar Systems*. McGraw-Hill, 1962.
- [106] J. Zuo, R. Yang, S. Luo, and Y. Zhou. Range sidelobe suppression for ofdm-integrated radar and communication signal. *The Journal of Engineering*, 2019(21):7624–7627, 2019.
- [107] J. Gu, J. Moghaddasi, and K. Wu. Delay and doppler shift estimation for ofdm-based radar-radio (radcom) system. In *2015 IEEE International Wireless Symposium (IWS 2015)*, pages 1–4, 2015.
- [108] F. Zhang, Z. Zhang, W. Yu, and T. Truong. Joint range and velocity estimation with intrapulse and intersubcarrier doppler effects for ofdm-based radcom systems. *IEEE Transactions on Signal Processing*, 68:662–675, 2020.
- [109] C. Sturm, E. Pancera, T. Zwick, and W. Wiesbeck. A novel approach to ofdm radar processing. In *2009 IEEE Radar Conference*, pages 1–4, 2009.

- [110] Ieee standard for information technology– local and metropolitan area networks– specific requirements– part 11: Wireless lan medium access control (mac)and physical layer (phy) specifications amendment 5: Enhancements for higher throughput. *IEEE Std 802.11n-2009 (Amendment to IEEE Std 802.11-2007 as amended by IEEE Std 802.11k-2008, IEEE Std 802.11r-2008, IEEE Std 802.11y-2008, and IEEE Std 802.11w-2009)*, pages 1–565, Oct 2009.
- [111] L. Cimini. Analysis and simulation of a digital mobile channel using orthogonal frequency division multiplexing. *IEEE Transactions on Communications*, 33(7):665–675, July 1985.
- [112] Reinhard Feger, Christoph Wagner, Stefan Schuster, Stefan Scheiblhofer, Herbert Jager, and Andreas Stelzer. A 77-ghz fmcw mimo radar based on an sige single-chip transceiver. *IEEE Transactions on Microwave theory and Techniques*, 57(5):1020–1035, 2009.
- [113] Cemin Zhang, Michael J Kuhn, Brandon C Merkl, Aly E Fathy, and Mohamed R Mahfouz. Real-time noncoherent uwb positioning radar with millimeter range accuracy: Theory and experiment. *IEEE Transactions on Microwave Theory and Techniques*, 58(1):9–20, 2009.
- [114] Andreas Stelzer, Christian G Diskus, Kurt Lubke, and Hartwig W Thim. A microwave position sensor with submillimeter accuracy. *IEEE Transactions on Microwave Theory and Techniques*, 47(12):2621–2624, 1999.
- [115] C Meier, A Terzis, and S Lindenmeier. A robust 3d high precision radio location system. In *2007 IEEE/MTT-S International Microwave Symposium*, pages 397–400. IEEE, 2007.
- [116] Zhengyu Peng, Lixin Ran, and Changzhi Li. A k -band portable fmcw radar with beam-forming array for short-range localization and vital-doppler targets discrimination. *IEEE Transactions on Microwave Theory and Techniques*, 65(9):3443–3452, 2017.
- [117] J. E. Hodkin, K. S. Zilevu, M. D. Sharp, T. M. Comberiate, S. M. Hendrickson, M. J. Fitch, and J. A. Nanzer. Microwave and millimeter-wave ranging for coherent distributed rf systems. In *2015 IEEE Aerospace Conference*, pages 1–7, March 2015.
- [118] Rudolph Emil Kalman. A new approach to linear filtering and prediction problems. *Journal of basic Engineering*, 82(1):35–45, 1960.
- [119] S. J. Julier and J. K. Uhlmann. Unscented filtering and nonlinear estimation. *Proceedings of the IEEE*, 92(3):401–422, March 2004.
- [120] Andrew H Jazwinski. *Stochastic processes and filtering theory*. Courier Corporation, 2007.
- [121] Harold Wayne Sorenson. *Kalman filtering: theory and application*. IEEE, 1985.
- [122] Simon J Julier and Jeffrey K Uhlmann. New extension of the kalman filter to nonlinear systems. In *Signal processing, sensor fusion, and target recognition VI*, volume 3068, pages 182–193. International Society for Optics and Photonics, 1997.
- [123] S. J. Julier. The scaled unscented transformation. In *Proceedings of the 2002 American Control Conference (IEEE Cat. No.CH37301)*, volume 6, pages 4555–4559 vol.6, May 2002.

- [124] Eric A Wan and Rudolph Van Der Merwe. The unscented kalman filter for nonlinear estimation. In *Proceedings of the IEEE 2000 Adaptive Systems for Signal Processing, Communications, and Control Symposium (Cat. No. 00EX373)*, pages 153–158. Ieee, 2000.
- [125] S. Mghabghab and J. A. Nanzer. A self-mixing receiver for wireless frequency synchronization in coherent distributed arrays. In *2020 IEEE/MTT-S International Microwave Symposium (IMS)*, pages 1137–1140, 2020.
- [126] Ieee standard for a precision clock synchronization protocol for networked measurement and control systems. *IEEE Std 1588-2008 (Revision of IEEE Std 1588-2002)*, pages 1–300, 2008.
- [127] John C Eidson. *Measurement, control, and communication using IEEE 1588*. Springer Science & Business Media, 2006.
- [128] Jeremy Elson, Lewis Girod, and Deborah Estrin. Fine-grained network time synchronization using reference broadcasts. *ACM SIGOPS Operating Systems Review*, 36(SI):147–163, 2002.
- [129] Saurabh Ganeriwal, Ram Kumar, and Mani B Srivastava. Timing-sync protocol for sensor networks. In *Proceedings of the 1st international conference on Embedded networked sensor systems*, pages 138–149, 2003.
- [130] Miklós Maróti, Branislav Kusy, Gyula Simon, and Ákos Lédeczi. The flooding time synchronization protocol. In *Proceedings of the 2nd international conference on Embedded networked sensor systems*, pages 39–49, 2004.
- [131] Dave Zachariah, Satyam Dwivedi, Peter Händel, and Petre Stoica. Scalable and passive wireless network clock synchronization in los environments. *IEEE Transactions on Wireless Communications*, 16(6):3536–3546, 2017.
- [132] Marcelo Segura, Somasundaram Niranjayan, Hossein Hashemi, and Andreas F Molisch. Experimental demonstration of nanosecond-accuracy wireless network synchronization. In *2015 IEEE International Conference on Communications (ICC)*, pages 6205–6210. IEEE, 2015.
- [133] Benoit Denis, J-B Pierrot, and Chadi Abou-Rjeily. Joint distributed synchronization and positioning in uwb ad hoc networks using toa. *IEEE transactions on microwave theory and techniques*, 54(4):1896–1911, 2006.
- [134] S. D. Keller, W. D. Palmer, and W. T. Joines. Electromagnetic modeling and simulation of a directly-modulated l-band microstrip patch antenna. In *2007 IEEE Antennas and Propagation Society International Symposium*, pages 4489–4492, 2007.
- [135] E. J. Baghdady. Directional signal modulation by means of switched spaced antennas. *IEEE Transactions on Communications*, 38(4):399–403, 1990.
- [136] Carl M Elam and Dale A Leavy. Secure communication using array transmitter, August 14 2001. US Patent 6,275,679.

- [137] Constantine A Balanis. *Antenna theory: analysis and design*. John wiley & sons, 2016.
- [138] John Proakis. Masoud salehi digital communications, 2008.